

Properties of Zincblende GaN and (In,Ga,Al)N Heterostructures grown by Molecular Beam Epitaxy

JOCHEN R. MÜLLHÄUSER

PAUL-DRUDE-INSTITUT FÜR
FESTKÖRPERELEKTRONIK BERLIN
HUMBOLDT-UNIVERSITÄT ZU BERLIN
1998

Properties of Zincblende GaN and (In,Ga,Al)N Heterostructures grown by Molecular Beam Epitaxy

DISSERTATION

zur Erlangung des akademischen Grades

doctor rerum naturalium

(Dr. rer. nat.)

im Fach Physik

eingereicht an der

Mathematisch-Naturwissenschaftlichen Fakultät I

der Humboldt-Universität zu Berlin

von

DIPL. PHYS., MATH. JOCHEN R. MÜLLHÄUSER

geb. am 22.03.67 in Freiburg i. Brg.

Präsident der Humboldt-Universität zu Berlin

Prof. Dr. Dr. h.c. H. Meyer

Dekan der Mathematisch-Naturwissenschaftlichen Fakultät I

Prof. Dr. J. Rabe

Gutachter: 1. Prof. Dr. K.H. Ploog
2. Prof. Dr. F. Henneberger
3. Prof. Dr. M. Stutzmann

Tag der mündlichen Prüfung: 17.06.1999

Zusammenfassung

Die vorliegende Arbeit befaßt sich mit der Herstellung und der Charakterisierung von Gruppe III Nitriden, wobei der Schwerpunkt im Bereich der metastabilen, kubischen Modifikation liegt. Diese wurde auf GaAs(001) Substraten mittels Radiofrequenz-Plasma (RF) unterstützter Molekularstrahl-Epitaxie (MBE) hergestellt.

Während über hexagonales (α) GaN zum ersten Mal 1932 berichtet wurde, gelang erst 1989 die Synthese einer epitaktisch gewachsenen kubischen (β) GaN Schicht. Im Vergleich zur hexagonalen bietet die kubische Kristallstruktur auf Grund ihrer Symmetrie potentielle Vorteile für die Anwendung in optischen und elektronischen Bauelementen. Die Herstellung einkristalliner, kubischer Schichten erweist sich jedoch als schwierig, da dem Gitter angepaßte Substrate nicht zur Verfügung stehen. Es stellt sich daher die Frage, ob kubische Nitride überhaupt in einer für Bauelemente ausreichenden Qualität produziert werden können. Vor diesem Hintergrund ist zu verstehen, daß zahlreiche sowohl fundamental wichtige als auch technologisch relevante Materialgrößen dieser neuartigen Verbindungen noch gänzlich unbekannt sind.

Das Ziel dieser Arbeit ist es daher erstens, einen Beitrag zur Aufklärung der bis dato wenig bekannten optischen und elektronischen Eigenschaften des β -GaN und der Mischkristalle β -In_xGa_{1-x}N zu leisten und zweitens, die technologischen Grenzen der Herstellung von bauelementrelevanten kubischen (In,Ga,Al)N Heterostrukturen auszuweiten. Ein wesentliches Zwischenergebnis war die reproduzierbare Herstellung glatter, einphasiger β -GaN Nukleationsschichten auf GaAs in einer neuen MBE Maschine, welche mit einer RF Plasmaquelle hohen Stickstofflusses ausgestattet worden war. Die Optimierung der Epitaxie dicker β -GaN Schichten hinsichtlich Phasenreinheit und Oberflächenmorphologie lieferte dann die Grundlage für die Synthese komplizierterer β -(In,Ga,Al)N Strukturen.

Während die optischen Eigenschaften des α -GaN hinreichend bekannt sind, gibt es ein erhebliches Defizit an gesicherten Informationen zur kubischen Phase. Es wurden daher das Reflexions- und Transmissionsvermögen einer einkristallinen β -GaN Schicht im Spektralgebiet $2.0 \leq \hbar\omega \leq 3.8$ eV in Abhängigkeit der Temperatur untersucht. Auf Grundlage der bekannten Theorie für Mehrschichtsysteme wurde ein numerisches Verfahren entwickelt, welches eine Berechnung des kompletten Satzes der optischen Konstanten aus den Meßdaten ermöglicht. Abweichungen von der idealen Fabry-Pérot Struktur führen dabei zu einer Verringerung der Kohärenz der Meßstrahlung. Dieser Effekt wurde explizit behandelt und dazu benutzt, die räumliche Inhomogenität des Brechungsindex in der β -GaN Schicht abzuschätzen. Unter anderem erfolgte auch eine Bestimmung der Temperaturabhängigkeit der fundamentalen Absorptionskante im Bereich $5 \leq T \leq 300$ K.

Die Strahlungsemission wurde für beide Modifikationen des GaN untersucht. Dazu wurde die Photolumineszenz (PL) nahe der Bandkante hinsichtlich Übergangsenergien, Linienbreite und -form, sowie Intensität als Funktion der Temperatur vermessen. Mittlere Phononenenergien, -kopplungskonstanten und thermische Aktivierungsenergien wurden hieraus berechnet. Um den Einfluß nichtstrahlender Rekombinationsprozesse quantitativ zu erfassen, erfolgten PL Messungen mit variabler Anregungsdichte an kubischem und hexagonalem GaN bei 300 K. Mittels eines Minimalmodells für die Rekombination wurden die interne Quanteneffizienz, (nicht)strahlende Lebensdauern, sowie das Verhältnis der Koeffizienten für Elektronen- und Löchereinfang abgeschätzt. Das dominante nichtstrahlende Zentrum erweist sich dabei als Lochfalle, welches jedoch mit moderaten Anregungsdichten abgesättigt werden kann.

Es hat den Anschein, als ob strukturelle Defekte wie Stapelfehler und Versetzungen im GaN weit weniger Einfluß auf die optischen Eigenschaften haben als in anderen III-V Verbindungen, welche schwächer ionisch gebunden sind. Ein Vergleich zwischen beiden Phasen des GaN zeigt, daß strahlende Zentren, deren gelbe Lumineszenz im Wettbewerb zur Bandkantenemission steht, überraschenderweise ein geringeres Gewicht im β -GaN bei $T > 100$ K haben. Trotz der durch die Gitterfehlpassung verursachten hohen Defektdichten des β -GaN konnte selbst bei 500 K Lumineszenz nachgewiesen werden, deren Intensität mit der hochwertiger α -GaN Proben vergleichbar ist.

$\text{In}_x\text{Ga}_{1-x}\text{N}$ spielt eine wesentliche Rolle in kurzwelligen Lichtemittern. Die Synthese von Mischkristallen hoher Qualität mit $x > 0.3$ wird jedoch durch die im thermodynamischen Gleichgewicht vorliegende Mischungslücke – als Folge der stark unterschiedlichen Bindungsstärken im GaN und InN – drastisch erschwert. Während bereits seit einigen Jahren auf der hexagonalen Modifikation basierende, blau-grüne Leuchtdioden kommerziell erhältlich sind, ist kaum etwas über das kubische β - $\text{In}_x\text{Ga}_{1-x}\text{N}$ bekannt.

Zur Untersuchung der strukturellen und optischen Eigenschaften des β - $\text{In}_x\text{Ga}_{1-x}\text{N}$ wurden daher etwa 200 nm dicke Schichten mit hohen In-Gehalten auf β -GaN hergestellt. Mit $x = 0.17$ und $x = 0.4$ wurden jeweils blaue und grüne Photolumineszenz bei Raumtemperatur und darüber erzielt. Die erhebliche inhomogene Linienbreite dieser PL im Zusammenhang mit der schwachen Temperaturabhängigkeit der Übergangsenergien, der homogenen Verbreiterung, sowie der Intensitäten legt den Schluß nahe, daß es sich hierbei um Übergänge zwischen lokalisierten Zuständen handelt, welche ihrerseits mit Kompositionsschwankungen in Verbindung gebracht werden. Durch Transmittanz- und Reflektanzmessungen konnte einerseits nachgewiesen werden, daß diese Lumineszenz mit der Absorptionskante korreliert. Andererseits zeigt sich, daß die Bandlücke des kubischen Mischkristalls um 0.2 eV kleiner ist als die der hexagonalen Form im untersuchten Bereich von $0 \leq x \leq 0.4$. Nach bestem Wissen sind die vorliegenden optischen Daten die ersten ihrer Art über β - $\text{In}_x\text{Ga}_{1-x}\text{N}$.

Neben dicken β - $\text{In}_x\text{Ga}_{1-x}\text{N}$ Schichten konnten die ersten kohärent verspannten β - $\text{In}_x\text{Ga}_{1-x}\text{N}$ /GaN (Multi-)Quantengräben mit In-Gehalten von 50% und abrupten Grenzflächen mittels RF-Plasma unterstützter Molekularstrahl-Epitaxie hergestellt werden. Dies ist ein aufregendes Ergebnis, da es zunächst einmal zeigt, daß vermöge einer Nichtgleichgewichtswachstumsmethode ein ternärer Mischkristall in einer metastabilen Struktur weit jenseits der Mischungslücke seiner binären Komponenten gezüchtet werden kann. Dabei wurden Grenzflächen mit Rauigkeiten von etwa 1 nm erreicht. Darüber hinaus sind die Quantengräben erheblich verspannt. Deren Dicken belaufen sich auf 4 bis 7 nm und liegen damit jenseits der erwarteten kritischen Schichtdicken für die vorliegenden Restverspannungen von über 3%. Da mittels hochaufgelöster Transmissions-Elektronenmikroskopie keinerlei Anzeichen für Phasenseparation gefunden werden konnten, ist zu erwarten, daß noch höhere In-Gehalte in Schichten mit Dicken von weniger als 5 nm erreicht werden können. Eine potentielle Anwendung solcher β - $\text{In}_x\text{Ga}_{1-x}\text{N}$ /GaN Multi-Quantengräben mit $x \geq 0.4$ wären daher Dioden-Laser, welche im grün-gelben Bereich emittieren.

List of Publications

Parts of this work have already been published or accepted for publication:

J. Müllhäuser, O. Brandt, H. Yang, K. Ploog,
Exciton luminescence of single-crystal GaN,
Proceedings of the 1st International Symposium on GaN and Related Materials, Boston (USA)
(Material Research Society, Pittsburg, 1995), edited by R.D. Dupuis, F.A. Ponce, S. Nakamura,
J.A. Edmond
Mat. Res. Soc. Ser. Vol. **395**, 607, (1996).

B. Yang, O. Brandt, B. Jenichen, J. Müllhäuser, K.H. Ploog,
Cubic (In,Ga)N layers grown on GaAs(001) by DC plasma-assisted molecular beam epitaxy,
J. Appl. Phys. **82**, 1918 (1997).

J.R. Müllhäuser, B. Jenichen, M. Wassermeier, O. Brandt, K.H. Ploog,
Characterization of zinc blende $\text{In}_x\text{Ga}_{1-x}\text{N}$ layers grown by plasma-assisted molecular beam epitaxy on GaAs(001),
Appl. Phys. Lett. **71**, 909 (1997).

O. Brandt, H. Yang, J.R. Müllhäuser, A. Trampert, K. Ploog,
Properties of cubic GaN grown by MBE,
1996 Spring Meeting of the European Material Research Society, Strasbourg (France),
Mat. Sci. Eng. B **43**, 215 (1997).

O. Brandt, J.R. Müllhäuser, B. Yang, H. Yang, K.H. Ploog,
Optical properties of cubic GaN and (In,Ga)N,
8th Conference on Modulated Semiconductor Structures, Santa Barbara (USA) 1997, to be published.

O. Brandt, J.R. Müllhäuser, A. Trampert, B. Jenichen, K.H. Ploog,
Properties of cubic (In,Ga)N grown by MBE,
1998 Spring Meeting of the European Material Research Society, Strasbourg (France),
Mat. Sci. Eng. B (to be published).

J.R. Müllhäuser, R. Klann, H. Yang, O. Brandt, K.H. Ploog,
Are cubic nitrides viable materials for optoelectronic devices ?
in *Light-Emitting Diodes: Research, Manufacturing, and Applications II* (ISBN 0-8194-2718-7),
edited by E.F. Schubert,
Proceedings of the International Society for Optical Engineering, **3279**, 38-47 (1998).

J.R. Müllhäuser, B. Jenichen, A. Trampert, M. Wassermeier, O. Brandt, K.H. Ploog,
Plasma-assisted molecular beam epitaxial growth and characterization of zincblende (In,Al,Ga)N heterostructures on GaAs(001)
in *Light-Emitting Diodes: Research, Manufacturing, and Applications II* (ISBN 0-8194-2718-7),
edited by E.F. Schubert,
Proceedings of the International Society for Optical Engineering, **3279**, 48-58 (1998).

J.R. Müllhäuser, O. Brandt, A. Trampert, B. Jenichen, K.H. Ploog,
Green photoluminescence from cubic $\text{In}_{0.4}\text{Ga}_{0.6}\text{N}$ grown by RF plasma assisted molecular beam epitaxy on GaAs(001),
Appl. Phys. Lett. **73**, 1230 (1998).

T. Wethkamp, K. Wilmers, C. Cobet, N. Esser, W. Richter, O. Ambacher, O. Brandt, J.R. Müllhäuser, K.H. Ploog, M. Cardona
Optical properties of GaN, AlN, and $\text{Al}_x\text{Ga}_{1-x}\text{N}$ films in the spectral range 3-20 eV,
1998 Spring meeting of the European Material Research Society, Strasbourg (France),
Mat. Sci. Eng. B. (1998) (to be published).

Contents

1	Introduction	1
1.1	Zincblende Nitrides: A new material class	1
1.2	What we know about zincblende nitrides	3
1.3	The goal of this work	3
2	Wurtzite–Zincblende Polytypism	5
2.1	Stability of the wurtzite structure:	
	Qualitative concepts	5
2.2	Structural Energies and Epitaxial Stabilization	6
2.3	Group-III Nitrides	7
2.3.1	Prospective substrates for β -GaN	7
2.3.2	β -GaN on GaAs(001): Impossible ?	8
3	Growth of Zincblende GaN	9
3.1	Nitrogen Precursors and Nitridation	9
3.2	MBE Growth: Early Results at the PDI	10
3.3	The New MBE System	11
3.4	Nucleation of β -GaN/GaAs(001)	11
3.4.1	Substrate Preparation	11
3.4.2	The Nucleation Scheme	11
3.4.3	The Role of As	12
3.4.4	Optimization of RF Plasma Nucleation	14
3.5	Degradation of thick GaN layers	17
3.5.1	Ga-rich conditions	17
3.5.2	N-rich conditions	18
3.5.3	Growth temperature and growth rate	18
3.6	Growth under optimized conditions	19
3.6.1	Structural Properties	19
3.6.2	Surface Morphology	21
4	Reflectance & Transmittance of β-GaN	23
4.1	Experimental Setup	24
4.2	Basic Theory of the Fabry-Pérot Resonator	25
4.2.1	Incoherent Intensities	26
4.2.2	Coherent Intensities	26
4.3	Finite Coherence Effects	27
4.4	Analysis of Real Data: The Numerical Scheme	28

4.4.1	Initial Value Calculation	29
4.4.2	Determination of s and n_{Sub}	30
4.5	The Optical Constants of β -GaN	31
4.5.1	Room-Temperature Properties	32
4.5.2	Low-Temperature Properties	36
4.5.3	Fundamental Absorption Edge	38
4.6	Incoherence and Optical Inhomogeneity	41
5	Photoluminescence of GaN versus Temperature	45
5.1	Photoluminescence Spectra of α - and β -GaN	46
5.1.1	α - and β -GaN Microcrystals	46
5.1.2	β -GaN Film	46
5.1.3	α -GaN Reference Film	48
5.2	Lineshape analysis	50
5.3	Transition energies and band gaps	51
5.4	Linewidths	53
5.5	Thermal quenching	55
5.6	Excitons in β -GaN ?	58
6	(Non)radiative Recombination	61
6.1	Band Edge Photoluminescence Intensity versus Carrier Injection Rate	61
6.2	Basic Rate Equation Model	62
6.3	Analysis of Photoluminescence Data	64
6.4	The X_{C} and X_{H} Transitions	66
7	Growth of Zincblende (In,Ga,Al)N Heterostructures	71
7.1	Thick β -In $_x$ Ga $_{1-x}$ N Films	72
7.1.1	MBE Growth	72
7.1.2	Composition and Structural Properties	73
7.1.3	Morphology	77
7.2	β -GaN/In $_x$ Ga $_{1-x}$ N/GaN (Multi) Quantum Wells	78
7.2.1	SQWs: Morphology and In Profiles	78
7.2.2	Strained MQWs	81
7.3	β -Al $_x$ Ga $_{1-x}$ N	83
7.3.1	Low Temperature Growth	84
8	Optical Properties of Zincblende (In,Ga,Al)N	87
8.1	Thick β -In $_x$ Ga $_{1-x}$ N Films	87
8.1.1	Reflectance & Transmittance	87
8.1.2	Photoluminescence	90
8.1.3	Band Edge Properties of β -In $_x$ Ga $_{1-x}$ N: Summary	92
8.2	β -Al $_x$ Ga $_{1-x}$ N	94
9	Summary and Outlook	97
9.1	What we don't know about cubic nitrides	99

List of Acronyms

AFM	:	Atomic Force Microscopy
CL	:	Cathodoluminescence
CW	:	Continuous Wave
(MO)CVD	:	(Metal Organic) Chemical Vapor Deposition
DC	:	Direct Current
(MO)MBE	:	(Metal Organic) Molecular Beam Epitaxy
PL	:	Photoluminescence
RBS	:	Rutherford Backscattering Spectrometry
(S, M)QW	:	(Single, Multiple) Quantum Well
RF	:	Radio Frequency
RHEED	:	Reflection High-Energy Electron Diffraction
RMS	:	Root-Mean-Square
SAD	:	Selected Area Diffraction
SEM	:	Scanning Electron Microscopy
SIMS	:	Secondary Ion Mass Spectrometry
(HR, X)TEM	:	(High-Resolution, Cross Sectional) Transmission Electron Microscopy
UV	:	Ultraviolet
(MO)VPE	:	(Metal Organic) Vapor Phase Epitaxy
XRD	:	X-Ray Diffraction

List of Symbols

If not otherwise defined, the symbols used have the following meanings:

a	:	Lattice constant
α	:	Absorption coefficient
\mathcal{A}	:	Absorbance
A	=	b_h/b_e
b_e	:	Electron capture coefficient
b_h	:	Hole capture coefficient
b_R	:	Radiative recombination coefficient
\mathcal{C}	:	Empirical coherence factor
$\mathcal{C}_{\Delta\delta}$:	Statistical coherence factor
d	:	Reciprocal lattice constant;
	:	Film thickness
\mathcal{E}	:	Electric field
E	:	Photon energy
E_G	:	Band gap energy
E_i	:	Activation energy
E_Ω	:	Effective phonon energy
E_X	:	Band edge luminescence energy
ΔE	:	Linewidth
ϵ_c	=	$\epsilon_1 + i\epsilon_2$: Complex dielectric constant
ε	:	Strain

η	:	Internal quantum efficiency
η_{max}	:	Calibration factor for internal quantum efficiency
g	:	Growth rate
G	:	Carrier injection rate
I_{PL}	:	Photoluminescence intensity
$I_{(\text{N})\text{R}}$:	(Non-)radiative recombination rate
I_{Total}	:	Total integrated photoluminescence intensity
I_X	:	Band edge luminescence intensity
k	=	$2\pi/\lambda$: Wavenumber
K	:	Boltzmann constant
κ	:	Extinction coefficient
λ	:	Wavelength
n	=	$n_o + \Delta n$: Electron concentration;
	:	Refractive index;
n_o	:	Background electron concentration
Δn	:	Excess electron concentration
n_c	=	$n + i\kappa$: Complex index of refraction
ν	:	Poisson ratio
p	=	$p_o + \Delta p$: Hole concentration
p_o	:	Background hole concentration;
	:	Base pressure
Δp	:	Excess hole concentration
P_{Ex}	:	Excitation power density
r	:	Reflection coefficient
\mathcal{R}	:	Reflectance
ρ	:	Reflectivity
R_X	:	Exciton Rydberg
s	:	Effective film thickness
S_{Ω}	:	Phonon coupling constant
$S^{\circ,+}$:	Density of filled, empty Shockley-Read-Hall centers
T	:	Absolute Temperature
T_{G}	:	Growth temperature
\mathcal{T}	:	Transmittance
τ	:	Transmittivity;
	:	Total lifetime
$\tau_{(\text{N})\text{R}}$:	(Non-)radiative lifetime
τ_{rel}	=	$\tau_{\text{R}}/\tau_{\text{NR}}$
Θ	:	Bragg angle
ω	:	Phase velocity;
	:	Angle of incidence in x-ray diffraction

Chapter 1

Introduction

Tremendous research effort has been devoted during the past decade to the wide band gap semiconductors SiC, ZnSe, and GaN with the aim of high-temperature electronic and short-wavelength optical devices. Since SiC and GaN offer outstanding thermal and chemical stability, these materials are suitable for high-power operation in hostile environments. In contrast to the group IV compounds, ZnSe and GaN have a direct band gap and are therefore particularly attractive for opto-electronic applications. Indeed, the first blue lasers demonstrated were based on the ZnSe system. However, the II-VI compounds suffer in general from a low damage threshold causing rapid device degradation.

The physical properties of a crystal are very sensitive to its real structure, which is a direct manifestation of the valence electron density distribution. Materials which exhibit *polymorphism*¹ may therefore have widely ranging electronic, optical, and electrical characteristics depending on the actual crystal structure. Most III-V and II-VI compounds crystallize at ambient pressures in either the hexagonal wurtzite (α) or the cubic zincblende (β) structure which are both tetrahedrally coordinated and differ only in the handedness of the fourth interatomic bond along the [111] direction. These structural similarities manifest themselves in small differences in the bulk structural energies, $\Delta E_{\alpha-\beta} := E_{\alpha} - E_{\beta}$, being typically of the order of 20 meV/atom or less and can thus give rise to the *wurtzite-zincblende polytypism*². Despite a small $|\Delta E_{\alpha-\beta}|$, the physical characteristics of the wurtzite and zincblende phase can differ significantly. The so-called *metastable phase*, which is less favorable in terms of the intrinsic stability measure $\Delta E_{\alpha-\beta}$ may be stabilized by providing a corresponding template which serves as epitaxial constraint.

1.1 Zincblende Nitrides: A new material class

The group III nitrides GaN, InN, AlN, and their alloys have long been thought to crystallize exclusively in the wurtzite modification due to the strongly ionic character of the III-N bond. The strength of this bond causes very high melting points and, thus, makes epitaxial growth of high-quality crystals difficult, anyway. Considering the hardness of these materials and bearing in mind the lack of a sufficiently well lattice-matched zincblende substrate, any attempt to synthesize the cubic phase may be regarded to be hopeless *a priori*. Therefore, it was not until

¹Crystallization of a compound in at least two distinct forms.

²One-dimensional polymorphism, i.e. the occurrence of different stacking sequences of atomic planes.

the end of the 80's that the first *monocrystalline*³ β -GaN epilayer was obtained on 3C-SiC by means of a non-equilibrium growth technique. *Tab. 1.1* displays milestones in the research and development of cubic nitrides.

Time	Event	Author
1974	Discovery of β -GaN	Seifert [1]
1978	Discovery of β -Al _x Ga _{1-x} N inclusions in α -Al _x Ga _{1-x} N	Baranov [2]
1986	Observation of β -GaN inclusions in polycrystalline GaN grown on GaAs by metal organic chemical vapor deposition in the course of surface passivation studies.	Mizuta [3]
1989	First monocrystalline β-GaN epilayer grown on 3C-SiC/Si by microwave plasma assisted molecular beam epitaxy.	Paisley [4]
1992	Synthesis of the β -AlN polytype by the solid-state reaction $4\text{Al} + \text{TiN} \rightarrow \text{AlN} + \text{Al}_3\text{T}$ between monocrystalline Al(001) and TiN(001) layers grown on MgO(001).	Petrov [5]
1993	Discovery of the β -InN polytype in polycrystalline InN grown on vicinal GaAs(001) by plasma enhanced MBE.	Strite [6]
1995	First monocrystalline β-In_xGa_{1-x}N grown on GaAs(001) by metal organic MBE.	Abernathy [7]
1995	Epitaxial growth of β -AlN on Si(100)	Lin [8]

Table 1.1: History of zincblende group-III nitrides

Work on zincblende nitrides is motivated by the potential advantages that these materials would offer for (opto-)electronic applications, compared to the commonly employed hexagonal nitrides, once they can be synthesized in sufficiently high quality:

- Band gap engineering by strain-induced effects similar to other zincblende III-V compounds is, in principle, possible. In contrast, neither compressive nor tensile biaxial strain in the c -plane are feasible for effectively reducing the threshold carrier density of wurtzite GaN/Al_xGa_{1-x}N lasers.[9, 10, 11]
- A smaller electron effective mass has been reported for β -GaN [12] and a better amenability to p-type doping as well as a lower hole mass are to be expected [13, 14].
- A higher saturated electron drift velocity has been predicted [15] for cubic nitrides as a result of the reduced phonon scattering rate due to the higher degree of crystal symmetry.
- Output facets of lasers can be obtained by simple cleavage in combination with technologically relevant substrates like GaAs, GaP, Si.

³The attribute *monocrystalline* or *single-phase* is used for materials which exhibit under electron and x-ray diffraction (TEM, RHEED, XRD) a single-crystal symmetry and a well-defined epitaxial orientation with respect to the substrate. The crystal may, however, possess structural defects such as dislocations, stacking faults, and micro-twins as long as the abundancy of these imperfections merely leads to a broadening in the diffraction patterns. As soon as disorder on a macroscopic scale or the macroscopic presence of another phase is observed, the material will be called *polycrystalline*. This operational definition of a mono-crystal is by far less stringent than that of a *single-crystal* usually encountered in the Si research community.

With the exception of BN, all compounds showing zincblende–wurtzite polytypism exhibit a lower band gap in their cubic modification. It is anticipated that the same holds for the (In,Ga,Al)N system which would be beneficial for $\text{In}_x\text{Ga}_{1-x}\text{N}$ -based visible light emitters.

1.2 What we know about zincblende nitrides

Due to the immaturity of the zincblende nitrides being currently available, not much is known about these new materials. In fact, the only fairly well established quantities are the lattice constants. Many issues concerning growth, structural, optical, and electrical properties are yet to be addressed since the progress in improving the crystal quality is aggravated by the current inavailability of a suitable substrate.

The synthesis of thick epitaxial monocrystalline layers, which can be used for fundamental optical investigations is, hence, a highly non-trivial task. Thus, even such a fundamental and important parameter like the direct band gap E_G of β -GaN has been subject of controversy at the beginning of this study in 1995. Low-temperature values ranging from 3.3 – 3.8 eV, i.e. even higher than $E_G(\alpha\text{-GaN}) = 3.47$ eV, have been reported as can be seen in *Tab. 1.2*.

E_G [eV]	T[K]	Substrate	Method	Time	Author
3.52	4	GaAs	CL	1991	Strite [16]
3.45	300				
3.81	77	GaAs	CL	1991	Okumura [17]
3.21	300	MgO	Absorption	1993	Powell [18]
3.35	4	3C-SiC	PL, Reflectance	1994	Okumura [19]
3.30	10	MgO	Photoreflectance	1994	Ramírez-Flores [20]
3.23	300				
3.22	300	GaP	Reflectance	1995	Lacklison [21]
3.26	300	Si	Ellipsometry	1995	Logothetidis [22]
3.39	300	—	Calculated	1997	Van de Walle [23]

Table 1.2: Reported values for the direct band gap of β -GaN

The discrepancies in E_G arise in many cases from a lack of phase purity as well as from ambiguities in the interpretation of optical data. Also, it is not clear *a priori* as to how strain caused by the use of highly mismatched substrates affects the fundamental gap. Significant strain-induced shifts were observed in the case of hexagonal GaN. [24, 25, 26, 27]

1.3 The goal of this work

The objective of this study is to address both the physics and the materials science of zincblende nitrides concerning the potential application of these metastable compounds in visible light emitters. The present thesis is therefore divided into two parts: The first part (chapters 2 to 6) mainly covers growth, microstructure, and especially, fundamental optical properties of β -GaN. It is intended to constitute the basis for the second part (chapters 7 and 8), dealing with zincblende (In,Ga,Al)N heterostructures. In the latter, special emphasis is put on the optical characterization of $\beta\text{-In}_x\text{Ga}_{1-x}\text{N}$.

In more detail, the work is organized as follows: After closer inspection of wurtzite-zincblende polytypism in the following chapter, the RF plasma assisted growth of β -GaN on GaAs(001) by MBE will be treated in chapter 3. Chapter 4 is devoted to a method by which the complete set of optical constants of β -GaN is determined from reflectance and transmittance measurements in the below as well as the above band gap energy range. The temperature dependent photoluminescence of both polytypes of GaN will be compared in chapter 5 where particular attention is paid to the band edge related transitions. The role of nonradiative recombination in GaN is studied in chapter 6 on the grounds of excitation density dependent PL investigations in conjunction with a rate equation model.

Chapter 7 deals in general with the growth of β -(In,Ga,Al)N heterostructures and in particular with β -In_xGa_{1-x}N/GaN (multi) quantum wells with large x . The optical properties of thick β -In_xGa_{1-x}N layers will be presented in chapter 8 comprising reflectance, transmittance, and photoluminescence investigations. Finally, a brief account will be given on β -Al_xGa_{1-x}N.

Yet another important topic is the tailoring of electric properties which is, however, beyond the scope of this dissertation.

Chapter 2

Wurtzite–Zincblende Polytypism

2.1 Stability of the wurtzite structure: Qualitative concepts

Wurtzite–zincblende polytypism is a well-known phenomenon that has been observed during the past 30 years for various semiconductors such as ZnS, ZnSe, ZnTe, CdS, CdSe, CdTe, CuCl, CuBr, or SiC. [28, 29] Since an ideal wurtzite (α) structure with $(c/a)_{\text{ideal}} = \sqrt{8/3}$ can be transformed into the zincblende structure and vice versa by merely changing the stacking sequence of atomic layers along the [111]-axis (c-axis)

$$(\alpha) \text{ AaBbAaBb} \dots \longleftrightarrow (\beta) \text{ AaBbCcAaBbCc} \dots,$$

the coexistence of both phases as mixture of differently stacked (111)-planes is possible. The tetrahedral coordination remains unaffected by such a phase transition and the two structures differ only in the relative position of third nearest neighbors and beyond. Therefore, weak long-range Coulomb interactions, being most dominant in covalently bonded materials, are of relevance for controlling the $\alpha \leftrightarrow \beta$ transition.

In contrast, the coordination, i.e. the number of nearest neighbors in a crystal, is determined by strong short-range ionic forces. Such interactions are a measure of the character of the individual bond and, thus, account for the elastic properties of the solid. The ionicity scales introduced by Van Vechten [30] and Phillips [31] adequately describe the transitions between different coordinations but cannot always explain polytypism within a given coordination.

The lower symmetry of the wurtzite structure allows for an internal distortion $\Delta(c/a) = c/a - (c/a)_{\text{ideal}}$ from the ideal arrangement of atoms in terms of dense packing in order to minimize the structural energy. The low-temperature deviation $\Delta(c/a)$ from the isotropic tetrahedral coordination and the associated energy differences can be qualitatively described as follows:

- For a purely ionic crystal, the Madelung constant of a wurtzite configuration with $(c/a)_{\text{ideal}}$ is $M_\alpha = 1.6406$ while the Madelung constant in the zincblende case is given by $M_\beta = 1.6381$ [32], corresponding to an energy difference per valence electron of about 10 meV. Therefore, considerations of the ionic energy favor the wurtzite phase.

Since a decrease in c/a increases M_α [32], wurtzite structures should deviate from the ideal configuration by a relaxation $\Delta(c/a) < 0$ in order to minimize the ionic energy as long as long-range effects can be neglected.

- In the case of a covalent crystal, the valence electron distribution extends beyond the nearest neighbors as opposed to an ionic crystal where stable closed-shell configurations are reached. The minimization of the covalent energy leads to a $\Delta(c/a) > 0$. Under these circumstances, an $\alpha \rightarrow \beta$ phase transition may be energetically more favorable, though.

In the intermediate case, ionic and covalent forces are competing in minimizing the total structural energy. Empirically, the following correlation between the internal structure parameter c/a and the low-temperature stability of the wurtzite phase is observed (*Tab. 2.1*):

Compounds with $\Delta(c/a) < 0$ favor the wurtzite structure while those for which $\Delta(c/a) > 0$, preferentially crystallize in the zincblende configuration. However, since c/a is very sensitive to crystal imperfections, impurities and stresses, care has to be taken in interpreting experimental data and a decision about the structural stability of a certain material may not be straightforward.

For materials with zincblende as stable low-temperature phase, a reversible $\beta \rightarrow \alpha$ transition usually takes place above a certain temperature which is mediated by the vibrational part of the crystal energy. For ZnS, CdSe, CuCl, CuBr, and CuI, the critical temperatures are $T_{\beta \rightarrow \alpha} = 1020 \pm 5^\circ\text{C}$, [33] $950 \pm 5^\circ\text{C}$, [34] 407 , 386 , and 396°C , [35] respectively. These temperatures essentially reflect the hardness of the material being determined by the bond strength.

Apart from the c/a ratio, several other (non)classical structural coordinates have been born out of the desire of an at least qualitative systematization of structural trends. Based on Phillips and Van Vechtens semi-empirical dielectric theory for 4- and 6-fold coordinated binary compounds, electronegativity variables such as homo- and heteropolar dielectric band gaps [30, 31, 36, 37] and effective charges [29] were proposed.

With the availability of sufficient computing power, wavefunction and local-density pseudopotential orbital radii were determined. The latter have been successfully applied to systematize the structure types of numerous binary, ternary, and quaternary compounds. However, for a quantitative assessment of structural regularities within, e.g., homological sequences like $\text{AlN} \rightarrow \text{InN} \rightarrow \text{GaN}$, the calculation of total structural energies is required.

2.2 Structural Energies and Epitaxial Stabilization

Based on local-density-functional calculations employing plane-wave nonlocal pseudopotential methods, the $T = 0$ K wurtzite-zincblende total structural energy difference per atom,

Compound	$\Delta E_{\alpha-\beta} [\text{meV}]$	$\Delta(c/a)$	Compound	$\Delta E_{\alpha-\beta} [\text{meV}]$	$\Delta(c/a)$
AlN	-18.4	-3.3×10^{-1}	CdSe	1.4	2.7×10^{-3}
InN	-11.4	-2.4×10^{-1}	ZnS	3.1	4.6×10^{-3}
GaN	-9.9	-5.2×10^{-2}	ZnSe	5.3	4.2×10^{-3}
CdS	-1.1	-9.5×10^{-3}	AlAs	5.8	—
MgTe	-1.0	≈ 0	GaAs	12.0	—
<i>Wurtzite (α)</i>			<i>Zincblende (β)</i>		

Table 2.1: Calculated structural energy differences per atom between wurtzite and zincblende phase and measured relaxation parameter of the wurtzite structure. [38]

$\Delta E_{\alpha-\beta} = E_{\alpha} - E_{\beta}$, has been calculated by Yeh *et al.* [38] for many octet binary semiconductors and correlated with atomistic orbital-radii coordinates. The values of $\Delta E_{\alpha-\beta}$ for selected III-

V and II-VI compounds are compared in *Tab. 2.1* with the structural relaxation parameter $\Delta(c/a)$.

These structural energies defining the bulk stability of a given compound, however, can be overruled by imposing a suitable epitaxial boundary condition. Put the case that the wurtzite structure is thermodynamically favored by $\Delta E_{\alpha-\beta} < 0$. Then, the metastable cubic phase may nevertheless crystallize as a result of geometrical compatibility or epitaxial size selectivity:

1. By offering a well lattice-matched (001)-oriented zincblende substrate, the β -phase will be automatically selected since this is the only geometrically compatible structure. Growth of the α -modification would cause miscoordinated atoms and, thus, result in high densities of structural defects which in turn considerably raise the total crystal energy. Growth of ZnS, ZnSe, [39] ZnTe,[40] and CdTe [41] on GaAs(001) hence results in the metastable cubic form in defiance of the bulk structural energies.
2. In contrast, a (111)- β substrate is geometrically compatible with both the wurtzite and the zincblende structure. The driving force for nevertheless selecting the β -modification may, however, be the minimization of elastic strain caused by lattice mismatch between substrate and epilayer.[42]

2.3 Group-III Nitrides

2.3.1 Prospective substrates for β -GaN

Since the nitrides rank on top of the $\Delta E_{\alpha-\beta}$ and $\Delta(c/a)$ scale in *Tab. 2.1*, their wurtzite phase is highly stable. Indeed, even on a polycrystalline AlN layer, GaN forms in the α -modification. The use of such an AlN buffer layer for lattice mismatched growth of α -GaN on Al_2O_3 or 6H-SiC is therefore common practice. In contrast, the attempt to force GaN or InN into the zincblende structure encounters an energy barrier $\Delta E_{\alpha-\beta}$ comparable to that separating the wurtzite phase of GaAs from its extremely stable zincblende groundstate.

The only good reason for convincing the nitrides to crystallize in the β -phase would be a well lattice matched substrate which, unfortunately, does not exist to date. The relative lattice mismatch between a substrate material with lattice constant a_{Sub} and a GaN epilayer with a_{GaN} is defined ¹ as

$$\delta_{\text{GaN}} = 2 \frac{a_{\text{Sub}} - a_{\text{GaN}}}{a_{\text{Sub}} + a_{\text{GaN}}} . \quad (2.1)$$

In *Tab. 2.2*, δ_{GaN} , density ρ , coefficient of thermal expansion $\Delta a/a$, thermal conductivity κ , melting point T_{m} , and lowest band gap energy E_{G} are compiled for different zincblende structure substrates and compared to β -GaN.

Due to the comparatively small $\delta_{\text{GaN}}(3\text{C-SiC})$ of 3.6%, this – rare and expensive – material seems to be the best candidate for an epitaxial stabilization of zincblende GaN. Indeed, the first monocrystalline cubic GaN film was synthesized on a 3C-SiC/Si substrate in 1989. [4] Epitaxial growth of β -GaN has also been reported on MgO [18] and attempts were made to nucleate cubic GaN on Si(001). [43, 44] Since in this case a polar material is grown on a non-polar substrate, antiphase domains readily form which cause high densities of structural defects and may result in polycrystalline GaN.

¹Depending on the actual analysis technique, other definitions of the mismatch may be applied: In x-ray diffraction, e.g., the difference in lattice constants is usually referred to a_{Sub} .

Substrate	a [Å]	δ_{GaN} [%]	ρ [g/cm ³]	$\frac{\Delta a}{a}$ [10^{-6} /K]	κ [W/(cm K)]	T_m [K]	E_G [eV]
InP	5.8687	25.97	4.81	4.5	0.8	1335	1.344
GaAs	5.6533	22.28	5.318	6.0	0.5	1513	1.424
GaP	5.4502	18.68	4.138	4.65	1.2	1730	2.272
Si	5.4310	18.29	2.329	3.59	1.58	1685	1.124
β -GaN	4.52	0.0	3.23
3C-SiC	4.3596	−3.60	3.166	...	4.9	3100	2.416
MgO	4.216	−6.96	3.576	10.5	0.24	3073	7.833

Table 2.2: Room temperature properties of prospective cubic (001) substrates for zincblende GaN [45]

2.3.2 β -GaN on GaAs(001): Impossible ?

Growth of cubic GaN on technologically attractive GaAs substrates seems to be, at first sight, impossible in view of the large mismatch of $\delta_{\text{GaN}}(\text{GaAs})=22$ %. However, closer inspection reveals that the spacings between 4 GaAs and 5 GaN atoms in the (001) plane nearly match. This gives rise to hope that at least thin layers of β -GaN could be nucleated on GaAs(001) via the formation of a regular dislocation network, usually referred to as coincidence lattice, which accounts for the extra $\{110\}$ planes to be introduced into the GaN lattice. [46]

The synthesis of epitaxial layers of β -GaN on GaAs(001) was pioneered by Strite *et al.* [16] and Okumura *et al.* [17] in 1991 by molecular beam epitaxy. In 1995, it was discovered that the cubic structure cannot only be prepared on GaAs(001) but also, at least partially, on (111)A and $(\bar{1}\bar{1}\bar{1})$ B substrates [47]. For layers grown on GaAs(111)A, a temperature-mediated reversible $\beta \leftrightarrow \alpha$ phase transition has been observed, the cubic structure being stable up to about 850°C.

An *amorphous to crystalline transformation* has been observed to occur in N ion implanted GaAs(001) upon furnace annealing at 850–950°C. [48] The GaN precipitates were found to consist of predominantly the cubic phase in coexistence with small amounts of the wurtzite structure. Despite the presence of these hexagonal seeds, a prolonged thermal treatment at $T_{\beta \rightarrow \alpha} = 950^\circ\text{C}$ was necessary to induce a $\beta \rightarrow \alpha$ phase transition in the cubic GaN clusters.

Chapter 3

Growth of Zincblende GaN

3.1 Nitrogen Precursors and Nitridation

Surface nitridation, i.e. exclusive exposure to a nitrogen containing agent, is common practice as substrate preparation step prior to growth of hexagonal nitrides. In the case of the popular sapphire substrate such a treatment is frequently applied to form a polycrystalline AlN buffer layer onto which α -GaN can be nucleated. Nitridation may also be used for simply removing oxide layers and contaminations from, e.g., SiC.

Whether a substrate nitridation procedure for growth of β -GaN on GaAs is useful or not strongly depends on the precursor and nitrogen source used. In what follows, a brief review is given on the most commonly applied nitrogen precursors with respect to the benefits of nitridation.

- Compounds like $N_2H_{4-n}(CH_3)_n$ are sometimes used in CVD, MOMBE or MOCVD. In the course of GaAs surface passivation studies with dimethylhydrazine [17], the formation of β -GaN was observed. No growth of thick GaN layers was possible unless the GaAs substrate has been nitridized for several minutes at 660°C. However, the material obtained by this procedure was essentially polycrystalline.
- *Thermal nitridation* of GaAs with N_2 results in polycrystalline GaN. [49, 50]

NH_3 , N_2 , or mixtures of these gases are the most common nitrogen precursors for MBE and MOCVD and will now be considered in conjunction with plasma sources.

- Nitridation of a (2×4) -reconstructed GaAs surface with *electron cyclotron resonance (ECR) plasma sources* for a minute or less was reported to lead to thin, dominantly cubic GaN layers with rough surface morphology.[51] A (3×3) reconstruction was observed during the first seconds of this nitrogen treatment and attributed to the formation of a commensurate GaN layer of one monolayer thickness.[52]
- Nitridation with *radio frequency (RF) plasma sources* is disastrous: The GaAs is highly selectively etched along the $\{111\}$ planes leading to facets on which α -GaN can easily nucleate. As a consequence, only polycrystalline GaN is obtained.[50, 53] Nitrogen-rich growth was even observed to lead to the formation of the hexagonal phase on the cubic GaAs(001). [54]

It appears that the less reactive the nitrogen precursor or source, the more beneficial a nitridation step may be for the formation of β -GaN. However, most of the nitridation studies published do not actually cover the growth of thick β -GaN layers and many of the so-called single phase cubic nucleation layers obtained by one of the above treatments exhibit more or less severe polycrystalline features in the RHEED patterns shown. As a bottom line, nitridation of GaAs is in general very critical and in most cases deleterious for further growth of β -GaN.

3.2 MBE Growth: Early Results at the PDI

At the Paul-Drude-Institute, the first cubic GaN samples were grown in a two chamber MBE system on GaAs. The growth chamber which is evacuated by a cryo pump (1500 l/s) and an ion pump is equipped with 4 solid source cells (Ga, As, Si, Be) and a DC plasma source (Riber) for providing atomic and ionic nitrogen species.

The epitaxial stabilization of the first 3–10 monolayers of GaN on GaAs is of vital importance for the subsequent growth of β -GaN. The DC plasma assisted nucleation has therefore been thoroughly investigated [55]. Due to the low growth rate of $g = 10 - 30$ nm/h, imposed by the limited nitrogen flux of the DC source, the parameter window for this essential process showed to be sufficiently wide. In particular, the growth temperature could be varied over a range of about 50°C without significantly affecting the quality of the nucleation layer. Therefore, the DC nucleation procedure as described in [55, 56] turned out uncritical regarding reproducibility.

However, a major problem consisted in obtaining thick single-phase zincblende layers with smooth surface morphology: The synthesis of a 1.5 μm thick film, e.g., required approximately 50 hours, making it almost impossible to achieve stable growth conditions throughout such a run. Even worse, the thicker the layers, the rougher the samples' morphology usually became. This roughening phenomenon represents not only a fundamental obstacle for obtaining heterostructures with abrupt interfaces but gives also way for the formation of $\{111\}$ facets which serve as nucleation sites for the hexagonal phase.

The photoluminescence properties of the following two samples grown in this MBE system on GaAs(001) will be considered in detail within this work (chapters 5, 6):

1. (# 2058)

On top of a 1.5 μm thick zincblende GaN film, cubic and hexagonal microcrystals with diameters of $\approx 3 \mu\text{m}$ were synthesized by a vapor-liquid-solid like epitaxial process under Ga-rich conditions. [57] The crystals are very pure and of high structural quality. As will be shown below, the luminescence of this sample is dominated by the band edge recombination taking place in the crystals which are basically unstrained since they grew virtually independently of the underlying film. Therefore, this sample structure defines an optical standard in terms of band edge transition energies.

2. (# 2070)

This sample consists of a 900 nm thick dominantly β -GaN film on GaAs with comparatively smooth surface morphology which has been grown under near stoichiometric conditions ($\text{Ga}/\text{N} \approx 1$). [58] In contrast to sample #2058, no micro-crystals are present as proved by scanning electron microscopy.

3.3 The New MBE System

The need for a new MBE system with a sufficient number of ports for effusion cells, high growth rate, and high-quality vacuum arose from the desire to obtain (In,Ga,Al)N heterostructures for device applications. To meet these criteria, a custom-designed three chamber machine featuring 7 solid source cells (Ga, Al, In, As, Be, Mg, Si) and a water-cooled radio frequency plasma source (SVT Associates) has been built by CREATEC. The N source is typically operated at a plasma power of 300–500 Watt with N₂ flows of 1–10 sccm, which allows growth rates in excess of 1 $\mu\text{m}/\text{h}$.

The growth chamber is equipped with a continuously rotatable sample holder, *in situ* RHEED, heatable viewports for optical monitoring, an ion gauge for beam flux measurements and a continuous flow liquid nitrogen cryoshroud. A cryopump (4500 l/s) in combination with an ion pump yield a base pressure of $p_o \approx 3 \times 10^{-10}$ Torr. The middle chamber houses a sample holder carroussel and is pumped by an ion pump identical to that of the growth chamber, resulting in $p_o \approx 5 \times 10^{-10}$ Torr. In the load lock chamber being evacuated by a cryo pump ($p_o \approx 8 \times 10^{-9}$ Torr), two samples can be accommodated at a time for water desorption prior to transfer into the middle chamber. In what follows, the optimization of the nucleation and growth of β -GaN on GaAs by means of RF plasma assisted MBE are described.

3.4 Nucleation of β -GaN/GaAs(001)

3.4.1 Substrate Preparation

As substrates, exactly [001]-oriented, semi-insulating, epi-ready, quarter 2" GaAs wafers (AXT) were used. They were first outgased in the load lock chamber by front-side radiation heating at 150–200°C. After thermal removal of the native oxide at 580°C under an As ambient pressure of $\approx 3 \times 10^{-7}$ Torr, a 20–50 nm thick GaAs buffer layer was grown to yield a smooth β -(2 \times 4)-reconstructed surface which is a suitable template for the subsequent nucleation of zincblende GaN (*Fig. 3.04a*).

As opposed to the DC plasma source, the nucleation of β -GaN on GaAs(001) with the RF source represented a major problem for two technological reasons:

1. The flux of active nitrogen of the RF source is higher by almost an order of magnitude.
2. The different ignition procedure of the RF source makes a precise timing of the nucleation very difficult and may result in uncontrolled exposure of the GaAs surface to active nitrogen even with closed shutter.

Unintentional nitridation of the GaAs as well as plasma etching are therefore serious issues, making the freshly prepared β -(2 \times 4) surface easily unsuitable for epitaxial stabilization.

3.4.2 The Nucleation Scheme

In principle, the RF plasma assisted nucleation of β -GaN/GaAs follows the same concepts than the DC plasma process:

1. Arrangement of a dense array of sufficiently small β -GaN nuclei by three dimensional growth.

2. Vertical as well as lateral growth of these seeds and formation of a coincidence lattice of edge-type misfit dislocations within each of the β -GaN islands at the GaAs/GaN interface to account for the 4 : 5 ratio of the respective mismatched $\{110\}$ planes.
3. Island coalescence and incorporation of stacking faults along the $\{111\}$ planes since the dislocation networks of adjacent islands are, in general, out of phase.

Provided that the interfacial strain is completely relieved, the surface of such a GaN template is smooth enough, and the density of stacking faults is not too high, subsequent two dimensional growth of single-phase β -GaN is possible.

Let the island growth rate $g = g_{\parallel} + g_{\perp}$ be decomposed into a lateral (in-(001)-plane) and a vertical (out-of-plane) component, then the ratio $\zeta = g_{\parallel}/g_{\perp}$ controls the growth mode: $\zeta = 0$ corresponds to 3D growth without any surface diffusion while $\zeta \gg 1$ is necessary to establish the step-flow growth mode. Unless ζ attains an optimum value, no transition from the initial 3D to 2D growth will occur and the outlined nucleation mechanism will not work.

If the growth temperature T_G is low enough such that desorption processes may be neglected, then g is essentially determined by the minimum of the Ga and the N flux. In contrast, ζ depends strongly on the thermally activated surface diffusion processes and sticking coefficients and is therefore a function of T_G . In addition, it may be influenced by a deviation of the Ga/N flux ratio from unity and (un)intentional adsorbants (C, O, As,...). An excess in nitrogen, e.g., will reduce the mean-free path of Ga atoms by surface scattering. Thus, prerequisites for a succesful β -GaN nucleation are a well-prepared GaAs surface and a proper, time dependent, adjustment of the absolute Ga and N fluxes as well as the growth temperature T_G .

The high-resolution TEM micrograph in *Fig. 3.01* shows an example of a polycrystalline, rough GaN nucleation layer as a result of non-ideal process parameters. Even though no obvious plasma damage of the GaAs substrate is perceivable, the epitaxial constraint is lost as evidenced by the α -GaN seeds at the interface and the misoriented grains.

Unless the nucleation layer is absolutely phase pure, no thick monocrystalline β -GaN film can be obtained. Hexagonal grains will laterally expand with increasing film thickness and will finally take over. This can be seen in the dark-field cross-sectional transmission electron micrograph *Fig. 3.03*, where hexagonal (α) cone-like inclusions appear as dark regions while the dying-out cubic (β) phase exhibits bright contrast.

3.4.3 The Role of As

A necessary condition for the successful RF plasma nucleation of β -GaN is an As-terminated GaAs surface obtained by providing an As flow until coalescence of the three dimensional GaN islands. Nucleations carried out without As resulted inevitably in polycrystalline material. In contrast, no such As stabilization was necessary in the case of the low-nitrogen-flow DC plasma source. There, the As shutter was closed immediately upon initiating the nucleation procedure [55].

This suggests that the role of As in achieving a single-phase cubic template is to protect the GaAs surface from premature nitridation. As a result of the higher strength of the Ga-N bond (93 kJ/mol) compared to the Ga-As bond (47 kJ/mol) [59], GaN can form through an $\text{As} \rightarrow \text{N}$ exchange reaction despite an elevated As background. However, a sufficiently low growth rate and a high V/III ratio are necessary for this mechanism to completely take place.

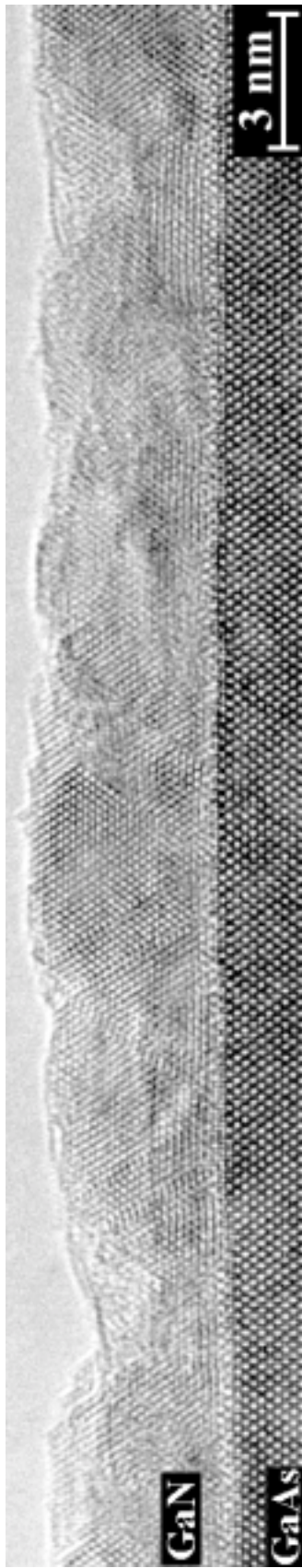


Fig. 3.01: HRTEM micrograph [AT] of a polycrystalline β -GaN nucleation on GaAs with rough surface morphology.

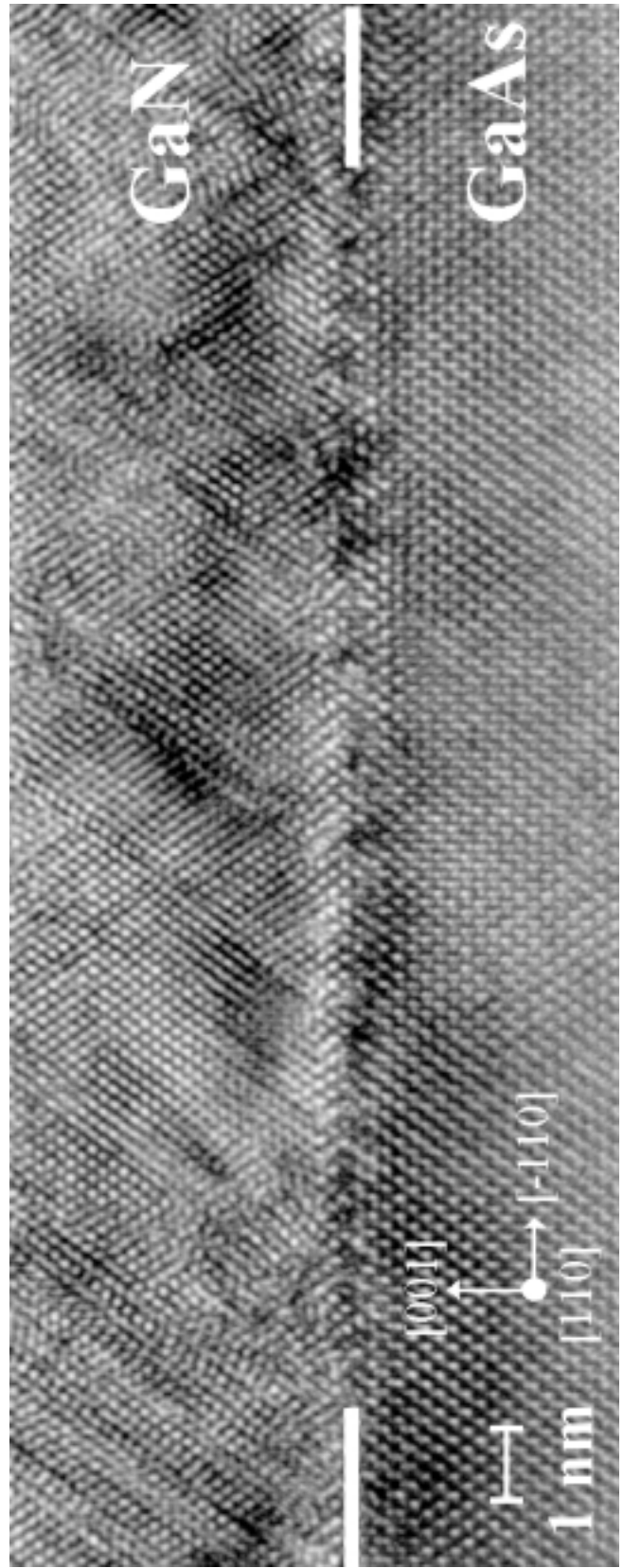


Fig. 3.02: HRTEM micrograph [AT] of a single-phase β -GaN nucleation on GaAs.

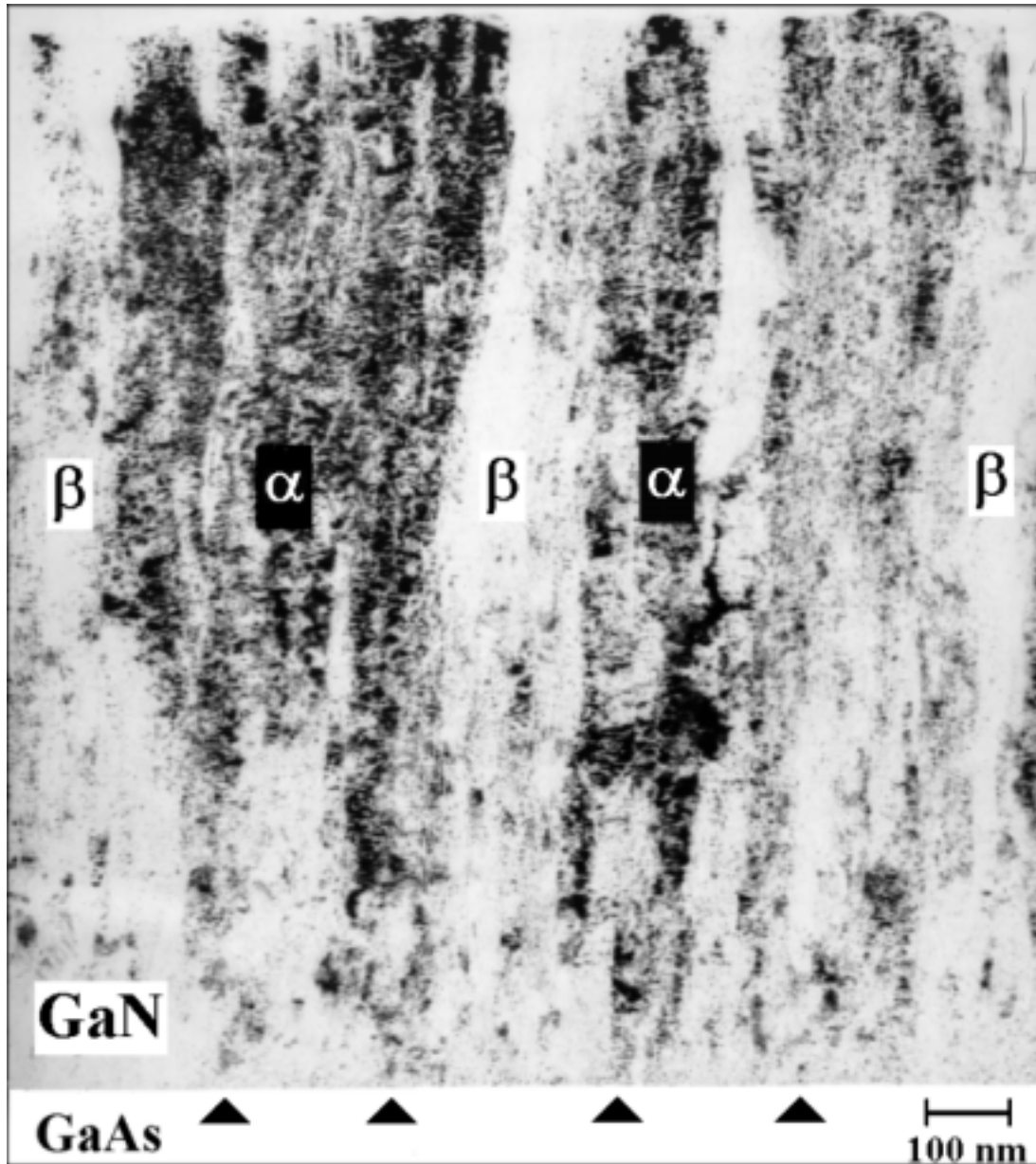


Fig. 3.03: XTEM micrograph [AT] of a sample with dominantly cubic (grey) nucleation where the hexagonal phase (black) is taking-over with increasing thickness. The α -GaN seeds are arrowed.

While an impinging As_4 flux is beneficial for achieving a 2–5 nm thin, connected film of β -GaN, it may have detrimental effects on the growth of thick layers. In the latter case, competitive growth of GaAs will not be completely suppressed as a result of the substantially higher growth rate ($V/\text{III} \approx 1$). Due to the immiscibility of β -GaN and GaAs [59, 60], phase-separated GaAs clusters can thus form which may trigger a $\beta \rightarrow \alpha$ phase transition. This phenomenon was observed for even moderate As backgrounds at film thicknesses of about 50 nm.

3.4.4 Optimization of RF Plasma Nucleation

Apart from the afore-mentioned Ga flux and the growth temperature, the plasma power, the N_2 -flow, and the As flux are relevant process parameters, thus, amounting to 5 independent

quantities which have to be optimized as a function of time.

About 70 samples were necessary to establish a reproducible RF plasma process yielding β -GaN nucleation layers of sufficient quality. Once the N_2 -flow was reduced down to about 0.3 sccm/min, i.e. far beyond the values of 1–10 sccm/min being recommended by the manufacturer of the RF source for the applied plasma power of 300 Watt, the optimization proceeded at a quick pace. In conjunction with a Ga flux of $g \approx 0.05$ monolayers/s, uncontrolled nitridation of the GaAs can be effectively suppressed. On the other hand, the nitrogen abundance under these conditions ($V/III \approx 4$) is just enough to limit the diffusion of Ga in order to avoid the formation of large GaN clusters. Also, the ideal substrate temperature of $T_G=590^\circ\text{C}$ turns out to be a critical parameter.

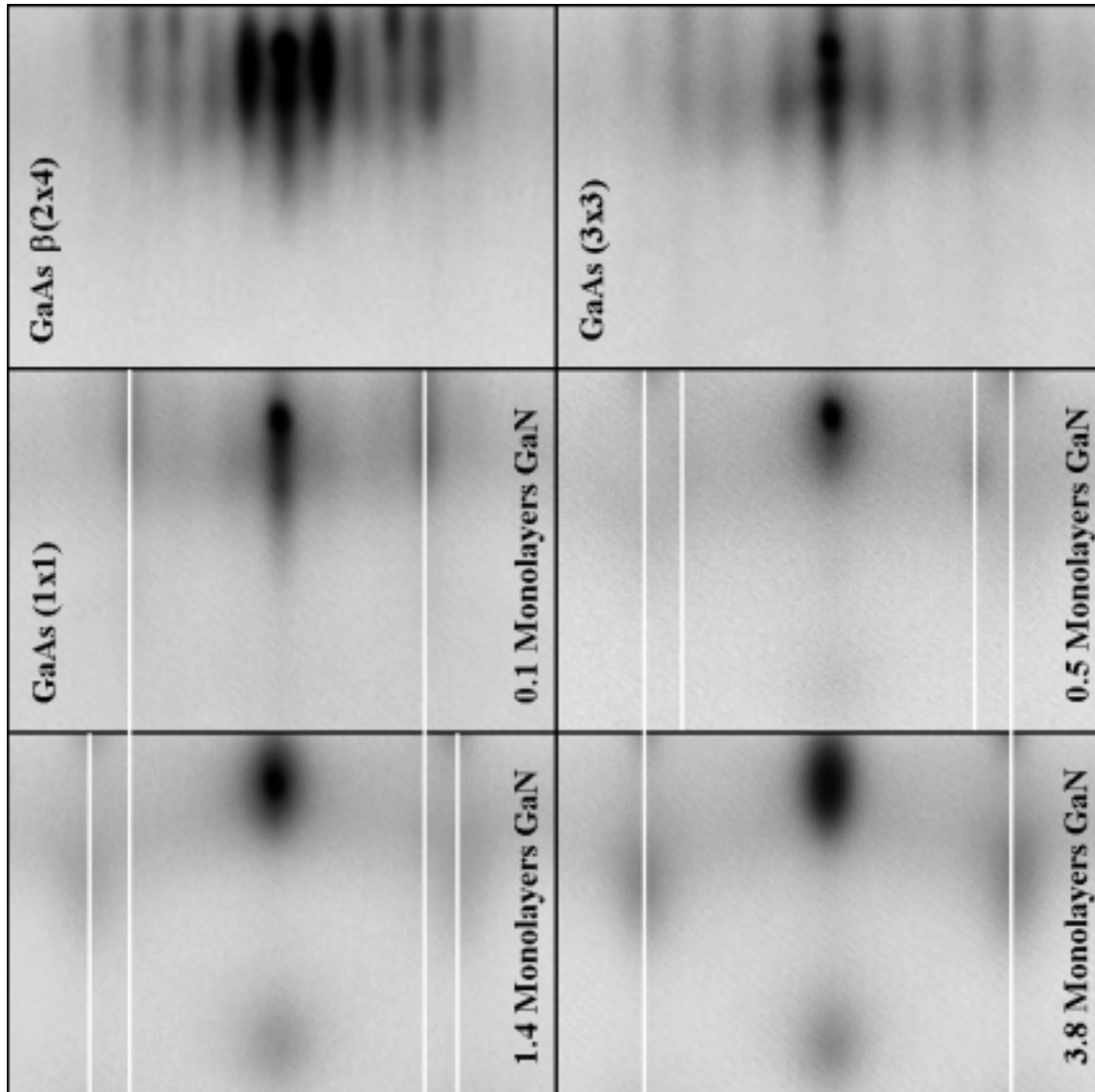


Fig. 3.04a: RHEED patterns taken along the $[\bar{1}10]$ -azimuth at different stages of an optimized RF plasma assisted nucleation of β -GaN/GaAs (see text). The reciprocal lattice spacings of GaAs and GaN are indicated by the white lines.

Fig. 3.04a shows different stages of an optimized nucleation of zincblende GaN on GaAs, recorded along the $[\bar{1}10]$ azimuth. The conditions are as stated above. Right after ignition of the RF plasma source, the β -(2 \times 4)-reconstructed GaAs pattern is replaced by a (3 \times 3) pattern.

Upon simultaneously opening the Ga and the N shutters, the latter transforms readily into a (1×1) -surface where the reciprocal lattice spacing is the same as that of the initial (2×4) -GaAs surface, d_{GaAs} . After deposition of only 0.5 monolayers of GaN – referred to the bulk lattice constant of $a_{\text{GaN}} = 4.514 \text{ \AA}$ – new diffraction spots, separated by d_{GaN} , appear in the upper part of the respective snap shot. As the nucleation proceeds, these blurred reflexes become more intense at the expense of the GaAs spots which disappear at a GaN coverage of about 1.4 monolayers. At an equivalent thickness of 4 monolayers, the new pattern with larger period remains essentially invariant under further deposition.

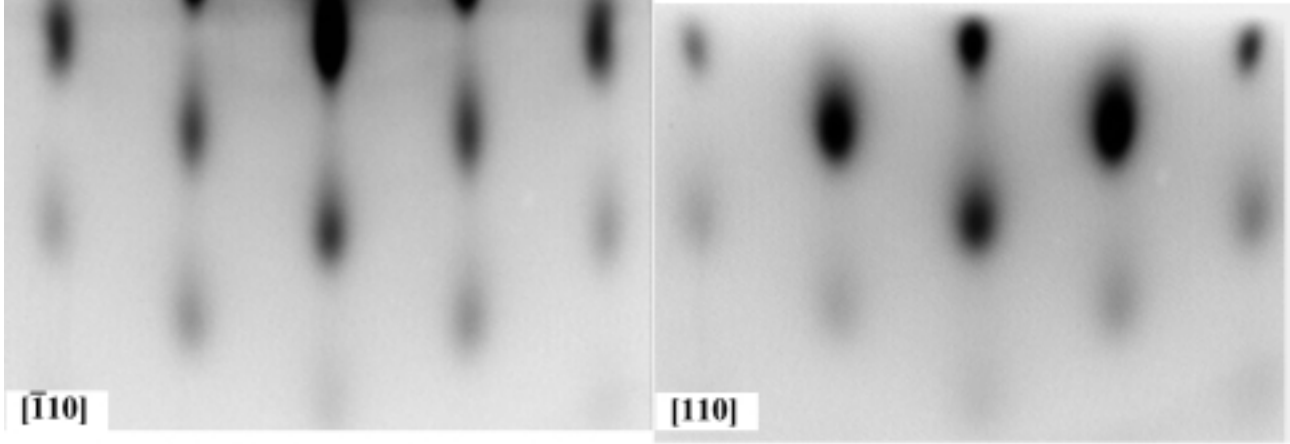


Fig. 3.04b: RHEED patterns after completion of the nucleation (5 monolayers β -GaN) taken during a growth interruption.

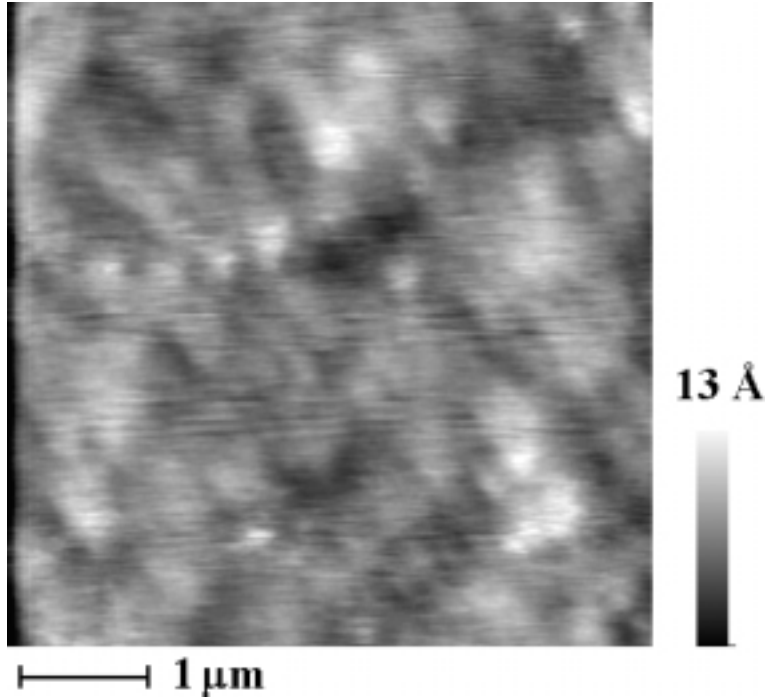


Fig. 3.05 : Atomic force microscopy scan [MW] of an optimized β -GaN nucleation layer.

Measuring the spacings $d_{\text{GaAs, GaN}}$ as indicated by the white lines, the ratio $d_{\text{GaN}}/d_{\text{GaAs}} = 1.25 \pm 0.01$ is obtained. On the grounds of the GaAs lattice constant of $a_{\text{GaAs}} = 5.65 \text{ \AA}$, the β -GaN lattice constant at growth temperature $a_{\text{GaN}} = 4.52 \pm 0.04 \text{ \AA}$ can be estimated. This

finding shows that already at equivalent coverages of as little as one monolayer, the GaN is fully relaxed. The interpretation of the (3×3) reconstruction as to a commensurate GaN film of one monolayer thickness given by Gwo *et al.* [52] can thus not be supported.

The nucleation procedure was typically stopped at coverages of 5–7 monolayers. Heating up the substrate temperature to $T_G = 640^\circ\text{C}$ brings along a tremendous improvement in intensity and contrast of the RHEED patterns as shown in *Fig. 3.04b*. Along all major azimuths, elongated spots aligned in parallel are observed, which have their origin in the formation of a connected, epitaxial layer of monocrystalline β -GaN. TEM studies of such nucleation layers confirm this interpretation (*Fig. 3.02*).

In the course of the thermal treatment, a very weak $2 \times$ reconstruction evolved along the $[\bar{1}10]$ azimuth, indicating a rather smooth surface morphology. Indeed, an AFM scan of a typical nucleation layer shown in *Fig. 3.05* yields a peak-to-valley roughness of 13 Å and a root-mean-square value of only 1.5 Å.

3.5 Degradation of thick GaN layers

Once a single-phase, connected layer of β -GaN is obtained, (near) stoichiometric growth conditions $V/\text{III} \approx 1$ are to be adjusted and the substrate temperature T_G has to be raised. The possibilities for ruining a good β -GaN template are numerous and, as in the case of the nucleation stage, the ideal parameter window for the RF plasma process is tighter than that of the DC plasma growth.

3.5.1 Ga-rich conditions

Gallium-rich conditions and low growth temperatures may lead to the formation of microcrystals through a vapor-liquid-solid like epitaxial process. *Fig. 3.06* displays an example of this

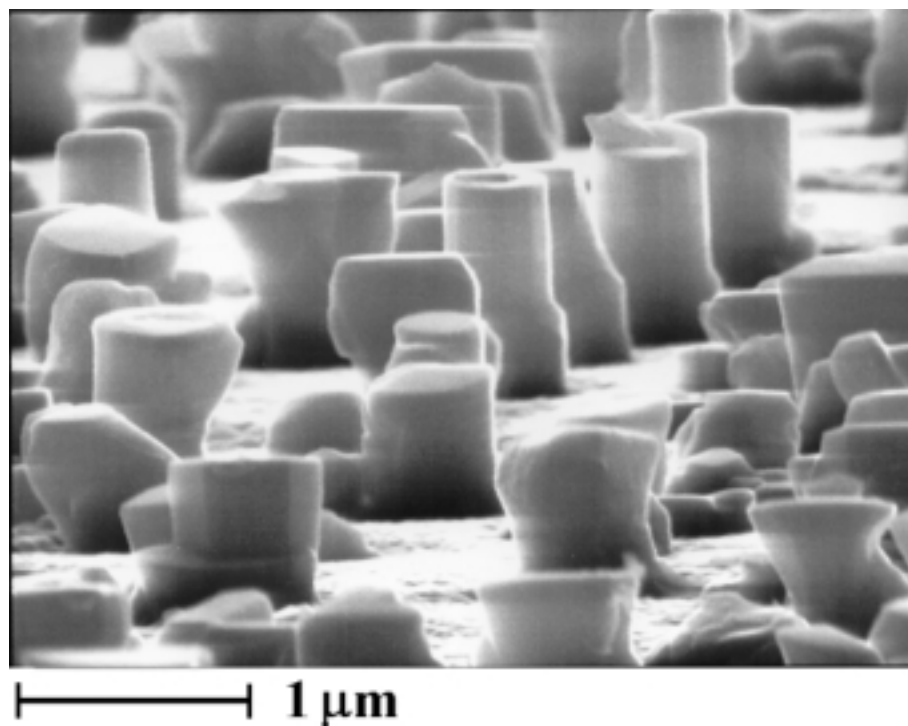
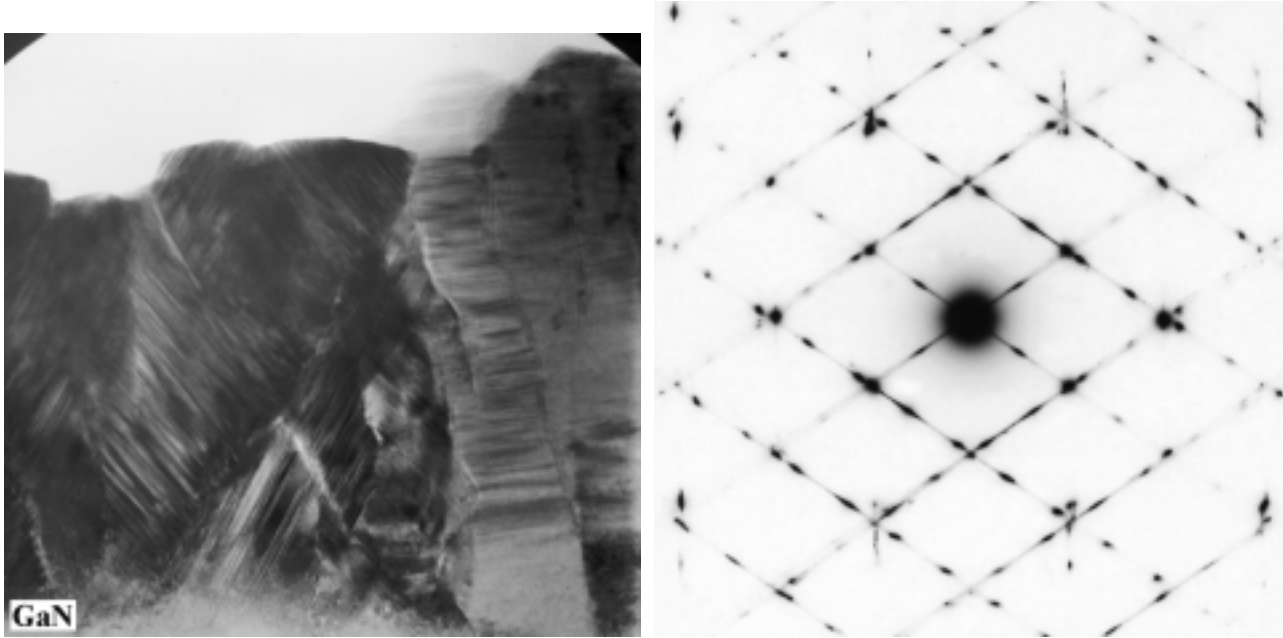


Fig. 3.06 : Crystallite growth under Ga-rich conditions at low temperatures as viewed by SEM. [IP]

growth mode where mesa-like zincblende structure crystals have formed on top of the underlying β -GaN film. Cathodoluminescence measurements carried out on these mesas yield spectra similar to those obtained from the cubic crystallites of sample #2058. In contrast to the latter, no evidence for wurtzite phase crystallites could be found.

3.5.2 N-rich conditions

Nitrogen-rich growth will lead to columnar, polycrystalline material with poor surface morphology as shown in the cross-sectional transmission electron micrograph (*Fig. 3.07*) and the atomic force microscopy scan (*Fig. 3.13*) on page 22. Selected area diffraction (*Fig. 3.08*) reveals a superposition of the cubic and hexagonal pattern along with stacking faults and twins.



Figs. 3.07,08: XTEM (left) and SAD (right) micrographs [AT] of columnar, polycrystalline GaN (#8004) obtained under N-rich conditions.

However, it has to be emphasized that the brick-like morphology (*Fig. 3.13*) does not necessarily correlate with the structural quality of the GaN film. It was observed for many single-phase β -GaN films grown with the RF plasma and basically for all samples obtained by the DC source. Even nearly amorphous GaN grown on GaAs at room temperature exhibited this surface morphology. Since these bricks could also be detected on the surfaces of very thin GaN layers, the underlying GaAs being atomically smooth, the crucial question arises whether this roughening phenomenon is an intrinsic feature of the GaN/GaAs heteroepitaxy. If this is the case, then cubic GaN grown on GaAs can be ruled out as a viable material for (opto-)electronic applications: Neither (In,Ga,Al)N heterostructures like quantum wells nor even sufficiently thick single-phase GaN layers were possible.

3.5.3 Growth temperature and growth rate

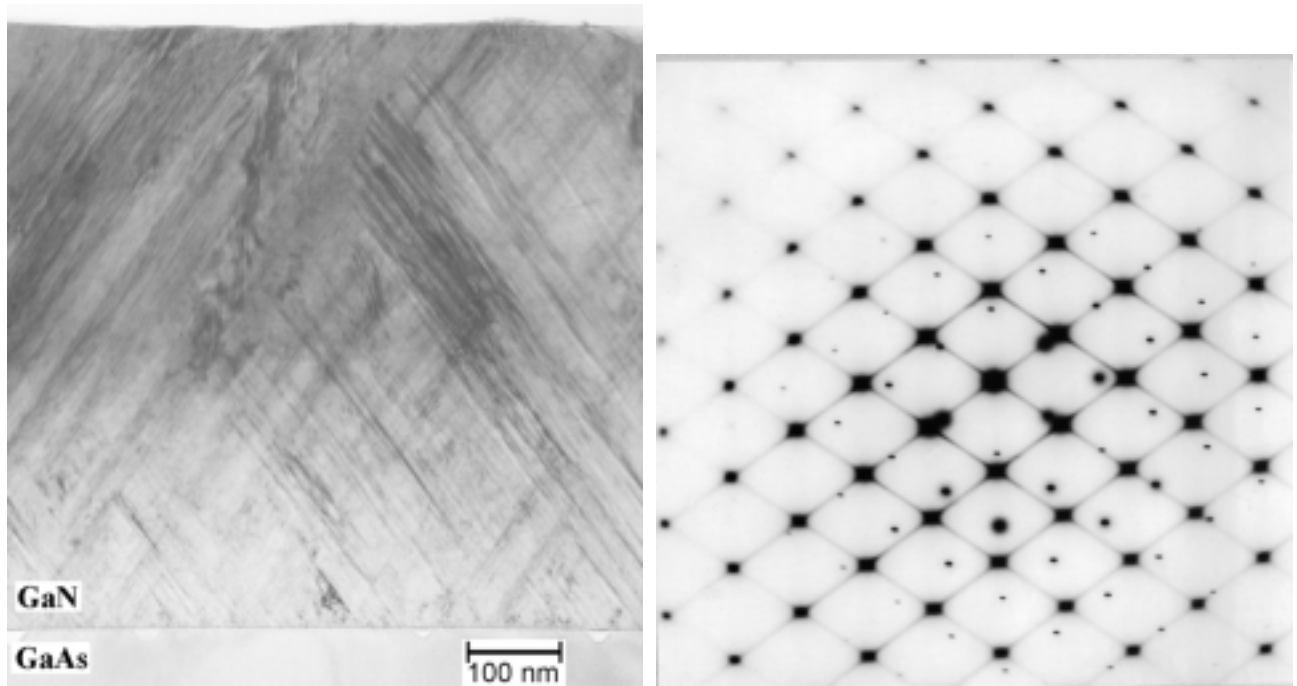
The ideal growth rate g and temperature T_G are intimately correlated via the collision-limited surface diffusion of Ga and N. Being unable to state a quantitative law of the form $g_{\text{ideal}}(T_G)$, growth experience shows that raising either of both quantities too quickly upon nucleation may

lead to a degradation of the β -GaN in terms of phase purity and/or morphology. A rather conservative set of parameters resulting in stable zincblende growth with the RF plasma source is $g = 130$ nm/h and $T_G = 640\text{--}650^\circ\text{C}$.

3.6 Growth under optimized conditions

3.6.1 Structural Properties

Figs. 3.09,10 depict XTEM and SAD data, both taken along the $[110]$ azimuth, of a representative $0.7\text{ }\mu\text{m}$ thick β -GaN film which will be referred to as *reference sample #8092*. It was grown under stoichiometric conditions $V/\text{III} \approx 1$ with $T_G = 640^\circ\text{C}$ and $g = 140$ nm/h on top of a smooth, single-phase nucleation layer. The GaN is relaxed and of zincblende structure as proved by selected area diffraction. Even though strongly overexposed, the diffraction pattern visible in Fig. 3.10 does not exhibit any hexagonal reflexes. The diffraction spots are symmetric, intense and, in contrast to Fig. 3.08, no twinning or facetting is observed. The same applies for the $[\bar{1}10]$ azimuth (not shown).



Figs. 3.09,10: XTEM and SAD micrographs [AT] of the single-phase β -GaN reference film #8092 obtained under optimized conditions.

An interesting feature is the pronounced anisotropy of the stacking fault density, being considerably higher along the $[110]$ direction than along the $[\bar{1}10]$ azimuth. This asymmetry may be due to the fact that in the polar zincblende lattice one set of $\{111\}$ planes terminates on Ga atoms while the other one ends in N atoms.

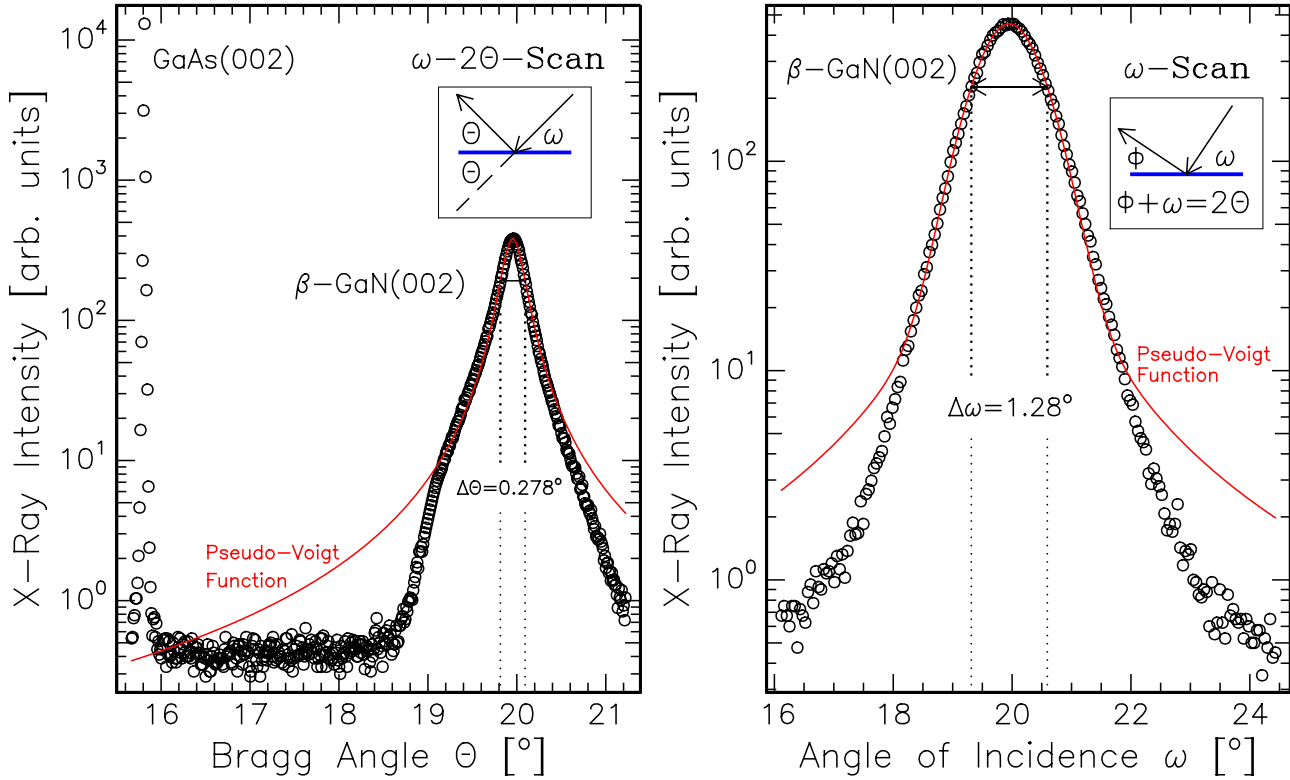
It is also noteworthy that the sensitivity of (SAD) TEM towards stacking faults is considerably higher than that of RHEED: Not only in the early-stage-of-growth patterns displayed in Fig. 3.12 but throughout the entire growth process of the present sample, no stacking faults could be detected by means of *in situ* RHEED. In contrast, the RHEED patterns belonging

to structurally inferior samples clearly exhibit stacking faults along both the $[\bar{1}10]$ and $[110]$ azimuths.

The x-ray diffraction data shown inhere were acquired with a diffractometer in double crystal configuration using $\text{CuK}\alpha_1$ ($\lambda = 0.154 \text{ nm}$) radiation. An x-ray $\omega - 2\theta$ diffraction profile of the sample under investigation is viewed in *Fig. 3.11a*. It was measured with a $100 \mu\text{m}$ aperture placed in front of the detector across the symmetric (002) reflections of GaAs at $\Theta_{\text{GaAs}} = 15.8138^\circ$ and $\beta\text{-GaN}$ at $\Theta_{\text{GaN}} = 19.954^\circ$, corresponding to a lattice constant of $a_{\text{GaN}} = 4.514 \text{ \AA}$. A *Pseudo-Voigt function*

$$f(x) = m \frac{ac^2}{(x - x_0)^2 + c^2} + (1 - m)a \exp \left\{ -\ln 2 \left(\frac{x - x_0}{c} \right) \right\} \quad (3.1)$$

was used to model the GaN peak, having a full width at half mean of $\Delta\Theta_{\text{GaN}} = 0.28^\circ$. This value correlates to fluctuations in the lattice constant of $\Delta a_{\text{GaN}} = \pm 0.03 \text{ \AA}$. The curve shape is close to a Lorentzian as indicated by $m = 0.93$ and exhibits a slight asymmetry in the low-signal tails.



Figs. 3.11a,b: XRD $\omega - 2\theta$ and ω scans of the $\beta\text{-GaN}$ reference sample #8092 grown under optimized conditions

For comparison, *Fig. 3.11b* depicts an ω -scan which was measured about the (002) Bragg reflex of $\beta\text{-GaN}$ by rotating the sample whereas the wide-open detector was kept fixed. The width of the Gaussian-like peak ($m=0.22$) amounts to $\Delta\omega = 1.3^\circ$. It stems from misoriented domains as well as from the high densities of dislocations and stacking faults which result in considerable local strain. Further optimization of growth parameters, especially of T_G in conjunction with the growth rate g is necessary to improve the crystal quality.

3.6.2 Surface Morphology

In situ RHEED patterns taken during growth of the β -GaN reference sample at a thickness of 30 nm are shown in *Fig. 3.12*. The cubic symmetry of the diffraction patterns is in accordance with the TEM results (*Figs. 3.09,10*). No hexagonal or polycrystalline features could be detected throughout the entire growth sequence. Starting from a smooth nucleation layer with parallel and slightly elongated diffraction spots, a streaky pattern showing a $2\times$ reconstruction along the $[\bar{1}10]$ azimuth evolves at a film thickness of about 20 nm.

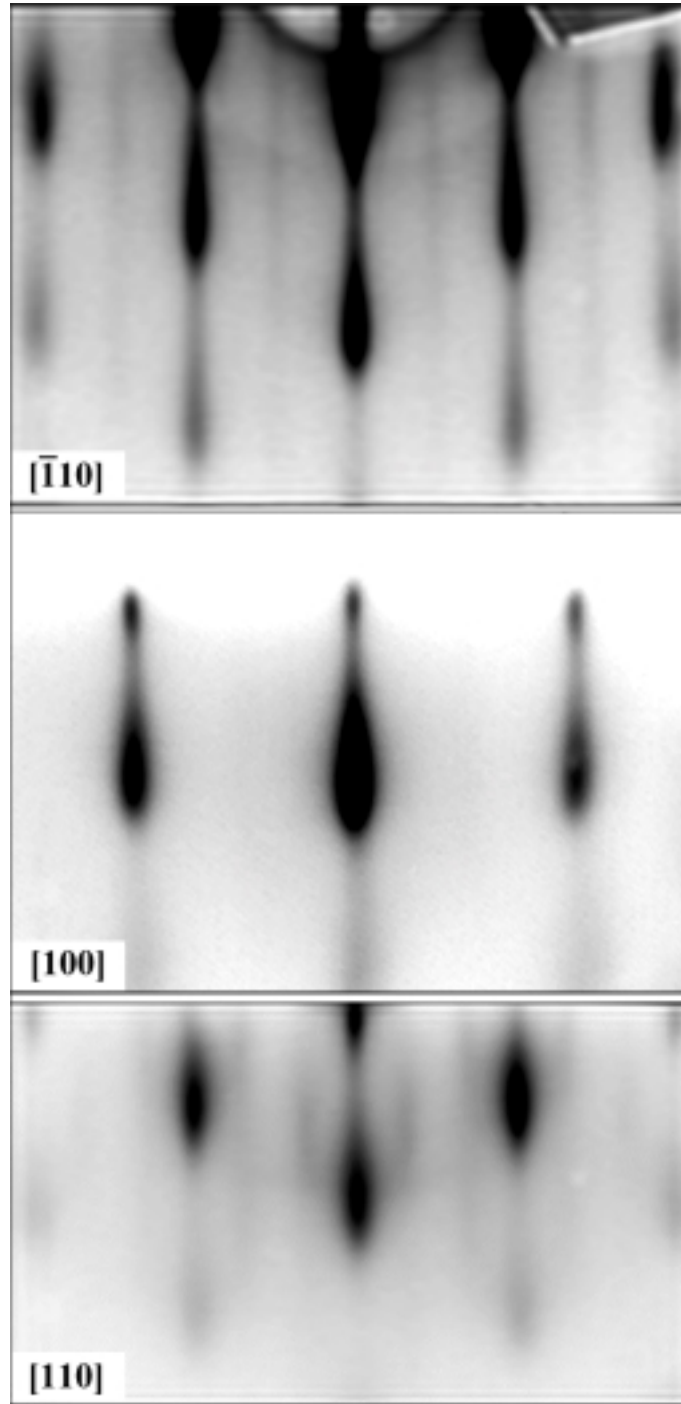


Fig. 3.12: RHEED patterns of the epilayer #8092 recorded at a thickness of 30 nm

Along the $[110]$ direction, a weak $4\times$ superstructure with missing half-order streak is visible. In contrast to the gallium-stable (2×2) and $c\text{-}(2\times 2)$ reconstructions observed so far for DC plasma grown films [61, 62, 63], this (4×2) reconstruction is nitrogen-stable. It appears during growth interruptions and is unaffected by an exposure to the nitrogen plasma. In contrast, the (4×2) disappears immediately upon deposition of $0.3 - 0.6$ monolayers of Ga. Once the Ga has been desorbed, the reconstructions recover.

The improvement in the RHEED patterns shown is in accordance with the AFM scan displayed in *Fig. 3.14*. The surface morphology of the β -GaN reference sample is not only considerably smoother, having an RMS roughness of about 1.5 nm, but in particular, it is lacking the brick-like features observed so far for all DC as well as RF plasma grown GaN films. An example of such is given in *Fig. 3.13* where AFM data of a sample grown under N-rich conditions is viewed. This achievement gives rise to hope that growth of thick single-phase zincblende heterostructures may not be an illusion.

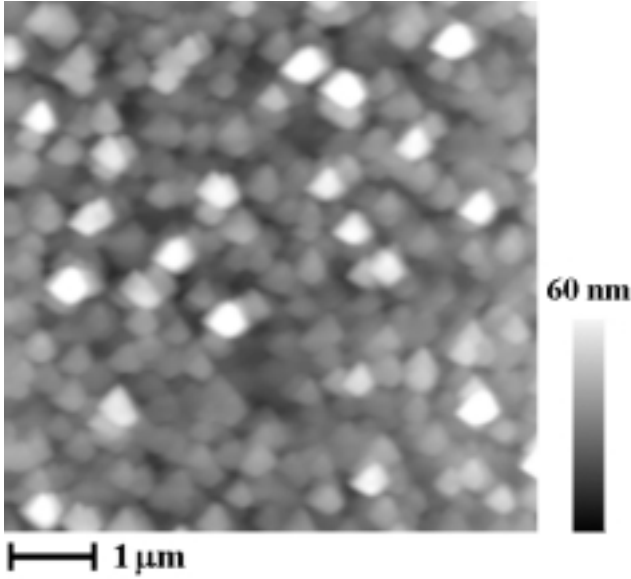


Fig. 3.13: AFM scan [MW] of the columnar, polycrystalline GaN sample #8004.

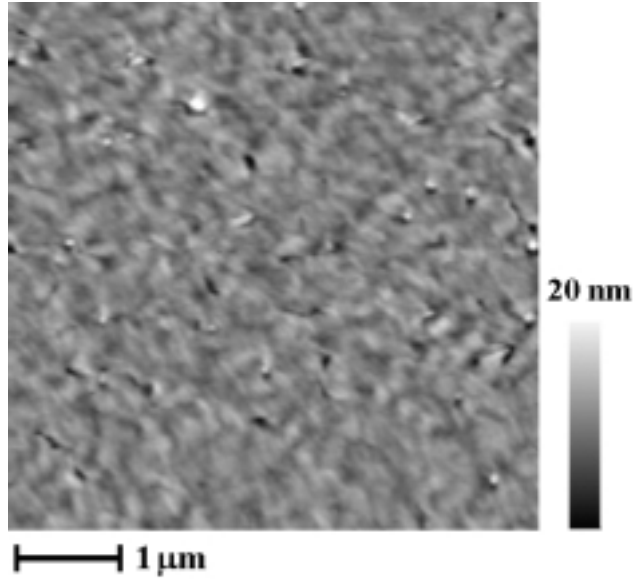


Fig. 3.14: AFM scan [MW] of the single-phase β -GaN sample #8092.

Chapter 4

Reflectance & Transmittance of β -GaN

To date, very little is known about the dielectric properties of β -GaN. No complete and consistent set of optical constants, i.e. the spectral dependence of the complex dielectric constant $\epsilon_c = \epsilon_1 + i\epsilon_2$ or the index of refraction $n_c = n + i\kappa$, are available for photon energies covering both the below- and above-band-gap range. Investigations published so far are either restricted to the regime of strong absorption [64, 65] or to the transparent spectral range [66]. In the former case, spectroscopic ellipsometry was used to measure ϵ_c for $3.3 \leq E \leq 20$ eV.

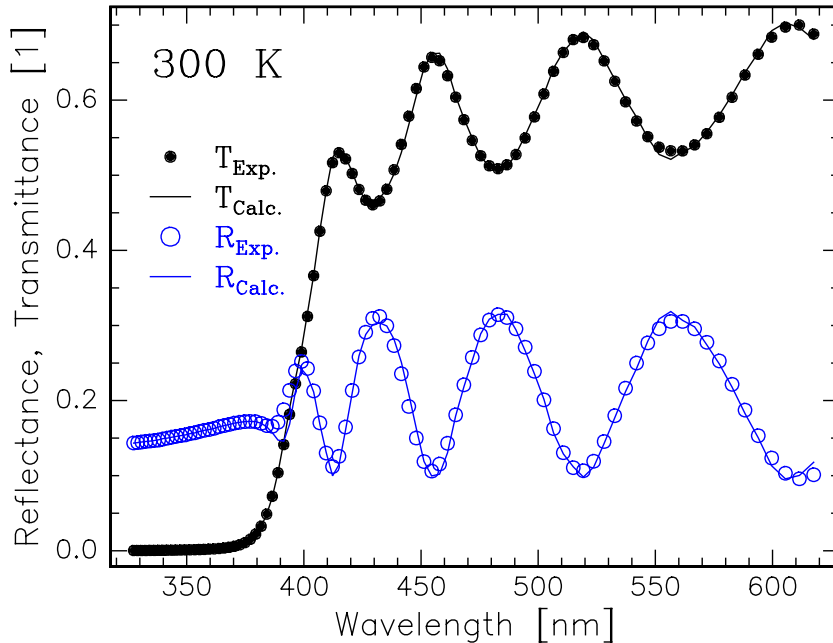


Fig. 4.01: Measured (symbols) and calculated (lines) reflectance \mathcal{R} and transmittance \mathcal{T} of the $0.7 \mu\text{m}$ thick β -GaN reference film #8092 at room temperature.

For energies below the fundamental band gap energy E_G , the refractive index n is usually assessed by analyzing interference fringes modulating optical data. In transmission or photoluminescence, e.g., maxima of order l occur for normal incidence if

$$n_l = \frac{\lambda_l(2l + 1)}{4d}. \quad (4.1)$$

Provided that the film thickness d is sufficiently large ($d \geq 3\mu\text{m}$ for $\lambda \geq 350$ nm), the observed interference maxima at wavelengths λ_l are densely enough spaced such that the optical constants

may be considered as being roughly constant in between the intervals $[\lambda_l, \lambda_{l+1}]$. The discrete set of values $\{n_l\}$ can then be interpolated to obtain $n(\lambda)$. This method was applied to determine the refractive index of α -GaN from the modulations of a deep-level luminescence band [67].

Here, the reflectance and the transmittance of the $0.7 \mu\text{m}$ thick β -GaN reference film introduced in chapter 3 will be considered (*Fig. 4.01*) for photon energies covering almost the entire visible and near-ultraviolet spectral range ($2.0 \leq E \leq 3.8 \text{ eV}$). Due to the low film thickness, the spacings between the extrema λ_l are by far too large to allow for a determination of $n(E)$ by virtue of equation (4.1). Considerable numerical effort will be required to calculate the optical constants of the β -GaN reference sample.

4.1 Experimental Setup

The experimental setup used to carry out transmittance and reflectance measurements is sketched in *Fig. 4.02*. The light of a halogen lamp was passed through a monochromator, modulated by a chopper and focused onto the respective sample which was mounted in an evacuated cryostat, adjustable via an x-y-z-table. The sample holder could be rotated to vary the angle of incidence β . Behind the cryostat, a photomultiplier tube with an integrated lens was adjusted in line with the optical axis to acquire the transmitted light. A second detector of the same type was used to collect the reflected radiation. Due to the finite detector aperture, near-normal incidence $\beta = 5 \pm 2^\circ$ is given. This setup enables measurements for photon energies $2 \leq E \leq 4 \text{ eV}$.

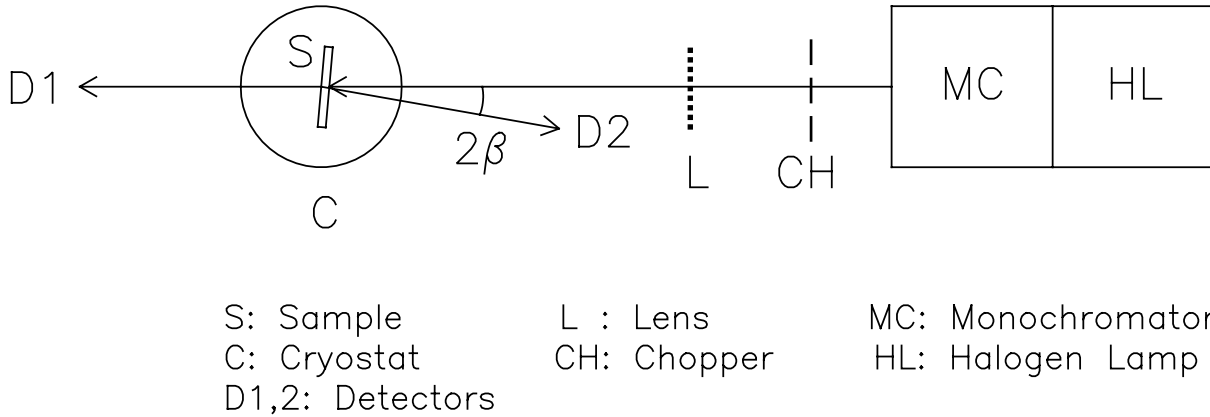


Fig. 4.02 : Transmittance and reflectance setup (Top view, not to scale).

Absolute measurements of the transmittance \mathcal{T} or reflectance \mathcal{R} require the determination of the apparatus function being the product of the incident light intensity \mathcal{I} and the detector sensitivity \mathcal{S} . The vertically displaceable sample holder possesses for this purpose a second pinhole located underneath that one onto which the sample is mounted, both holes having the same diameter (2 mm). By measuring the transmittance through the free hole without modifying the optical adjustment, the apparatus function $\mathcal{S}\mathcal{I}$ is obtained by which \mathcal{T} can be calibrated. The same procedure is applied to the reflectance detector placed in the transmission path for calibration.

In order to extract the optical constants of the layer under investigation from the measured transmittance and reflectance spectra $(\mathcal{T}, \mathcal{R})(E)$, the film will first be idealized as being a parallel plate of thickness d with perfectly plane surfaces. In chapter 4.2, the theory of reflection and refraction at the boundaries of such a plate embedded in air is briefly reviewed. [68, 69]

4.2 Basic Theory of the Fabry-Pérot Resonator

We consider a plane wave $\mathcal{E}(\mathbf{x}, t) = \mathcal{E}_0 e^{i(\mathbf{k}\mathbf{x} - \omega t)}$ with angular frequency $\omega = c|\mathbf{k}|$ striking the interface between air and a medium of thickness d with plane surfaces and complex index of refraction

$$n_c = n + i\kappa, \quad (4.2)$$

which is linked to the dielectric constant $\epsilon_c = \epsilon_1 + i\epsilon_2$ by the Maxwell relation $n_c = \sqrt{\epsilon_c}$. The *Reflectivity* ρ and *Transmittivity* τ of the two interfaces are given by the Fresnel-Stokes equations

$$\boxed{\rho = \pm \frac{n_c - 1}{n_c + 1}, \quad \tau = \sqrt{1 - \rho^2},} \quad (4.3)$$

where '+' applies for the air/plate and '-' for the plate/air interface. Therefore, the reflected wave is $\mathcal{E}'(\mathbf{x}, t) = \rho \mathcal{E}(\mathbf{x}, t)$, whereas the refracted wave in the plate at a distance x from the first interface ($\mathbf{x} \parallel \mathbf{k}$) states $\mathcal{E}''(\mathbf{x}, t) = \tau \mathcal{E}_0 \exp\left\{i\omega \left(x \frac{n_c}{c} - t\right)\right\}$. Let $\mathcal{I}_0 = |\mathcal{E}_0|^2$ and the *Reflection Coefficient* r and *Absorption Coefficient* α be defined as

$$\boxed{r = |\rho|^2, \quad \alpha = \frac{4\pi}{hc} \kappa E} \quad \text{and} \quad E = \hbar\omega, \quad (4.4)$$

then the respective intensities are

$$\begin{aligned} |\mathcal{E}'|^2 &= r \mathcal{I}_0, \\ |\mathcal{E}''|^2 &= \sqrt{1 - r} \exp\{-\alpha x\} \mathcal{I}_0. \end{aligned} \quad (4.5)$$

Since at each of the two interfaces, the wave is being split into a reflected and a refracted part (*Fig. 4.03*) according to equations (4.3), the total transmitted and reflected intensities, \mathcal{T} and \mathcal{R} , are obtained by an infinite series over the individual reflected and refracted rays at the respective interfaces.

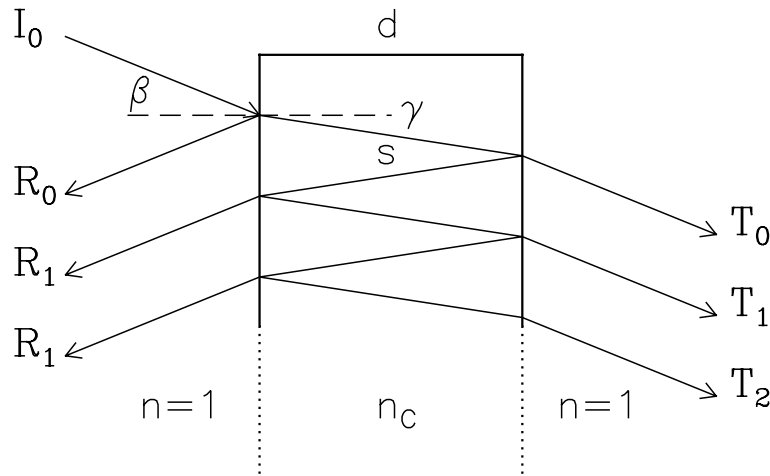


Fig. 4.03: Reflection and refraction at the boundaries between a parallel plate of thickness d and air. In the example shown, a real index of refraction $n_c = 2.6$ and an angle of incidence of $\beta = 22^\circ$ was adopted.

4.2.1 Incoherent Intensities

Repeatedly applying (4.5) the intensities of the reflected and transmitted beams of order j read

$$\begin{aligned}\mathcal{R}_o &= r \mathcal{I}_o, \\ \mathcal{R}_j &= r^{2j-1}(1-r)^2 e^{-2j\alpha s} \mathcal{I}_o, \quad j \in \mathbb{N}, \quad \text{and} \\ \mathcal{T}_j &= r^{2j}(1-r)^2 e^{-(2j+1)\alpha s} \mathcal{I}_o, \quad j \in \mathbb{N}_o,\end{aligned}\tag{4.6}$$

respectively, with $s = d/\cos \gamma$ and $\sin \beta = n \sin \gamma$. Ignoring interference effects, i.e. incoherently adding the individual intensities \mathcal{R}_j and \mathcal{T}_j , the total reflected and transmitted intensities are obtained

$$\boxed{\begin{aligned}\mathcal{R}_I &= \sum_{j=0}^{\infty} \mathcal{R}_j = r \frac{1 + (1-2r)re^{-2\alpha s}}{1 - r^2 e^{-2\alpha s}} \mathcal{I}_o, \\ \mathcal{T}_I &= \sum_{j=0}^{\infty} \mathcal{T}_j = \frac{(1-r)^2 e^{-\alpha s}}{1 - r^2 e^{-2\alpha s}} \mathcal{I}_o.\end{aligned}}\tag{4.7}$$

4.2.2 Coherent Intensities

For an adequate treatment of the multiple reflections occurring in the plate with perfect interfaces, the *Relative Phase* between the amplitudes of the interfering rays,

$$\boxed{\delta = 2|\mathbf{k}|nd \cos \gamma},\tag{4.8}$$

has to be considered. Using (4.3) the amplitudes of reflected and transmitted rays of order j are then

$$\begin{aligned}R_o &= \rho \mathcal{E}_o, \\ R_j &= -e^{ij\delta}(1-\rho^2)\rho^{2j-1}e^{-2j\alpha s} \mathcal{E}_o, \quad j \in \mathbb{N}, \quad \text{and} \\ T_j &= e^{ij\delta}(1-\rho^2)\rho^{2j}e^{-2(j+1)\alpha s} \mathcal{E}_o, \quad j \in \mathbb{N}_o.\end{aligned}\tag{4.9}$$

By coherently summing the amplitudes, the total intensities become

$$\boxed{\begin{aligned}\mathcal{R}_A(\delta) &= \left| \sum_{j=0}^{\infty} R_j \right|^2 = r \frac{1 - 2e^{-\alpha s} \cos \delta + e^{-2\alpha s}}{1 - 2re^{-\alpha s} \cos \delta + r^2 e^{-2\alpha s}} \mathcal{I}_o \\ \mathcal{T}_A(\delta) &= \left| \sum_{j=0}^{\infty} T_j \right|^2 = \frac{(1-r)^2 e^{-\alpha s}}{1 - 2re^{-\alpha s} \cos \delta + r^2 e^{-2\alpha s}} \mathcal{I}_o\end{aligned}}\tag{4.10}$$

and the total absorbed intensity yields

$$\boxed{\mathcal{A}(\delta)} = \mathcal{I}_o - \mathcal{R}_A(\delta) - \mathcal{T}_A(\delta) = (1-r)(1-e^{-\alpha s}) \frac{1 + re^{-\alpha s}}{1 - 2re^{-\alpha s} \cos \delta + r^2 e^{-2\alpha s}} \mathcal{I}_o.\tag{4.11}$$

Provided that r and α are δ -independent, the *Consistency Relations*

$$\boxed{\mathcal{R}_I = \frac{1}{2\pi} \int_0^{2\pi} \mathcal{R}_A(\delta) d\delta \quad \text{and} \quad \mathcal{T}_I = \frac{1}{2\pi} \int_0^{2\pi} \mathcal{T}_A(\delta) d\delta}\tag{4.12}$$

hold. Whereas equations (4.10) are a direct consequence of energy conservation and the boundary conditions of the electromagnetic field at the interface between two media with different

dielectric constants, the relations (4.12) may be interpreted as a conservation law for the integral field energy taken over one complete period.

In what follows, we assume normal incidence $\beta = 0$, i.e. $s = d$ and require \mathcal{R} , \mathcal{T} to be normalized such that $\mathcal{I}_0 \equiv 1$.

4.3 Finite Coherence Effects

So far, the layer whose optical constants are to be assessed was idealized as being a homogeneous, continuous medium with uniform thickness. The fact that, in reality, any solid is composed of discrete entities such as nano-crystals or, ultimately, atoms gives rise to structural inhomogeneities on a microscopic scale. The dielectric constants of bulk matter which rely on the macroscopic Maxwell equations may therefore deviate from the values measured on ultra-thin films. Such discrepancies between bulk and thin film properties were observed by Schulze, Goos, and Malé at the beginning of this century who carried out measurements on thinned gold foils or evaporated films having thicknesses of $d \leq 20$ nm [71, 72, 73]. The Maxwell Garnet theory [74] and their extensions [75, 76] try to account for this phenomenon by treating a thin film as a random distribution of isolated particles which, themselves, are assumed to have the bulk refractive index. By varying the volume filling ratio, it is possible to model the effective index of refraction of the entire film.

Since in the present work we are not seeking to characterize ultra-thin films but samples having thicknesses of at least 200 nm, we will not question the concept of macroscopic material parameters. Instead, we have to face the problem that a real sample is in general subject to thickness variations and to inhomogeneities in the index of refraction, leading to random fluctuations in the phase δ . Apart from these sample-inherent effects, there may be also extrinsic sources of incoherence such as the thick, transparent sapphire/glue sandwich onto which the GaN film has been mounted (*Fig. 4.04*, page 31).

Let δ be the average phase, then each reflected or transmitted beam of order j will encounter its own phase

$$\boxed{\delta_j = \delta + \Delta\delta_j}, \quad j \in \mathbb{N}, \quad (4.13)$$

where $\Delta\delta_j$ are equally distributed, stochastically independent random variables with probability density \mathcal{P} and expectation values

$$\langle \Delta\delta_j \rangle = \int_{-\infty}^{+\infty} \Delta\delta_j \mathcal{P}(\Delta\delta_j) d\Delta\delta_j = 0 \quad (4.14)$$

$$\langle \Delta\delta_j \Delta\delta_k \rangle = \langle \Delta\delta_j \rangle \langle \Delta\delta_k \rangle \quad \text{for } j \neq k. \quad (4.15)$$

Based on the standard deviation σ_δ of \mathcal{P} , the degree of incoherence can be quantified by the *Statistical Coherence Factor*

$$\boxed{\mathcal{C}_{\Delta\delta} := 1 - \pi^{-1} \sigma_\delta^2} \quad \text{with} \quad \sigma_\delta^2 = \langle (\Delta\delta_j - \langle \Delta\delta_j \rangle)^2 \rangle. \quad (4.16)$$

The measured reflectance $\mathcal{R}_A(\delta)$ and transmittance $\mathcal{T}_A(\delta)$ are now to be replaced by the expectation values $\langle \mathcal{R}_A \rangle$ and $\langle \mathcal{T}_A \rangle$, respectively, obtained by taking the stochastical mean over $\mathcal{P}(\Delta\delta_j)$, $j \in \mathbb{N}$. Irrespective of the actual \mathcal{P} , values of $\mathcal{C}_{\Delta\delta}$ nearby unity will lead to a reflectance and transmittance being close to the coherent limit, whereas a vanishingly small $\mathcal{C}_{\Delta\delta}$ will result in a complete loss of coherence:

$$\langle (\mathcal{R}_A, \mathcal{T}_A) \rangle \approx \begin{cases} (\mathcal{R}_A(\delta), \mathcal{T}_A(\delta)) & \text{for } \mathcal{C}_{\Delta\delta} \approx 1 \\ (\mathcal{R}_I, \mathcal{T}_I) & \text{" } \mathcal{C}_{\Delta\delta} \approx 0. \end{cases} \quad (4.17)$$

Provided that the root-mean-square value σ_s of the interfacial roughness is known, a stochastic analysis of the reflectance and transmittance data may be performed to estimate the optical inhomogeneity σ_n caused by local variations of the refractive index (Chapter 4.6).

Instead, the finite coherence effects may be treated effectively without resorting to details about the underlying stochastic processes. To do so, an analytical expression $(\mathcal{R}_C, \mathcal{T}_C)$ is required which complies with the boundary conditions $(\mathcal{R}_C, \mathcal{T}_C)_{C=0} = (\mathcal{R}_I, \mathcal{T}_I)$ and $(\mathcal{R}_C, \mathcal{T}_C)_{C=1} = (\mathcal{R}_A(\delta), \mathcal{T}_A(\delta))$ and leaves the integral mean reflectance and transmittance invariant for all \mathcal{C} . The convex combinations

$$\boxed{\begin{aligned}\mathcal{R}_C(\delta) &:= \mathcal{C} \cdot \mathcal{R}_A(\delta) + (1 - \mathcal{C}) \cdot \mathcal{R}_I \\ \mathcal{T}_C(\delta) &:= \mathcal{C} \cdot \mathcal{T}_A(\delta) + (1 - \mathcal{C}) \cdot \mathcal{T}_I\end{aligned}} \quad (4.18)$$

with the *Effective Coherence Factor* \mathcal{C} are in accordance with these requirements and, in particular,

$$(\mathcal{R}_I, \mathcal{T}_I) = \frac{1}{2\pi} \int_0^{2\pi} (\mathcal{R}_C, \mathcal{T}_C)(\delta) d\delta \quad \text{for } 0 \leq \mathcal{C} \leq 1 \text{ and } \alpha, r = \text{const.} \quad (4.19)$$

4.4 Analysis of Real Data: The Numerical Scheme

By measuring the normal incidence reflectance $\mathcal{R}(E)$ and transmittance $\mathcal{T}(E)$ as a function of photon energy $E = \hbar\omega$ in $[E_{\min}, E_{\max}]$, the optical constants $r(E)$ and $\alpha(E)$ and thus $n_c(E) = \sqrt{\epsilon_c(E)}$ can be determined. Two cases have to be distinguished:

1. Sample free-standing in air

Since the sample has two equivalent interfaces, an analytical expression for the refractive index as function of reflectivity,

$$\Rightarrow n = \frac{1+r}{1-r} + \sqrt{\frac{4r}{(1-r)^2} - \kappa^2} \quad , \quad \kappa = \frac{hc}{4\pi E} \alpha \quad (4.20)$$

exists which greatly facilitates the numerical procedure. The tradeoff of such a configuration is the lack of mechanical stability. In the case of thin films ($s \leq 5 \mu\text{m}$), corrugated interfaces may result which cause diffuse scattering of the reflected light as well as artefactual modulations of the interference oscillations and lead thus to unbearable systematical errors.

2. Sample mounted on a transparent substrate

Thin films have to be mechanically supported by a transparent substrate. Provided that in the energy range $[E_{\min}, E_{\max}]$ of interest, the substrate real index of refraction n_{Sub} is essentially energy independent and the extinction coefficient $\kappa_{\text{Sub}} \approx 0$, then the roundtrip reflection coefficient reads

$$\Rightarrow r = |\rho_1 \rho_2| = \sqrt{\frac{(n-1)^2 + \kappa^2}{(n+1)^2 + \kappa^2} \frac{(n-n_{\text{Sub}})^2 + \kappa^2}{(n+n_{\text{Sub}})^2 + \kappa^2}} \quad (4.21)$$

Here, ρ_1 denotes the reflectivity of the air/sample interface and ρ_2 the reflectivity of the sample/substrate boundary. In contrast to (4.20) where $|\rho_1 \rho_2| = \{(n-1)^2 + \kappa^2\} / \{(n+1)^2 + \kappa^2\}$, no analytical solution of the form $n(r, n_{\text{Sub}}, \kappa)$ exists. Furthermore, n_{Sub} may not be exactly known a priori.

Since we are dealing with thin films with $s \leq 1 \mu\text{m}$, the second case is given and the following system of equations has to be solved for each photon energy E :

$$\boxed{\begin{aligned}\mathcal{R}(E) &= r \left\{ \mathcal{C} \frac{1 - 2e^{-\alpha s} \cos \delta + e^{-2\alpha s}}{1 - 2re^{-\alpha s} \cos \delta + r^2 e^{-2\alpha s}} + (1 - \mathcal{C}) \frac{1 + (1 - 2r)re^{-2\alpha s}}{1 - r^2 e^{-2\alpha s}} \right\} \\ \mathcal{T}(E) &= (1 - r)^2 e^{-\alpha s} \left\{ \frac{\mathcal{C}}{1 - 2re^{-\alpha s} \cos \delta + r^2 e^{-2\alpha s}} + \frac{1 - \mathcal{C}}{1 - r^2 e^{-2\alpha s}} \right\} \\ \delta(E) &= \frac{4\pi}{hc} E s n \quad , \quad \kappa = \frac{hc}{4\pi} \frac{\alpha}{E} \\ r(E) &= \sqrt{\frac{(n - 1)^2 + \kappa^2}{(n + 1)^2 + \kappa^2} \frac{(n - n_{\text{Sub}})^2 + \kappa^2}{(n + n_{\text{Sub}})^2 + \kappa^2}}\end{aligned}} \quad (4.22)$$

Even if the film thickness s and the substrate index of refraction n_{Sub} are sufficiently well known and finite coherence effects can be neglected ($\mathcal{C} = 1$), the solution of (4.22) from scratch by standard numerical methods represents an ill-posed problem.

Since no *a priori* assumptions about the energy dependence of the film index of refraction $n(E)$ are being made and (4.22) has to be solved pointwise for each E , no mathematical correlation between the respective pairs of optical constants $(r, \alpha s)(E)$ exists for different energies. Unless a good set of initial values $(r_I, \alpha_I)(E)$ is available as starting point, the physical meaning of $\delta(E)$ as a monotonically increasing, continuous phase to control the modulations in $(\mathcal{R}, \mathcal{T})$ can easily get lost during the numerical processing. The consequence is a mathematical solution without any physical relevance, though.

Actually, not even s or n_{Sub} are precisely known and one may therefore wonder if (4.22) can be tackled at all without resorting to a model refractive index. In what follows, a numerical scheme is presented that solves the above equations on different stages.

4.4.1 Initial Value Calculation

The key to the problem of solving equations (4.22) over the entire energy range $E_{\min} < E_G < E_{\max}$ lies in appropriately exploiting the consistency relations (4.12). If we assume that s and n_{Sub} are approximately adjusted and neglect for the moment finite coherence effects, i.e. $\mathcal{C} = 1$, the task of initial value calculation can be roughly split as follows:

1. Low-energy : $E \leq E_G - 0.5 \text{ eV}$

Since in this regime the optical constants (r, α) , respective (n, κ) , are approximately energy independent, equations (4.12) hold. These imply that solving the coherent equations (4.10) with the raw data $(\mathcal{R}, \mathcal{T})$, is equivalent to applying the incoherent equations (4.7) to the integral-mean data $(\bar{\mathcal{R}}, \bar{\mathcal{T}})$:

$$(\mathcal{R}_A, \mathcal{T}_A)(\delta(E)) = (\mathcal{R}, \mathcal{T})(E) \quad (4.23)$$

$$\begin{aligned} \Leftrightarrow \quad & \boxed{\begin{aligned} (\mathcal{R}_I, \mathcal{T}_I)(E) &= (\bar{\mathcal{R}}, \bar{\mathcal{T}})(E) \\ &:= \frac{1}{\Delta_E} \int_{E-\Delta_E/2}^{E+\Delta_E/2} (\mathcal{R}, \mathcal{T})(\bar{E}) d\bar{E} \\ \delta(E + \Delta_E) &:= \delta(E) + 2\pi. \end{aligned}} \end{aligned} \quad (4.24)$$

The *Integral Approach* (4.24), however, requires the implicitly defined energy period Δ_E and thus, the knowledge of n respective (r, α) which are actually to be determined ! Nevertheless, the distinct advantage of the latter method lies in its amenability to iteration and in its high numerical stability since the phase $\delta(E)$ enters only implicitly: Starting with almost arbitrary initial values (r_0, α_0) , rapidly converging sequences $\left((\bar{\mathcal{R}}, \bar{\mathcal{T}}, \Delta_E)_j, (r, \alpha)_j\right)_{0 \leq j \leq N}$ are obtained by repeatedly solving equations (4.24). Apart from errors in the calculation of $(\bar{\mathcal{R}}, \bar{\mathcal{T}})$, the exact solution is obtained by (r_N, α_N) , for N sufficiently large, and the *a posteriori* calculated phase $\delta(r_N, \alpha_N, E)$ has the correct physical meaning. In this way, the explicit treatment of interference effects is circumvented and the phase-related problems of numerical instability are avoided.

2. Close-to-band-gap : $E_G - 0.5 \text{ eV} < E \leq E_G$

This energy range is the most critical due to the significant energy dependence of r and α . However, even in this regime where the consistency relations do not hold, the integral approach will at least give initial values $(r_1, \alpha_1)(E)$ suitable as starting point for the next stage of calculation.

3. Above-band-gap : $E_G < E$

Above the fundamental absorption edge, the Fabry-Pérot oscillations are getting heavily quenched. Therefore, the incoherent equations (4.7) adequately describe the regime of strong absorption and yield the exact solution $(r, \alpha)(E)$.

Since the empirical coherence factor \mathcal{C} merely controls the peak-to-valley ratio of the interferences but leaves the integral mean of the transmittance, reflectance, and in particular, the phase $\delta(E)$ invariant, it does not affect the mean values of the optical constants. Thus, \mathcal{C} is not a critical parameter and can easily be determined by adjusting the amplitude of the Fabry-Pérot oscillations (*Fig. 4.06*, page 33).

4.4.2 Determination of s and n_{Sub}

So far, it was assumed that the film thickness s and the energy independent substrate index of refraction n_{Sub} are known. We will now address the determination of these important parameters as well as the issue of numerical stability. The absorption coefficient α is comparatively insensitive to n_{Sub} and relates to s according to $\alpha \sim s^{-1}$. In contrast, r and n are very sensitive to (s, n_{Sub}) since they depend non-linearly on these parameters. Even small deviations of (s, n_{Sub}) from their correct values bring the measured and calculated $(\mathcal{R}, \mathcal{T})(E)$ spectra out of phase. This is numerically compensated for by artefactual variations in r which, consequently, raise the *Curvature of $n(E)$*

$$\int_{E_{\min}}^{E_{\max}} \left| \frac{\partial^2 n}{\partial E^2} \right| (E) dE. \quad (4.25)$$

Furthermore, failure to properly adjust s and n_{Sub} leads to intrinsic inconsistencies between (r, α) and (n, κ) : Suppose that (r, α) and $n(E)$ have been determined by solving the equations $(\mathcal{R}_A, \mathcal{T}_A) = (\mathcal{R}, \mathcal{T})$ and $(\tilde{r}, \tilde{\alpha})$, \tilde{n} by repeating the calculation under the constraint $n(E)$:

$$(\mathcal{R}_A, \mathcal{T}_A) \Big|_{n(E)} \stackrel{!}{=} (\mathcal{R}, \mathcal{T}) \Rightarrow (\tilde{r}, \tilde{\alpha}) \Rightarrow \tilde{n}(E). \quad (4.26)$$

Then $(r, \alpha) \neq (\tilde{r}, \tilde{\alpha})$ and $n(E) \neq \tilde{n}(E)$ unless (s, n_{Sub}) attain their correct values. The unknowns (s, n_{Sub}) can thus be determined by minimizing the *Inconsistency Measure*

$$\mathcal{D}n(s, n_{\text{Sub}}) := (E_{\text{max}} - E_{\text{min}})^{-1} \int_{E_{\text{min}}}^{E_{\text{max}}} \left\{ |n - \tilde{n}| + \left| \frac{\partial^2 n}{\partial E^2} \right| \right\} (E) \, dE, \quad (4.27)$$

which may also be used for a fine-tuning of \mathcal{C} due to the curvature term. Numerical tests show that the contribution from the first term in (4.27) saturates if (s, n_{Sub}) are too far from the right values while the curvature term dominates in this regime. Once (s, n_{Sub}) are close to the optimum, the latter does not exhibit significant variations anymore in contrast to the actual inconsistency term. Therefore, the incorporation of (4.25) into (4.27) serves to accelerate the convergence.

4.5 The Optical Constants of β -GaN

The preceding method is now being applied to the $0.7 \, \mu\text{m}$ thick β -GaN reference layer introduced in chapter 3. The sample preparation consists in locally removing the GaAs substrate by wet chemical etching. For achieving plane surfaces and the required mechanical stability, the resulting thin film was fixed face down onto a sapphire substrate (*Fig. 4.04*) using an optical UV glue.

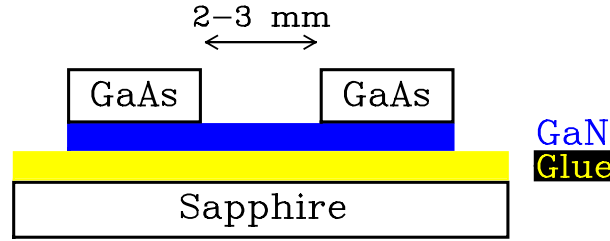


Fig. 4.04: Sample preparation for transmittance and reflectance measurements.

The optical properties of the sapphire and the glue were investigated separately. Transmission measurements with the sapphire did not reveal any measurable absorption up to the detection limit at $E_{\text{max}} = 3.8 \, \text{eV}$ of the optical setup used. An approximately $1 \, \mu\text{m}$ thick glue layer sandwiched between two sapphire plates showed to be transparent up to $3.6 \, \text{eV}$ in accordance with the manufacturer's data sheet of the glue. Thus, the consideration of the transmission curve of the UV glue in analyzing the GaN data resulted in just a minor correction.

In contrast, the incorporation of the index of refraction of the glue, n_{Sub} , in the determination of the optical constants of the β -GaN film is essential since it determines the roundtrip reflection coefficient $r = \rho_{\text{Glue/GaN}} \cdot \rho_{\text{GaN/Air}}$. Simple tests indicated $n_{\text{Sub}} \leq 1.4$, i.e. close to the index of refraction of glass. Since $n_{\text{Sapphire}} = 1.8$, also the glue/sapphire interface gives rise to reflection and refraction. However, compared to the difference between n_{Sub} and $n_{\text{GaN}} \geq 2.6$, back-reflections from the former boundary into the GaN film may be neglected. Even though the discontinuity in the index of refraction at the sapphire/air interface is appreciable, interference effects in the sapphire are suppressed by its large thickness of $250 \, \mu\text{m}$. This was verified by independently measuring the sapphire. Thus, the latter rather constitutes a source of incoherence.

In summary, the optical glue is treated as a substrate establishing a boundary condition to the problem of assessing the optical constants of the β -GaN film. All quantities obtained are to be considered as effective ones within the validity of the equations (4.22).

4.5.1 Room-Temperature Properties

Initial Value Calculation

The first step in extracting the optical constants from the room temperature transmittance and reflectance data, shown in *Figs. 4.01,08*, consists in establishing initial values $(r_I, \alpha_I)(E)$ and the parameters (s, n_{Sub}) . This is achieved by minimizing $\mathcal{D}n$ according to (4.27) by using the integral approach (4.24) in the energy range [2.0, 2.8] eV. The topology of $\mathcal{D}n(s, n_{\text{Sub}})$ for $650 \leq s \leq 730$ nm and $1.0 \leq n_{\text{Sub}} \leq 1.8$ in *Fig. 4.05* exhibits a global minimum at $s = 685$ nm and $n_{\text{Sub}} = 1.35$.

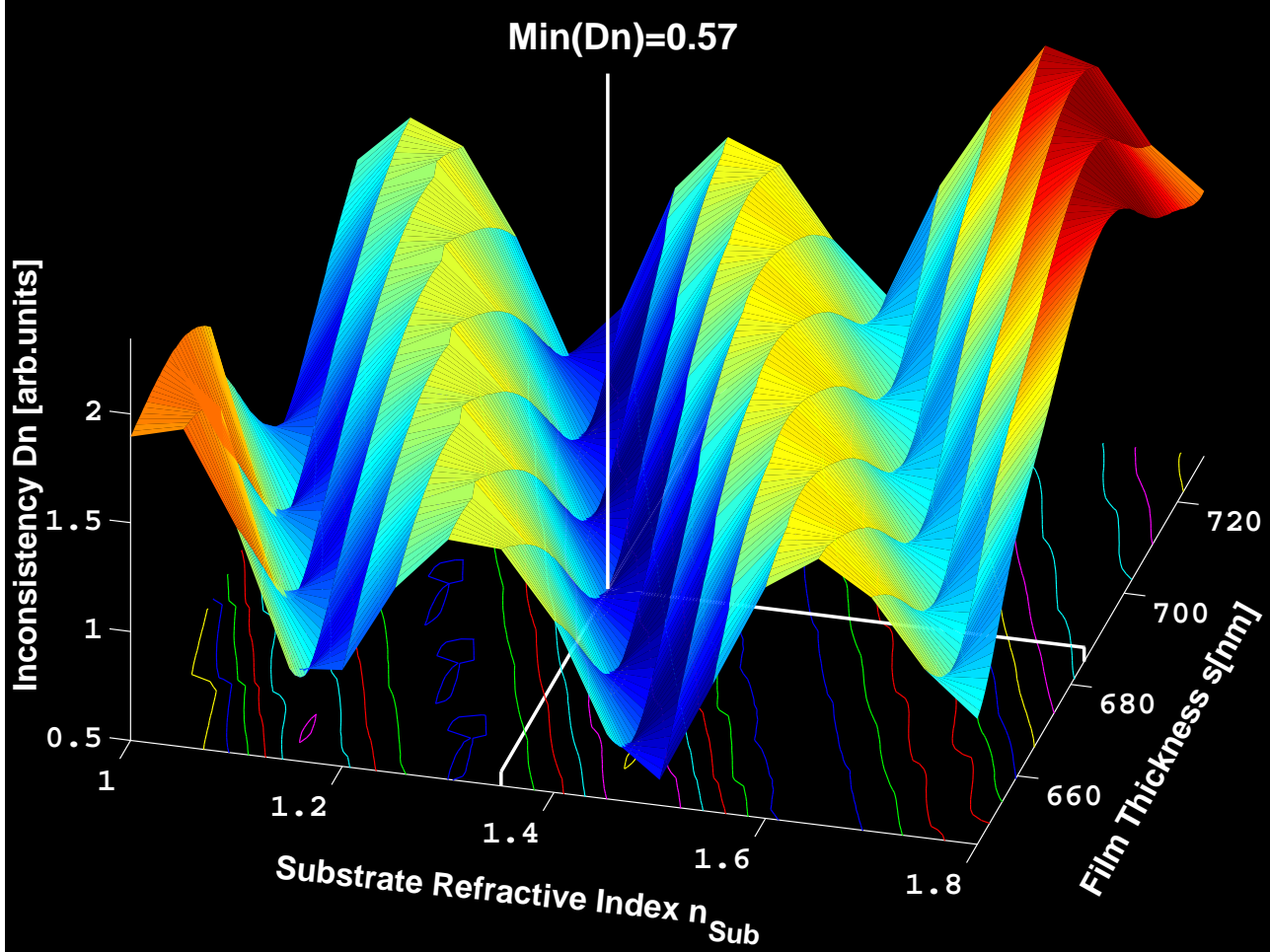


Fig. 4.05: 3D-Contour plot of $\mathcal{D}n(s, n_{\text{Sub}})$ for $s \in [650, 730]$ nm, $n_{\text{Sub}} \in [1.0, 1.8]$ and $\mathcal{C} = 0.6$ with absolute minimum at $s = 685$ nm and $n_{\text{Sub}} = 1.35$. The resolution of the grid is $\Delta s = 1.0$ nm and $\Delta n_{\text{Sub}} = 0.05$.

This optically determined, preliminary, thickness value is in accordance with scanning electron and transmission electron microscopy measurements carried out on the sample under investigation. The estimated value for the substrate index of refraction, on the other hand, is consistent with the previously mentioned tests. It is clearly seen in *Fig. 4.05* that choosing $n_{\text{Sub}} \geq 1.5$ causes large intrinsic inconsistencies, no matter what film thickness is adjusted. Especially, setting $n_{\text{Sub}} = 1.8$, i.e. to the refractive index of sapphire leads to the most divergent results.

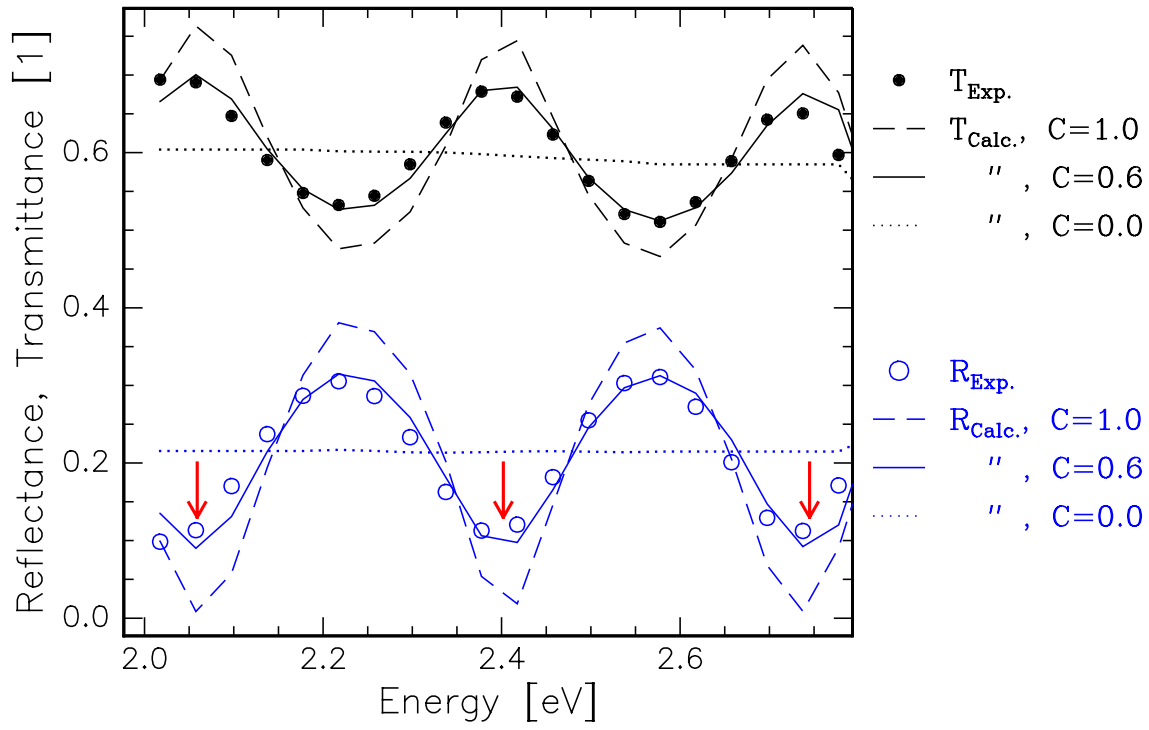


Fig. 4.06: Initial value calculation with $s = 685$ nm, $n_{\text{Sub}} = 1.35$. The symbols are the measured data while the lines are the calculated reflectance and transmittance for $C = 0, 0.6, 1.0$. The arrows indicate the periods obtained from the phase δ in Fig. 4.07.

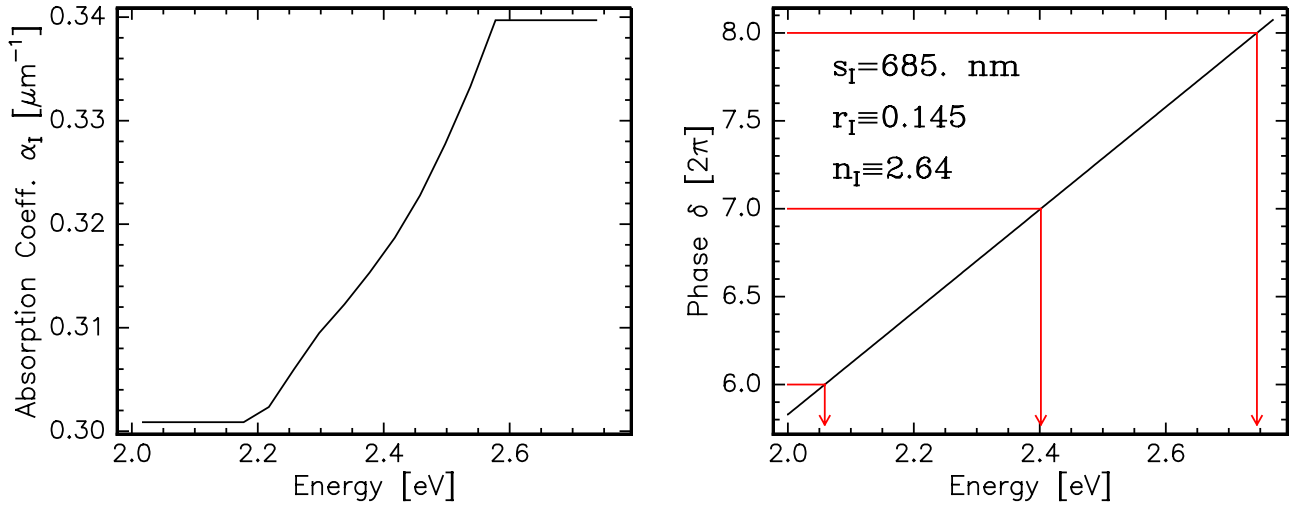


Fig. 4.07: Initial values for the optical constants (r_I, α_I)(E) and the phase δ . The energy periods of interference order 6–8 are arrowed (compare to Fig. 4.06).

The low-energy initial solution shown in Fig. 4.06 is obtained as a result of the above coarse optimization of $\mathcal{D}n(s, n_{\text{Sub}})$ and an adjustment of the coherence factor to $C = 0.6$. The corresponding initial values $\alpha_I(E)$ and the phase $\delta(E)$ are depicted in Fig. 4.07. Since the reflection coefficient (not shown) is varying around a mean value of $r_I = 0.145$ which correlates to $n_I = 2.64$, these quantities were set constant in the energy range under consideration. The

absorption coefficient, on the other hand, is monotonically increasing. The constant parts at the boundaries of half-period width are due to applying the integral method (4.24).

Since for $E \leq 2.6$ eV, the optical constants exhibit only little variation, the calculated transmittance and reflectance model the experimental data quite well at these low energies. Note also that the linear phase δ is in accordance with the observed interference extrema. The discrepancies between the measured and calculated data stem from the neglect in energy dependence of r and from the constant boundary values of α at $E = E_{\min}, E_{\max}$. Furthermore, the adjustment of (s, n_{sub}) has to improved by a more elaborate calculation solving the equations (4.22) over the entire energy range.

Complete Calculation

On the grounds of the initial values $(r_{\text{I}}, \alpha_{\text{I}})(E)$ and (s, n_{sub}) , the system of equations (4.22) can now be solved in conjunction with a fine-tuning of the film thickness and the substrate index of refraction by minimizing $\mathcal{D}n(s, n_{\text{sub}})$ over the entire energy range from 2.0 – 3.8 eV. As a result, the values $s = 690.0$ nm, $n_{\text{sub}} = 1.34$, and the optical constants depicted in *Fig. 4.09* are obtained. In *Fig. 4.08*, the corresponding calculated reflectance and transmission curves (solid lines) are compared to the experimental data (symbols). Apart from a few outliers, the theoretical curves match the measured ones and lead to a smooth, monotonically increasing phase $\delta(E)$ which is consistent with the observed extrema in $(\mathcal{R}, \mathcal{T})(E)$.

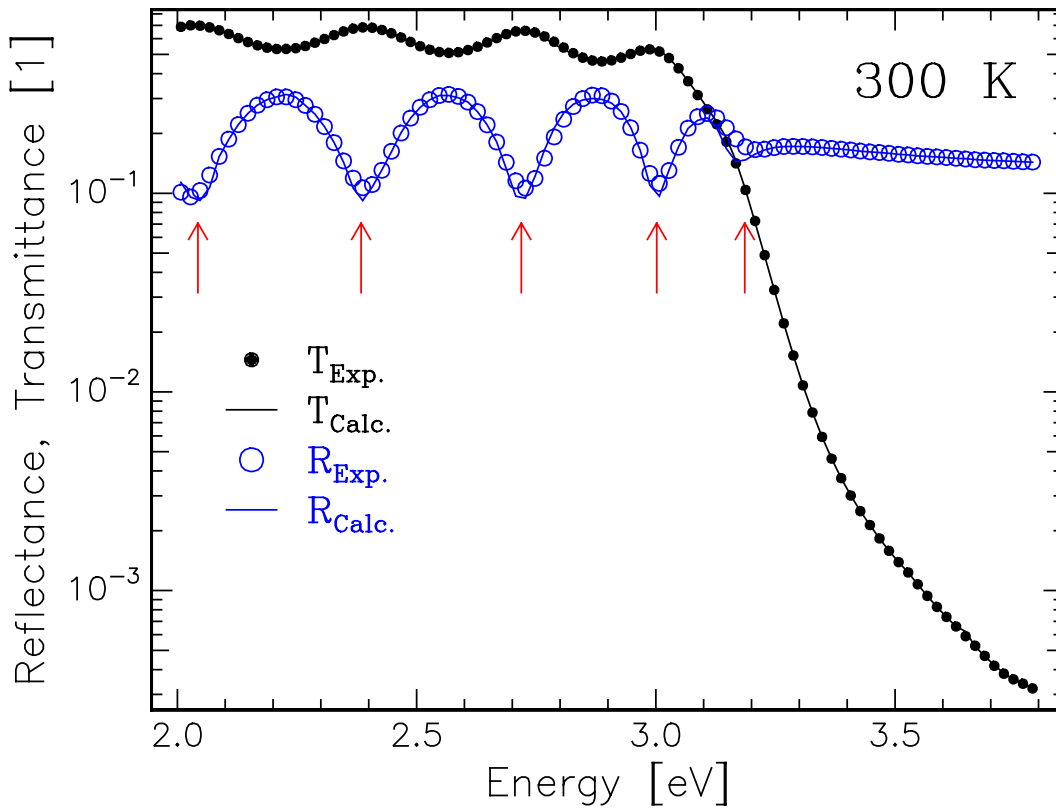


Fig. 4.08: Measured (symbols) and calculated (lines) reflectance and transmittance of β -GaN at $T=300$ K. The arrows indicate the periods as determined by the phase δ in *Fig. 4.09*.

The lower left subplot of *Fig. 4.09* shows the energy dependence of the index of refraction. Evidently, $n(E)$ cannot be understood as arising from a simple Lorentzian-oscillator-like

fundamental gap in which case $n^2(E)$ can be stated as

$$\bar{n}^2(E) = n_\infty^2 + (\Delta n)^2 \frac{(\Delta E)^2}{(E - E_o)^2 + (\Delta E)^2}. \quad (4.28)$$

However, $n^2(E)$ can be modelled in limited photon energy ranges by the equation (4.28), yielding the parameters listed in *Tab. 4.1*.

E_o [eV]	ΔE [eV]	n_∞	Δn	Photon Energy [eV]
3.22	0.13	2.63	1.10	$2.00 \leq E \leq 3.23$
3.23	0.33	2.47	1.91	$3.21 \leq E \leq 3.80$

Table 4.1: Model parameters for $\bar{n}^2(E)$ of β -GaN at 300 K.

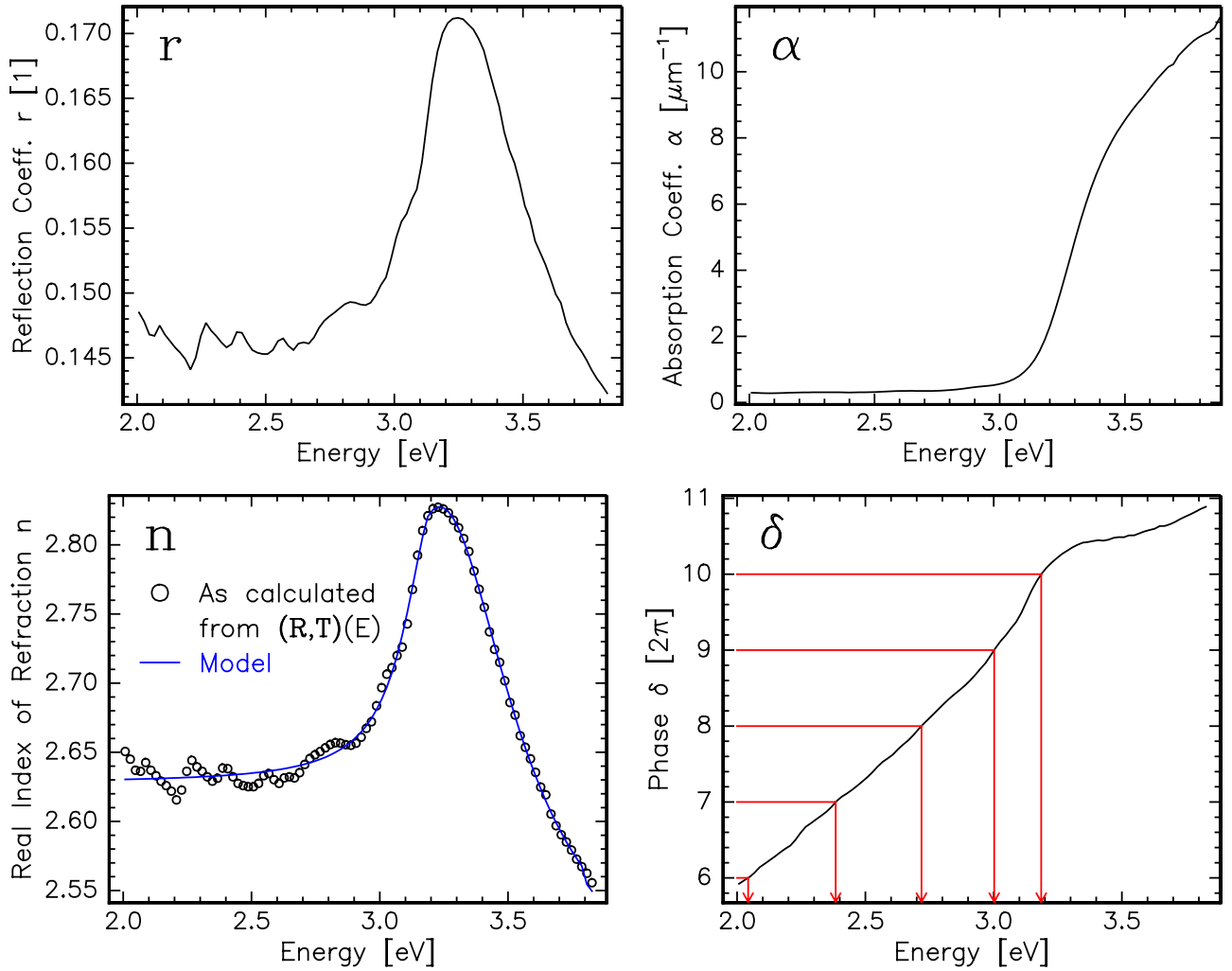


Fig. 4.09: Solution of equations (4.22) for β -GaN at $T=300$ K with $s = 690.0$ nm, $n_{\text{sub}} = 1.34$, and $\mathcal{C} = 0.6$. The energy periods in $\delta(E)$ of interference order 6–10 are arrowed (compare to *Fig. 4.08*). The line in the $n(E)$ plot shows the double-Lorentzian fit (4.28).

The two partial curves out of which $\bar{n}(E)$ is composed match smoothly in the overlap range $3.21 \leq \hbar\omega \leq 3.23$ eV. They adequately describe the experimental data (circles in *Fig.*

4.09) apart from the low-energy fluctuations in $n(E)$ which are not believed to be an intrinsic property of β -GaN but are rather assigned to error propagation. It has to be stressed that the values given in *Tab. 4.1* merely serve to mathematically model the overall trend in $n(E)$ and care has to be taken not to physically overinterpret those parameters. The complex dielectric constant ϵ_c is displayed in *Fig. 4.10* together with the smooth model function $\bar{\epsilon}_c = (\bar{n} + i\kappa)^2$.

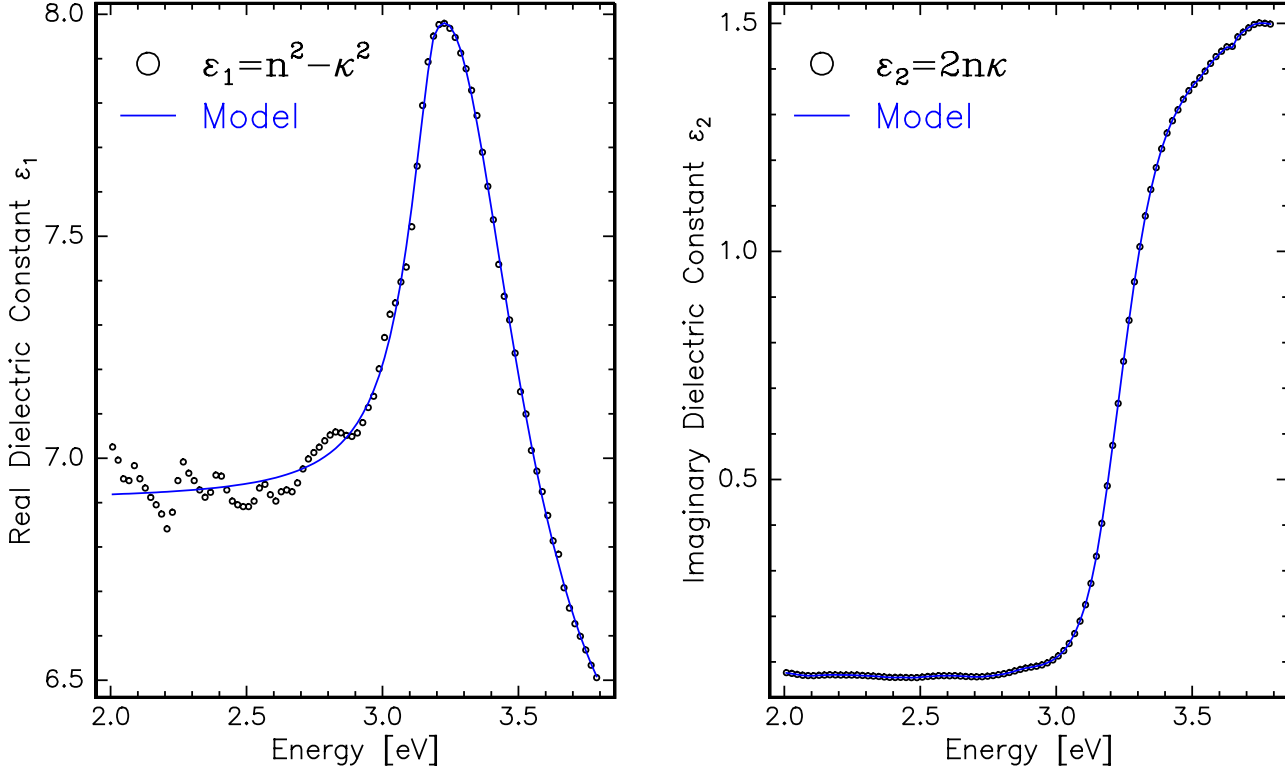


Fig. 4.10: Real and imaginary part of the dielectric constant at T=300 K (symbols). The lines arise from the modelled refractive index \bar{n} .

4.5.2 Low-Temperature Properties

The above scheme is also used to analyse reflectance and transmittance data acquired at 10, 150, and 260 K. For the lowest temperature considered, the (s, n_{sub}) -optimization was repeated in order to probe the consistency. Values of $n_{\text{sub}} = 1.335$ and $s = 688.9$ nm were obtained giving confidence in the method presented. In *Fig. 4.11*, the measured 10 K data are compared to the calculated spectra while *Figs. 4.12, 13* show the corresponding optical constants.

As expected, the prominent spectral features are shifted towards higher energies. The low-energy mean values of the reflection coefficient and the index of refraction are almost the same as those obtained at room temperature within the present accuracy ($\approx \pm 3\%$). If the 10 K refractive index is submitted to the same crude model than its 300 K counterpart, the parameters shown in *Tab. 4.2* are obtained.

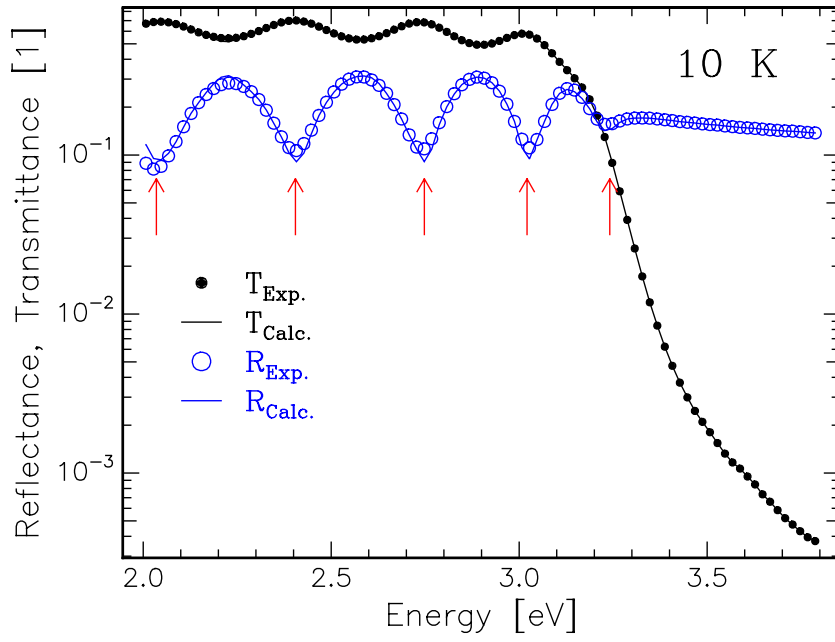


Fig. 4.11: Measured (symbols) and calculated (lines) reflectance and transmittance of β -GaN at $T=10$ K. The arrows indicate the periods as determined by the phase δ in Fig. 4.12.

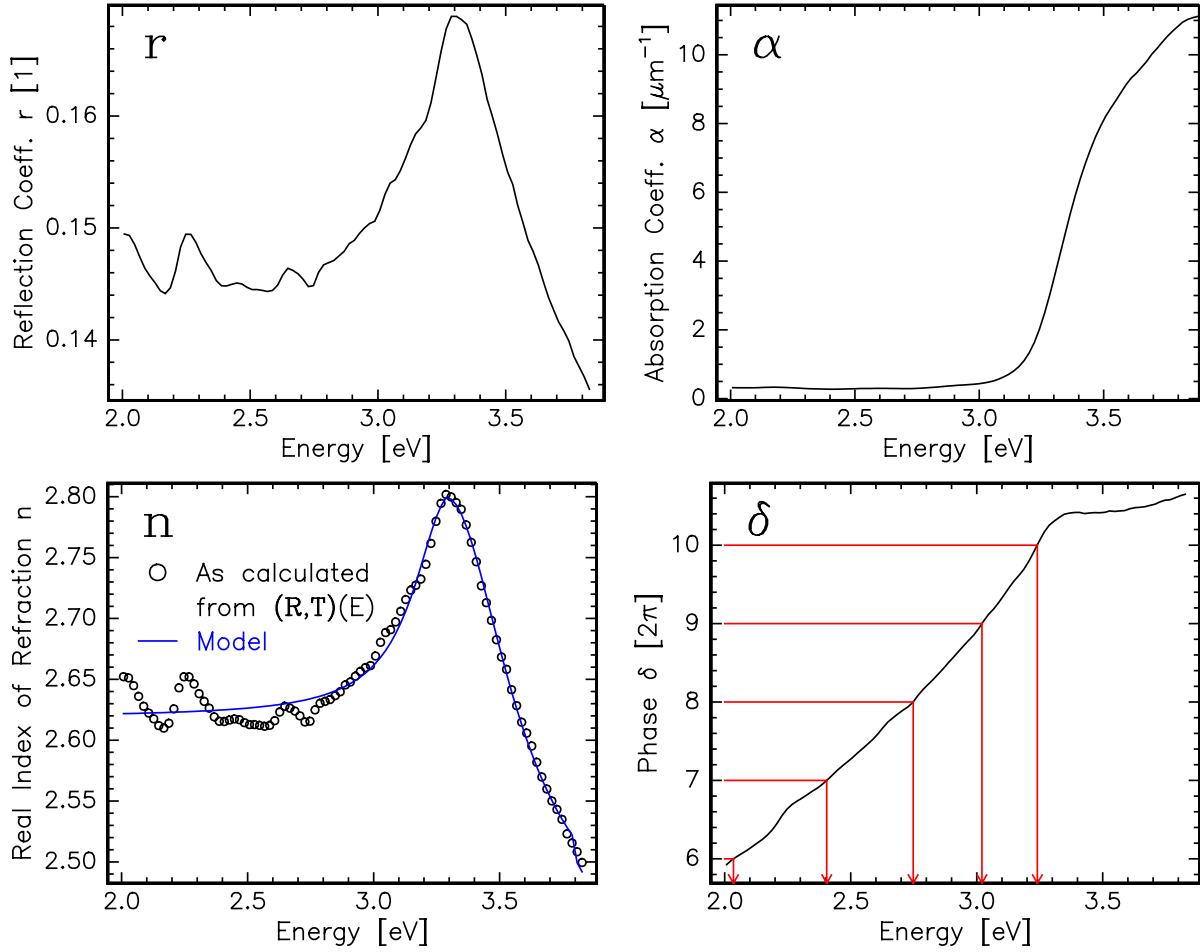


Fig. 4.12: Solution of equations (4.22) for β -GaN at $T=10$ K with $s = 688.9$ nm, $n_{\text{Sub}} = 1.335$, and $C = 0.6$. The energy periods in $\delta(E)$ of interference order 6–10 are arrowed (compare to Fig. 4.11). The line in $n(E)$ shows the double-Lorentzian fit (4.28).

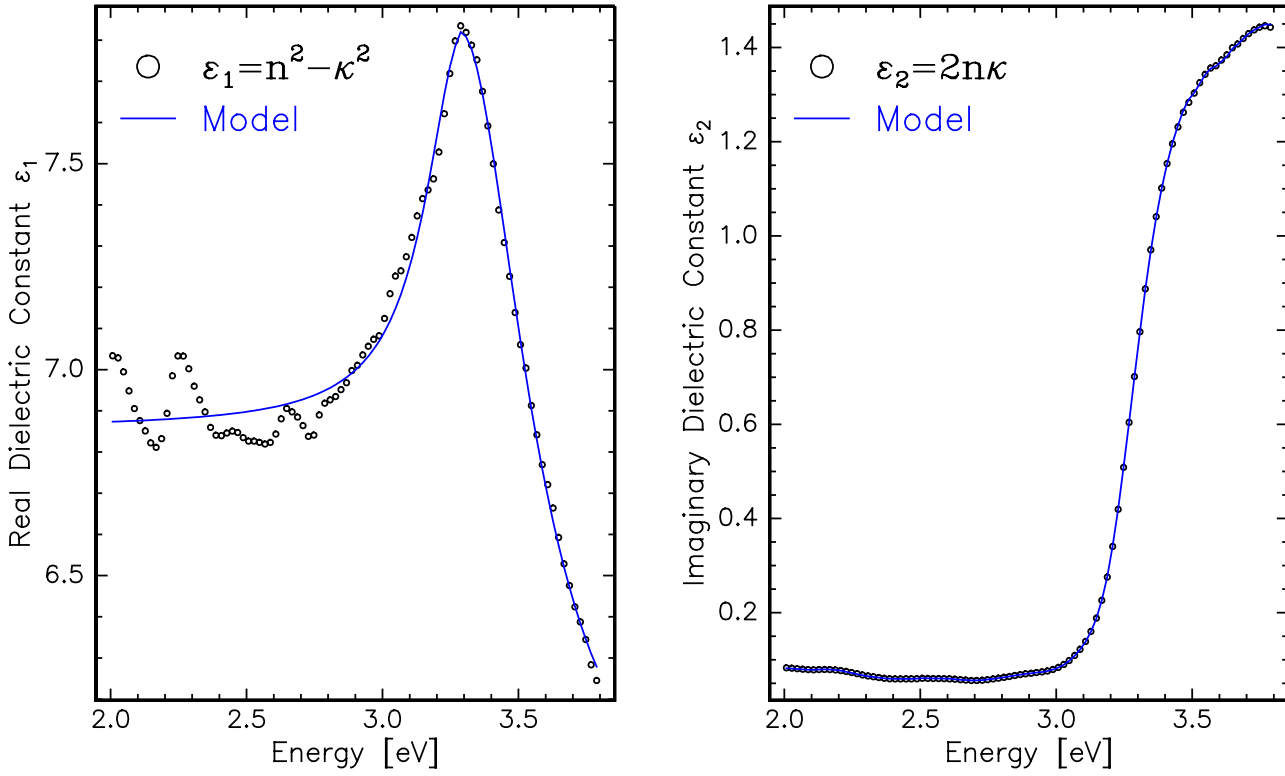


Fig. 4.13: Real and imaginary part of the dielectric constant at T=10 K (symbols). The lines arise from the modelled refractive index.

E_o [eV]	ΔE [eV]	n_∞	Δn	Photon Energy [eV]
3.30	0.16	2.62	0.98	$2.00 \leq E \leq 3.47$
3.29	0.29	2.42	1.97	$3.29 \leq E \leq 3.80$

Table 4.2: Model parameters for $n^2(E)$ of β -GaN at 10 K.

4.5.3 Fundamental Absorption Edge

Having determined the optical constants of the β -GaN reference sample, we will now consider its band edge properties in more detail. Within the validity of Fermi's Golden Rule the electric dipole transition probability per unit time between conduction and valence band states $|c\rangle$, $|v\rangle$ under the impact of an electric field $\mathcal{E}(r, t) = \mathcal{E}_o \exp\{i(kr - \omega t)\}$ is given by [70]

$$R = 2\pi\hbar \left(\frac{e}{m\hbar\omega}\right)^2 \left|\frac{\mathcal{E}_o}{2}\right|^2 \int \underbrace{|\langle c|\hat{x}p|v\rangle|^2}_{P_{cv}} D(E_{cv}) dE_{cv} \quad (4.29)$$

with the joint density of states

$$D(E_{cv}) = \frac{1}{4\pi^3} \int \frac{dS_k}{|\nabla_k(E_{cv})|}, \quad (4.30)$$

$$E_{cv} = E_c - E_v, \quad E_{cv} = \text{const. for } k \in S_k.$$

Since the power loss in the field equals to $R\hbar\omega = \alpha Ic/n$ where $I = |n\mathcal{E}_o|^2/(8\pi)$, the imaginary part of the dielectric constant

$$\epsilon_2 = \frac{8\pi\hbar}{|\mathcal{E}_o|^2} R \quad (4.31)$$

follows. For an *ideal direct-gap semiconductor with parabolic bands* $E_{cv} = E_G + (\hbar k)^2/(2\mu)$, $\mu^{-1} = m_c^{-1} + m_v^{-1}$,

$$D(E_{cv}) = \frac{\sqrt{2\mu^3}}{\pi^2\hbar^3} \sqrt{E_{cv} - E_G} \quad (4.32)$$

and thus

$$\epsilon_2(E) = \frac{4e^2\sqrt{2\mu^3}}{\hbar m^2} |P_{cv}|^2 \frac{\sqrt{E - E_G}}{E^2}, \quad E = \hbar\omega \quad (4.33)$$

for $E \geq E_G$ and $\epsilon_2(E < E_G) = 0$. Provided that the semiconductor complies with the above idealizations, the band gap E_G is obtained by the intercept of $(\epsilon_2(E)E^2)^2$, or equivalently, $(\alpha(E)E)^2$ with the photon energy axis at $\epsilon_2 = 0$.

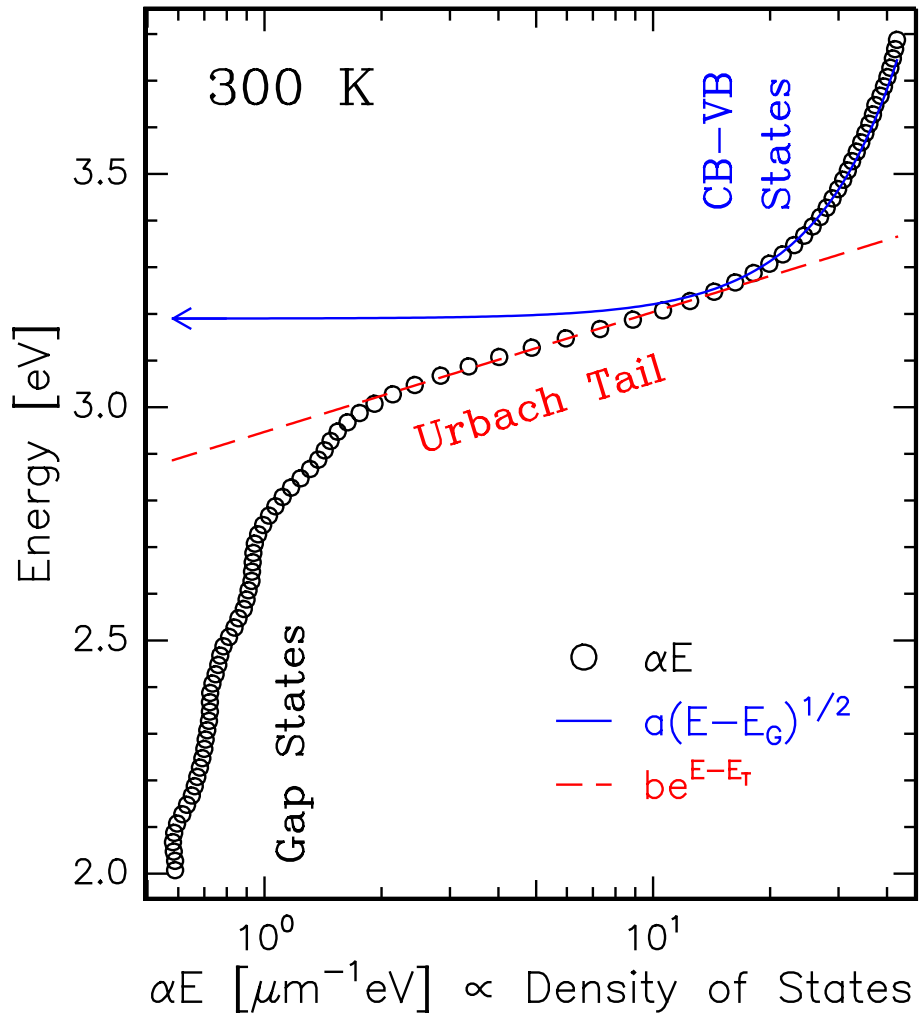


Fig. 4.14: Fundamental absorption edge of β -GaN at 300 K

In praxis, however, the assignment of E_G may not be straightforward. Even in high-purity material, an Urbach tail at energies close to E_G generally is observed [77]. In addition, impurity-related acceptor and donor levels can merge with the intrinsic bands and further blur the

fundamental band gap. An example of such is shown in *Fig. 4.14* where the present room temperature absorption data of the β -GaN reference sample, αE , are plotted against energy.

A least-squares fit of the expression $a\sqrt{E - E_G}$ (solid line) leads to a value of $E_G = 3.19 \pm 0.05$ eV. If the reduced effective mass μ of β -GaN was known, the momentum matrix element $|P_{cv}|$ could be calculated from the slope a . For $3.0 \leq E \leq 3.2$ eV, an exponential behavior $\alpha E = b \exp(E - E_T)$ with $E_T = 2.95 \pm 0.05$ eV is observed. At even lower energies measurable absorption still prevails which is attributed to transitions between gap states. Even if the latter were not present, the fundamental absorption edge would be smeared out by the Urbach tail such that a determination of E_G on the grounds of the square root density of states may lead to an underestimation of the band gap.

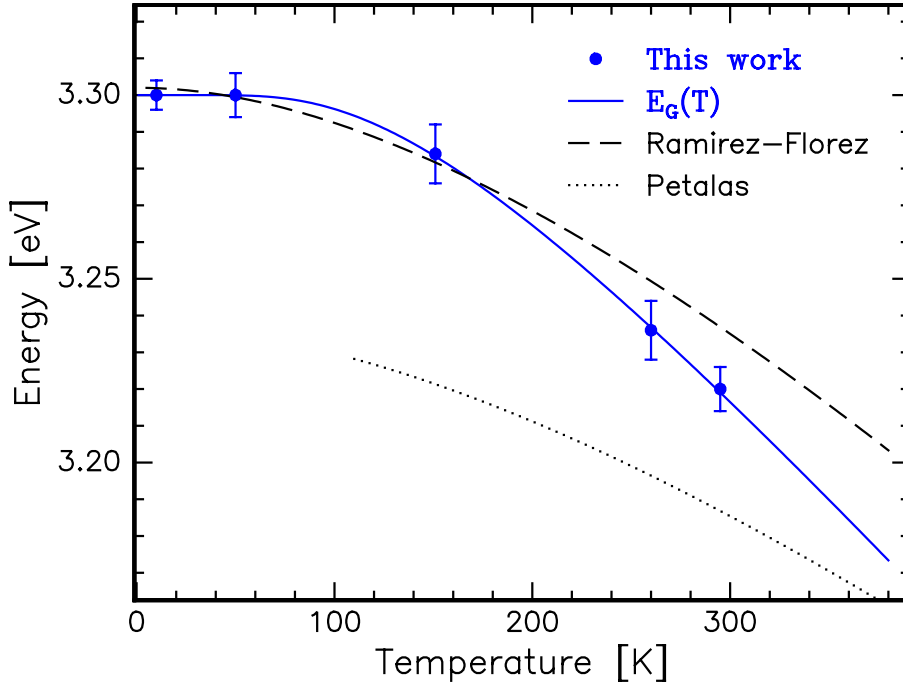


Fig. 4.15: Temperature dependence of the fundamental absorption edge of β -GaN

Rather than resorting to absorption data alone, the refractive index n being a result of reflectance \mathcal{R} in conjunction with transmittance \mathcal{T} will now be used to determine the temperature dependence of the fundamental band gap of the β -GaN sample. Since an ideal absorption edge is correlated with the onset of anomalous dispersion $dn/dE < 0$, the band gap E_G will be defined by the maximum in the refractive index at which $\frac{dn}{dE}(E_G) = 0$. The values $E_G(T)$ obtained in this fashion (symbols in *Fig. 4.15*) are larger by about 25 meV than those extracted from the simple square root fit to αE .

The temperature dependence of the inter-band energy behaves as

$$E_G(T) = E_G(0) - S_\Omega E_\Omega \left\{ \coth \left(\frac{E_\Omega}{2KT} \right) - 1 \right\} \quad (4.34)$$

where E_Ω stands for an average phonon energy and S_Ω is a coupling constant [78, 79, 80]. In contrast to the frequently used Varshni empirical relation, this expression is physically motivated by phonon occupation numbers obeying Bose-Einstein statistics.

The parameters obtained by fitting the expression (4.34) to the band edge data shown in *Fig. 4.15* (symbols) are summarized in *Tab. 4.3*. For comparison, data published by Ramirez-Florez [81] and Petalas [82] are displayed (broken lines).

$E_G(0)$ [eV]	E_Ω [meV]	S_Ω [1]
3.3 ± 0.04	37 ± 2	3.5 ± 0.35

Table 4.3: Model parameters for the temperature dependent band gap energy of β -GaN.

These authors have used the Varshni expressions $E_G(T) = 3.302 - 6.697 \times 10^{-4} T^2 / (T + 600)$ eV and $E_G(T) = 3.237 - 5.161 \times 10^{-4} T^2 / (T + 600)$ eV, respectively, to model their data.

4.6 Incoherence and Optical Inhomogeneity

So far, effects of incoherence were analytically treated by linearly interpolating between the two extreme cases of perfect coherence (sum over amplitudes $\Rightarrow \mathcal{R}_A(\delta), \mathcal{T}_A(\delta)$) and entire incoherence (sum over intensities $\Rightarrow \mathcal{R}_I, \mathcal{T}_I$). A so-called *empirical coherence factor* $0 \leq \mathcal{C} \leq 1$ has been defined which allows for a quantitative treatment of intermediate degrees of coherence.

Even though this approach is intuitively evident and leads to reasonable values for the optical constants of the β -GaN reference sample, it is not obvious at all whether the effect of random phase fluctuations on the observed reflectance and transmittance can indeed be quantified in such a simple manner. Further, even if a linearized description of (in)coherence by virtue of a macroscopic parameter \mathcal{C} is justified, no microscopic interpretation of \mathcal{C} is possible at the present stage.

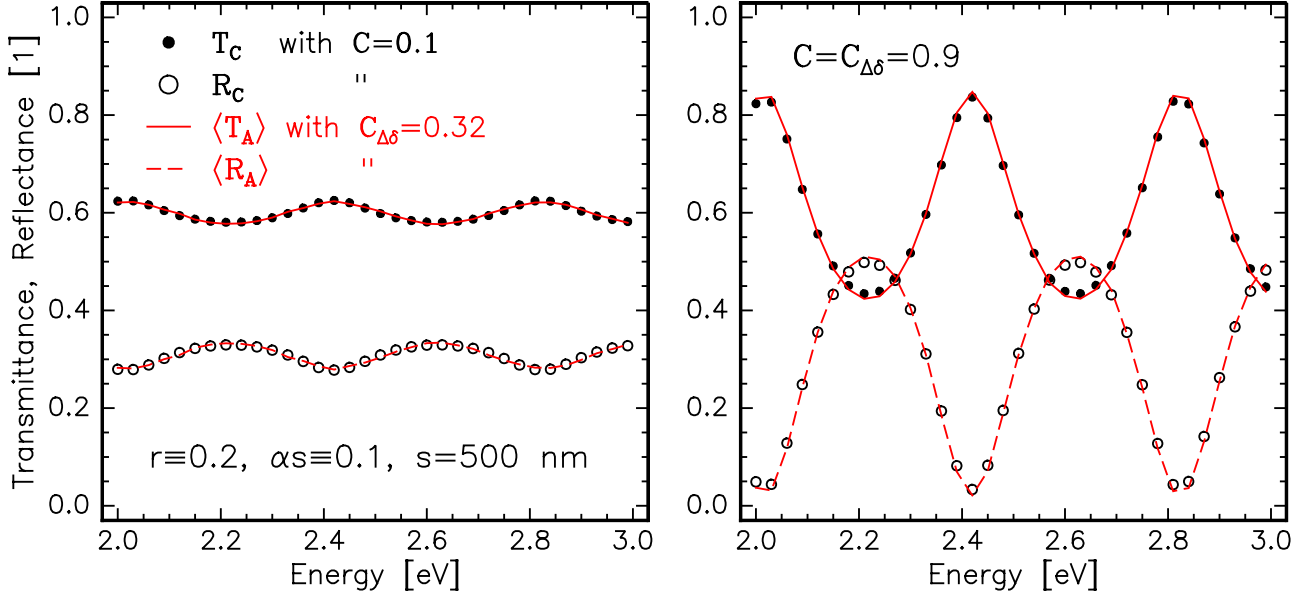
Since many stochastically independent processes caused by interfacial roughness and spatial inhomogeneities in the refractive index sum up in contributing to the random phase fluctuations $\Delta\delta_j$ in (4.13), the resulting probability density \mathcal{P} will be a normal distribution

$$\boxed{\begin{aligned} \mathcal{P}(\Delta\delta_j) &= \frac{1}{\sqrt{2\pi}\sigma_\delta} \exp\left\{-\frac{(\Delta\delta_j)^2}{2\sigma_\delta^2}\right\} \\ \sigma_\delta &= \pi(1 - \mathcal{C}_{\Delta\delta}), \end{aligned}} \quad (4.35)$$

characterized in width by the *statistical coherence factor* $\mathcal{C}_{\Delta\delta}$. Indeed, the statistical distribution of the surface roughness alone has a Gaussian profile as revealed by AFM investigations. Given such a probability density $\mathcal{P}(\Delta\delta)$, we now have to investigate if for each $\mathcal{C}_{\Delta\delta}$, there exists an empirical coherence factor \mathcal{C} such that for all δ , $|\rho|^2 = r$ and α :

$$\boxed{\begin{aligned} \langle \mathcal{R}_A \rangle &= \left\langle \left| \rho - \sum_{j=1}^{\infty} e^{ij(\delta + \Delta\delta_j)} (1 - \rho^2) \rho^{2j-1} e^{-2j\alpha s} \right|^2 \right\rangle \\ &\approx r \left\{ \mathcal{C} \frac{1 - 2e^{-\alpha s} \cos \delta + e^{-2\alpha s}}{1 - 2re^{-\alpha s} \cos \delta + r^2 e^{-2\alpha s}} + (1 - \mathcal{C}) \frac{1 + (1 - 2r)re^{-2\alpha s}}{1 - r^2 e^{-2\alpha s}} \right\} = \mathcal{R}_c \\ \text{and} \\ \langle \mathcal{T}_A \rangle &= \left\langle \left| \sum_{j=0}^{\infty} e^{ij(\delta + \Delta\delta_j)} (1 - \rho^2) \rho^{2j} e^{-2(j+1)\alpha s} \right|^2 \right\rangle \\ &\approx (1 - r)^2 e^{-\alpha s} \left\{ \frac{\mathcal{C}}{1 - 2re^{-\alpha s} \cos \delta + r^2 e^{-2\alpha s}} + \frac{1 - \mathcal{C}}{1 - r^2 e^{-2\alpha s}} \right\} = \mathcal{T}_c. \end{aligned}} \quad (4.36)$$

A rigorous analytical proof of the above relations is not at all straightforward and actually not even necessary. It suffices to verify that these equations hold to within the accuracy in reflectance and transmittance data acquisition for the values of $(r, \alpha s)$ being typically encountered in praxis. Therefore, $(\mathcal{R}_C, \mathcal{T}_C)$ spectra were calculated with fixed $(r, \alpha s)$ for $0 \leq \mathcal{C} \leq 1$ and the corresponding $\mathcal{C}_{\Delta\delta}(\mathcal{C})$ was determined which yields the best match between the Monte Carlo simulated $(\langle \mathcal{R}_A \rangle, \langle \mathcal{T}_A \rangle)$ and the given $(\mathcal{R}_C, \mathcal{T}_C)$.



Figs. 4.16a,b: Comparison between $(\mathcal{R}_C, \mathcal{T}_C)$ calculated for $r \equiv 0.2$, $\alpha s \equiv 0.1$, $s = 500$ nm (symbols) and the corresponding Monte Carlo simulation $(\langle \mathcal{R}_A \rangle, \langle \mathcal{T}_A \rangle)$ with adjusted statistical coherence factor $\mathcal{C}_{\Delta\delta}$ (lines). In the left figure $\mathcal{C} = 0.1$ and in the right one, $\mathcal{C} = 0.9$ were given.

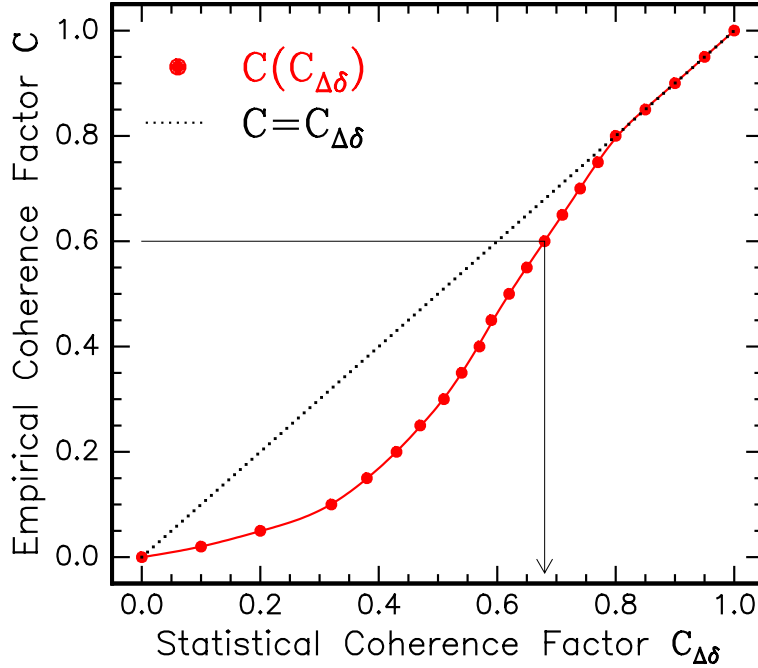


Fig. 4.17: Empirical \mathcal{C} versus statistical coherence factor $\mathcal{C}_{\Delta\delta}$.

This comparative study was carried out for various combinations of $(r, \alpha s)$. In general, good agreement can be reached between the empirical and the statistical reflectance and transmittance curves provided that $\mathcal{C}_{\Delta\delta}$ is optimized to within an accuracy of ± 0.01 . The random phase fluctuations model with Gaussian density \mathcal{P} exhibits slightly less abrupt minima in \mathcal{R} and, accordingly, maxima in \mathcal{T} . For reflectance coefficients $r \leq 0.5$, these systematical deviations are typically $\leq 1\%$ for $0 \leq \mathcal{C} \leq 1$. Examples of such are given in *Figs. 4.16a,b* where $(r, \alpha s) \equiv (0.2, 0.1)$ and $s = 500$ nm were used and the two cases of $\mathcal{C} = 0.1$ and 0.9 are depicted.

It has to be emphasized that the optimum $\mathcal{C}_{\Delta\delta}(\mathcal{C}) \pm 0.01$ found is independent of the values of $(r, \alpha s)$ assumed. Thus, the correlation between the empirical and the statistical coherence factor shown in *Fig. 4.17* has universal meaning in the sense that it applies for a wide range of optical constants and for all (mean) phases δ . While the equality in equations (4.36) does not hold exactly, the discrepancies between $(\langle \mathcal{R}_A \rangle, \langle \mathcal{T}_A \rangle)$ and $(\mathcal{R}_C, \mathcal{T}_C)$ are within the experimental error in $(\mathcal{R}, \mathcal{T})$ of typically 1–2%.

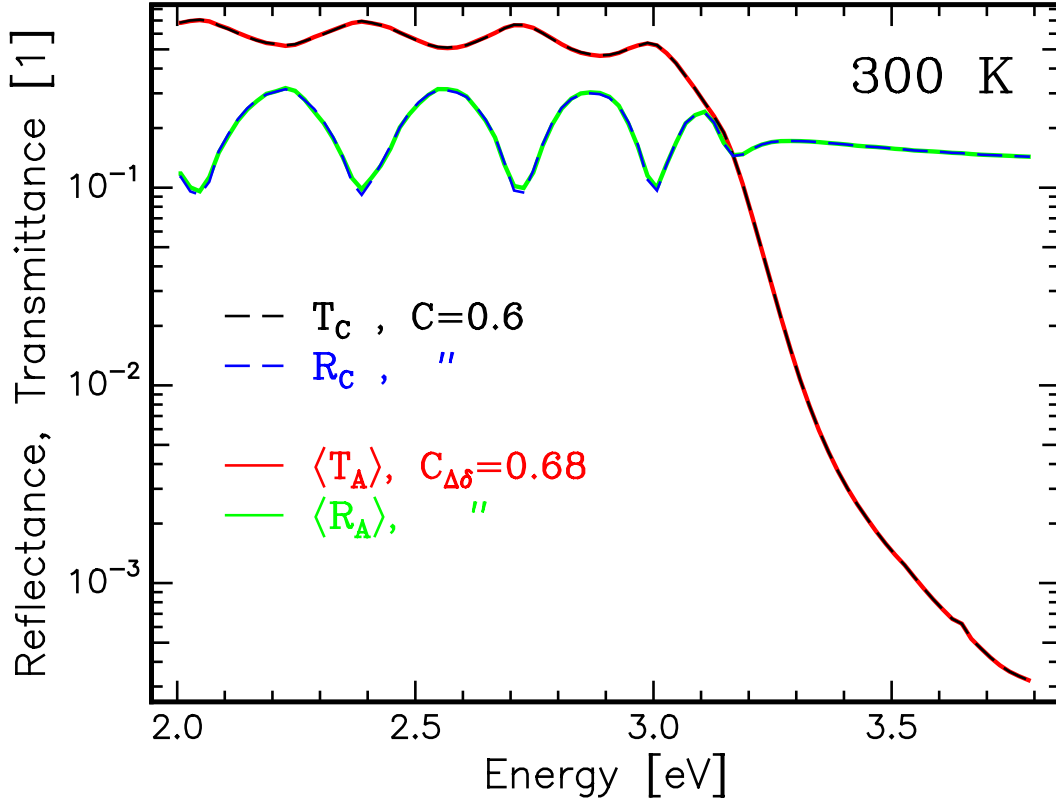


Fig. 4.18: Calculated 300 K reflectance \mathcal{R}_C and transmittance \mathcal{T}_C spectra (dashed lines) of the β -GaN reference sample, based on equations (4.22) with $\mathcal{C} = 0.6$ and the determined optical constants $(r, \alpha s)(E)$. In comparison, $(\langle \mathcal{R}_A \rangle, \langle \mathcal{T}_A \rangle)$ spectra are shown (solid lines) which were obtained by a Monte Carlo simulation with $\mathcal{C}_{\Delta\delta} = 0.68$ employing the same $(r, \alpha s)(E)$.

According to *Fig. 4.17*, the empirical factor $\mathcal{C} = 0.6$ employed so far to model the experimental $(\mathcal{R}, \mathcal{T})$ data of the β -GaN reference sample should be equivalent to a statistical coherence factor of $\mathcal{C}_{\Delta\delta} = 0.68$. Indeed, performing a statistical simulation using the previously determined optical constants $(r, \alpha s)(E)$ seen in *Fig. 4.09* leads to $(\langle \mathcal{R}_A \rangle, \langle \mathcal{T}_A \rangle)(E)$ spectra (bright lines in *Fig. 4.18*) which almost exactly match the empirically determined $(\mathcal{R}_C, \mathcal{T}_C)(E)$ curves (dark dashed lines in *Fig. 4.18*). Since the extrema in the Monte Carlo simulations are slightly smoother than those of the $(\mathcal{R}_C, \mathcal{T}_C)$ spectra, the agreement between the former and the experimental data is even better (compare *Fig. 4.08* on page 34).

The fact that, despite significant gradients in the real-live-data $(r, \alpha s)(E)$ of the β -GaN sample, the conformity in the reflectance and transmittance curves depicted in *Fig. 4.18* is so good, exemplifies the correctness of the correlation $\mathcal{C}_{\Delta\delta}(\mathcal{C})$ shown in *Fig. 4.17* over a wide range of optical constants. Further, it should be pointed out that the damping in the peak-to-valley ratio of the sub-band-gap $(\mathcal{R}, \mathcal{T})$ data, which has been attributed to incoherence, is independent of the photon energy. Therefore, it was possible to model $(\mathcal{R}, \mathcal{T})$ with constant \mathcal{C} and $\mathcal{C}_{\Delta\delta}$. From the latter, the standard deviation of the phase fluctuation $\sigma_\delta = 1.00$ is obtained

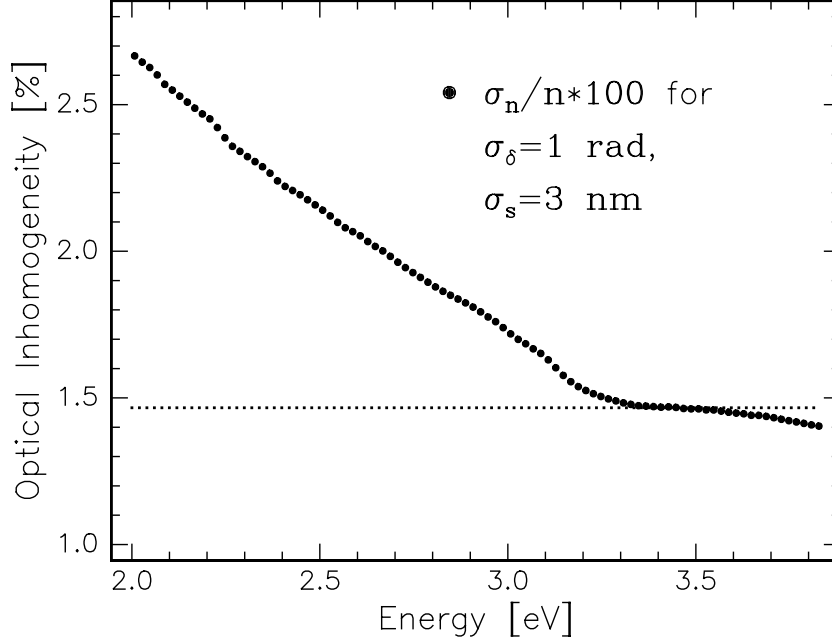


Fig. 4.19: Relative inhomogeneity σ_n/n [%] in the refractive index of the β -GaN reference sample extracted from the room temperature $(\mathcal{R}, \mathcal{T})$ data with $\mathcal{C}_{\Delta\delta} = 0.68$, corresponding to $\sigma_\delta = 1.00$, and $\sigma_s = 3 \text{ nm}$.

On the other hand, AFM measurements yield a RMS surface roughness of 1.5 nm (*Fig. 3.14*, page 22), which is comparable to the roughness of the GaN/GaAs interface as shown by HRTEM. Thus, the mean deviation in the sample thickness is $\sigma_s \approx 3 \text{ nm}$. With this value we are now in a position to estimate the relative contribution¹ of the statistical variations σ_n in the refractive index to the observed phase fluctuations:

$$\frac{\sigma_n}{n} = \sqrt{\frac{\left(\frac{\sigma_\delta}{\delta}\right)^2 - \left(\frac{\sigma_s}{s}\right)^2}{\left(\frac{\sigma_s}{s}\right)^2 + 1}}. \quad (4.37)$$

The energy dependence of this *optical inhomogeneity* inherent to the β -GaN reference sample is displayed in *Fig. 4.19*. At the band edge, e.g., the spread in n is about 1.5% and therefore $n(3.2 \text{ eV}) = 2.83 \pm 0.04$. These variations in the refractive index are assigned to the local strain fields caused by structural inhomogeneity which can be perceived in the bright-field XTEM micrograph *Fig. 3.09* on page 19.

¹For stochastically independent random variables A, B with probability densities $\mathcal{P}_{A,B}$ and respective $\sigma_{A,B}$, the standard deviation of the product AB can be stated as $\sigma_{AB}^2 = \sigma_A^2 \langle B \rangle^2 + \sigma_B^2 \langle A \rangle^2 + \sigma_A^2 \sigma_B^2$ for all $\mathcal{P}_{A,B}$.

Chapter 5

Photoluminescence of GaN versus Temperature

In view of the high density of structural defects encountered in zincblende GaN grown on highly lattice-mismatched substrates, it is not obvious at all that any detectable radiative recombination will take place even at cryogenic temperatures. However, the high luminescence intensities observed in the case of wurtzite GaN are also astonishing since the crystal quality in terms of defect densities of even the best available α -GaN is by orders of magnitude inferior than that of any other III-V or II-VI compound used for opto-electronic applications. Even more contradicting to common sense is the fact that, on the grounds of such an immature material system, room temperature lasing is obtained with device lifetimes being of the order of 10000 hours.[83]

While the temperature dependent optical constants and especially, the band edge of the β -GaN reference sample are amenable to reflection and absorption measurements, it is not possible to clearly link a distinct emission process to the fundamental absorption edge over the entire temperature range. The sample does exhibit weak photoluminescence up to 500 K. However, the spectra are dominated by broad defect luminescence bands covering quantum energies from about 2.5 to 3.2 eV, in particular at low temperatures.

In order to systematically investigate the luminescence properties of β -GaN, we therefore have to resort to the two DC plasma grown samples (#2058, 2070) mentioned in chapter 3. The band edge emission energies, linewidths, and intensities will be studied as a function of temperature and compared to the exciton recombination of an α -GaN reference layer courteously provided by Prof. Akasaki (Meijo University, Japan).

The continuous wave photoluminescence measurements were carried out in a standard apparatus using the 325 nm line of a 50 mW He-Cd laser for carrier excitation. Neutral density filters were employed to vary the excitation power which was measured in front of the sample by a calibrated power meter. The luminescence signal was detected by a cooled GaAs photomultiplier after having been dispersed in a grating spectrometer (600 lines/mm, $\Delta\lambda = 0.1$ nm). The sample itself was kept in an evacuated continuous-flow cryostat allowing stable temperatures in the range of $T = 4 - 500$ K.

5.1 Photoluminescence Spectra of α - and β -GaN

5.1.1 α - and β -GaN Microcrystals

The solid lines in *Figs. 5.01,02* show PL spectra of sample #2058 for T ranging between 5 and 500 K. The low temperature luminescence is dominated by fairly sharp emission lines, denoted by X_C and X_H . Upon raising T , an overall drop in luminescence intensity is observed and the linewidths of X_C and X_H strongly increase while the transition energies monotonically decrease. The transitions with $\hbar\omega \leq 3.2$ eV overwhelm when T is increased from 5 to 70 K and get finally quenched as soon as room temperature is reached. At $T \geq 400$ K, a weak yellow luminescence band is evolving. Since the sample comprises cubic and hexagonal microcrystals sitting on top of a zincblende-phase film, the PL spectra are a superposition of the various emission processes occurring in the different phases.

Selected-area-excitation in cathodoluminescence measurements [57] revealed the X_C and X_H transitions to originate from cubic and hexagonal GaN, respectively. Even though X_C appears most strongly upon excitation of cubic microcrystals, it can also be detected in the cubic-phase film underneath the crystals. In this case, the linewidth of the X_C transition is larger due to the inferior structural quality of the film as compared to the cubic crystals. In contrast, X_H can only be detected in hexagonal crystals and not in the film. While the CL spectra acquired from α - as well as the β -GaN crystals are very clean in terms of low-energy defect luminescence, the low-temperature cathodoluminescence of the film exhibits an intense band at 3.2 eV attributed to donor-acceptor pair recombination. [57]

5.1.2 β -GaN Film

The luminescence spectra of sample #2070 taken at cryogenic temperatures differ markedly from those of the crystallite sample. Instead of the distinct, intense line X_C , a shoulder is detected having a local maximum at slightly lower energy which will be referred to as BX_C . At the X_H energy, only a very weak hump is observed stemming from a small volume fraction of local α -GaN inclusions.

For $T > 50$ K, however, the two samples behave qualitatively quite similar in terms of peak positions and relative intensities. Especially, the BX_C transition being nearly masked by a strong impurity recombination band at $T < 50$ K is taking over with rising T and approaching the same energy as the X_C peak of sample #2058 (*Fig. 5.05*, page 52). The room temperature spectra of the two samples are possessing almost the same characteristics apart from the X_H transition which is virtually missing in the case of sample #2070. In contrast to sample #2058, the β -GaN film exhibits no yellow luminescence even at 500 K.

In order to study the absorption edge of sample #2070, reflectance and transmittance measurements were carried at various temperatures having the GaAs substrate removed. As opposed to the β -GaN reference sample #8092, an attempt was made to measure the present 900 nm thick film free-standing. The lack of mechanical support, however, led to an undulated surface unfeasible for a sound assessment of the reflection coefficient.

The band edge of sample #2070 can thus only be estimated from the transmittance curve $\mathcal{T}(E)$ by virtue of the 0th-order relation $\mathcal{T} \sim e^{-\alpha s}$, $s = 900$ nm (4.10). Underneath each set of luminescence spectra in *Fig. 5.01*, $-\ln(\mathcal{T})$ is plotted against energy and compared to the position of the X_C transition of sample #2058. Both X_C and BX_C correlate with the onset of the fundamental absorption edge.

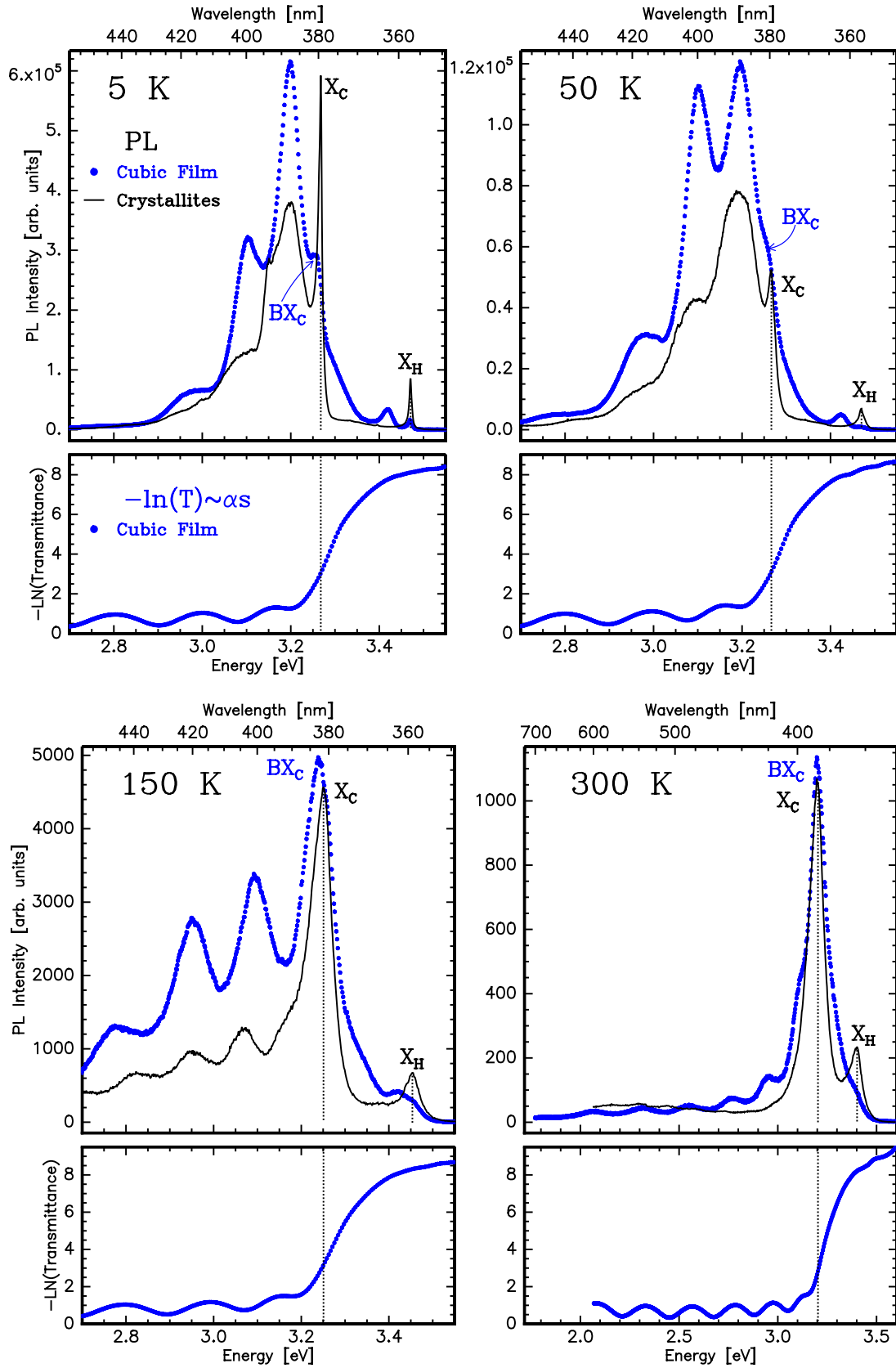


Fig. 5.01: Photoluminescence (upper plots) of samples #2058 (solid lines) and #2070 (symbols) for $T = 5 - 300$ K with the X_C , X_H , and BX_C transitions labeled. The lower plots show the corresponding absorption data $-\ln(\mathcal{T})$ (symbols) of the film #2070 based on the observed transmittance \mathcal{T} .

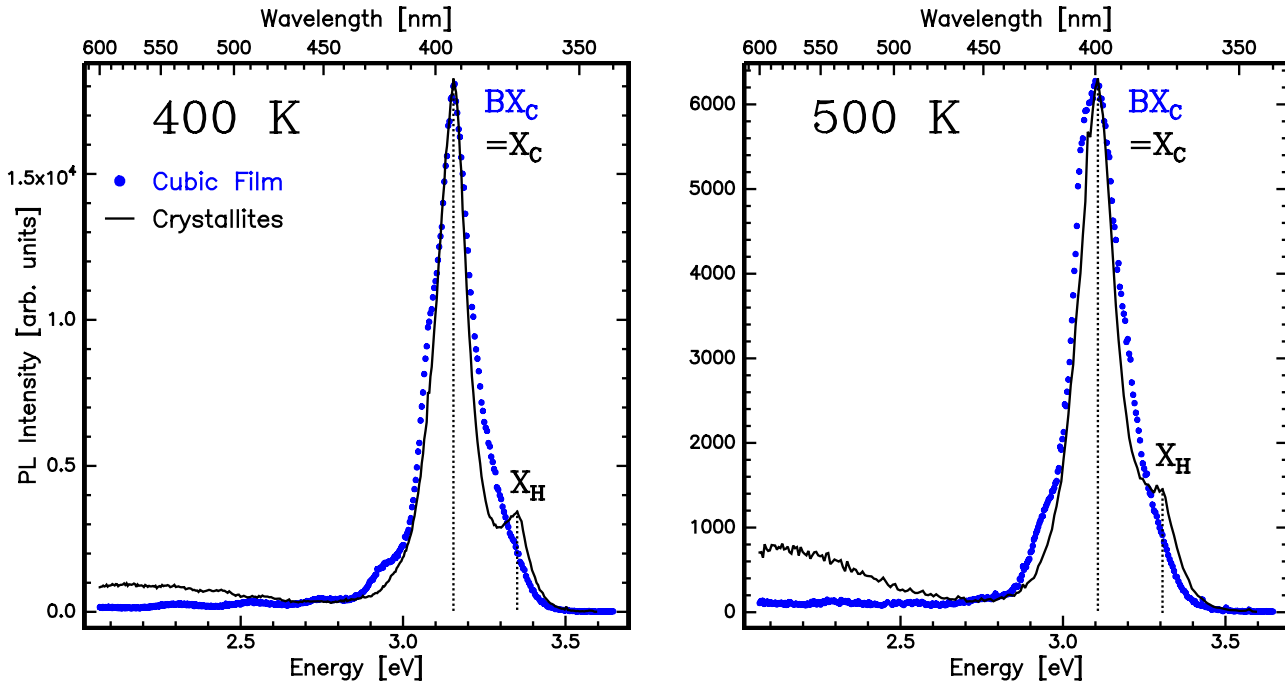


Fig. 5.02: Photoluminescence of samples #2058 (lines) and #2070 (symbols) for $T = 400 - 500$ K

Note that for $T \leq 50$ K and $E \leq 3.0$ eV the local maxima in $-\ln(\mathcal{T})$ coincide with those of the PL signal of sample #2070 while at higher temperatures, this correlation holds for all $E < BX_C$. Apart from the 3.2 eV donor-acceptor transition being prominent at low temperatures, the modulations in the sub-band-gap luminescence band of this sample are therefore due to interference effects.

5.1.3 α -GaN Reference Film

A 10 μm thick α -GaN layer grown on sapphire by MOVPE serves as optical reference and will be compared to the two previous samples. 5 and 300 K photoluminescence data of the α -GaN reference sample are shown in *Fig. 5.03a* and, magified around the band edge spectral range, in the upper plots of *Fig. 5.03b*. The latter are complemented by reflectance spectra (lower plots).

At low temperatures narrow emission lines located around 3.5 eV preponderate the spectra. These transitions are of excitonic origin as evidenced by the distinct resonances in the reflectance which correlate with the emission peaks denoted as $FX_{A,B}$. The most intense peak labeled BX_H is assigned to a bound exciton whereas $FX_{A,B,C}$ are attributed to the free A-, B-, and C-excitons of the wurtzite-structure GaN [24, 26].

Rising the temperature above 120 K causes the BX_H peak to vanish and at room temperature, only the A-exciton prevails. In conjunction with a broadening of the emission peaks, the reflectance resonances get more and more washed out as T increases. At 300 K only a weak structure can be seen which, however, relates to the PL peak observed and indicates that, even at this elevated temperature, the luminescence is still excitonic in nature. This finding is in accordance with the large free exciton binding energy of $R_X = 27$ meV [84].

Evidently, the excitonic luminescence of the α -GaN reference is much more narrow in linewidth and considerably less superposed by defect-mediated recombination than the $X_{C,H}$ and BX_C transitions, especially at low temperatures. Consequently, a quantitative assess-

ment of the BX_H and FX_A transitions is straightforward. The peak positions as well as the linewidths are gained almost by inspection while the total excitonic intensity X_{All} is obtained by integrating the luminescence over the BX_H , $FX_{A,B,C}$ transitions.

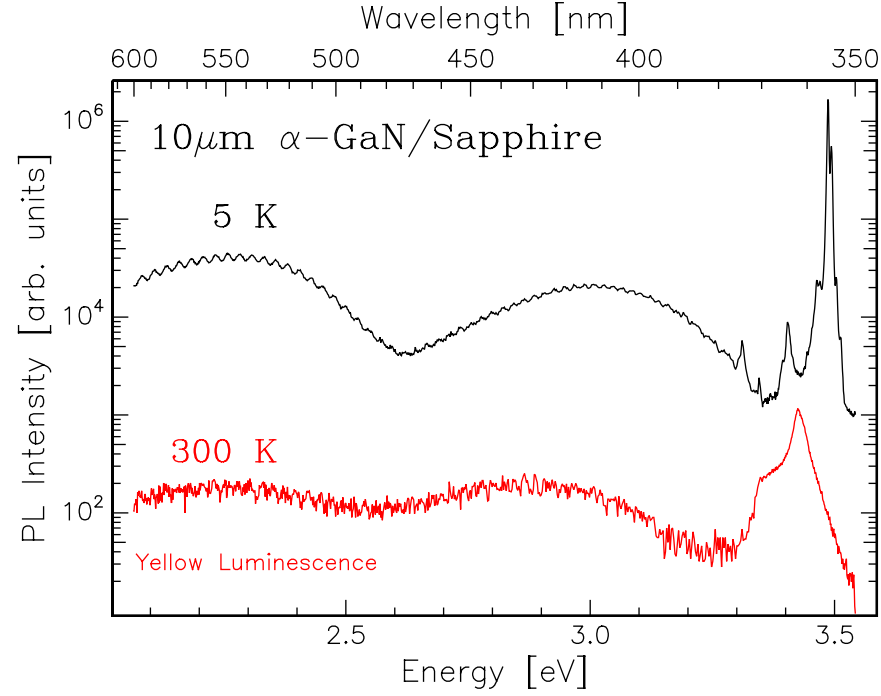


Fig. 5.03a: Photoluminescence of the α -GaN reference sample at 5 and 300 K.

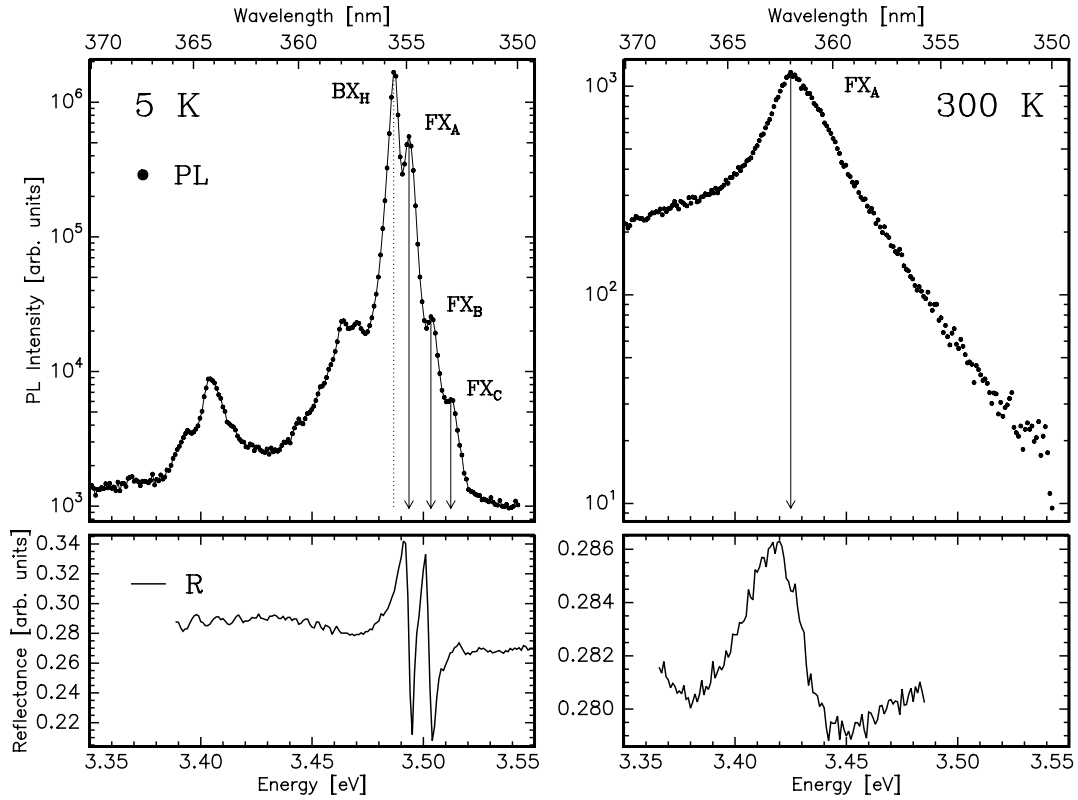


Fig. 5.03b: Band edge photoluminescence (symbols, upper plots) and reflectance (lines, lower plots) of the α -GaN reference sample at 5 and 300 K.

5.2 Lineshape analysis

The positions of the X_C , X_H , and BX_C transitions can be determined with reasonable accuracy directly from the raw data. In contrast, a quantitative interpretation of the luminescence spectra in terms of peak widths and areas requires a lineshape analysis in order to separate the different overlapping PL peaks. Being aware that the results obtained from such an analysis are only as reliable as reasonable and unambiguous the model actually is, an attempt was made to describe the experimental data by a minimum number of model parameters.

Plotting the data logarithmically, it is seen that peaks with energies E lower than X_C or BX_C have simple Gaussian profiles over the whole temperature range. Since we are primarily interested in the close-to-band-edge transitions, no explicit distinction between true PL peaks and interference-related maxima at lower energies will be made. The X_C and X_H peaks of sample #2058 are asymmetric with high-energy tails dropping single-exponentially. This asymmetry is most strongly pronounced at low temperatures and nearly disappears at 300 K where a Lorentzian shape is assumed. Such a behavior can be quantified by the function

$$X_\xi(E) = \frac{2}{1 + \exp\left(\frac{E-E_o}{\xi}\right)} \frac{I_o}{(E - E_o)^2 + (\Delta E)^2}, \quad (5.1)$$

giving good agreement with the X_H peak for all temperatures and with X_C for $T \geq 50$ K. The parameter ξ is monotonically increasing with temperature and of the order of $2KT$. It is straightforward to verify that the area underneath $X_\xi(E)$ is independent of the asymmetry parameter $1/\xi$:

$$\int_{-\infty}^{+\infty} X_\xi(E) dE = \sqrt{\pi} I_o \Delta E \quad \forall \xi \quad (5.2)$$

- *Fig. 5.04a* compares the experimental data of sample #2058 (symbols) with a least-squares fit involving only 4 Gaussians and $X_\xi(E)$ which will be referred to as **model (A)**. Apart from systematical deviations of the order of $\leq 8\%$ at the tails of the X_C transition, a reasonable agreement with the experimental data is obtained.

Model (A) is also applicable to sample #2070 by setting $\xi = \infty$ in $X_\xi(E)$: For $T > 50$ K, the BX_C transition exhibits a symmetric Lorentzian shape, while at lower T , the BX_C peak is too weak relative to the low-energy Gaussians for being clearly resolved. Nevertheless, also in this temperature range, a Lorentzian matches the observed data for $E < 3.3$ eV best, compared to other line shapes and, thus, gives at least an estimate for the width and intensity of the BX_C transition. The weak peak at $E \approx 3.42$ eV being present for $T < 150$ K only, is of unknown origin and is not included in the analysis.

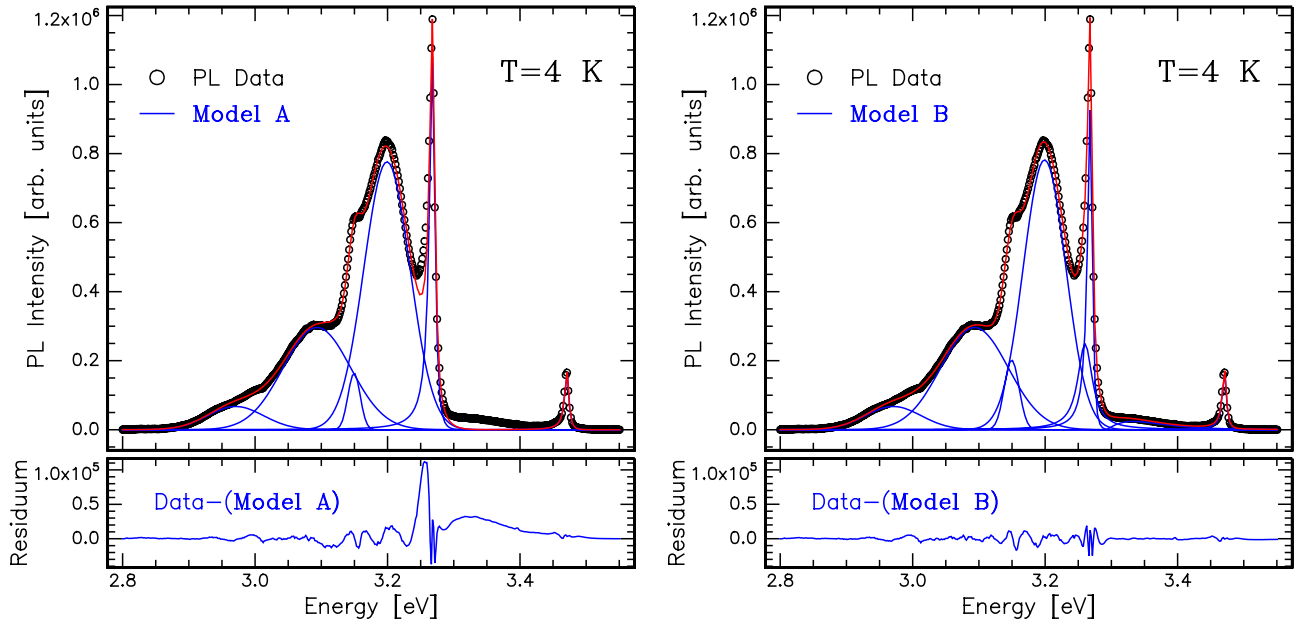
- The aforementioned discrepancies between model (A) and the low-energy tail of the X_C peak can be made to virtually vanish by adding a Lorentzian shape peak, referred to as Y_C . Significantly worse fits were obtained with Gaussians or asymmetric Lorentzians of the form $X_\xi(E)$, $\xi \in \mathbb{R}$. Indeed, time-resolved PL studies carried out by R. Klann indicated the presence of another transition at $X_C - 20 \text{ meV} \leq E < X_C$ at low temperatures which is difficult to spectrally resolve. For $T > 70$ K this peak cannot be detected anymore.

The only remaining feature to be modelled is the asymmetric, broad profile located between X_C and X_H , being denoted by BB . It has the characteristic shape of an excitonic

band-to-band transition [85] with exponential tail

$$BB(E) = \max \left\{ 1 - \exp \left(\frac{E - E_G}{KT} \right), 0 \right\} \frac{\exp \left(-\frac{E}{KT} \right)}{1 - \exp \left(-\sqrt{\frac{R_X}{E - E_G}} \right)}. \quad (5.3)$$

The band gap E_G estimated from this profile, assuming an exciton Rydberg of $R_X = 25$ meV, is close to the values obtained in chapter 3. However, it cannot be ruled out that this finding is by coincidence only and that the physical origin of the BB peak is actually defect-mediated recombination in the hexagonal phase. Furthermore, the BB peak cannot be resolved anymore at higher temperatures due to the strong broadening of the X_C and X_H transitions. **Model (B)** which comprises model (A) as well as the Y_C and BB profiles (*Fig. 5.04b*) may therefore be considered as a low-temperature extension to the 2-profile model (A), the latter yielding stable and good fits to both the #2058 and #2070 data for $T \geq 50$ K.



Figs. 5.04a,b: Lineshape analysis of the 4 K photoluminescence spectrum of sample #2058 with a simple 2-profile fit (A) (left plot) and a more sophisticated model (B) (right plot).

5.3 Transition energies and band gaps

Fig. 5.05 shows the temperature dependence of the FX_A , X_H , X_C , and BX_C transition energies compared to the band gap energies $E_G^{\text{Hex., Cub.}}$ of cubic and hexagonal [82, 94] GaN (broken lines) where the curve for the Γ -gap of β -GaN was adopted from chapter 3. The solid lines are least-squares fits of

$$E_X(T) = E_X(0) - S_\Omega E_\Omega \left\{ \coth \left(\frac{E_\Omega}{2KT} \right) - 1 \right\} \quad (5.4)$$

to the respective transitions, where E_Ω stands for an average phonon energy and S_Ω is a coupling constant as in equation (4.34). The parameters obtained are compiled in *Tab. 5.1*.

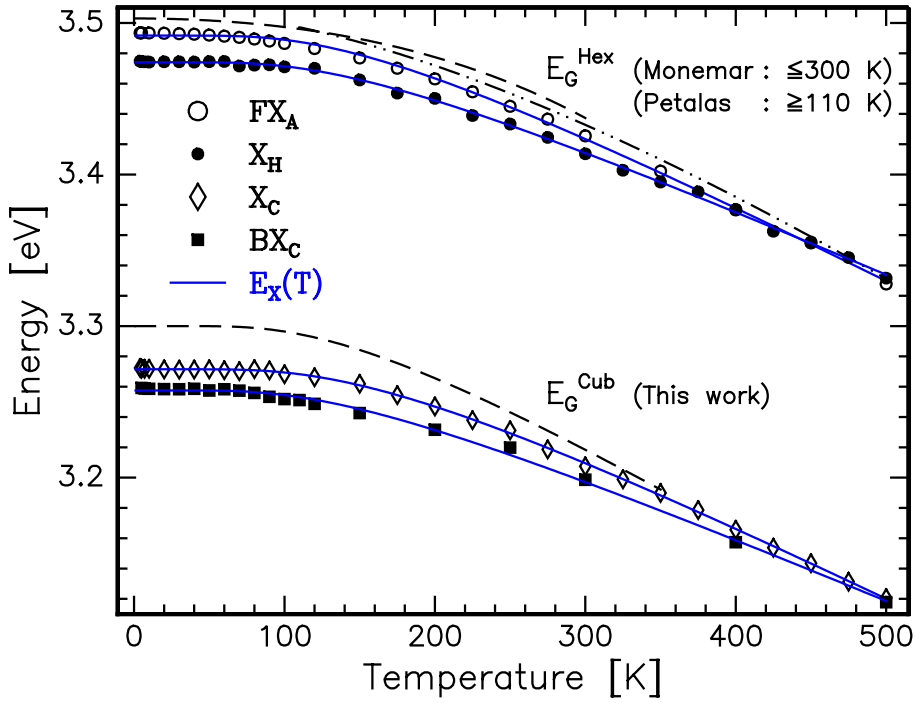


Fig. 5.05: Energies of the FX_A , X_H , X_C , and BX_C transitions (symbols) compared to the band gaps of α - and β -GaN (dashed lines) as function of temperature. The solid lines are fits to (5.4).

At $T \leq 50$ K, X_C and X_H are rigidly shifted by $\Delta E_X \approx -30$ meV compared to the band gaps $E_G^{\text{Cub.}}$ and $E_G^{\text{Hex.}}$ whereas the shift of BX_C amounts to $\Delta E_{BX} \approx -40$ meV. At higher temperatures, the fundamental inter-band energies are being approached by the mentioned PL peaks. The X_C , X_H , and BX_C transitions are therefore assigned to band edge related recombination. Comparing the exciton Rydberg $R_X = 27$ meV and ΔE_X , one may be tempted to interpret the $X_{C,H}$ transitions as being due to exciton annihilation in, respectively, the cubic and hexagonal phase. However, neither the absorption nor the reflectance data acquired on the samples #2058, #2070, and the β -GaN reference film #8092 (chapter 3) exhibit features characteristic to discrete exciton levels as those observed with the α -GaN reference.

Transition	$E_X(0)$ [eV]	E_Ω [meV]	S_Ω [1]
FX_A	$3.497 \pm 5 \times 10^{-4}$	38 ± 1	3.05 ± 0.08
X_H	$3.474 \pm 4 \times 10^{-4}$	37 ± 1	2.57 ± 0.04
X_C	$3.272 \pm 3 \times 10^{-4}$	41 ± 1	2.93 ± 0.01
BX_C	$3.258 \pm 6 \times 10^{-4}$	35 ± 2	2.51 ± 0.09

Table 5.1: Model parameters for the temperature dependent band edge transition energies of α - and β -GaN.

5.4 Linewidths

In what follows, the temperature dependence of the widths of the FX_A , BX_H , X_H , X_C , and BX_C transitions will be investigated. A commonly employed expression to describe the thermal broadening of the fundamental band gap of a semiconductor is

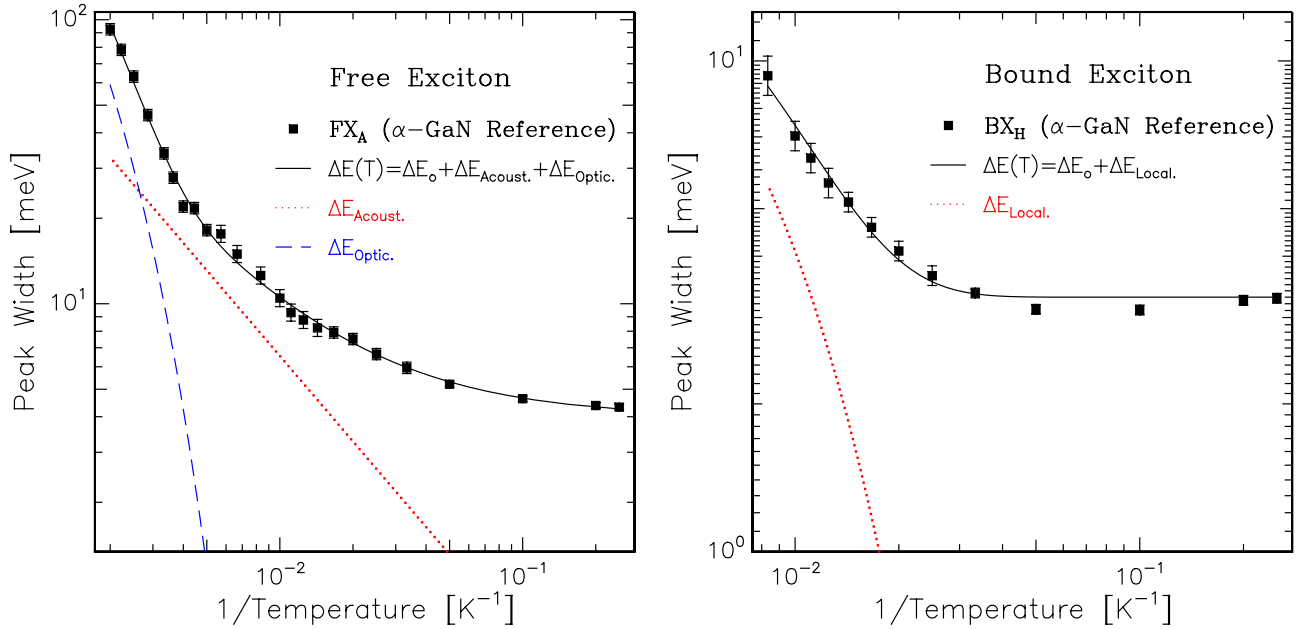
$$\Delta E(T) = \Delta E_0 + \Delta E_{\text{Acoust.}}(T) + \Delta E_{\text{Optic.}}(T) \quad (5.5)$$

$$\Delta E_{\text{Acoust.}} = S_A K T \quad (5.6)$$

$$\Delta E_{\text{Optic.}} = \frac{S_O}{e^{E_O/KT} - 1}. \quad (5.7)$$

The first term, ΔE_0 , denotes the temperature independent inhomogenous broadening which may originate from electron–electron interaction, Auger recombination, and various kinds of scattering processes (surface, dislocation, impurity, alloy) which essentially account for crystal imperfections.

Temperature dependent homogenous broadening is caused by electron(exciton)–phonon interactions. Electron – acoustical phonon scattering is usually modelled by the linear term $\Delta E_{\text{Acoust.}}$ and electron – longitudinal optical (LO) phonon scattering gives rise to the bosonic expression $\Delta E_{\text{Optic.}}$ where E_O stands for an average LO phonon energy. $S_{A,O}$ are the respective phonon coupling constants. Typically, $\Delta E_{\text{Acoust.}}$ is dominant for $T \leq 70$ K while $\Delta E_{\text{Optic.}}$ is taking over at higher temperatures.



Figs. 5.06a,b: Free and bound exciton linewidth versus temperature of the α -GaN reference sample.

Fig. 5.06a shows a fit of the above expression $\Delta E(T)$ to the free exciton FX_A linewidth of the α -GaN reference sample. Good agreement is obtained with the parameters broken down in Tab. 5.2. In particular, the low-temperature linewidth is linearly increasing in consistency with $\Delta E_{\text{Acoust.}}$

The bound exciton BX_H on the other hand, exhibits a virtually constant broadening for $T \leq 30$ K which cannot be accounted for by the acoustical phonon scattering term. Instead, the thermal increase in peak width is exponentially activated according to

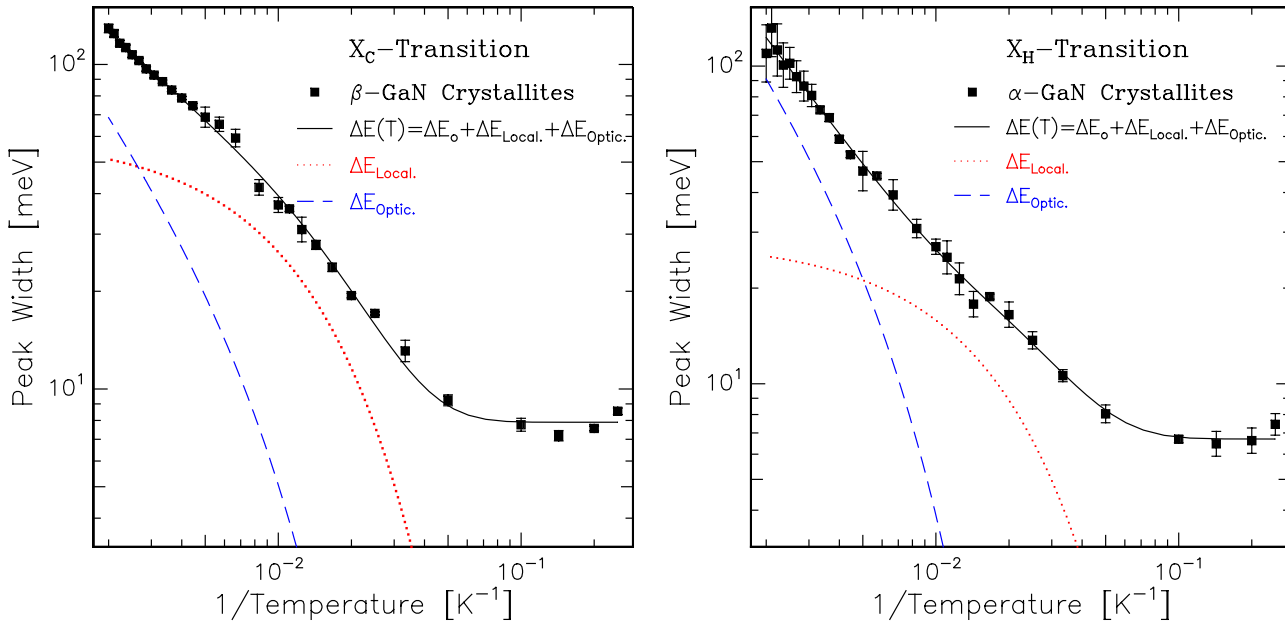
$$\Delta E_{\text{Local.}}(T) = S_L e^{-E_A/KT}. \quad (5.8)$$

For $4 \leq T \leq 120$ K, the experimental data can be described by the model function $\Delta E_0 + \Delta E_{\text{Local.}}(T)$ as viewed in *Fig. 5.06b*. At even higher temperatures the bound exciton cannot be detected anymore.

Transition	ΔE_0 [meV]	E_A [meV]	E_O [meV]	S_A [1]	S_L [meV]	S_O [meV]
FX_A	4.0 ± 0.2	—	110 ± 9	0.76 ± 0.04	—	700 ± 150
BX_H	3.3 ± 0.1	16 ± 1	—	—	27 ± 4	—
X_H	6.7 ± 0.6	5.0 ± 1.5	26 ± 11	—	28 ± 1	76 ± 2
X_C	8.1 ± 0.4	8 ± 1	35 ± 19	—	79 ± 14	70 ± 40
BX_C	46 ± 1	2.0 ± 0.3	63 ± 6	—	39 ± 2	290 ± 50

Table 5.2: Model parameters for the temperature dependent band edge transition widths of α - and β -GaN.

The same low-temperature behavior is found for the X_H and X_C transitions (*Figs. 5.07a,b*) of the crystallite sample #2058 as well as for the BX_C peak (*Fig. 5.08*) of the β -GaN film #2070. Attempting to use $\Delta E_{\text{Acoust.}}(T) = S_A KT$ instead of $\Delta E_{\text{Local.}}$ results in a negative optical phonon coupling constant. This evidence does not support the assignment of $X_{C,H}$ to free exciton recombination [57]. On the contrary, it rather suggests that these peaks stem from transitions between localized states having their origin in band fluctuations as a result of local strain fields.



Figs. 5.07a,b : X_C and X_H linewidth versus temperature of the crystallite sample #2058.

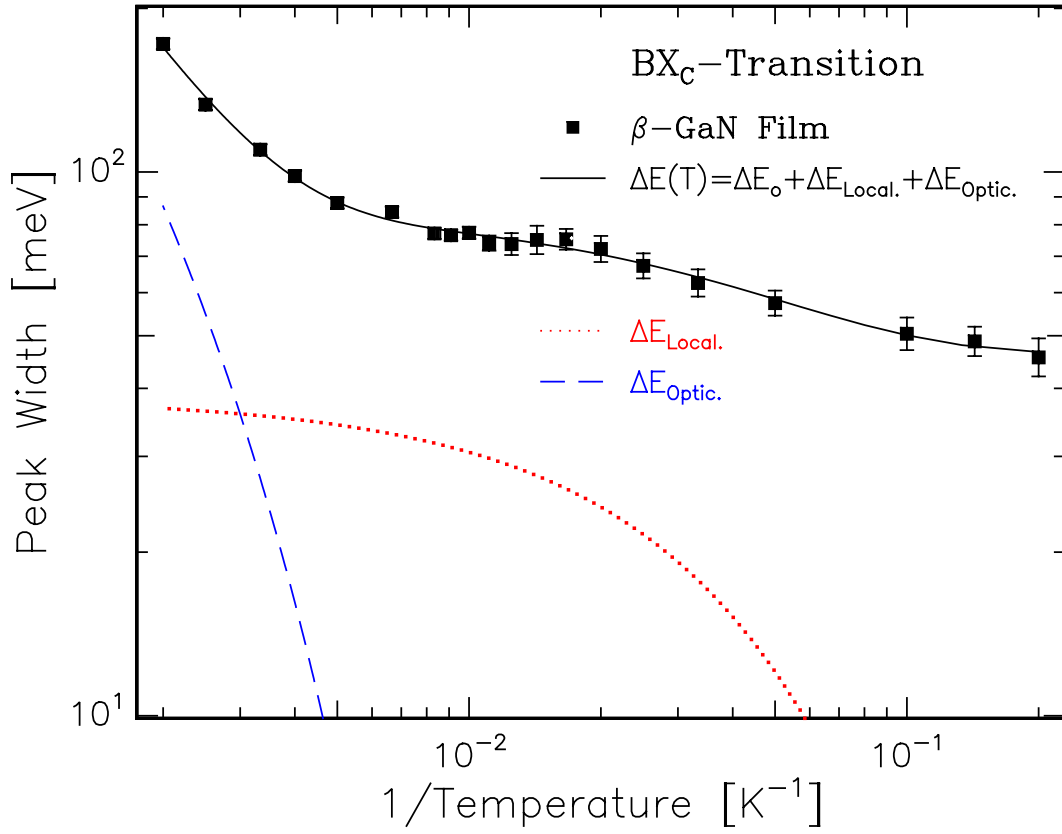


Fig. 5.08 : BX_C linewidth versus temperature of the β -GaN film #2070.

5.5 Thermal quenching

In *Fig. 5.09*, the temperature dependent intensities I_X of the X_C and BX_C transitions are compared to the total exciton luminescence of the α -GaN reference sample, $X_{All} = BX_H + FX_A + FX_B + FX_C$. The data were taken under small-signal excitation conditions ($P_{ex} \approx 30 \text{ W/cm}^2$) and are normalized to unity at 4 K. The fact that the observed intensities are getting heavily quenched is a clear indication for the presence of thermally activated nonradiative recombination. The strongest drop in intensity by more than an order of magnitude, especially for BX_C , is taking place between 5 and 100 K. Remarkably, $I(X_C)$ and $I(BX_C)$ remain nearly constant for $100 < T < 300 \text{ K}$. Above room temperature, though, another nonradiative process sets in. $I(X_{All})$, in contrast, does not exhibit such a plateau-like behavior at intermediate temperatures but continues to decrease at an exponential rate.

Temperature dependent intensities can frequently be characterized by n exponentially activated processes with activation energies E_i [86] such that

$$I_X(T) = \frac{1}{1 + \sum_{i=1}^n a_i \exp\left(-\frac{E_i}{KT}\right)}. \quad (5.9)$$

For $T \leq 300 \text{ K}$, two processes have to be postulated to give an account of the experimental data X_C and BX_C , while in the case of X_{All} , $n = 3$ is necessary in this temperature range. The high-temperature luminescence ($T > 300 \text{ K}$) can only be described well if an additional third and fourth process are considered for the cubic and hexagonal GaN, respectively. The solid

lines in *Fig. 5.09* indicate least-squares fits of I_X to the data, giving the activation energies E_i quoted in *Tab. 5.3*.

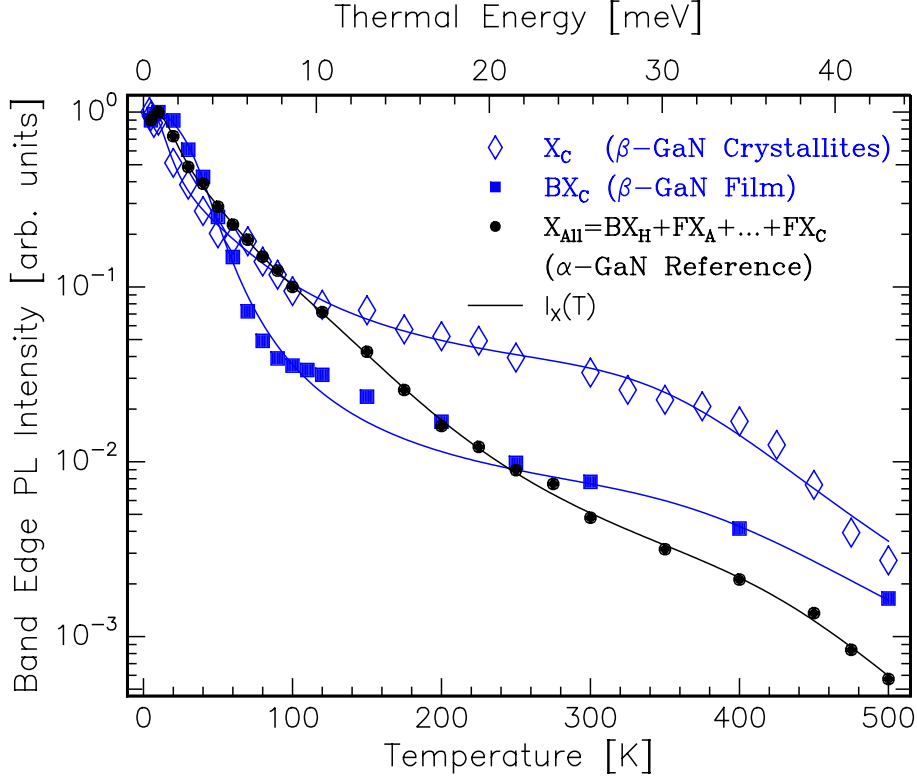
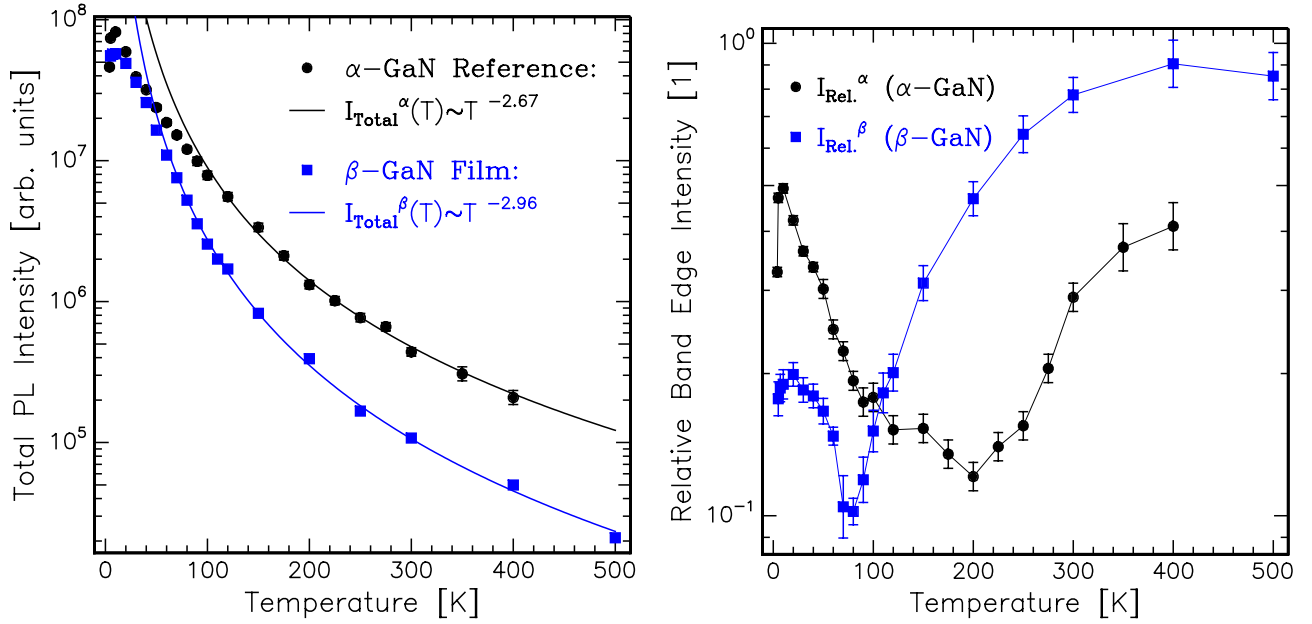


Fig. 5.09: Normalized intensity of the excitonic α -GaN luminescence X_{All} and of the X_C , BX_C transitions (symbols) against T acquired at small signal excitation ($P_{\text{ex}} \approx 30 \text{ W/cm}^2$) conditions. The solid lines are fits of expression (5.9).

Transition	T [K]	E_1 [meV]	E_2 [meV]	E_3 [meV]	E_4 [meV]
X_C	5–300	2.9 ± 0.3	20 ± 4	—	—
BX_C		6 ± 2	21 ± 3	—	—
X_{All}		5.1 ± 0.2	27 ± 3	100 ± 10	—
X_C	5–500	3.5 ± 0.3	21 ± 2.5	320 ± 45	—
BX_C		6 ± 2	21 ± 2.5	300 ± 50	—
X_{All}		5.0 ± 0.7	24 ± 3	80 ± 8	480 ± 20

Table 5.3: Activation energies for the thermal quenching of the band edge luminescence of β - and α -GaN as determined from (5.9) for the data shown in *Fig. 5.09*.

The aforementioned similarity in the temperature dependence of $I(X_C)$ and $I(BX_C)$ is also reflected in the activation energies which are basically identical within the quoted errors. In contrast, X_{All} behaves differently in that an additional process with $E_3 \approx 90 \text{ meV}$ determines the decay at intermediate temperatures. However, $E_{1,2}$ are of comparable magnitude for both cubic and hexagonal GaN. The values of E_1 are compatible with potential fluctuations that typically result from structural defects or compositional inhomogeneities. E_2 , on the other hand, is close to the free exciton binding energy R_X .



Figs. 5.10a,b: Total PL intensities $I_{\text{Total}}^{\alpha,\beta}$ of the β -GaN film #2070 and the α -GaN reference sample versus temperature T (left). The lines show least-squares fits of the power law aT^{-b} to the data (symbols). The fractions of the band edge luminescence intensities $I_{\text{Rel.}}^{\beta} = I(BX_C)/I_{\text{Total}}^{\beta}$ and $I_{\text{Rel.}}^{\alpha} = I(X_{\text{All}})/I_{\text{Total}}^{\alpha}$ are displayed in the right figure. The thin solid lines are a linear interpolation as guide to the eye.

Having focused so far on the temperature dependence of the band edge luminescence, we now investigate the total PL intensity I_{Total} , obtained by integrating the radiative spectrum between $350 \leq \lambda \leq 600$ nm. Fig. 5.10a shows $I_{\text{Total}}^{\alpha,\beta}(T)$ of the α -GaN reference sample and the β -GaN film #2070, respectively.¹ It is seen that the data points follow the simple power laws

$$\begin{aligned} I_{\text{Total}}^{\alpha} &\sim T^{-2.67} \quad \text{for } T \geq 100 \text{ K} \quad \text{and} \\ I_{\text{Total}}^{\beta} &\sim T^{-2.96} \quad \text{" } T \geq 60 \text{ K}. \end{aligned} \quad (5.10)$$

It may be worth recalling that if the situation of nonequilibrium carrier concentrations $n = n_o + \Delta n$, $p = p_o + \Delta p$ brought about by photoexcitation can be adequately described by thermal equilibrium Fermi-Dirac distribution functions with appropriately shifted quasi-Fermi levels, then the spontaneous emission rate of an ideal cubic crystal with parabolic bands is to first order given by [87]

$$R_{\text{Spont.}}(E) \sim np(KT)^{-3} \sqrt{E - E_G} e^{-(E - E_G)/KT} \quad \text{for } E = \hbar\omega \geq E_G \quad (5.11)$$

and consequently,

$$I_{\text{Total}}^{\text{Ideal}} = \int_{E_G}^{\infty} R_{\text{Spont.}}(E) dE \sim T^{-2}. \quad (5.12)$$

The deviations observed from this intrinsic thermal quenching are due to nonradiative centers and will be investigated in more detail in the next chapter.

Finally, we consider the relative contribution $I_{\text{Rel.}}$ of the band edge recombination to I_{Total} in order to assess the losses caused by low-energy luminescence from radiative centers. The temperature dependence of the ratios $I_{\text{Rel.}}^{\alpha} = I(X_{\text{All}})/I_{\text{Total}}^{\alpha}$ and $I_{\text{Rel.}}^{\beta} = I(BX_C)/I_{\text{Total}}^{\beta}$ are

¹The crystallite sample #2058 will not be considered in this context since it is not possible to separate the contributions from the cubic and the hexagonal crystals to the measured low-energy luminescence intensity

displayed in *Fig. 5.10b*. It is seen that the fractional band edge intensities of both samples behave qualitatively similar. In essence, three thermal regimes can be identified:

- (i) At very low temperatures, I_{Total} as well as $I_{\text{Rel.}}$ are rising with increasing temperature. It appears as if part of the carriers are frozen out for thermal energies $E_{\text{Therm.}} < 1$ meV. This may be due to shallow localized states stemming from potential fluctuations.
- (ii) For $2 \leq E_{\text{Therm.}} \leq 8$ meV, $I_{\text{Rel.}}$ is steeply decreasing by thermal activation of radiative centers such as donor-acceptor pairs and at intermediate temperatures, $I_{\text{Rel.}}$ assumes a minimum.
- (iii) Rising the temperature further leads to a recovery in the contribution of the band edge PL to the total radiative recombination since the centers which account for low-energy luminescence are getting ionized.

Surprisingly, the thermal quenching of deep-level luminescence occurs more efficiently for the β -GaN sample than in the case of the α -GaN reference. For the latter, $I_{\text{Rel.}}^{\alpha}$ is roughly constant in between 100 and 200 K while $I(BX_C)$ is already taking over in this temperature range. Consequently, the fraction of excitonic luminescence in the α -GaN is only about 30% of the total PL at room temperature whereas for the β -GaN, the band edge contribution amounts to 80%. Thus, even though the low temperature luminescence of the α -GaN is by far superior, the (above) room temperature band edge intensities are quite comparable for both polytypes.

5.6 Excitons in β -GaN ?

Even at room temperature, the band edge luminescence of high-quality α -GaN is clearly excitonic in nature as a consequence of the large exciton rydberg of about 27 meV. In contrast, no direct evidence of free excitons has been published so far for the zincblende modification even though $R_X(\beta\text{-GaN})$ is supposed to be of the same order.

In consideration of the photoluminescence data shown, the most promising candidate for unveiling excitonic features in β -GaN seems to be the crystallite sample #2058. However, the multioriented facets of the cubic and hexagonal microcrystals sitting on top of a rough film prohibit the acquisition of conclusive reflectance data whereas no clear resolution of the fundamental absorption edge is possible due to the appreciable film thickness of $\approx 1.5 \mu\text{m}$. An interesting technique for investigating the band edge properties of thick films is two-photon absorption, which has proved to be sensitive enough to detect $n = 2$ excitons in α -GaN. [88] This method was therefore applied to sample #2058, but the spectra obtained do not show any hint of excitonic resonances. [89] One may speculate whether the volume of the microcrystals is too small to give rise to a measurable signal above the noise level.

A prerequisite for the occurrence of discrete exciton levels are, however, sufficiently low background carrier concentrations n_0 and p_0 such that the effective electron-hole Coulomb interaction is strong enough to give rise to a bound state. In the case of strong dielectric screening, no clear distinction can be made anymore between weakly bound e-h pairs and free carriers. Further, large impurity concentrations as well as structural defects smear out the intrinsic bands such that the resulting increase in linewidths makes a resolution of spurious excitonic features very difficult, if not impossible.

No sound electrical data are available on the crystals of the DC plasma grown sample #2058. Hall measurements on the film revealed $n_0 \approx 10^{18} \text{cm}^{-3}$. A comparison between the defect luminescence obtained from the crystals and the film by selected-area-excitation CL measurements indicates that the crystals are cleaner by at least an order of magnitude. [57] Firm values for their impurity concentrations cannot be given, though. In comparison, the

0.9 μm thick film #2070 exhibits a background electron level of $n_o = 2 \times 10^{18} \text{cm}^{-3}$ being too high to give rise to distinct excitonic resonances. The RF plasma grown β -GaN reference sample #8092 has a Hall concentration of $n_o \approx 2 \times 10^{16} \text{cm}^{-3}$, but mobility measurements reveal that this value is in part due to compensation. Indeed, a SIMS analysis disclosed carbon concentrations of the order of 10^{17}cm^{-3} which could be traced back to the inferior-quality steel out of which the prototype RF plasma source has been manufactured. Thus, none of the β -GaN samples presented inhere really complies with the condition that n_o and p_o be at most in the mid 10^{17}cm^{-3} range being necessary for the observation of discrete exciton states.

Except for the α -GaN reference sample where the excitonic linewidth is linearly increasing with temperature for $T \leq 70 \text{ K}$, the peak width of the β -GaN close-to-band-edge luminescence is essentially constant at low temperatures. This behavior is indicative of the presence of localized states caused by spatial band fluctuations. For thermal energies low enough that the carriers are confined to potential minima, the interaction with acoustical phonons is suppressed. Once the carriers are free to move within the crystal, phonon scattering becomes effective in increasing the homogeneous linewidth. In conclusion, the band edge related β -GaN luminescence which can be observed up to temperatures as high as 500 K is attributed to transitions between localized states in or close to the intrinsic bands. At low temperatures, localized excitons may prevail which are either trapped to potential minima or bound to impurities such as shallow donors.

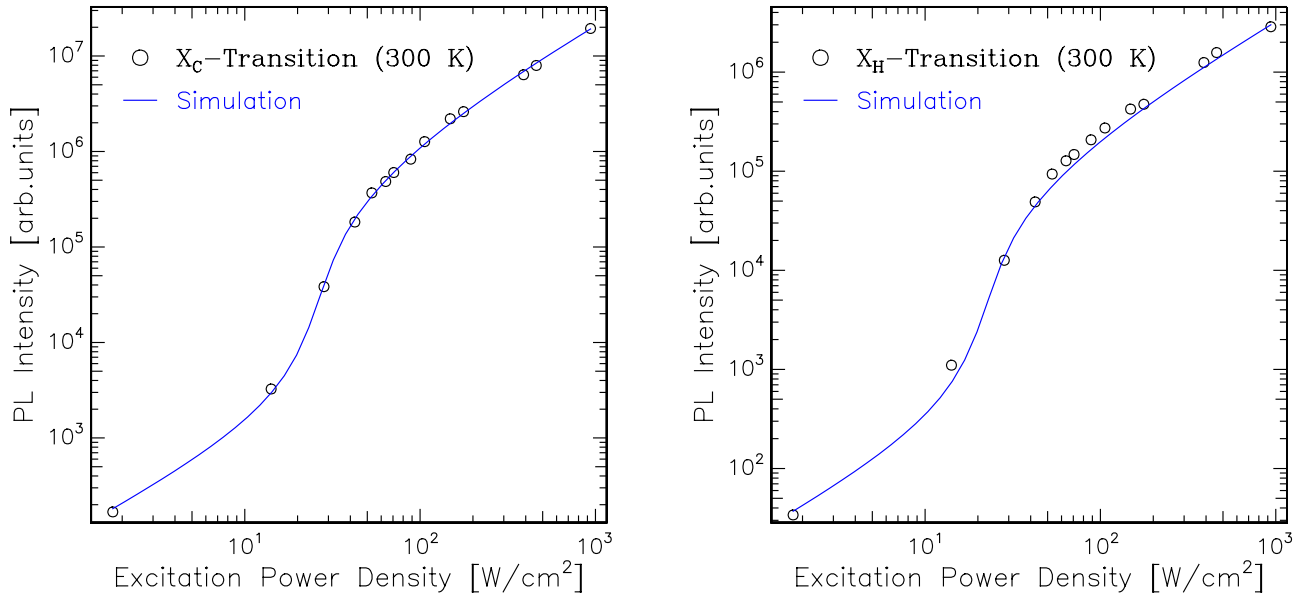
At room temperature and above, not only the integrated, but even the peak intensity of the band edge related radiative recombination taking place in β -GaN is competitive to that of state-of-the-art α -GaN exciton luminescence. The fact, however, that the intensity drops by more than two orders of magnitude for both polytypes when increasing T from 4 to 300 K clearly shows that nonradiative recombination plays an important role in GaN.

Chapter 6

(Non)radiative Recombination

6.1 Band Edge Photoluminescence Intensity versus Carrier Injection Rate

So far all PL measurements presented were conducted at low excitation power densities of $P_{\text{ex}} \approx 30 \text{ W/cm}^2$ where P_{ex} was kept constant within each temperature series. The observed strong thermal quenching of the photoluminescence intensity I_{PL} is indicative of the presence of nonradiative recombination processes. To obtain order-of-magnitude estimates of (non)radiative lifetimes and an idea of internal quantum efficiencies, P_{ex} -dependent measurements were carried out at room temperature as shown in *Figs. 6.01a,b* for the X_{C} and X_{H} transitions. The impinging laser power was varied by means of continuously adjustable neutral density filters in the range of $5 \times 10^{-3} - 30 \text{ mW}$ and measured directly in front of the sample with a calibrated powermeter supplied by the laser manufacturer. The excitation spot diameter was kept at a value of $d \approx 30 \mu\text{m}$.

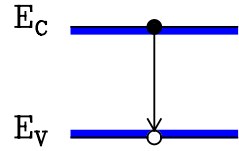


Figs. 6.01a,b: Intensity of the X_{C} - and X_{H} -transition (circles) against applied excitation power density with modelled radiative (solid line) recombination intensities. The errors in the intensities are typically of order of the symbol sizes except for the lowest power density points where the error amounts to about 20%.

An attempt to account for the pronounced nonlinearity of $I_{\text{PL}}(P_{\text{ex}})$ with a recombination model ¹ that relies on symmetric electron and hole capture [90] failed. Not even qualitative agreement between the measured and the simulated intensities could be reached. In the following sections a simple extension of the latter rate equation model is discussed, which explicitly distinguishes between nonradiative minority and majority carrier recombination at a Shockley-Read-Hall (SRH) center. The leverage of an asymmetry in the corresponding recombination rates is investigated under the aspect of defect saturation and the extended model is applied to the present data yielding the solid curves plotted in *Figs. 6.01a,b*.

6.2 Basic Rate Equation Model

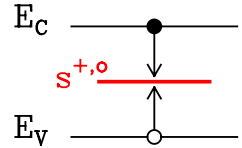
We consider a semiconductor with thermal equilibrium electron and hole concentrations n_o and p_o and assume that the associated donor and acceptor levels are shallow enough to practically merge with the conduction and valence band, respectively. An optical excitation at a carrier injection rate $G[\text{cm}^{-3}\text{s}^{-1}]$ will establish the nonequilibrium concentrations $n = n_o + \Delta n$, $p = p_o + \Delta p$ and result in radiative (close-to) band edge recombination



$$e + h \xrightarrow{b_R} \hbar\omega, \quad (6.1)$$

where the radiative recombination coefficient $b_R [\text{cm}^3\text{s}^{-1}]$ covers the intrinsic band-to-band as well as the shallow impurity-to-band and, possibly, shallow donor-to-acceptor transitions. Defect-mediated radiative recombination between deep levels is neglected.

Furthermore, it is presumed that the cumulative effect of the nonradiative recombination channels is equivalent to the presence of *one kind of Shockley-Read-Hall centers* [91, 92] with total density $S[\text{cm}^{-3}] = S^+ + S^o$ where S^+ and S^o denote the sites being filled with holes and electrons, respectively. The according carrier capture processes induced by such a center s ,



$$\begin{aligned} e + s^+ &\xrightarrow{b_e} s^o \\ h + s^o &\xrightarrow{b_h} s^+, \end{aligned} \quad (6.2)$$

are characterized by the nonradiative recombination coefficients b_e and b_h . Provided that Auger recombination and photon recycling can be omitted, the spatially uniform, bilinear carrier dynamics is described by the rate equations

$$\begin{aligned} \frac{\partial n}{\partial t} &= G - b_R(np - n_o p_o) - b_e n S^+ \\ \frac{\partial p}{\partial t} &= G - b_R(np - n_o p_o) - b_h p S^o \\ \frac{\partial S^+}{\partial t} &= b_h p S^o - b_e n S^+, \quad S = \text{const.} \end{aligned}$$

$$(6.3)$$

The recombination coefficients are assumed to be constants for the moderate excitation densities considered. Since no account is given of spatial nonuniformities, the above concentrations are

¹This model has been successfully applied to the (In,Ga)As system.

to be interpreted as effective ones and the parameters extracted from the present model are to be considered as first-order estimates.

The incorporation of diffusion processes into the simple model (6.3) is particularly desirable when considering the *transient solutions* $\frac{\partial n}{\partial t}, \frac{\partial p}{\partial t}, \frac{\partial S^+}{\partial t} \neq 0$. The latter are studied in [93]. However, an adequate treatment of spatially nonuniform carrier concentrations is not at all straightforward since it requires the knowledge of the electron and hole diffusion constants D_e, D_h and the surface recombination velocities. Apart from D_e , which can be estimated from the mobility μ_e using the Einstein relation $D_e = \mu_e KT/e$, these material parameters are essentially unknown and would have to be extracted from the present optical data in conjunction with the (non)radiative recombination coefficients. As a consequence, the large number of free parameters may cause considerable ambiguity in the interpretation of the experimental data and therefore mask the benefits of such a more complete model.

We are seeking the *equilibrium solutions* $\frac{\partial n}{\partial t} = \frac{\partial p}{\partial t} = \frac{\partial S^+}{\partial t} = 0$ for $t \rightarrow \infty$ under the assumption that the *equilibrium within the nonradiative centers is reached quasi-instantaneously*, i.e.

$$\frac{\partial S^+}{\partial t}(t) \equiv 0 \iff \Delta n(t) \equiv \Delta p(t), \quad (6.4)$$

based on common experience that nonradiative processes are occurring on a much shorter timescale than radiative ones. The stationary equations to be solved are then

$$G = b_R(np - n_o p_o) + b_e n S^+ \quad (6.5)$$

$$0 = b_e n S^+ + b_h p(S^+ - S). \quad (6.6)$$

For *n-type material* with $p_o \ll n_o$ and $p_o \ll \Delta p$,

$$S^+ = S \frac{b_h \Delta n}{b_e(n_o + \Delta n) + b_h \Delta n} \quad (6.7)$$

and thus

$$G = \underbrace{b_R \Delta n(n_o + \Delta n)}_{I_R} + \underbrace{S \Delta n \frac{b_e b_h (n_o + \Delta n)}{b_e(n_o + \Delta n) + b_h \Delta n}}_{I_{NR}}. \quad (6.8)$$

Since in the small-signal limit $\Delta n \ll n_o$ the above equation tends to

$G = \Delta n[b_R n_o + b_h S] =: \Delta n/\tau_0$, we define the *Asymptotic (Non-)Radiative Lifetimes*

$$\tau_R := \frac{1}{b_R n_o}, \quad \tau_{NR} := \frac{1}{b_h S} \quad \text{and} \quad A := \frac{b_h}{b_e} \quad (6.9)$$

and finally obtain

$$G = \Delta n \frac{\Delta n + n_o}{n_o} \underbrace{\left[\frac{1}{\tau_R} + \frac{1}{\tau_{NR}} \frac{n_o}{n_o + (A+1)\Delta n} \right]}_{=: \tau^{-1}}. \quad (6.10)$$

It is seen from the polynomial coefficients of this third order equation that for $G, n_o, \tau_R, \tau_{NR}, A \in \mathbb{R}^+$, one branch $\Delta n(G) \in \mathbb{R}^+$ and two complex conjugate branches of solutions exist. The physically relevant solution is thus unique. Furthermore, there exists a kind of turning point of Δn at

$$G^* = \frac{n_o}{\tau_{NR}(A+1)}. \quad (6.11)$$

The *Total Lifetime* τ is a nonlinear function of the excess carrier concentration Δn as opposed to τ_{NR} and τ_{R} , which are – by definition – material constants. The asymptotic behavior of τ in the small- and large-signal limit, respectively, is

$$\tau^{-1}(\Delta n_{\text{eff.}}) \rightarrow \begin{cases} \tau_0^{-1} = \tau_{\text{R}}^{-1} + \tau_{\text{NR}}^{-1} & \text{for } \Delta n_{\text{eff.}}/n_o \rightarrow 0 \\ \tau_{\text{R}}^{-1} & \text{" } n_o/\Delta n_{\text{eff.}} \rightarrow 0 \end{cases} \quad (6.12)$$

in terms of the *Effective Excess Carrier Density*

$$\boxed{\Delta n_{\text{eff.}} := (A + 1)\Delta n.} \quad (6.13)$$

On the other side, the *Effective Nonradiative Lifetime* $\tilde{\tau}_{\text{NR}}$ with $\tau^{-1} = \tau_{\text{R}}^{-1} + \tilde{\tau}_{\text{NR}}^{-1} \forall \Delta n$ is given by

$$\boxed{\tilde{\tau}_{\text{NR}}(\Delta n_{\text{eff.}}) = \tau_{\text{NR}} \left(1 + \frac{\Delta n_{\text{eff.}}}{n_o} \right).} \quad (6.14)$$

Evidently, an asymmetry between electron and hole capture $A > 1$ brings τ closer to its radiative limit τ_{R} whereas $\tilde{\tau}_{\text{NR}}$ tends to infinity for $n_o/\Delta n_{\text{eff.}} \rightarrow 0$.

The *(Non-)Radiative Recombination Rates* yield

$$\boxed{\begin{aligned} I_{\text{R}} &= \frac{\Delta n}{\tau_{\text{R}}} \frac{n_o + \Delta n}{n_o} \\ I_{\text{NR}} &= \frac{\Delta n}{\tau_{\text{NR}}} \frac{n_o + \Delta n}{n_o + \Delta n(A + 1)} \end{aligned}} \rightarrow \begin{cases} \frac{\Delta n}{\tau_{\text{R}}} & \text{for } \Delta n/n_o \rightarrow 0 \\ \frac{(\Delta n)^2}{\tau_{\text{R}} n_o} & \text{" } n_o/\Delta n \rightarrow 0, \end{cases} \quad (6.15)$$

$$\rightarrow \begin{cases} \frac{\Delta n}{\tau_{\text{NR}}} & \text{for } (A + 1)\Delta n/n_o \rightarrow 0 \\ \frac{\Delta n}{\tau_{\text{NR}}(A + 1)} & \text{" } n_o/\Delta n \rightarrow 0, \end{cases}$$

and the ratio of radiative to nonradiative recombination can be stated as

$$\frac{I_{\text{R}}}{I_{\text{NR}}} = \frac{\tau_{\text{NR}}}{\tau_{\text{R}}} \frac{n_o + \Delta n_{\text{eff.}}}{n_o} \rightarrow \begin{cases} \frac{\tau_{\text{NR}}}{\tau_{\text{R}}} = \frac{b_{\text{R}}}{b_{\text{h}}} \frac{n_o}{S} & \text{for } \Delta n_{\text{eff.}}/n_o \rightarrow 0 \\ \frac{\Delta n_{\text{eff.}}}{n_o} \frac{\tau_{\text{NR}}}{\tau_{\text{R}}} & \text{" } n_o/\Delta n_{\text{eff.}} \rightarrow 0. \end{cases} \quad (6.16)$$

Within the large-signal regime $\Delta n_{\text{eff.}} \gg n_o$, the ratio $I_{\text{R}}/I_{\text{NR}}$ is thus linearly rising with $\Delta n_{\text{eff.}}$. A preferential minority carrier capture $A = b_{\text{h}}/b_{\text{e}} > 1$ therefore effectively increases the excess carrier density $\Delta n = \Delta p$ as well as $\tilde{\tau}_{\text{NR}}$ and, in essence, favors radiative recombination.

6.3 Analysis of Photoluminescence Data

To access the material parameters $[\tau_{\text{R}}, \tau_{\text{NR}}, A]$ – given a certain n_o – within the framework of the above model, a solution Δn to equation (6.10) has to be found such that the calculated $I_{\text{R}}(\Delta n, \tau_{\text{R}})$ (6.15) matches the measured radiative recombination rate. Equivalently, the *Internal Quantum Efficiency*

$$\boxed{\eta := \frac{I_{\text{R}}}{G} = \left\{ 1 + \tau_{\text{rel}} \frac{n_o}{n_o + \Delta n_{\text{eff.}}} \right\}^{-1} \quad \text{with} \quad \tau_{\text{rel}} := \frac{\tau_{\text{R}}}{\tau_{\text{NR}}}} \quad (6.17)$$

may be used to link the theory with the experiment. In practice, however, G and I_R cannot be absolutely determined but only up to multiplicative factors. Typically, the band edge luminescence intensity $I_{PL} \sim I_R$ is being measured as a function of excitation power density $P_{Ex}[\text{W}/\text{cm}^2] \sim G$. Let I_{PL} be normalized such that

$$1 = \max_{P_{Ex}} \{I_{PL}(P_{Ex})/P_{Ex}\}, \quad \text{then} \quad (6.18)$$

$$\eta(P_{Ex}) = \eta_{\max} \frac{I_{PL}(P_{Ex})}{P_{Ex}}, \quad (6.19)$$

where the *calibration factor*

$$\boxed{\eta_{\max} := \max_G \{\eta(G)\}} \quad (6.20)$$

is *a priori* unknown. Furthermore, the background carrier concentration n_o may not be exactly known in the case of, e.g., semi-insulating or very inhomogeneous samples.

We therefore have to investigate the transformation properties of the solution to (6.10) under the variation

$$T_{\alpha\beta} : \begin{pmatrix} n_o \\ G \end{pmatrix} \rightarrow \begin{pmatrix} \alpha n_o \\ \beta G \end{pmatrix}. \quad (6.21)$$

Let $[\Delta n, \tau_R, \tau_{NR}, A]$ be a solution in compliance with n_o and G , then

$$T_{\alpha\beta} [\Delta n, \tau_R, \tau_{NR}, A] = \left[\alpha \Delta n, \frac{\alpha}{\beta} \tau_R, \frac{\alpha}{\beta} \tau_{NR}, A \right] \quad (6.22)$$

solves the transformed equation $T_{\alpha\beta}(6.10)$ and leaves not only τ_{rel} and A , but in particular η invariant. Thus, the ignorance in the absolute carrier injection rate G and the actual background carrier concentration does not affect the relative material parameters τ_{rel} and A as long as the proportionality relations $P_{Ex} \sim G$ and $I_{PL} \sim I_R$ hold. Since according to (6.9), $b_R = (n_o \tau_R)^{-1}$, a variation (6.21) results in $T_{\alpha\beta}[b_R] = \beta \alpha^{-2} b_R$. Consequently, no sound judgement of the radiative recombination coefficient is possible unless the background carrier concentration is sufficiently well known.

As opposed to the G -axis, the internal quantum efficiency cannot be arbitrarily scaled since η , τ_{rel} , and A are intimately correlated. Thus, the factor η_{\max} has to be determined for an absolute calibration of the internal quantum efficiency. The numerical procedure is as follows:

Let $(P_{Exj}, I_{PLj})_{1 \leq j \leq n}$ be a set of photoluminescence data, $G_j = \text{const.} * P_{Exj}$ and $I_{Rj} = I_R(G_j)$ the respective, calculated radiative recombination rates obtained from (6.15) by solving for Δn in (6.10). Then, the parameters η_{\max} , τ_R , τ_{NR} , and A can be determined by minimizing

$$\chi^2(\eta_{\max}, \tau_R, \tau_{NR}, A) := \sum_{j=1}^n \left(\frac{I_{Rj} - I_{PLj}}{G_j} \right)^2, \quad (6.23)$$

i.e. from a four parameter least-squares fit. In turn, η and the fraction of nonradiative centers filled with minority carriers, S^+/S , are obtained. The orders of magnitude of τ_R and τ_{NR} can be appraised from n_o and the absolute range of G .

6.4 The X_C and X_H Transitions

In order to estimate the room temperature values of η , τ_R/τ_{NR} , and A for the zincblende- and wurtzite-phase GaN crystals of sample #2058, the above model will now be applied to the intensities of the X_C and X_H transitions, which were measured as a function of the exciting laser power covering $5 \times 10^{-5} - 2.65 \times 10^{-2}$ W. Using the 325 nm line of the He-Cd laser, hot carriers were thus injected into the GaN.

With a circular excitation spot diameter of $d \approx 30 \mu\text{m}$, power densities in the range of $1.8 \leq P_{\text{Ex}} \leq 940 \text{ Wcm}^{-2}$ could be achieved. The corresponding photon flux is then $N[\text{s}^{-1}\text{cm}^{-2}] = 6.24 \times 10^{18} P_{\text{Ex}}[\text{Wcm}^{-2}] / (\hbar\omega[\text{eV}])$, where in the present case $\hbar\omega = 3.81 \text{ eV}$. Since the absorption coefficient of GaN is $\alpha(3.8 \text{ eV}) = 11 \mu\text{m}^{-1}$ (chapter 3), a light penetration depth $\alpha^{-1} \approx 90 \text{ nm}$ is to be expected. The average carrier injection rate is thus estimated to vary in the range of $3 \times 10^{23} \leq G \leq 2 \times 10^{26} \text{ cm}^{-3}\text{s}^{-1}$ for the values of P_{Ex} given.

The statistical errors in the measured intensities and excitation powers are typically 1–3%, i.e. of the size of the symbols shown in *Figs. 6.01a,b*, apart from the weakest intensity points. At the lowest injection rate used, the intensities of the X_C and X_H transitions could only be measured up to a relative error of about 20 %. To assess the influence of this uncertainty on the modelled curves, the calculations in the case of the cubic GaN were done (i) with the complete data set and (ii) omitting the two lowest intensity data points. The corresponding simulations are compared to each other in *Figs. 6.02,03* where the dark curves belong to the full data and the bright ones to the culled data points.

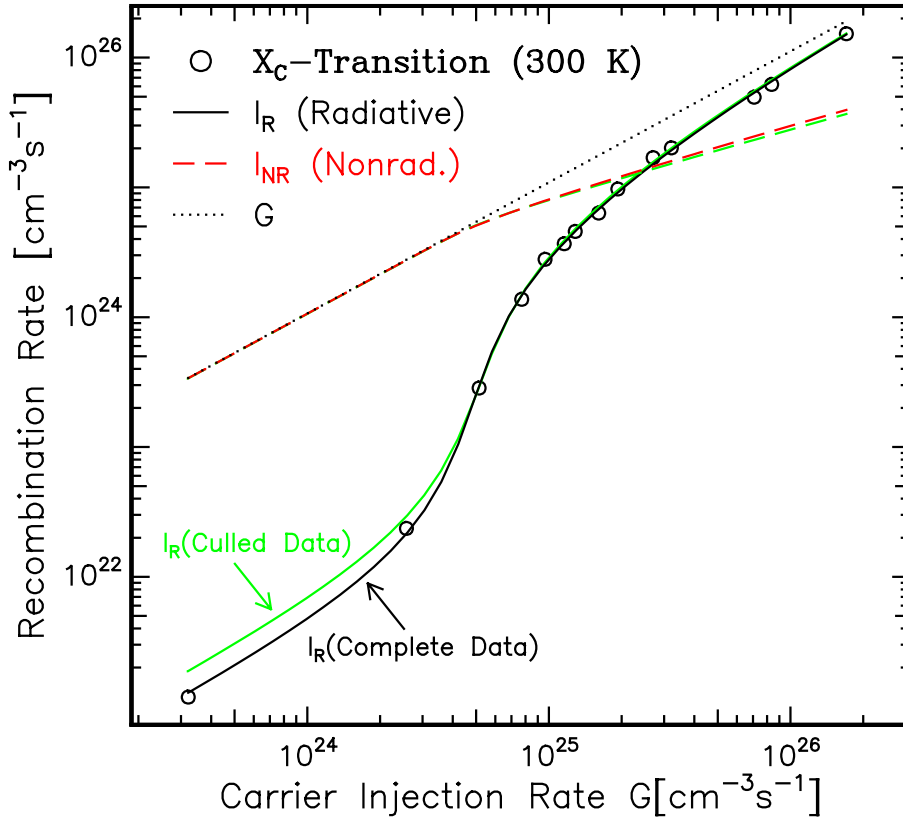


Fig. 6.02: X_C transition intensity (circles) with modelled radiative (solid line) and nonradiative (dashed line) recombination rates versus carrier injection rate G (dotted line). The dark lines are based on the complete data set whereas the bright ones were calculated omitting the first two data points with the lowest G .

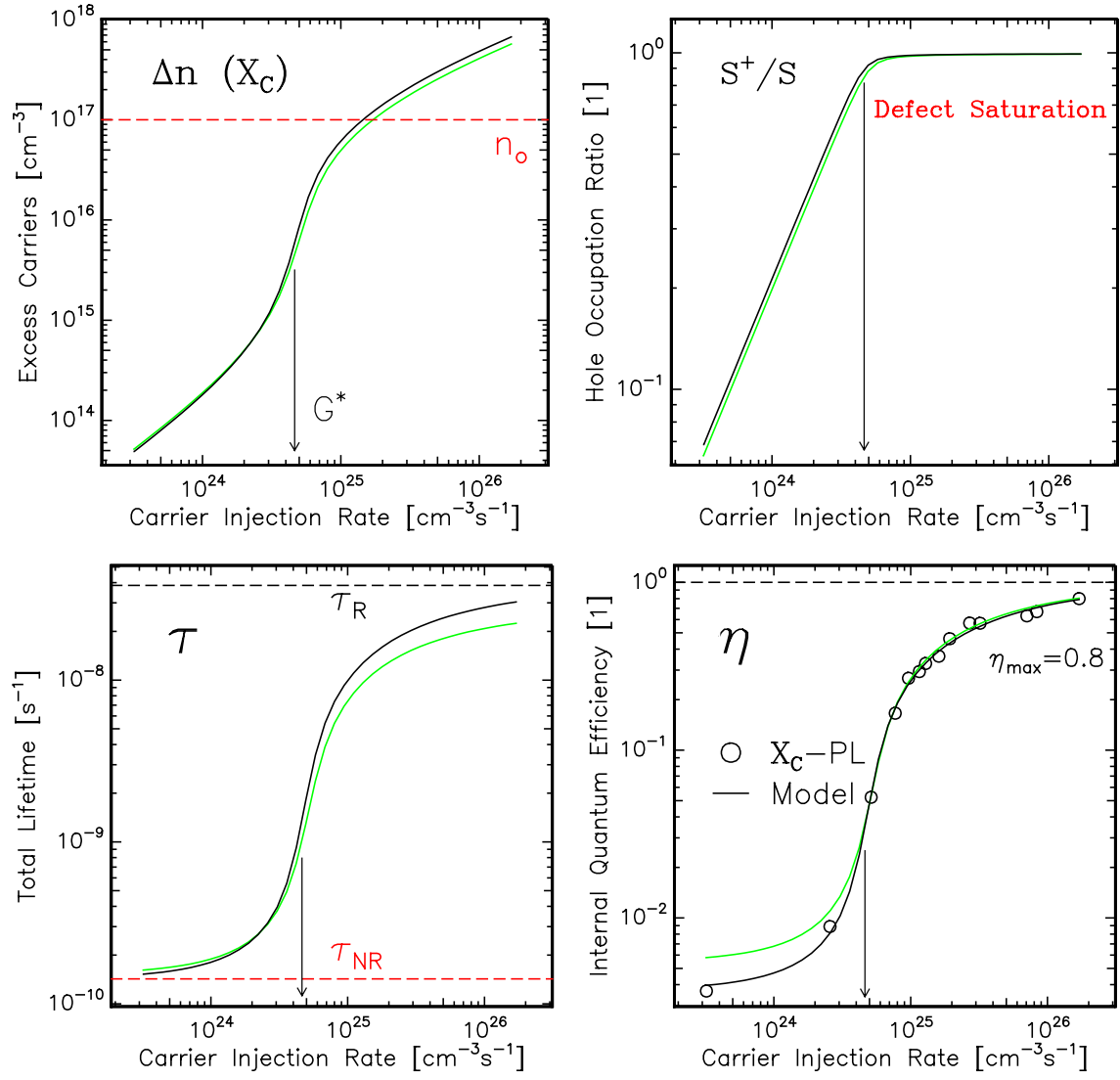


Fig. 6.03: Excess carrier concentration Δn , fraction of nonradiative centers filled with holes S^+/S , total lifetime τ , and absolute internal quantum efficiency η versus carrier injection rate G for the X_C transition. The dark lines stem from the complete photoluminescence data while the bright lines are due to the culled data set. The dashed lines indicate n_o and the limiting τ_R , τ_{NR} . The arrows point to $G^* = n_o/(\tau_{NR}(A+1))$.

The simulated curves with their characteristic parameters η , τ_R/τ_{NR} , and A were obtained by minimizing χ^2 in (6.23). *Fig. 6.04* displays the determination of the internal quantum efficiency parameter η_{\max} in the case of the X_C transition (complete data set): Under the constraint of a given η_{\max} , the unknowns τ_R , τ_{NR} , A , and the corresponding $I_R(G)$ which best suits the experimental data are determined and the discrepancy $\chi^2(\eta_{\max})$ is calculated. In this way, a unique minimum at $\eta_{\max} = 0.80$ is found which has been adopted for the absolute calibration of the internal quantum energy. The optimized parameters leading to a good agreement between the measured and the calculated data are compiled in *Tab. 6.1*.

The prominent S-shape of I_R and η can only be explained by a pronounced asymmetry in the nonradiative recombination coefficients $b_h \gg b_e$. Since the material under investigation is n-type, radiative recombination is limited by the availability of holes. In the small-signal regime, the majority of SRH centers are filled with electrons, $S^+/S \ll 1$, and the few holes being excited are getting captured very efficiently. However, as G is ramped up, the preferential

minority carrier capture leads to a saturation of the nonradiative SRH centers at already modest excitation levels (*Fig. 6.03*, top right). Once enough excess carriers are generated such that $S^+/S \approx 0.9$, a strong rise in $\Delta n = \Delta p$, τ , and η sets in. Finally, τ and η tend to saturate while Δn and I_R continue to linearly increase in the large-signal regime.

It should be pointed out that the asymmetry in the nonradiative recombination $A > 1$ does not contradict to the equality in excess carrier densities $\Delta n = \Delta p$ as long as the condition of quasi-instantaneous capture $\frac{\partial S^+}{\partial t}(t) \equiv 0$ is fulfilled. While the capture coefficients $b_h \neq b_e$, the actual capture rates are given by the products $b_h p S^0 = b_e n S^+$ containing the densities of available centers $S^{+,0}$ as well as the total carrier densities adjusted in such a way that the equality holds.

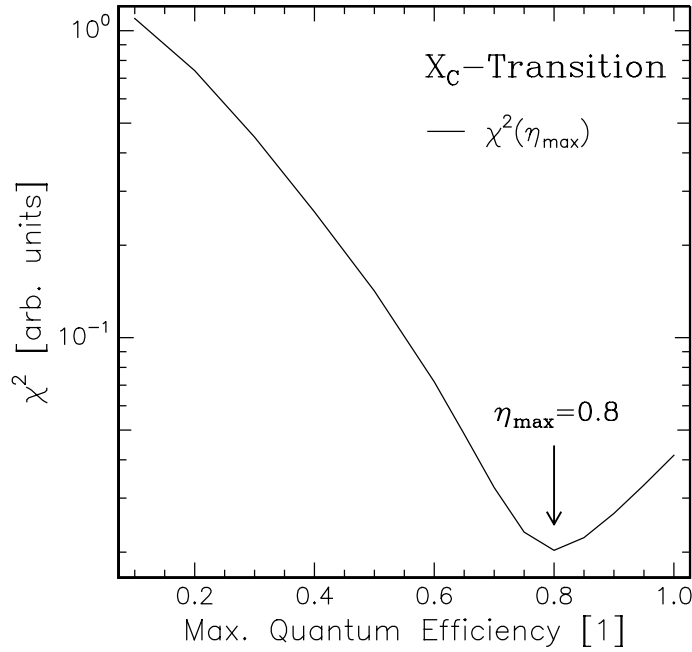


Fig. 6.04: Determination of η_{\max} by minimization of χ^2 in the case of β -GaN.

The above statements about the X_C transition hold for the simulated curves based on the entire as well as the reduced data set. In comparison, the analysis of the latter yields $\eta_{\max} = 0.83$, $\tau_{\text{rel}} = 180$, and $A = 130$. Thus, even though the culled data does at first sight not unambiguously define the characteristic S-shape, basically the same qualitative conclusions can be drawn. The quantitative agreement in the parameters obtained is to within an error of less or equal 50%.

	X_C (β -GaN)	X_H (α -GaN)
η_{\max}	0.80	0.80
$\tau_{\text{rel}} = \frac{\tau_R}{\tau_{\text{NR}}}$	270	200
$A = \frac{b_h}{b_e}$	150	170

Table 6.1: Modell parameters for the excitation density dependent band edge transition intensity of α - and β -GaN.

Investigating the X_H transition in the same way leads to very similar results, the overall agreement between the calculated and measured radiative recombination rates being slightly worse than in the case of the X_C transition (*Fig. 6.01b*). The parameters extracted from the α -GaN band edge luminescence are also quoted in *Tab. 6.1*. However, it has to be emphasized that the dominant nonradiative center(s) in the cubic and hexagonal GaN under investigation, which were effectively treated within the SRH model, may be different in origin. We cannot simply interpret the nonradiative processes competing with the X_C and X_H PL peaks as arising from the same kind of defect located in just a different crystallographic environment.

An estimation of the (non)radiative lifetimes requires the background electron concentration n_o of the present sample #2058. Hall measurements carried out on the $1.5\ \mu\text{m}$ thick, dominantly cubic GaN film underneath the crystals resulted in n_o of the order of 10^{18}cm^{-3} . The effective n_o may, however, be considerably smaller due to the contribution of the crystals which dominate the samples emission properties. Spatially-resolved cathodoluminescence measurements [57] on these crystals hardly showed any defect luminescence while the film did exhibit low-energy luminescence stronger by approximately 2 orders of magnitude. This indirectly evidences that the crystals which have grown within Ga droplets are by far cleaner than the underlying film. If we assume an average $n_o = 10^{17}\text{cm}^{-3}$ for both the X_C and the X_H transition, the values shown in *Tab. 6.2* are obtained.

$n_o = 10^{17}\text{cm}^{-3}$		
	X_C	X_H
τ_R [ns]	39	28
τ_{NR} [ps]	143	145

Table 6.2: Modelled radiative and nonradiative lifetimes for the band edge transition of α - and β -GaN assuming $n_o = 10^{17}\text{cm}^{-3}$.

Care has to be taken in generalizing the results obtained with this specific sample. The processes contending band edge recombination may be dissimilar in material grown on different substrates by unlike methods. An example of such is the α -GaN reference sample where defect-mediated luminescence (*Fig. 5.03a*, page 49) at quantum energies $\hbar\omega \leq 3\ \text{eV}$ is making a significant contribution to the total radiative recombination. This sample does therefore not comply with the stringent requirements of the simple recombination model used.

The BX_C transition from the $900\ \text{nm}$ thick β -GaN film #2070, on the other hand, is too heavily vied by nonradiative losses as to be feasible for the preceeding analysis. The acquired P_{Ex} -dependent data (not shown) leads to the conclusion that carrier injection rates higher by about 2 orders of magnitude than those that are possible with the present He-Cd laser would be required to saturate the defects in this sample.

Chapter 7

Growth of Zincblende (In,Ga,Al)N Heterostructures

So far, only the binary compound GaN was considered where special emphasis was put on the optical properties of the metastable cubic phase. It was shown that the fundamental band gap energies E_G of zincblende (β) and wurtzite (α) GaN are related according to

$$E_G(\beta\text{-GaN}) = E_G(\alpha\text{-GaN}) - 0.2 \text{ eV} \quad \text{for} \quad 4 \leq T \leq 500 \text{ K} \quad (7.1)$$

and that $E_G(\beta\text{-GaN}) = 3.22 \text{ eV}$ at room temperature, i.e. in the near-ultraviolet energy range.

For reaching visible band edge luminescence, the ternary $\text{In}_x\text{Ga}_{1-x}\text{N}$ has to be involved. Since the room temperature band gaps of $\alpha\text{-GaN}$ and $\alpha\text{-InN}$ are, respectively, 3.40 eV and 1.89 eV [94, 95], it is – in principle – possible to cover almost the entire visible and ultraviolet spectral range by adjusting the In content x in the alloy. Hexagonal $\text{In}_x\text{Ga}_{1-x}\text{N}$ is therefore in the focus of interest due to its application as the active region in group III nitride based light emitters.[96] In reality, the incorporation of high amounts of In for achieving $E_G(\alpha\text{-In}_x\text{Ga}_{1-x}\text{N}) \leq 2.9 \text{ eV}$ represents a major problem. [97, 98] This is due to several reasons:

- $\text{In}_x\text{Ga}_{1-x}\text{N}$ suffers from phase separation [99, 100, 101, 102, 103] as a consequence of the miscibility gap between GaN and InN, which has been predicted to exist in thermodynamic equilibrium. [99, 101] For $\alpha\text{-In}_x\text{Ga}_{1-x}\text{N}$, this phenomenon was observed for thick layers with $x > 0.3$ even under nonequilibrium growth conditions. [102, 103] However, also growth of high-quality thin films with large x , which are required for (multi) quantum well structures, is a challenging task.
- The high vapor pressure of N over $\text{In}_x\text{Ga}_{1-x}\text{N}$ results in significant In segregation. [104, 105, 106, 107] Low growth temperatures $T_G \approx 500 - 600^\circ\text{C}$ [105, 106] and very high group V/III ratios [106, 107] are necessary to prevent In droplet formation and to reach high In contents. In contrast, the crystalline and optical quality has been shown to be best at $T_G \approx 800^\circ\text{C}$ for layers with low In mole fraction.[97, 98, 104]
- Yet another problem is the thermal instability of $\text{In}_x\text{Ga}_{1-x}\text{N}$. Post-growth annealing even below 700°C results in a decomposition of the crystal rather than in a reduction of defect densities.[102]

Impressive progress has been made in addressing these issues. However, the emission efficiency of even the best $\alpha\text{-In}_x\text{Ga}_{1-x}\text{N}$ quantum well light emitting diodes [108] still drops significantly

in going from the blue to the green-yellow spectral range, whereas the peak linewidth distinctly increases. The aforementioned problems are even more detrimental for the performance of lasers and have thus far prevented the room temperature CW operation of devices which lase at photon energies lower than 2.9 eV.

Due to the similarity in the band structures of GaN and InN [109], one would expect that, at least for small In contents, the band gap energy of cubic β - $\text{In}_x\text{Ga}_{1-x}\text{N}$ is likewise significantly smaller than that of hexagonal α - $\text{In}_x\text{Ga}_{1-x}\text{N}$. The relation (7.1) is anticipated to hold also for such ternaries whose In content is not too large. In view of the above-listed difficulties, β - $\text{In}_x\text{Ga}_{1-x}\text{N}$ could be the material of choice for visible light emitters, provided that its potential advantages are not overruled by problems of phase purity and poor structural quality. Apart from the aspect of In incorporation, it is reminded that the cubic nitrides in general offer the possibility of easy cleavage on compatible (001)-oriented substrates for obtaining high-quality laser facets.

As already detailed in chapters 2 and 3, progress in the synthesis of zincblende structure nitrides is aggravated by problems of phase purity and rough surface morphology [107, 110, 111] which stem from the inavailability of a sufficiently well lattice matched substrate required for epitaxial stabilization. Therefore, it was not until 1995 that first results on β - $\text{In}_x\text{Ga}_{1-x}\text{N}$ were published by C.R. Abernathy *et al.* who synthesized this alloy by means of MOMBE. [111, 112] However, no optical data were provided and in particular, no experimental values for the band gap energy E_G of this new material were available.

7.1 Thick β - $\text{In}_x\text{Ga}_{1-x}\text{N}$ Films

7.1.1 MBE Growth

Previous attempts of our group to grow β - $\text{In}_x\text{Ga}_{1-x}\text{N}$ with the DC plasma source in the two chamber MBE system [107] resulted in films showing no detectable luminescence signal above 70 K. Due to the low nitrogen flux of the DC source, the In mole fraction is limited to $x \leq 0.11$ as a result of massive In segregation.[107]

This limit in the In content could be overcome by the use of the water-cooled RF plasma source attached to the new MBE system providing a considerably higher nitrogen flux. [113, 114] There, the optimization of process parameters for RF plasma assisted nucleation and growth of β -GaN on GaAs(001) has paved the way for obtaining single phase cubic (In,Ga,Al)N heterostructures with high In contents and surface morphologies good enough to allow for the synthesis of $\text{In}_x\text{Ga}_{1-x}\text{N}/\text{GaN}$ (multi) quantum wells, as will be shown below. Two samples containing thick $\text{In}_x\text{Ga}_{1-x}\text{N}$ layers will be presented in detail:

1. $\text{In}_{0.17}\text{Ga}_{0.83}\text{N}/\text{GaN}/\text{GaAs}$ (#8027)

The – nonoptimized – nucleation of β -GaN on GaAs took place under N-rich conditions at a growth temperature of $T_G=610^\circ\text{C}$ and a growth rate $g = 95 \text{ nm/h}$. After deposition of 10 monolayers, the previously (2×4)-reconstructed GaAs RHEED pattern was replaced by an arrangement of intense spots with cubic symmetry but larger period along all major azimuths, indicating the formation of a closed but fairly rough layer of monocrystalline β -GaN.

During a short growth interruption, T_G was ramped up to 650°C and g was increased to $0.25 \text{ } \mu\text{m/h}$ for growth of a 400 nm thick GaN buffer layer ($\text{Ga}/\text{N}\approx 1$). On top of this,

a 200 nm thick $\text{In}_{0.17}\text{Ga}_{0.83}\text{N}$ layer was grown at $T_G=650^\circ\text{C}$ with $g = 0.14\ \mu\text{m}/\text{h}$ under N-rich conditions to suppress In segregation. Right after opening the In shutter, the RHEED intensity dropped by about 50%, and a spotty, faceted pattern evolved. However, the cubic symmetry along all major azimuths was unaffected during the entire growth sequence, and the RHEED intensity could actually be recovered by growth interruptions.

2. $\text{GaN}/\text{In}_{0.4}\text{Ga}_{0.6}\text{N}/\text{GaN}/\text{Al}_{0.17}\text{Ga}_{0.83}\text{N}/\text{GaN}/\text{GaAs}$ (#8095)

In this case, the – optimized – nucleation was carried out at a growth temperature $T_G=590^\circ\text{C}$ with a lower growth rate of $g = 40\ \text{nm}/\text{h}$ and a group V to III ratio of $N/Ga \approx 3$. Upon deposition of 5–7 monolayers, the characteristic β -GaN RHEED pattern evolved which consisted in contrast to sample #8027 of elongated, parallel spots along all major azimuths, having its origin in a considerably smoother epitaxial layer of monocrystalline β -GaN. Also, a weak $2\times$ reconstruction evolved along the $[\bar{1}10]$ azimuth when T_G was ramped up to 640°C .

After g was increased to $0.23\ \mu\text{m}/\text{h}$, a 220 nm thick GaN buffer layer ($\text{Ga}/\text{N}\approx 1$) was grown, followed by 110 nm $\text{Al}_{0.17}\text{Ga}_{0.83}\text{N}$ and 255 nm GaN. Further improvement of the cubic pattern in terms of intensity, sharpness and streakiness was observed with increasing thickness. The RHEED pattern was virtually unaffected by the growth of the $\text{Al}_{0.17}\text{Ga}_{0.83}\text{N}$ -cladding layer which also exhibited the aforementioned reconstruction during growth interruptions. Nonetheless, secondary ion mass spectrometry as well as XTEM investigations clearly show the incorporation of Al and the formation of abrupt β -GaN/ $\text{Al}_{0.17}\text{Ga}_{0.83}\text{N}$ interfaces. On top of this β -(Ga,Al)N structure, a 185 nm thick β - $\text{In}_{0.4}\text{Ga}_{0.6}\text{N}$ layer was grown at $T_G = 640^\circ\text{C}$ with $g = 0.1\ \mu\text{m}/\text{h}$ under N-rich conditions. After growth of 10 – 15 nm, relaxation took place and a more spotty RHEED pattern of cubic symmetry evolved. No traces of wurtzite structure inclusions could be detected. Finally, a 55 nm thick β -GaN cap layer was grown.

In what follows, SIMS, XRD, TEM, SAD, SEM, and AFM data will be presented for these samples.

7.1.2 Composition and Structural Properties

Secondary Ion Mass Spectrometry

To quantitatively determine the amount of In and Al incorporated, a SIMS analysis¹ was carried out with 15 kV O_2^+ ions. For calibration of the measured secondary ion intensities, Rutherford backscattering spectrometry [115] as well as Auger electron spectroscopy [116] were performed on free β - $\text{In}_x\text{Ga}_{1-x}\text{N}$ surfaces with $x \geq 0.11$ and β - $\text{Al}_x\text{Ga}_{1-x}\text{N}$ with $x \geq 0.15$.

The SIMS measurements on an alloy $\text{X}_x\text{Ga}_{1-x}\text{N}$, $\text{X} \in \{\text{In}, \text{Al}\}$ yield then the absolute atom density n_X of the species X from which the molar fraction x is calculated by solving

$$x(a_{\text{XN}} - a_{\text{GaN}}) - \left(\frac{4x}{n_X}\right)^{1/3} + a_{\text{GaN}} = 0. \quad (7.2)$$

This equation for the zincblende lattice having 8 atoms per unit cell is based on a linear interpolation between the lattice constants a_{GaN} and a_{XN} of GaN and XN, respectively, which are compiled in *Tab. 7.1*.

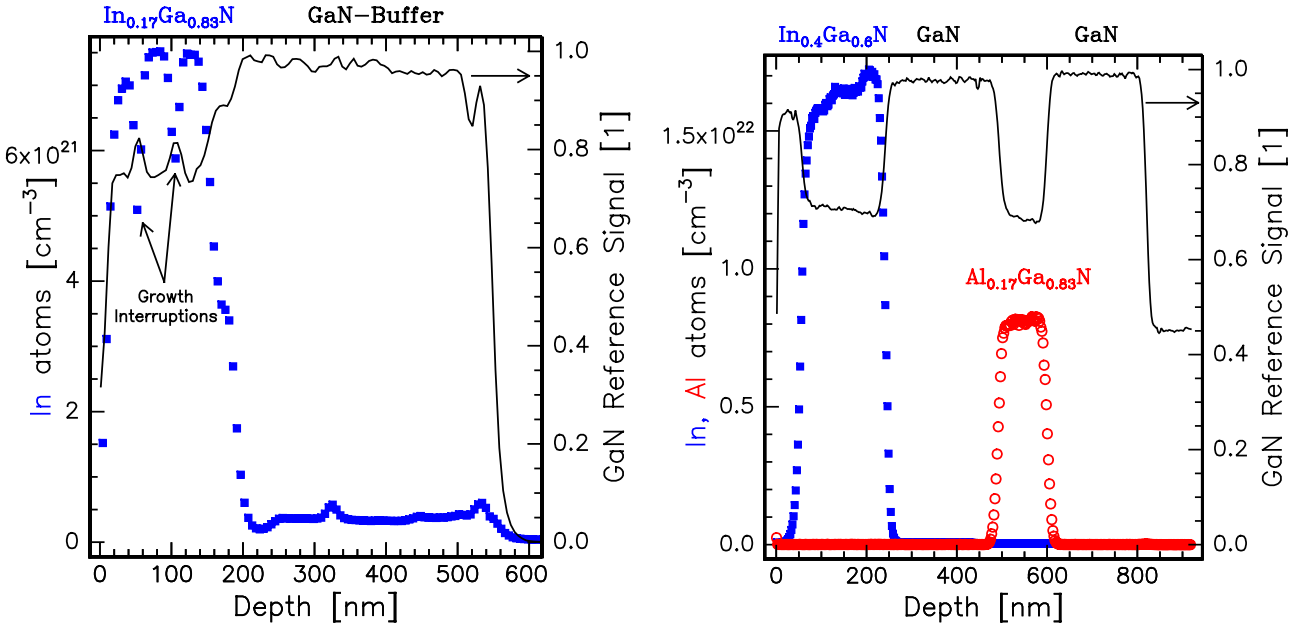
¹The measurements were done by the company RTG Mikroanalyse, Berlin.

Compound	a [Å]	$n_{\text{III}} [\text{cm}^{-3}]$
AlN	4.38	4.76×10^{22}
GaN	4.515	4.35×10^{22}
InN	4.98	3.24×10^{22}
GaAs	5.653	2.21×10^{22}

Table 7.1: Lattice constants and group-III atom densities of zincblende nitrides [127] and GaAs.

Figs. 7.01,02 show the respective spectra for samples #8027 and #8095. In addition to the In and Al depth profiles (left axis), the corresponding GaN reference signal is plotted (right axis) in order to clarify the layer sequence. The concentrations obtained by SIMS and by x-ray diffractometry (see below) are in accordance to within the experimental errors. The sharpness of the (In,Ga,Al)N interfaces of sample #8095 as compared to those of sample #8027 illustrate the improvement in the surface morphologies due to the optimization of nucleation and growth parameters.

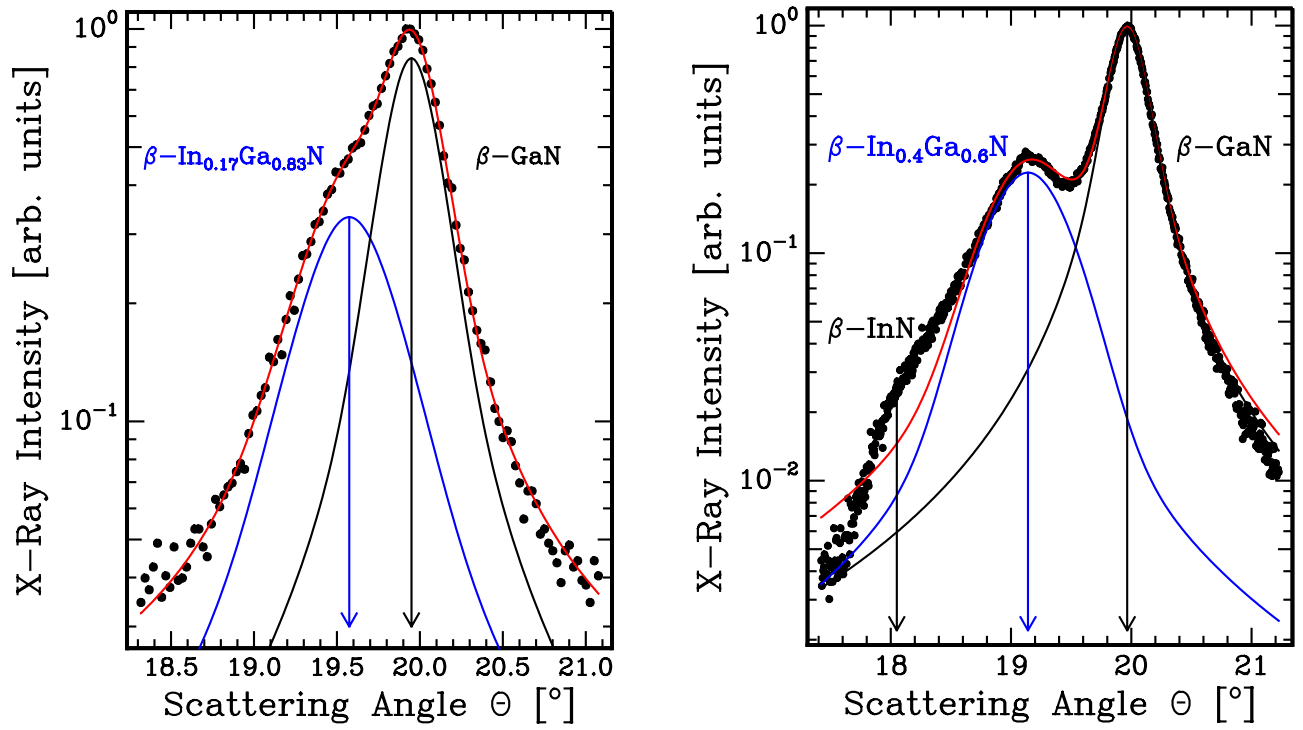
The kinks in the In profile of the $\text{In}_{0.17}\text{Ga}_{0.83}\text{N}$ sample are caused by the growth interruptions during which the cubic symmetry of the RHEED patterns was verified along different azimuths. Throughout these short breaks, In desorption has occurred leading to the observed reduction in the In content.



Figs. 7.01,02: SIMS spectra of the $\text{In}_{0.17}\text{Ga}_{0.83}\text{N}$ and $\text{In}_{0.4}\text{Ga}_{0.6}\text{N}$ sample. In each plot, the symbols show the absolute In and Al depth profiles (left axis) while the solid line depicts a normalized GaN reference signal (right axis).

X-Ray Diffractometry

With the setup described in chapter 3, $\omega - 2\theta$ XRD profiles were measured across the symmetric (002) reflections of GaAs, GaN, and $\text{In}_x\text{Ga}_{1-x}\text{N}$ to determine the lattice parameter difference of the two nitride layers.



Figs. 7.03,04: $\omega - 2\Theta$ x-ray scan of the $\text{In}_{0.17}\text{Ga}_{0.83}\text{N}$ and $\text{In}_{0.4}\text{Ga}_{0.6}\text{N}$ sample. The dots are the experimental data while the solid lines are least-squares fits with two Pseudo-Voigt functions. [113, 114]

Fig. 7.03 shows an $\omega - 2\Theta$ XRD scan of sample #8027. The (002) reflection of zincblende GaN at 19.95° , corresponding to a lattice constant of $a_{\text{GaN}} = 4.516 \text{ \AA}$, is clearly superposed by a broad peak which is not present in the case of pure $\beta\text{-GaN}$. It is therefore attributed to the $\text{In}_x\text{Ga}_{1-x}\text{N}$ layer. The profiles can be fitted well by Pseudo-Voigt functions giving the position of the second peak at $\Theta_{\text{InGa}} = 19.57^\circ$. Interpolating the lattice parameter [117] of $\beta\text{-InN}$, $a_{\text{InN}} = 4.98 \text{ \AA}$, and a_{GaN} linearly as a function of x (Vegards rule), we estimate the average In content to be $x = 0.18 \pm 0.01$, where the error is dominated by the uncertainty in a_{InN} . This compares well with the above SIMS analysis. The x-ray peak widths are given by $\Delta\Theta_{\text{GaN}} = 0.38^\circ$ and $\Delta\Theta_{\text{InGa}} = 0.66^\circ$. Assuming the crystalline imperfection of the $\text{In}_x\text{Ga}_{1-x}\text{N}$ layer to be comparable to that of the underlying GaN, an upper limit for the contribution of compositional fluctuations to $\Delta\Theta_{\text{InGa}}$ can be estimated from $\delta = \Delta\Theta_{\text{InGa}} - \Delta\Theta_{\text{GaN}}$, yielding $|\delta x| \leq 0.06$.

For sample #8095, part of an $\omega - 2\Theta$ scan between the (002) reflections of GaAs at $\Theta_{\text{GaAs}} = 15.814^\circ$ (not shown) and GaN at $\Theta_{\text{GaN}} = 19.966^\circ \hat{=} a_{\text{GaN}} = 4.512 \text{ \AA}$, is viewed in Fig. 7.04. The additional peak at $\Theta_{\text{InGa}} = 19.141^\circ \hat{=} 4.698 \text{ \AA}$ stems from the $\text{In}_x\text{Ga}_{1-x}\text{N}$ layer. The solid lines in Fig. 7.04 indicate a least-squares fit of Pseudo-Voigt functions to the data. *In situ* RHEED revealed the $\text{In}_x\text{Ga}_{1-x}\text{N}$ to be relaxed apart from the first 10 – 15 nm at the GaN/ $\text{In}_x\text{Ga}_{1-x}\text{N}$ interface. Thus, linear interpolation as above between a_{InN} and a_{GaN} yields an In content of $x = 0.40 \pm 0.01$.

The weak bump at $\Theta \approx 18^\circ$ is believed to arise from phase separated InN similar to what has been observed in the case of $\alpha\text{-In}_x\text{Ga}_{1-x}\text{N}$ with $x > 0.3$. [102, 103] From the difference in the peaks widths $\Delta\Theta_{\text{InGa}} - \Delta\Theta_{\text{GaN}} = 0.35^\circ$, an upper bound for the compositional inhomogeneity of the $\text{In}_{0.4}\text{Ga}_{0.6}\text{N}$ layer is estimated to $|\delta x| \leq 0.1$. These local variations in x will result in large photoluminescence linewidths and blurred absorption edges.

Transmission Electron Microscopy

A typical cross-sectional bright-field TEM micrograph of the $\text{In}_{0.4}\text{Ga}_{0.6}\text{N}$ sample in *Fig. 7.05(a)* clearly shows the sequence of the various nitride layers separated by comparatively smooth and abrupt interfaces. This result is amazing considering the high number of extended defects crossing the multilayer structure. These defects, which are of planar type, are not directly correlated to the strain relief between GaN and the GaAs substrate, but are generated during island coalescence or via defect interactions. Therefore, they remain relatively unaffected during growth.

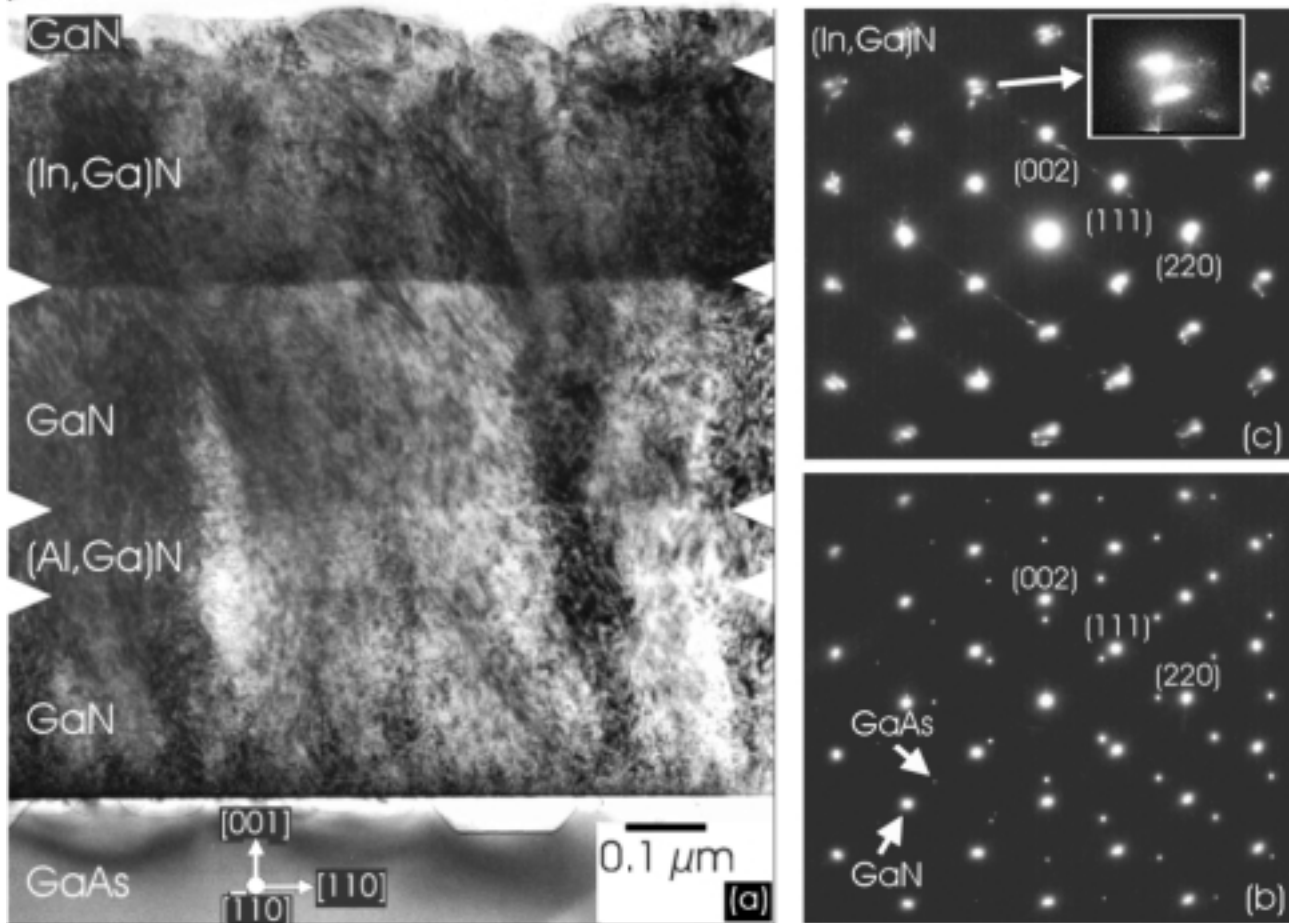


Fig. 7.05: The XTEM picture (a) of sample #8095 is clearly showing the sequence of the nitride layers. The respective interfaces are marked by arrows. The SAD patterns on the right-hand-side were taken from the GaN/GaAs interface (b) and the $\text{In}_{0.4}\text{Ga}_{0.6}\text{N}$ layer (c). The cubic symmetry of the respective epilayers can be verified. [114]

The crystallinity and the epitaxial orientation of the whole heterostructure and, in particular, of the $\text{In}_{0.4}\text{Ga}_{0.6}\text{N}$ epilayer was investigated by selected area diffraction as indicated in *Figs. 7.05(b)* and *(c)* along the $[\bar{1}10]$ zone axis. The SAD pattern in *Fig. 7.05(b)* was taken from the GaN/GaAs interfacial region demonstrating the perfect epitaxial alignment of both cubic lattices. The round and symmetric shape of the β -GaN spots reveals a high crystal quality with only little inhomogeneous strain.

The SAD pattern from the near surface region (*Fig. 7.05(c)*), which includes mainly the $\text{In}_{0.4}\text{Ga}_{0.6}\text{N}$ layer, is also of cubic symmetry without any hexagonal contributions. However, the diffraction peaks are more spread out, compared to the case of pure β -GaN. Indeed, a

magnification of the diffraction pattern (see inset in *Fig. 7.05(c)*) shows that these spots actually consist of two separate peaks corresponding to β -GaN and β - $\text{In}_x\text{Ga}_{1-x}\text{N}$, respectively. *In situ* RHEED revealed the $\text{In}_x\text{Ga}_{1-x}\text{N}$ layer to be relaxed apart from the initial 10–15 nm of growth. The observed separation of the peaks thus corresponds to an In content of $x = 0.37 \pm 0.05$ when linearly interpolating between the lattice constants of β -GaN and β -InN. The asymmetric shape of some of the reflexes may be a result of inhomogeneous strain induced by variations in the In content, or of low-angle boundaries separating small misaligned domains. In addition to the major cubic diffraction pattern, twin reflections and weak stacking fault streaks, being absent in *Fig. 7.05(b)*, can be perceived. As a consequence of the relaxation having occurred in the $\text{In}_{0.4}\text{Ga}_{0.6}\text{N}$ layer, the structural quality and the surface morphology of the following β -GaN cap layer is poor.

7.1.3 Morphology

Scanning Electron and Atomic Force Microscopy

The surfaces of both samples under investigation are mirror-like and featureless under optical microscopy. Scanning electron microscopy performed with sample #8027 (*Fig. 7.06a*) reveals a smooth, homogeneous $\text{In}_x\text{Ga}_{1-x}\text{N}/\text{GaN}$ layer with a total thickness of 640 nm. The sample is tilted by about 10° in order to visualize the $\text{In}_{0.17}\text{Ga}_{0.83}\text{N}$ surface as well as the $(\bar{1}10)$ GaN/GaAs facet obtained by cleavage. No In droplets or crystallites could be found.

The surface morphologies were studied by atomic force microscopy in ambient air with a commercially available AFM. The AFM micrograph in *Fig. 7.06b* shows details of the surface morphology of sample #8027. The peak-to-valley roughness amounts to 15 nm while the root-mean-square roughness is only 3.5 nm. The characteristic brick-shaped features are very similar to those observed for nonoptimized β -GaN (compare discussion in chapter 3).

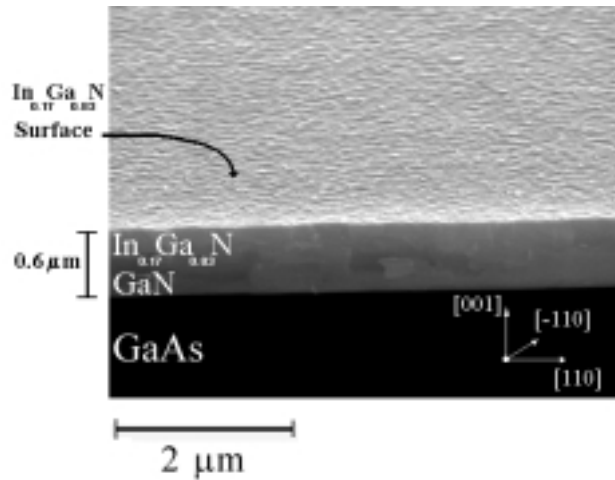


Fig. 7.06a: SEM micrograph [UJ] of the surface of the $\text{In}_{0.17}\text{Ga}_{0.83}\text{N}$ layer which is tilted to visualize the $(\bar{1}10)$ facet obtained by cleavage.

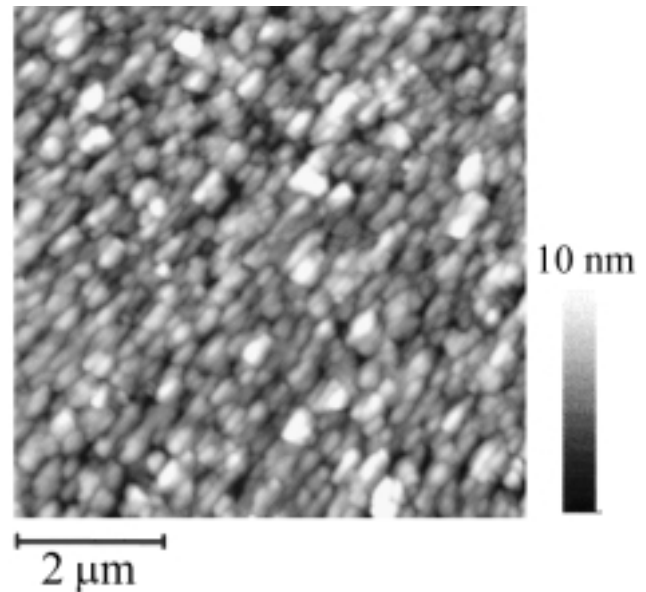


Fig. 7.06b: AFM micrograph of the surface of the $\text{In}_{0.17}\text{Ga}_{0.83}\text{N}$ layer. [113]

The surface of sample #8095 is, as already evidenced by XTEM, rougher as a result of the relaxation process which has taken place in the $\text{In}_{0.4}\text{Ga}_{0.6}\text{N}$ layer. In contrast, measurements on samples containing $\text{In}_x\text{Ga}_{1-x}\text{N}$ layers with thicknesses less than 10 nm and $0.4 \leq x \leq 0.5$ being coherently strained yield substantially smoother surfaces with RMS roughnesses of the order of 1 nm, as will be shown below.

7.2 $\beta\text{-GaN}/\text{In}_x\text{Ga}_{1-x}\text{N}/\text{GaN}$ (Multi) Quantum Wells

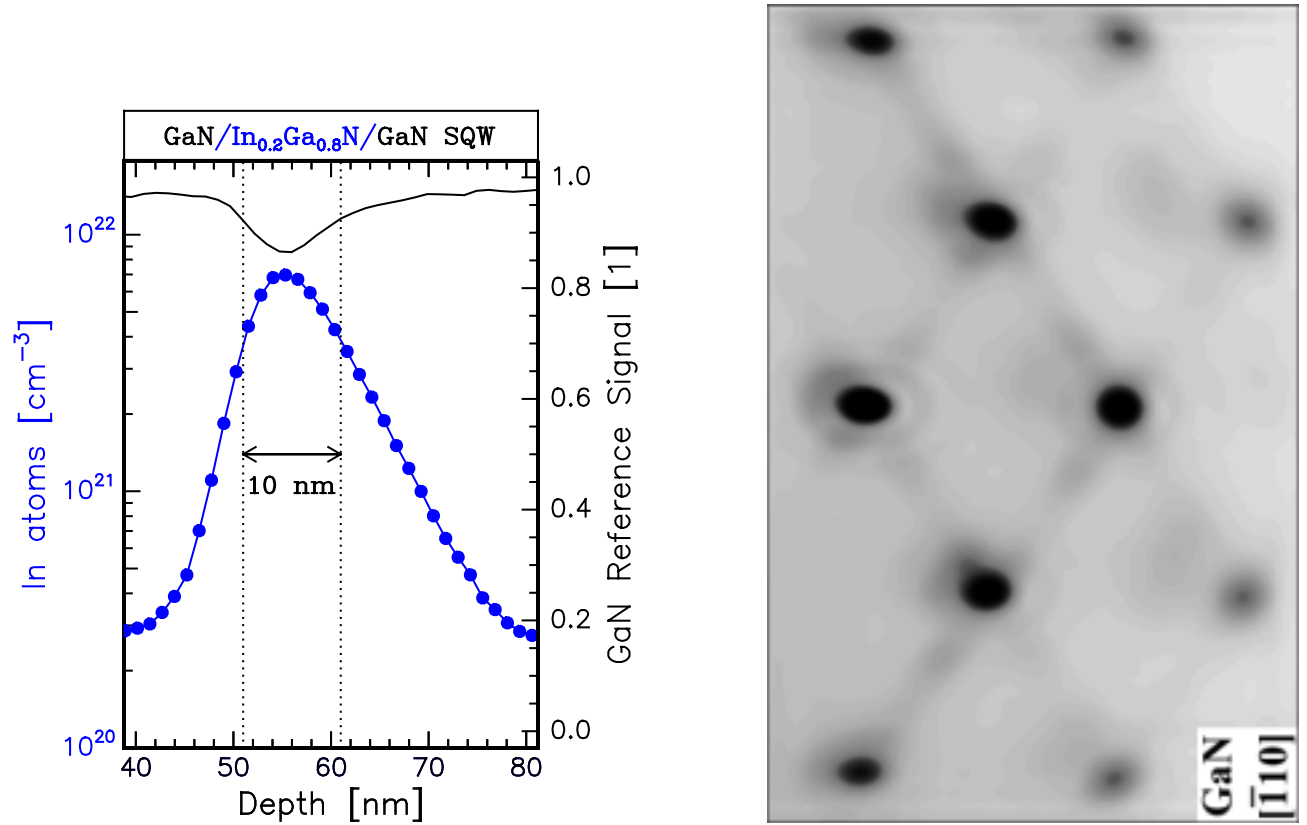
7.2.1 SQWs: Morphology and In Profiles

Wurtzite phase $\text{In}_x\text{Ga}_{1-x}\text{N}/\text{GaN}$ (multi) quantum wells are routinely employed as active regions of commercially available blue-green light emitting diodes and in prototypes of lasers emitting in the violet. In contrast, no reports are available to date about thin zincblende phase $\text{In}_x\text{Ga}_{1-x}\text{N}$ layers.

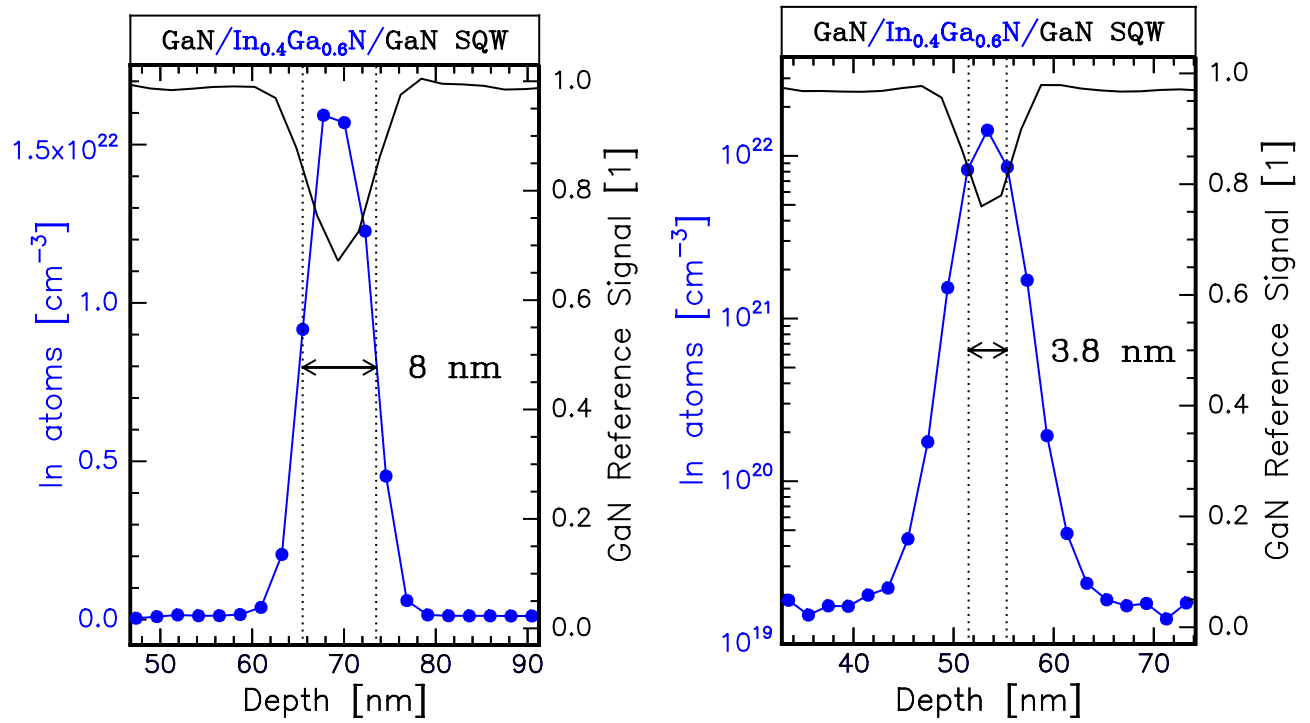
An important prerequisite for the synthesis of such quantum well structures is a sufficiently smooth surface morphology. The result of growing an $\text{In}_x\text{Ga}_{1-x}\text{N}/\text{GaN}$ structure on top of a rough $\beta\text{-GaN}$ buffer is viewed in *Fig. 7.07a*. The SIMS spectrum shown reveals an In profile with a peak concentration of 20% and a FWHM of 10 nm. Actually, a well thickness of $d = 5$ nm was anticipated. However, the poor brick-shaped morphology of the underlying GaN, which is already evidenced by the spotty RHEED pattern (*Fig. 7.07b*), induces a highly asymmetric shape of the In distribution. It appears as if the $\text{In}_x\text{Ga}_{1-x}\text{N}$ is gradually filling up the holes in the GaN surface resulting in a slowly increasing x . No further roughening during the $\text{In}_x\text{Ga}_{1-x}\text{N}$ growth could be observed. Thus, the $\text{GaN}/\text{In}_x\text{Ga}_{1-x}\text{N}$ interface is actually smoother than the $\text{In}_x\text{Ga}_{1-x}\text{N}/\text{GaN}$ boundary.

In comparison, *Figs. 7.08,09* view the depth profiles of two thin $\text{In}_x\text{Ga}_{1-x}\text{N}$ layers with $x \approx 0.4$ being sandwiched by considerably smoother $\beta\text{-GaN}$ barriers which were grown under optimized conditions ($T_G=640^\circ\text{C}$, $g = 130$ nm/h, high-quality $\beta\text{-GaN}/\text{GaAs}$ nucleation). Within the SIMS depth resolution of $\Delta d \approx 1.5$ nm, the In profiles are symmetric and have a FWHM of 8 and 3.8 nm, respectively. The surface morphologies of these samples are comparable to that shown in *Fig. 3.14* (page 22).

Fig. 7.10 shows RHEED snapshots of the growth of the $\text{In}_{0.4}\text{Ga}_{0.6}\text{N}/\text{GaN}$ quantum well with $d = 3.8$ nm. Unfortunately, almost half of the phosphorous coating of the RHEED screen was already brittle (white areas) such that only a small part of the diffraction patterns could be recorded. Since the resulting diffraction conditions were far from being ideal, the spots appear less streaky than under normal circumstances. In the bottom of *Fig. 7.10*, the RHEED pattern of the smooth $\beta\text{-GaN}$ template is seen onto which the $\text{In}_{0.4}\text{Ga}_{0.6}\text{N}$ was nucleated. At the initial stage of $\text{In}_{0.4}\text{Ga}_{0.6}\text{N}$ growth, the diffraction spots merely smear out and a slight decrease in intensity is perceived, an example of which is shown at a well thickness of 2.8 nm. With increasing thickness, the outmost reflexes are getting tilted towards smaller reciprocal lattice spacings due to either elastic or plastic relaxation. However, no deterioration of the zincblende phase could be detected. At $d = 3.8$ nm the $\text{In}_{0.4}\text{Ga}_{0.6}\text{N}$ growth was stopped and the GaN barrier was nucleated without interruption. After only 3 nanometers of $\beta\text{-GaN}$ growth, the original streaky diffraction pattern was almost recovered. In particular, the spots are aligned in parallel again. This shows that the $\text{In}_{0.4}\text{Ga}_{0.6}\text{N}$ is pseudomorphic to the $\beta\text{-GaN}$.



Figs. 7.07a,b: Graded, asymmetric In depth profile (left) of a $\text{In}_x\text{Ga}_{1-x}\text{N}$ /GaN SQW with $x = 0.2$ and $d = 10$ nm grown on a rough GaN surface. The RHEED pattern of the GaN template is shown on the right-hand-side.



Figs. 7.08,09: SIMS spectra showing symmetric In depth profiles and abrupt interfaces of two $\text{In}_x\text{Ga}_{1-x}\text{N}$ /GaN SQWs with $x = 0.4$ and $d = 8$ and 3.8 nm, respectively, grown on a smooth GaN template.

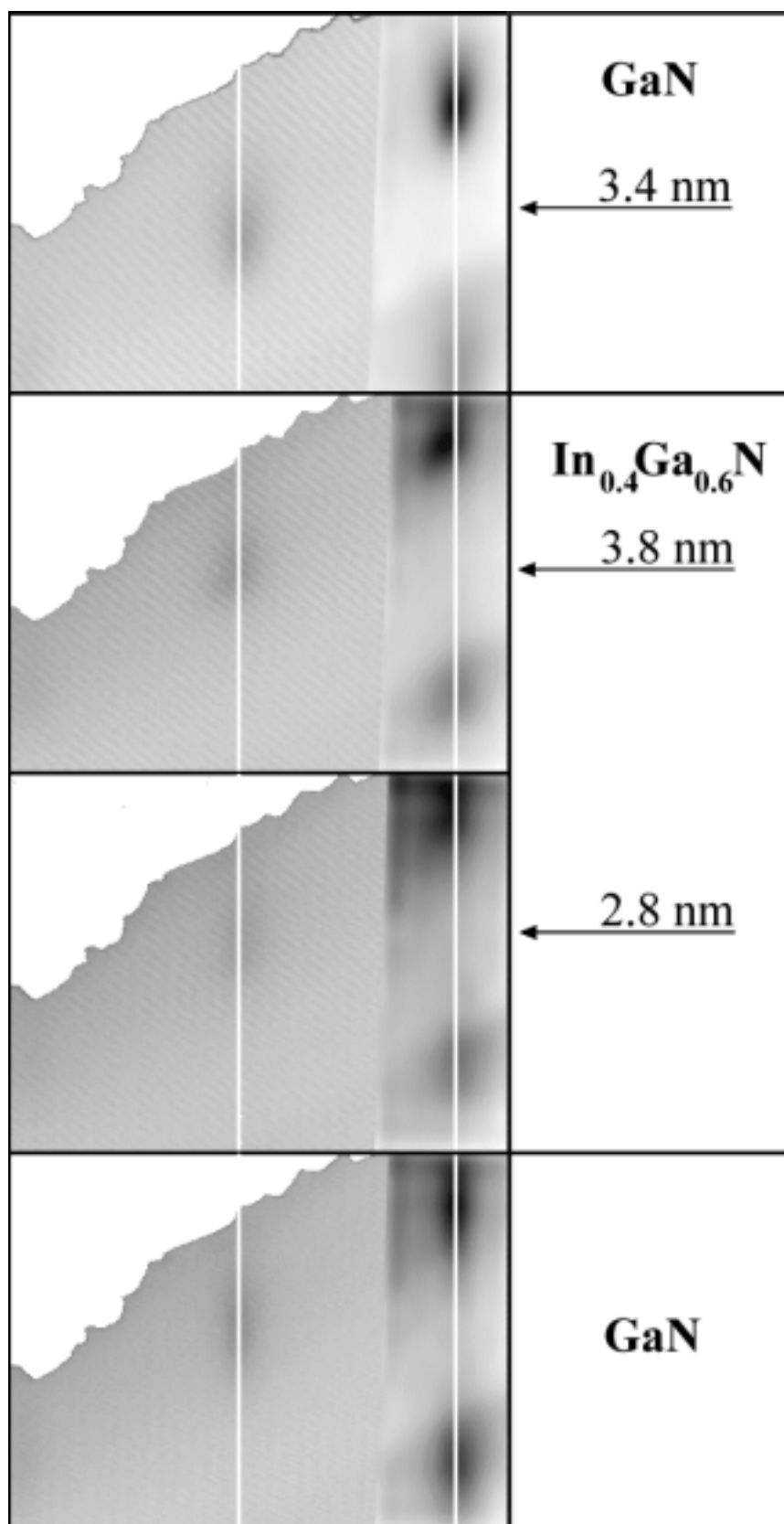


Fig. 7.10: RHEED patterns recorded along the $[110]$ azimuth at different stages of growth of the SQW with $x = 0.4$ and $d = 3.8$ nm shown in *Fig. 7.09*. The outer spots are Fourier-filtered to suppress a jittered noise signal.

7.2.2 Strained MQWs

The fact that strained $\beta\text{-In}_x\text{Ga}_{1-x}\text{N}/\text{GaN}$ SQWs with high In content can be grown without serious degradation in morphology or phase purity gives rise to hope that also zincblende phase multi quantum well structures may be synthesized.

Indeed, *Fig. 7.11* shows a SIMS spectrum of a sample consisting of four $\beta\text{-In}_x\text{Ga}_{1-x}\text{N}/\text{GaN}$ quantum wells with $x = 0.50 \pm 0.2$ and well widths of $d = 6.4 \pm 0.3$ nm. The respective layers appear as dark stripes in the bright-view XTEM picture *Fig. 7.13*. The corresponding interfaces are abrupt, basically parallel to each other, and hardly affected by the massive bundles of stacking faults being present in some parts of the sample.

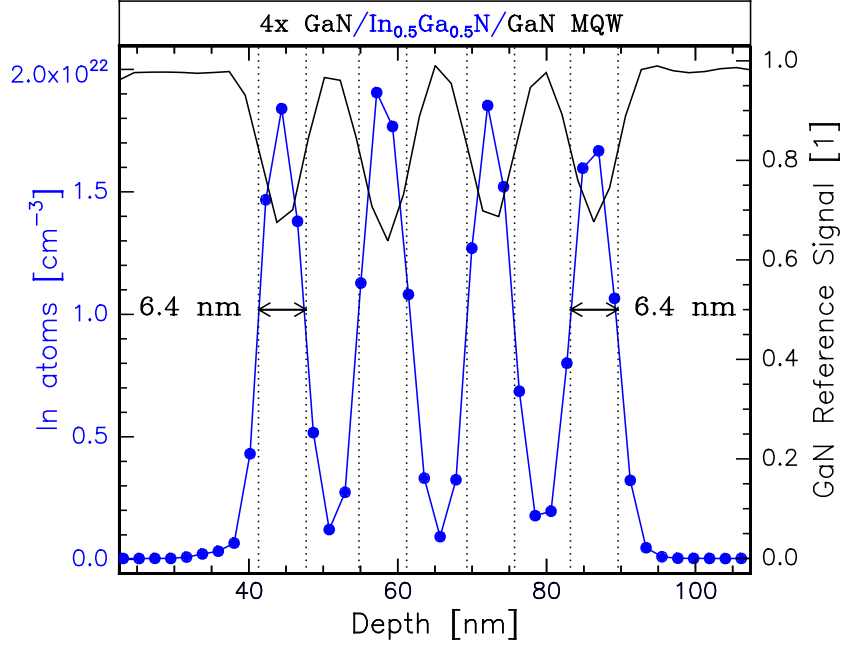


Fig. 7.11: SIMS spectrum showing the In depth profile (symbols, left axis) of a $\text{In}_x\text{Ga}_{1-x}\text{N}/\text{GaN}$ MQW with $x \approx 0.5$ and $d \approx 6$ nm. The GaN reference signal normalized to unity is displayed (line, right axis) for comparison.

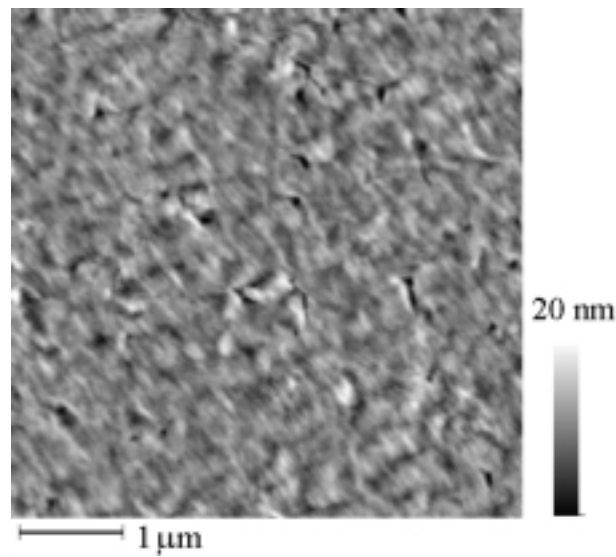


Fig. 7.12: AFM scan [MW] of the surface of the MQW sample.

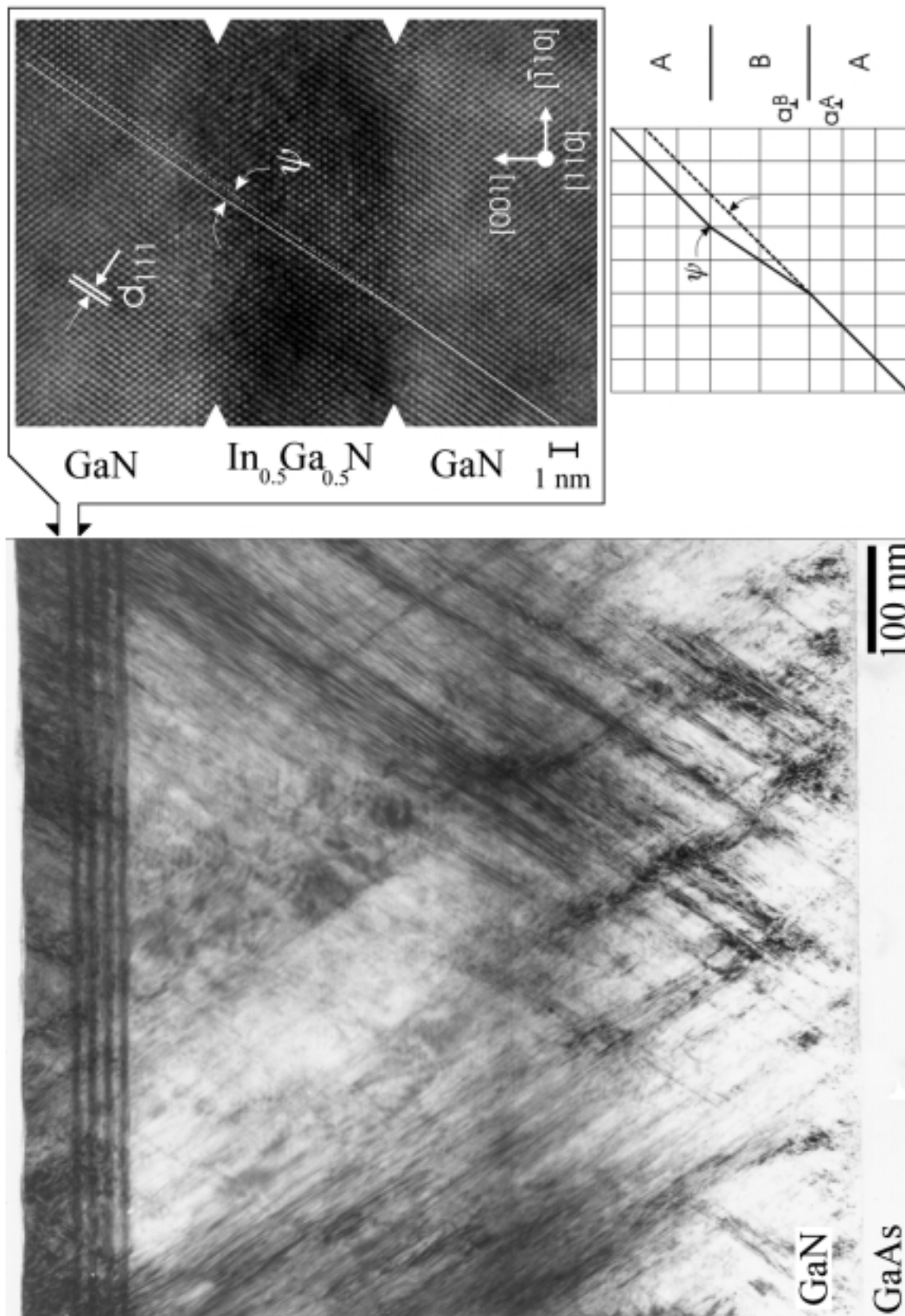


Fig. 7.13: XTEM and HRTEM micrographs [AT] of the MQW sample. The high-resolution picture views the topmost of the four QWs. A schematic plot to illustrate the determination of strain at a heterojunction is also shown.

A high resolution XTEM micrograph (*Fig. 7.13*) reveals structural details of the topmost $\text{In}_{0.5}\text{Ga}_{0.5}\text{N}/\text{GaN}$ quantum well. The interfacial widths are $\Delta d \approx 1$ nm ($\text{In}_{0.5}\text{Ga}_{0.5}\text{N}/\text{GaN}$) and $\Delta d \approx 1.5$ nm ($\text{GaN}/\text{In}_{0.5}\text{Ga}_{0.5}\text{N}$), i.e. equal to the root-mean-square roughness of the samples' surface, as determined by an AFM scan (*Fig. 7.12*). The peak-to-valley roughness amounts to 15–20 nm which is, however, observed at only a few locations. The surface morphology of this sample with a total thickness of 815 nm is very similar to that of the 0.7 μm thick $\beta\text{-GaN}$ reference layer (*Fig. 3.14*, page 22).

The most interesting question, however, concerns the degree of residual strain in such a heterostructure. Bearing in mind that the lattice mismatch between $\beta\text{-GaN}$ and $\beta\text{-In}_{0.5}\text{Ga}_{0.5}\text{N}$ is about 5 %, it would not be surprising if substantial relaxation took place beyond the first few monolayers of $\text{In}_{0.5}\text{Ga}_{0.5}\text{N}$, in compliance with common experience gained on similarly highly mismatched systems such as SiGe/Si [118, 119], $\text{InGaAs}/\text{GaAs}$ [120, 121, 122], or more recently GaN/AlN [123, 124].

The alignment of the $\{110\}$ planes at the $\text{GaN}/\text{In}_{0.5}\text{Ga}_{0.5}\text{N}$ interface, however, shows that at least the first few $\text{In}_{0.5}\text{Ga}_{0.5}\text{N}$ monolayers are coherently strained. According to elasticity theory, the mismatch at the interface between a commensurate $\text{In}_x\text{Ga}_{1-x}\text{N}$ thin film and the GaN barrier, $\varepsilon_{\parallel}^{\text{InGa}} = (a_{\parallel}^{\text{InGa}} - a_{\parallel o}^{\text{InGa}}) / a_{\parallel o}^{\text{InGa}}$, relates to the strained out-of-plane lattice constant a_{\perp}^{InGa} via the Poisson ratio ν

$$\varepsilon_{\perp}^{\text{InGa}} = (a_{\perp}^{\text{InGa}} - a_{\perp o}^{\text{InGa}}) / a_{\perp o}^{\text{InGa}} = \frac{-2\nu}{1 - \nu} \varepsilon_{\parallel}^{\text{InGa}}, \quad (7.3)$$

where $a_{\parallel o}^{\text{InGa}} = a_{\perp o}^{\text{InGa}}$ and $a_{\parallel}^{\text{InGa}} = a_{\parallel}^{\text{GaN}}$. Thus, an analysis of the angle Ψ between the respective $\{111\}$ planes of the two materials [125] allows to estimate the residual strain $\Delta\varepsilon_{\parallel} = \varepsilon_{\parallel}^{\text{InGa}} - \varepsilon_{\parallel}^{\text{GaN}}$ being present in the heterosystem:

$$\Psi_{111}[\text{rad}] = \frac{1}{2} \sin(2\theta_{111}) \frac{1 + \nu}{1 - \nu} \Delta\varepsilon_{\parallel}. \quad (7.4)$$

For the sample under investigation, values of $\Psi_{111} = 1.8 \pm 0.2^\circ$ were measured as indicated in *Fig. 7.13*. In contrast, the angle between the $\{111\}$ planes of the GaN barriers is $0 \pm 0.1^\circ$, i.e. the GaN layers below and on top of a well are structurally equivalent within the accuracy of the strain measurement. It is therefore presumed that $\varepsilon_{\parallel}^{\text{GaN}} \approx 0$. With $\theta_{111} = 54.7^\circ$ and $\nu = 0.366$ [126], the observed angles Ψ_{111} correspond to unexpectedly high strain values of $\varepsilon_{\parallel}^{\text{InGa}} = (3.4 \pm 0.3) \%$. This finding shows that despite the large well thicknesses of 6–7 nm, only little elastic relaxation has taken place in the $\text{In}_{0.5}\text{Ga}_{0.5}\text{N}$ layers. Direct evidence for defect mediated relaxation processes is given by stacking faults originating from the heterointerfaces at some places.

7.3 $\beta\text{-Al}_x\text{Ga}_{1-x}\text{N}$

Wurtzite $\text{Al}_x\text{Ga}_{1-x}\text{N}$ is finding numerous applications in (opto-)electronic devices. Since $\alpha\text{-AlN}$ has a direct room temperature band gap of $E_G(\alpha\text{-AlN}) = 6.3$ eV, compared to $E_G(\alpha\text{-GaN}) = 3.4$ eV, the alloy is employed as cladding layer for carrier confinement and as optical wave guide in $\text{Al}_x\text{Ga}_{1-x}\text{N}/\text{In}_x\text{Ga}_{1-x}\text{N}$ heterostructures, which are encountered in light emitting diodes and, especially, in lasers. In electronic devices based on parallel transport such as high-electron-mobility field effect transistors, the use of $\text{Al}_x\text{Ga}_{1-x}\text{N}$ is essential for realizing the two dimensional electron gas.

Zincblende $\text{Al}_x\text{Ga}_{1-x}\text{N}$, on the other hand, is just about to be discovered for device applications. Because the difference in the lattice constants between $\beta\text{-AlN}$ ($a_{\text{AlN}} = 4.38 \text{ \AA}$) and $\beta\text{-GaN}$ ($a_{\text{GaN}} = 4.51 \text{ \AA}$) is comparatively small, only little strain is created in $\text{Al}_x\text{Ga}_{1-x}\text{N}/\text{GaN}$ structures with $0 \leq x \leq 0.15$. Therefore, growth of such is relatively straightforward. This statement holds for zincblende as well as for wurtzite phase $\text{Al}_x\text{Ga}_{1-x}\text{N}$. First results on $\beta\text{-Al}_x\text{Ga}_{1-x}\text{N}$ grown on GaAs by MOCVD are reported in [128]. There, growth was performed at $T_G = 950^\circ\text{C}$ and layers with Al molar fractions up to 23% were achieved.

A systematic study of $\beta\text{-Al}_x\text{Ga}_{1-x}\text{N}$ is beyond the scope of this work. In what follows, the compositional and structural properties of a simple low-temperature $\beta\text{-Al}_x\text{Ga}_{1-x}\text{N}$ test structure will be discussed.

7.3.1 Low Temperature Growth

Due to the very high melting points of GaN and AlN, wurtzite $\text{Al}_x\text{Ga}_{1-x}\text{N}$ is usually grown at $T_G > 1000^\circ\text{C}$. In contrast, the zincblende GaN films considered within this work were synthesized at $T_G \leq 650^\circ\text{C}$ and only a few tests were carried out to grow $\beta\text{-Al}_x\text{Ga}_{1-x}\text{N}$. For the sake of compatibility with the $\beta\text{-GaN}$ process, the same low growth temperatures were chosen in these cases.

An example of such a heterostructure is seen in *Fig. 7.14* where a SIMS spectrum is visualizing the Al depth profile. The incorporation of Al was independently verified by means of RBS. [115] On top of a $\beta\text{-(2}\times\text{4)-GaAs(001)}$ surface, a 70 nm thick $\beta\text{-GaN}$ buffer layer was nucleated and grown by the same optimized procedure as that described in chapter 3, resulting in a smooth (4×2) reconstructed surface. Keeping the substrate temperature $T_G = 640^\circ\text{C}$ constant, a 35 nm thick $\text{Al}_{0.17}\text{Ga}_{0.83}\text{N}$ layer was grown, followed by 50 nm $\text{Al}_{0.2}\text{Ga}_{0.8}\text{N}$ and, finally, 75 nm $\text{Al}_{0.15}\text{Ga}_{0.85}\text{N}$. During growth of the $\text{Al}_{0.17}\text{Ga}_{0.83}\text{N}$ film, the RHEED pattern remained virtually unaffected and, in particular, the (4×2) surface reconstruction could be recovered by growth interruptions. This indicates that the $\text{Al}_{0.17}\text{Ga}_{0.83}\text{N}$ layer is commensurable to the underlying $\beta\text{-GaN}$ buffer, i.e. coherently strained.

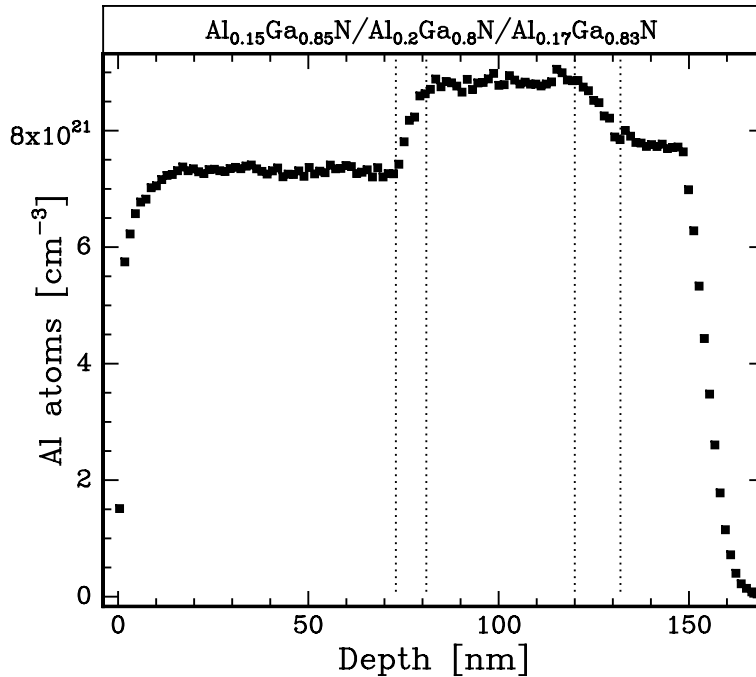


Fig. 7.14: SIMS spectrum showing the Al depth profile of sample #8100.

Raising the Al concentration up to 20% caused a gradual roughening of the growth front as evidenced by the evolution of a spottier RHEED pattern. Some of the spots got slowly tilted as a result of substantial amounts of strain being built up with increasing thickness. Lowering the Al content down to 15% lead to an improvement of the RHEED pattern in terms of elongation and parallel alignment of the diffraction spots, indicating a partial recovery in surface morphology.

Indeed, the AFM micrograph displayed in *Fig. 7.15* reveals a comparatively large peak-to-valley roughness of 25 nm and a RMS value of 3 nm for the $\text{Al}_{0.15}\text{Ga}_{0.85}\text{N}$ surface.

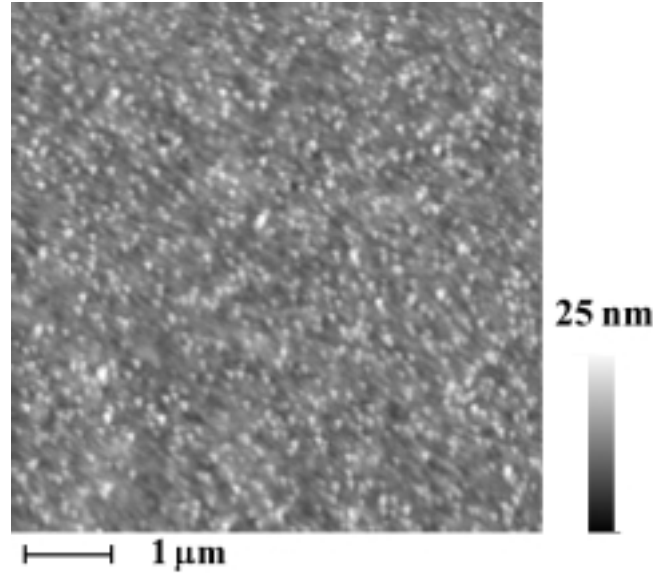
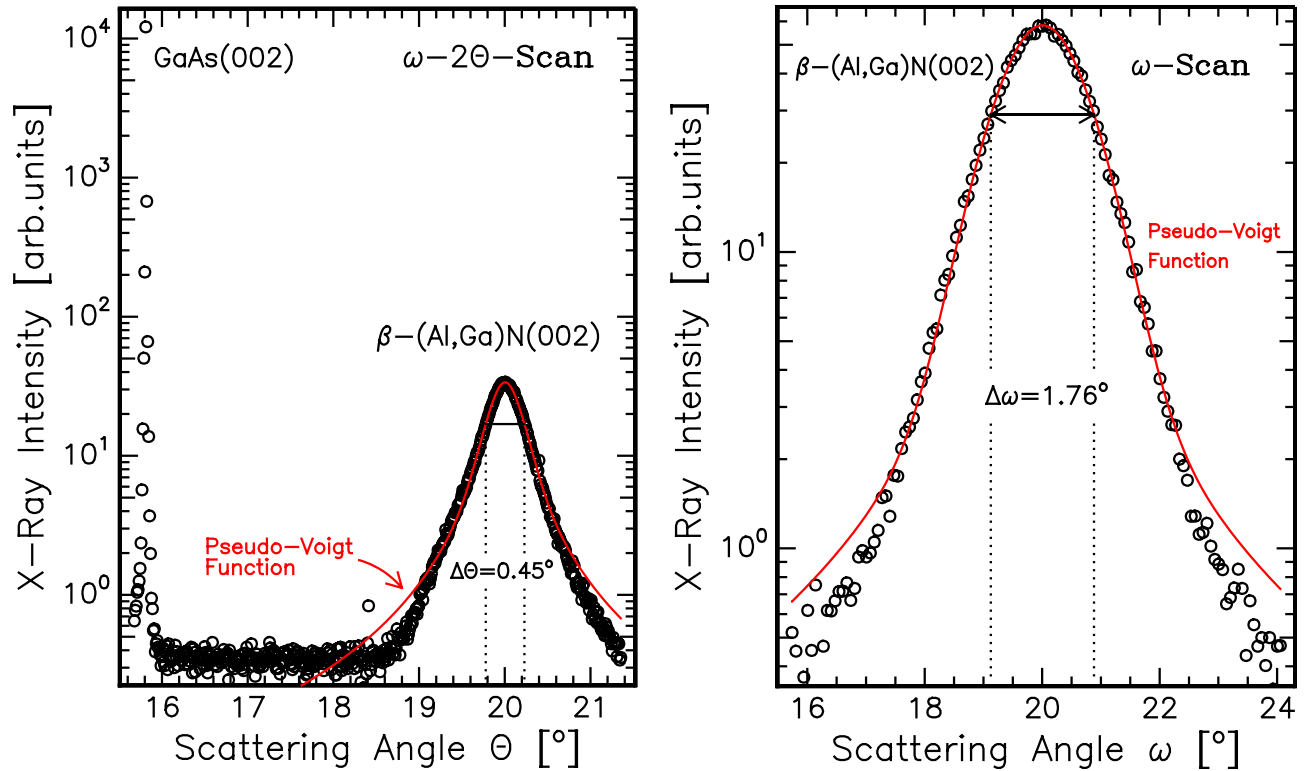


Fig. 7.15: AFM scan [MW] visualizing the surface morphology of sample #8100.



Figs. 7.16a,b: X-ray diffraction $\omega - 2\theta$ and ω scans of the $\text{Al}_x\text{Ga}_{1-x}\text{N}$ test structure #8100.

An $\omega - 2\Theta$ x-ray diffraction scan of the sample under investigation can be seen in *Fig. 7.16a*. The maximum of the broad peak at $\Theta = 20.004^\circ$ corresponds to a lattice constant of 4.504 Å, close to the value of $a_{\text{GaN}} = 4.51$ Å for the β -GaN reference sample. The full width at half maximum amounts to $\Delta\Theta = 0.45^\circ$. Applying Vegards' law, i.e. presuming a complete relaxation in the $\text{Al}_x\text{Ga}_{1-x}\text{N}$ structure, yields an average Al concentration of 6.6% in contradiction to the results obtained from the SIMS and RBS analysis. This leads to the conclusion that only little plastic relaxation has occurred during the growth of the various $\text{Al}_x\text{Ga}_{1-x}\text{N}$ layers in accordance with the RHEED observations. While $\Delta\Theta$ is a measure for the variation in the lattice constant, the width $\Delta\omega = 1.76^\circ$ as obtained by an ω -scan (*Fig. 7.16b*) is dominated by misaligned domains.

In conclusion, thick strained β - $\text{Al}_x\text{Ga}_{1-x}\text{N}$ layers with Al contents up to $x = 0.2$ were grown by RF plasma assisted MBE at $T_{\text{G}}=640^\circ\text{C}$ and a growth rate of $g = 150$ nm/h. The structural quality, however, is yet to be improved by a further optimization of growth temperature and growth rate.

Chapter 8

Optical Properties of Zincblende (In,Ga,Al)N

8.1 Thick β -In_xGa_{1-x}N Films

In what follows, the optical properties of cubic (In,Ga,Al)N heterostructures comprising thick β -In_xGa_{1-x}N films are investigated. Reflectance, transmittance and photoluminescence data of two films having In contents of $x = 0.17$ and $x = 0.4$ are presented. The growth, crystal structure and morphology of these samples were discussed in the preceeding chapter. An attempt is made to estimate the so far unknown band edge energy of β -In_xGa_{1-x}N for In mole fractions up to 40 % by combining the available data from RF and DC plasma grown films. The latter have a maximum In content of 11 % due to the limited active nitrogen flux of the DC source. [107]

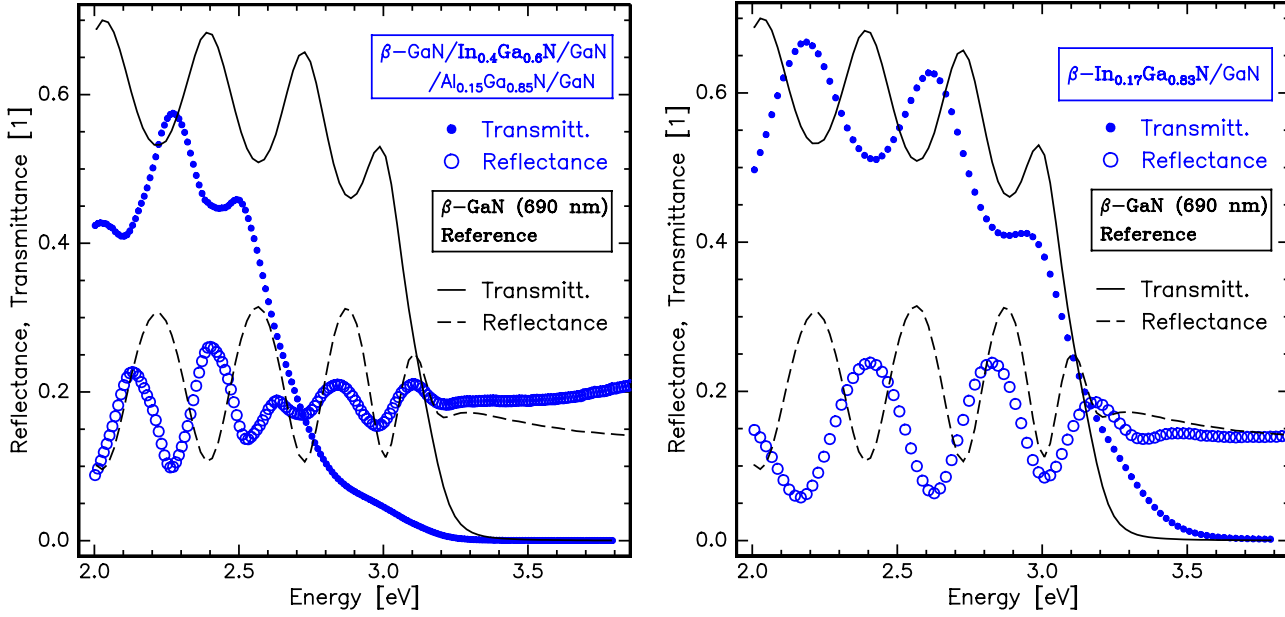
8.1.1 Reflectance & Transmittance

To appraise the absorption edges of the In_{0.17}Ga_{0.83}N and the In_{0.4}Ga_{0.6}N samples, reflectance and transmittance measurements were carried out after the GaAs substrates have been etched away and the resulting thin (In,Ga,Al)N films have been mounted on sapphire for mechanical stability. The sample preparation as well as the actual measurements were performed in the same fashion as in the case of the 690 nm thick β -GaN reference layer treated in chapter 4.

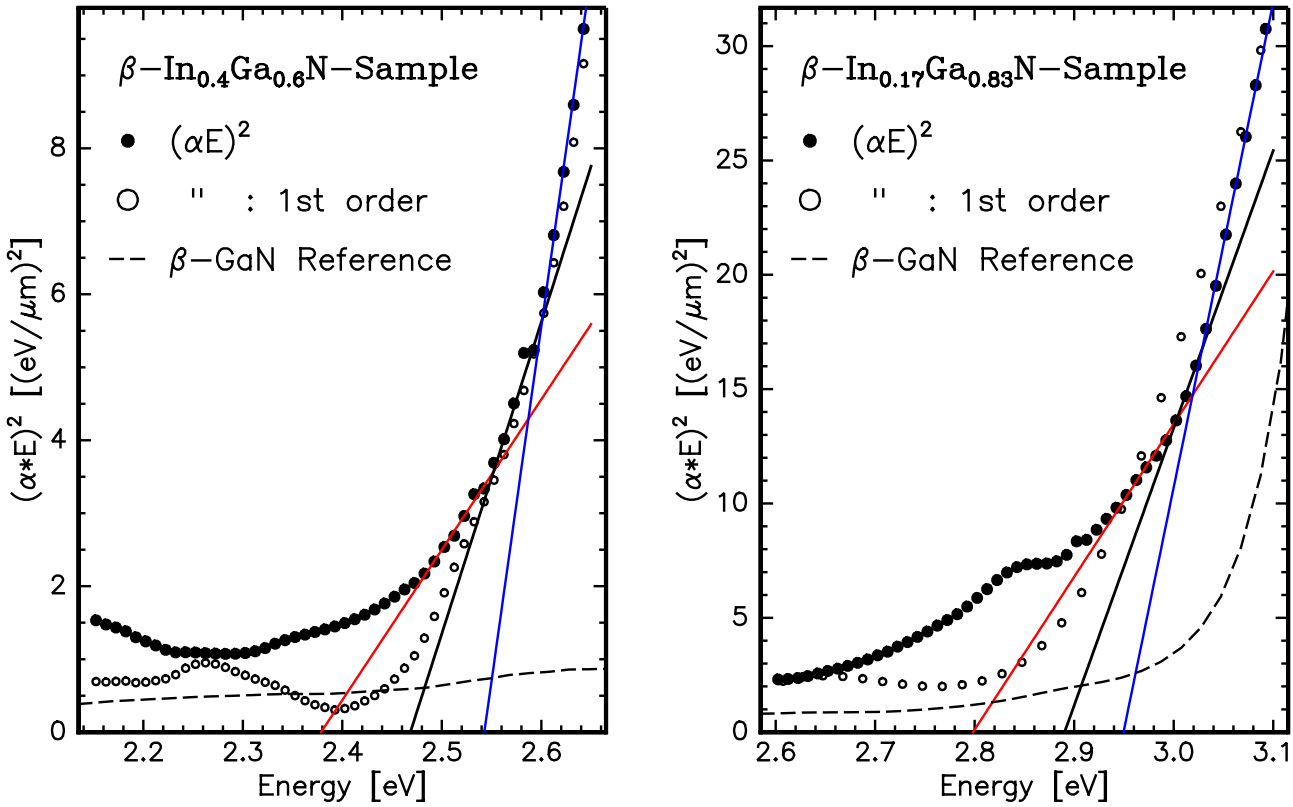
The symbols in *Figs. 8.01,02* show the room temperature transmittance $\mathcal{T}(E)$ and reflectance $\mathcal{R}(E)$ spectra of the In_{0.4}Ga_{0.6}N and In_{0.17}Ga_{0.83}N samples, respectively. As reference, the corresponding data of the β -GaN film #8092 are overlayed (lines). Comparing the two transmittance spectra in *Fig. 8.02*, one perceives that for the In_{0.17}Ga_{0.83}N structure #8027 absorption sets in at about 2.9 eV. The reflectance, however, is dominated by the underlying 400 nm thick β -GaN layer which is of inferior quality than the 690 nm thick reference film. Therefore, no abrupt damping of the oscillations at $E_G(\beta\text{-GaN}) = 3.2$ eV is observed.

In the case of the In_{0.4}Ga_{0.6}N sample #8095, significant absorption takes place already for $E \geq 2.45$ eV as evidenced by the transmittance spectrum in *Fig. 8.01*. In accordance, the corresponding interference fringes of the reflectance exhibit damping at about 2.5 eV. Interestingly, the transmittance spectrum is also markedly damped for $E \leq 2.1$ eV. This rise in absorption may be due to the combined action of low-energy defect bands in the In_xGa_{1-x}N alloy and phase-separated InN. A hint for the existence of such InN inclusions was given by x-ray diffraction in *Fig. 7.04* (page 75).

The sudden disappearance of reflectance oscillations at 3.2 eV for both the reference sample and the structure containing the $\text{In}_{0.4}\text{Ga}_{0.6}\text{N}$ layer indicates a well defined $\beta\text{-Ga}\text{N}$ band gap.



Figs. 8.01,02: Room temperature reflectance and transmittance spectra (symbols) of the $\text{In}_{0.4}\text{Ga}_{0.6}\text{N}$ (left) and $\text{In}_{0.17}\text{Ga}_{0.83}\text{N}$ (right) sample compared to the $\beta\text{-Ga}\text{N}$ reference (lines).



Figs. 8.03,04 : Linearization of $(\alpha E)^2$ to judge the absorption edges of the $\text{In}_{0.4}\text{Ga}_{0.6}\text{N}$ and $\text{In}_{0.17}\text{Ga}_{0.83}\text{N}$ epilayers.

As opposed to the β -GaN reference sample consisting of a single nitride layer, we are now facing the problem of how to analyse the reflectance and transmittance of an (In,Ga,Al)N heterostructure. A rigorous treatment would require the extension of the present theory (chapter 4) to multilayer systems involving the transfer matrix formalism [68]. In principle, the optical constants of one layer can be determined once the complete set of material parameters of all other constituents of the system are known. The task to solve the resulting set of equations, which are considerably more complex than those considered in chapter 4, however, is not only by orders of magnitude more elaborate but also very susceptible to error propagation.

Instead, we try to assess the effective absorption edge of the $\text{In}_x\text{Ga}_{1-x}\text{N}$ layers by applying the method introduced in chapter 4. The heterostructure will be treated as a pseudo-one-layer system having pseudo-optical constants $(\hat{r}, \hat{\alpha})$ which account for the observed behavior of the actual multilayer sample. This crude simplification raises the question as to how meaningful such pseudo-values really are. The reflection coefficient \hat{r} will certainly be strongly affected by the occurrence of the various interfaces in, e.g., the $\text{In}_{0.4}\text{Ga}_{0.6}\text{N}$ sample consisting of 5 nitride layers in total. Due to the variety of ways how light rays can be traced and superposed in such a multilayer system, there is no simple correlation between the roundtrip reflectivity of the individual layers, r_i , and that of the total system, \hat{r} . In contrast, the total absorption coefficient $\hat{\alpha}$ of a stack of layers with thicknesses s_i and individual absorption coefficients α_i may to first order be written as

$$\hat{\alpha} = \frac{\sum_i \alpha_i s_i}{\sum_i s_i}, \quad (8.1)$$

provided that the discontinuities in the refractive indices of adjacent layers, $|n_i - n_{i+1}|$ are not too large.

Treating the two samples under investigation as if they consisted of one effective layer, it is possible to model the observed reflectance and transmittance data with the set of equations (4.22). Whilst focusing on the pseudo-absorption coefficient $\hat{\alpha}$, the values obtained for the pseudo-refractive index \hat{n} and the effective film thickness \hat{s} are briefly mentioned in order to judge their consistency. In the case of the $\text{In}_{0.17}\text{Ga}_{0.83}\text{N}$ sample, the effective thickness is $\hat{s} = 573$ nm and $\hat{n}(2\text{eV}) = 2.6$, corresponding to a total reflection coefficient of $\hat{r} = 0.13$ for the multilayer system. At about 2.85 eV, \hat{r} and \hat{n} are steeply rising and for $3.0 \leq E \leq 3.3$ eV an average pseudo-refractive index of 2.9 is obtained. The analysis of the $\text{In}_{0.4}\text{Ga}_{0.6}\text{N}$ heterostructure yielded low-energy values of $\hat{r} = 0.14$ and $\hat{n} = 2.7$ for an effective film thickness of 810 nm. This time, a pronounced increase in the quantities \hat{r} and \hat{n} is observed at 2.5 eV which assume mean values of 0.19 and 3.1, respectively, in the high-energy range.

The values of \hat{s} are reasonable when comparing them to the real film thicknesses measured by SIMS and electron microscopy (chapter 7). The average pseudo-refractive indices, on the other hand, are somewhat larger than that of the β -GaN reference layer. Such a behavior is to be expected since the absorption edges of the $\text{In}_x\text{Ga}_{1-x}\text{N}$ samples set in at lower energies. Finally, it should be noted that the optimization of $(\hat{s}, \hat{n}_{\text{sub}})$ yielded for both samples an effective boundary value of $\hat{n}_{\text{sub}} = 1.44$, i.e. higher than the refractive index of 1.34 for the UV glue by which the heterostructures were mounted on the sapphire. This larger value accounts for the fact that the discontinuity between the refractive index of the $\text{In}_x\text{Ga}_{1-x}\text{N}$ and the glue layer is virtually graded by the presence of the intermittent GaN epilayer(s).

The effective absorption edges of the $\text{In}_{0.4}\text{Ga}_{0.6}\text{N}$ and the $\text{In}_{0.17}\text{Ga}_{0.83}\text{N}$ layers are visualized in *Figs. 8.03, 04* where $(\hat{\alpha}E)^2$ (symbols) are plotted against the photon energy E and compared to the corresponding values (dashed lines) of the β -GaN reference sample. The filled circles indicate the total absorption coefficient $\hat{\alpha}$ as calculated within the one-layer theory (4.22),

covering multiple reflections and finite coherence effects ($\mathcal{C} = 0.6$). As simple consistency check for the complete set of pseudo-optical constants ($\hat{\alpha}(E), \hat{r}(E), \hat{s}$), the open circles in *Figs. 8.03, 04* show $\hat{\alpha}_1(E)$ deduced from the first-order relation

$$\mathcal{T} = e^{-\hat{\alpha}_1 \hat{s}} (1 - \mathcal{R})^2, \quad (8.2)$$

which is based on the incoherent equations (4.7). The negligence of multiple reflections within the film leads in general to an underestimation of the absorption coefficient and to an overestimation of the reflection coefficient in the sub-band-gap energy range. Further, these first-order quantities are modulated by residual interference oscillations and they converge to the exact solution of the coherent equations (4.10) in the strongly absorbing regime. These phenomena can be seen in *Figs. 8.03, 04* and in particular, it is verified for both samples that $\hat{\alpha}_1$ tends to $\hat{\alpha}$ in the range of strong absorption.

The solid lines in *Figs. 8.03, 04* envisage attempts to determine the absorption edge of the $\text{In}_x\text{Ga}_{1-x}\text{N}$ layers by linearization of $(\hat{\alpha}E)^2$. Evidently, this simple method does not lead to satisfactory results for two reasons: First, the compositional inhomogeneity in the In content leads to a statistical broadening of the mean absorption edge. Second, the material under investigation may intrinsically not behave according to the idealized square-root-density-of-states law even if alloy effects can be neglected. Comparing the available absorption data with the above-mentioned steep rises in the refractive indices \hat{n} at 2.85 and 2.5 eV, respectively, we roughly estimate the effective band gaps $E_G(\beta\text{-In}_{0.17}\text{Ga}_{0.83}\text{N}) = 2.9 \pm 0.04$ eV and $E_G(\beta\text{-In}_{0.4}\text{Ga}_{0.6}\text{N}) = 2.5 \pm 0.04$ eV at 300 K. The same analysis was carried out for the 10 K data leading to similar values within the given accuracy.

8.1.2 Photoluminescence

PL data of the $\text{In}_{0.17}\text{Ga}_{0.83}\text{N}$ layer taken at various temperatures are depicted in *Fig. 8.05*. The maxima of the broad spectra, being distinctly different than those of $\beta\text{-GaN}$, occur at $\lambda = 440 - 450$ nm, i.e. in the blue spectral range. Upon raising the temperature from 5 to 500 K, the overall PL intensity decreases by only 50 % and the high-energy shoulder is becoming more pronounced at the expense of the lower energy transitions. Furthermore, a slight redshift can be observed.

To quantify this behavior, a lineshape analysis is performed. Good agreement is obtained between a model (solid lines) comprising four Gaussians and the experimental data. Usually, low-temperature band edge PL peaks of high quality $\alpha\text{-GaN}$ as well as $\beta\text{-GaN}$ have Lorentzian shape with a Boltzmann tail at the high-energy side, resulting in an asymmetric profile (chapter 5). However, in the case of an alloy subject to statistical compositional fluctuations, Gaussian profiles are to be expected. Even though the peaks overlap significantly, stable least-squares fits are achieved and thus allow an estimation of transition energies (*Tab. 8.1*) within the quoted errors. In comparison, the temperature dependence of the $\beta\text{-GaN}$ band edge transition energy X_C (chapter 5) is added in the last column of *Tab. 8.1*.

The consistency of the $E_0 = 2.9$ eV PL peak with the above absorption data suggests that this transition can be assigned to the band edge of the $\text{In}_{0.17}\text{Ga}_{0.83}\text{N}$ layer. In contrast, a band gap energy of 3.1 eV has been reported for $\alpha\text{-In}_{0.17}\text{Ga}_{0.83}\text{N}$. [100, 129] Note that the thermal redshift $\Delta E := E_0(5\text{ K}) - E_0(500\text{ K})$ of the $\beta\text{-In}_{0.17}\text{Ga}_{0.83}\text{N}$ PL is only 50 meV as opposed to 154 meV for $\beta\text{-GaN}$. Further, the intensity of this transition remains nearly constant over the whole temperature range from 5 to 500 K.

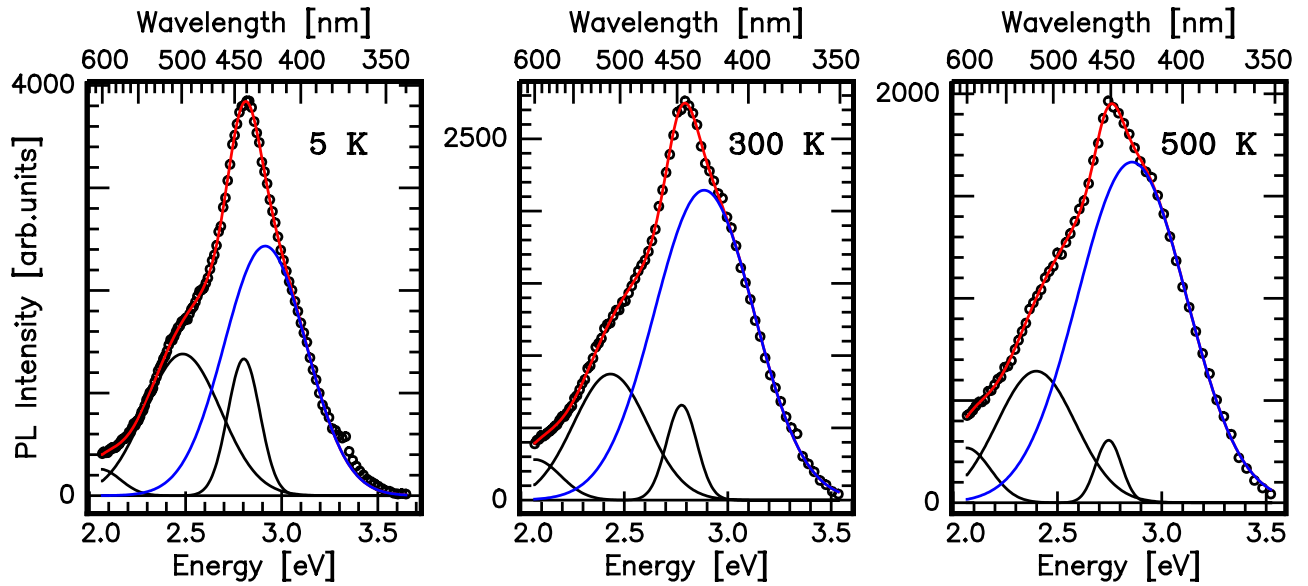


Fig. 8.05 : Photoluminescence spectra (symbols) of the $\text{In}_{0.17}\text{Ga}_{0.83}\text{N}$ sample #8027 as function of temperature. A superposition of 4 Gaussians (lines) is employed to model the data.

T [K]	E_2 [eV]	E_1 [eV]	E_0 [eV]	X_C [eV]
5	2.49 ± 0.02	2.803 ± 0.001	2.91 ± 0.01	3.272
300	2.43 ± 0.01	2.777 ± 0.002	2.89 ± 0.01	3.205
500	2.40 ± 0.01	2.745 ± 0.003	2.86 ± 0.01	3.118
	$\beta\text{-In}_{0.17}\text{Ga}_{0.83}\text{N}$			$\beta\text{-GaN}$

Table 8.1: Temperature dependent PL transition energies of the $\text{In}_{0.17}\text{Ga}_{0.83}\text{N}$ sample compared to the corresponding values of the $\beta\text{-GaN}$ band edge transition X_C .

Fig. 8.06 depicts PL data of the $\text{In}_{0.4}\text{Ga}_{0.6}\text{N}$ sample taken between 4 and 400 K along with the room temperature absorption curve $(\alpha E)^2$, part of which has already been shown in *Fig. 8.03*. For comparison, the 300 K absorption of the $\beta\text{-GaN}$ reference film is also displayed. The emission spectra are clearly dominated by a broad peak at $E_0 \approx 2.45$ eV which is absent in the PL of the reference sample (not shown). Luminescence at energies $E \geq 2.9$ eV stems from the poor quality GaN cap layer (*Fig. 7.05*, page 76).

The overall intensity of the green PL being modulated by interferences is weak but drops by no more than a factor of 4 upon raising the temperature from 4 to 400 K. The correlation of E_0 with the onset of absorption leads to the conclusion that the observed maxima in the PL stem from band edge related transitions in the $\text{In}_{0.4}\text{Ga}_{0.6}\text{N}$ layer. In the case of hexagonal $\text{In}_{0.4}\text{Ga}_{0.6}\text{N}$, a band gap energy of 2.7 eV would be obtained resulting in blue emission. To reach the green spectral range with $\alpha\text{-In}_x\text{Ga}_{1-x}\text{N}$, an In content of about $x = 0.55$ is required.

The two $\beta\text{-In}_x\text{Ga}_{1-x}\text{N}$ layers investigated share not only broad PL peaks and a fairly weak temperature dependence of the transition energies, widths, and intensities. They also have in common that the corresponding (002) Bragg reflexes observed by XRD (*Figs. 7.03, 04*, page 75) suffer from a strong broadening which was in part attributed to an appreciable spread Δx in the In content. These compositional inhomogeneities create spatial potential fluctuations and localized states which have been found to also dominate the emission of $\alpha\text{-In}_x\text{Ga}_{1-x}\text{N}$. [130, 131] Such states in turn give rise to large PL linewidths as well as to intense deep-level emissions.

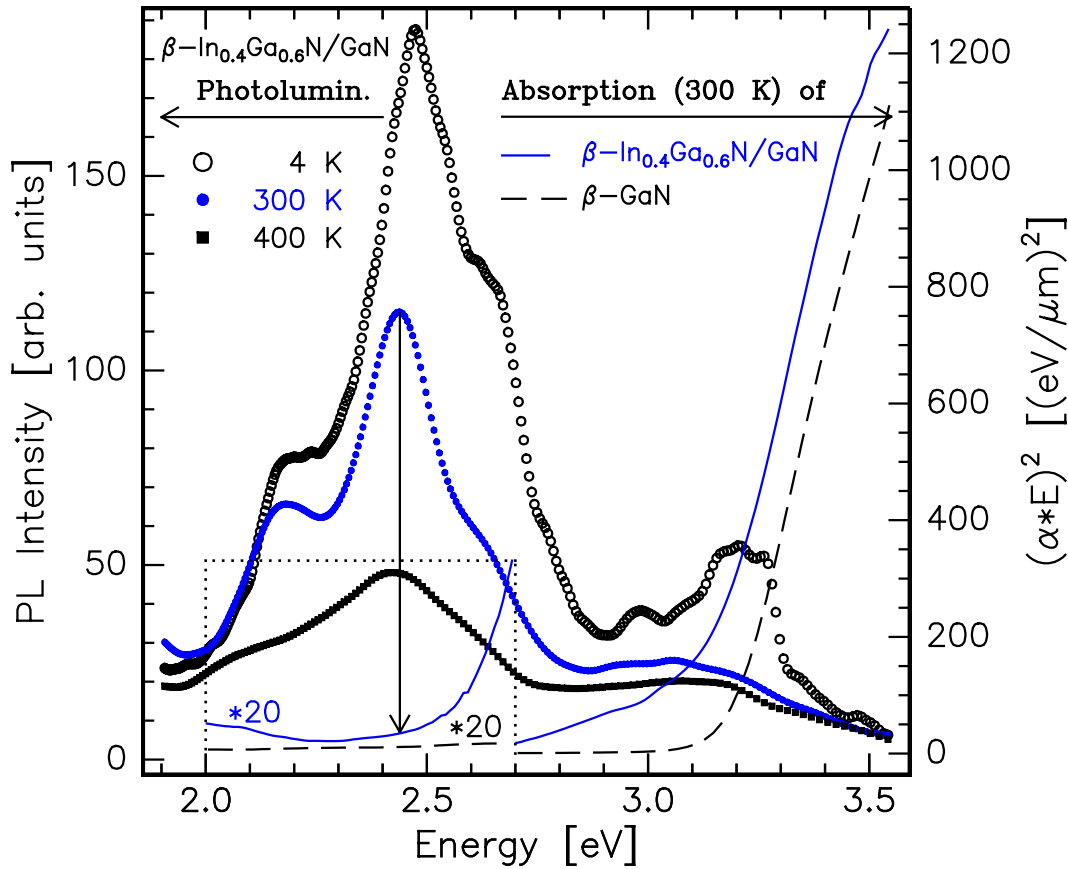


Fig. 8.06: Photoluminescence spectra (symbols) of the $\text{In}_{0.4}\text{Ga}_{0.6}\text{N}$ sample as function of temperature. The solid and broken lines indicate the absorption $(\alpha E)^2$ of the $\text{In}_{0.4}\text{Ga}_{0.6}\text{N}$ layer and the $\beta\text{-GaN}$ reference, respectively. In the inset both absorption spectra are magnified by a factor of 20.

8.1.3 Band Edge Properties of $\beta\text{-In}_x\text{Ga}_{1-x}\text{N}$: Summary

The data acquired on $\beta\text{-In}_x\text{Ga}_{1-x}\text{N}$ samples with In contents ranging between $0 \leq x \leq 0.4$ allows to sketch the compositional dependence of the – so far unknown – band gap $E_G(\beta\text{-In}_x\text{Ga}_{1-x}\text{N})$. In *Fig. 8.07*, the respective low-temperature band gap energies of zincblende and wurtzite $\text{In}_x\text{Ga}_{1-x}\text{N}$ are compared to each other, the latter (dashed line) being firmly established in literature [129].

The data points with $x \leq 0.11$ originate from samples grown with the DC plasma source. [107] Neither reflectance nor ellipsometry measurements carried out on these samples yielded conclusive information on E_G . On the other hand, these $\text{In}_x\text{Ga}_{1-x}\text{N}$ films are too fragile for a substrate removal step being a prerequisite for acquiring their transmittance. Therefore, the band gap energies had to be estimated by means of photoluminescence measurements. Since these samples did not exhibit any measurable PL signal at $T \geq 70$ K, the available room temperature band gap data is limited to the two RF plasma grown films having $x \geq 0.17$.

The open circles in *Fig. 8.07* display the 5 K band edge transition energy E_0 of $\beta\text{-In}_x\text{Ga}_{1-x}\text{N}$ while the solid circles show the corresponding room temperature values which have been substantiated by absorption data as discussed above. The compositional dependence of $E_0(5\text{ K})$ is modelled (solid line) by the parabolic expression

$$E_G(\beta\text{-In}_x\text{Ga}_{1-x}\text{N}) = xE_G(\beta\text{-InN}) + (1-x)E_G(\beta\text{-GaN}) + Bx(x-1), \quad 0 \leq x \leq 1, \quad (8.3)$$

containing the unknown band gap energy of cubic InN, $E_G(\beta\text{-InN})$, and the bowing parameter $B \geq 0$ as adjustable quantities. Reasonable agreement with the data is reached with $E_G(\beta\text{-InN}) = 1.8$ eV and $B = 0.9$ eV, where the bowing obtained is close to the calculated value of 1.02 by Wright *et al.* [109] and the experimental one of 1.05 by Osamura *et al.* [129]. Lacking data points with $x > 0.4$, the extrapolated value for the fundamental absorption edge of $\beta\text{-InN}$ may only be considered as a rough estimate. In comparison, the low-temperature band edge energy of hexagonal InN has been determined from absorption measurements to be $E_G(\alpha\text{-InN}) = 2.05$ eV. [132]

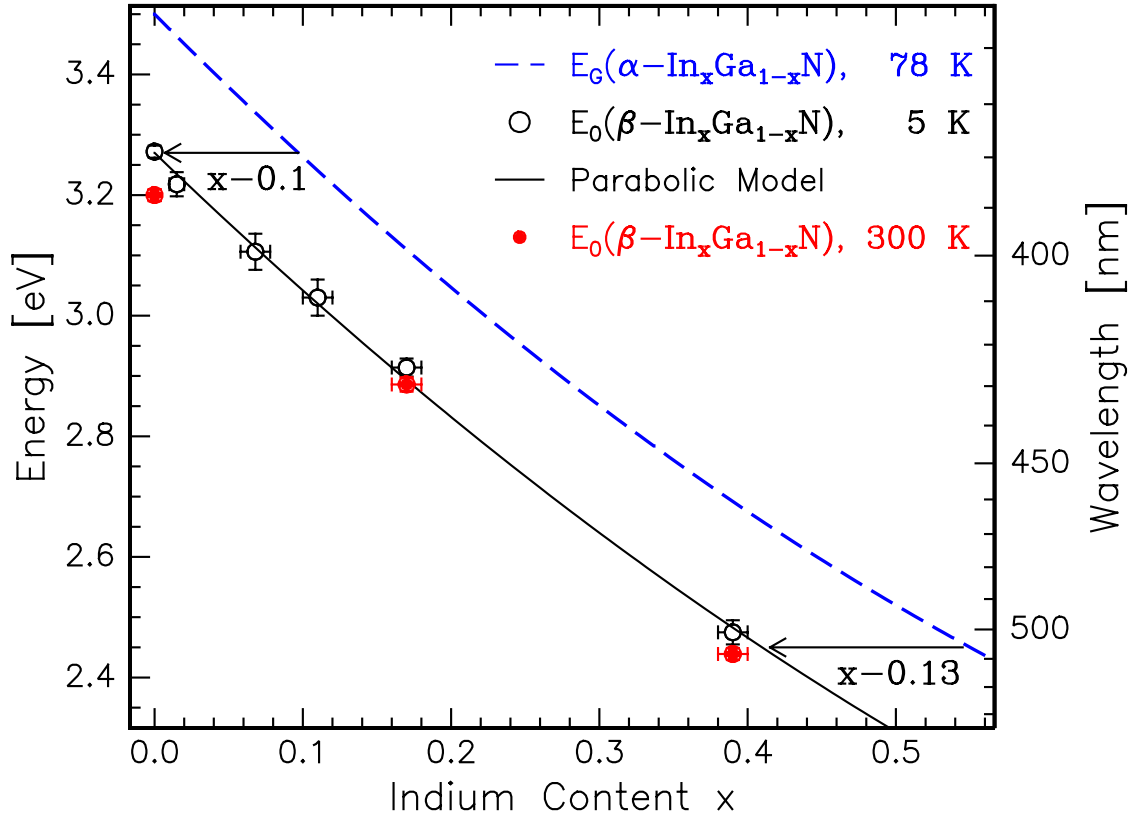


Fig. 8.07: Fundamental band edge of $\beta\text{-In}_x\text{Ga}_{1-x}\text{N}$ compared to $\alpha\text{-In}_x\text{Ga}_{1-x}\text{N}$ (see text).

Even though the entire compositional range of the zincblende alloy could not yet be covered, Fig. 8.07 shows that, at least for $0 \leq x \leq 0.4$,

$$E_G(\beta\text{-In}_x\text{Ga}_{1-x}\text{N}) \approx E_G(\alpha\text{-In}_x\text{Ga}_{1-x}\text{N}) - 0.2 \text{ eV}. \quad (8.4)$$

As a consequence, significantly less In is required by using the cubic phase for reaching the blue – green spectral range. In view of the previously mentioned problems concerning In incorporation the potential advantage of $\beta\text{-In}_x\text{Ga}_{1-x}\text{N}$ for visible light emitters becomes evident.

8.2 $\beta\text{-Al}_x\text{Ga}_{1-x}\text{N}$

The Γ band gap of $\alpha\text{-Al}_x\text{Ga}_{1-x}\text{N}$ is of direct nature over the whole compositional range. [133] In contrast, a *direct* \rightarrow *indirect transition* has been predicted for the lowest band gap of $\beta\text{-Al}_x\text{Ga}_{1-x}\text{N}$ at $x = 0.5$. [127] To date, only little experimental data are available on the electronic properties of $\beta\text{-Al}_x\text{Ga}_{1-x}\text{N}$. In reference [128], the room temperature band edge was estimated from photoluminescence data to depend linearly on the Al content according to $E_G(\beta\text{-Al}_x\text{Ga}_{1-x}\text{N}) = (3.2 + 1.85x)$ eV for $x \leq 0.23$.

The $\beta\text{-Al}_x\text{Ga}_{1-x}\text{N}$ heterostructure treated in the preceeding chapter is not suitable for a precise determination of $E_G(\beta\text{-Al}_x\text{Ga}_{1-x}\text{N})$ due to the inhomogeneity in the Al concentration. Nevertheless, it is important to verify the impact of the Al on the (effective) absorption edge of the alloy. Therefore, reflectance and transmittance measurements were carried out on the $\beta\text{-Al}_x\text{Ga}_{1-x}\text{N}$ film mounted face-down on quartz by means of optical UV-glue as described in chapter 4. The corresponding spectra are compared to those of the $\beta\text{-GaN}$ reference sample in Fig. 8.08.

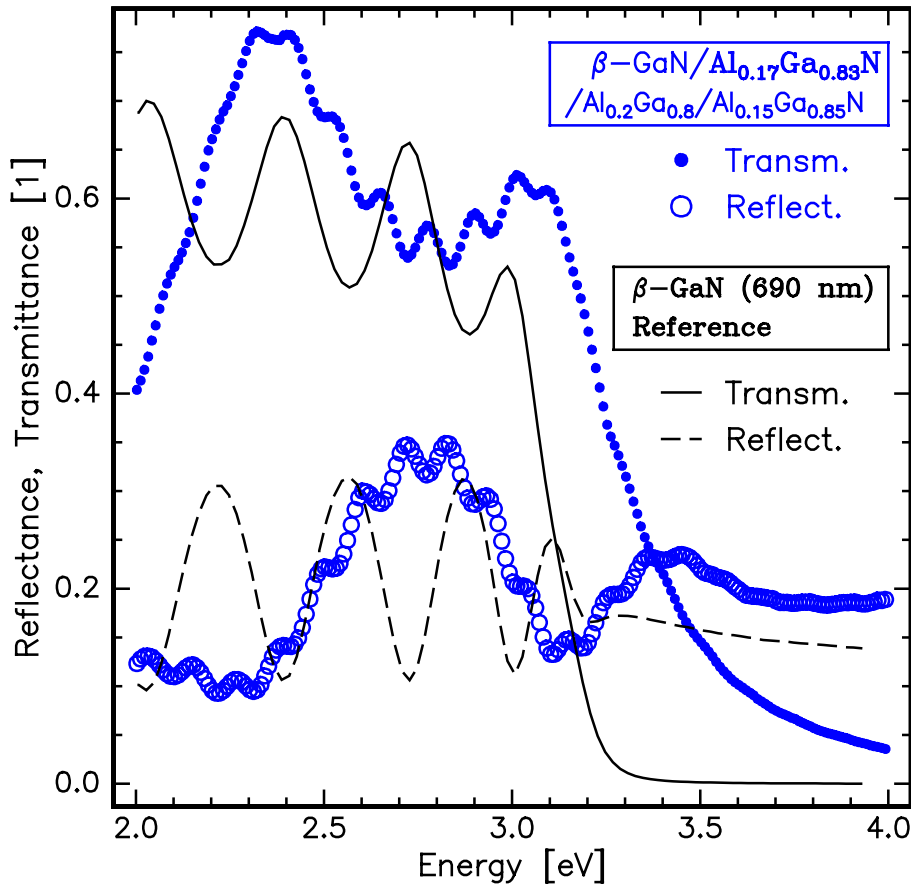


Fig. 8.08: Room temperature reflectance and transmittance spectra (symbols) of the $\beta\text{-GaN}/\text{Al}_{0.17}\text{Ga}_{0.83}\text{N}/\text{Al}_{0.2}\text{Ga}_{0.8}\text{N}/\text{Al}_{0.15}\text{Ga}_{0.85}\text{N}$ test structure compared to the $\beta\text{-GaN}$ reference (lines).

As opposed to all \mathcal{R} and \mathcal{T} data shown so far, the spectra of the 220 nm thick $\beta\text{-Al}_x\text{Ga}_{1-x}\text{N}$ sample are modulated by a short-period signal which is attributed to interference phenomena occuring in the glue layer. The long-period interference fringes, on the other hand, are consistent with the samples' thickness assuming a pseudo-refractive index of the order of 2.5. It

is apparent that the effective absorption edge of the heterostructure is shifted towards higher energies relative to the β -GaN reference. Considering the quenching of the modulations in the reflectance, an effective band gap of 3.6 ± 0.05 eV is estimated. In comparison, a value of 3.51 eV is obtained for the PL band gap of an alloy with $x = 0.17$ when applying the cited linear relation. [128]

Chapter 9

Summary and Outlook

The present work focuses on MBE growth, microstructure, and optical properties of the metastable zincblende (β) (In,Ga,Al)N system on GaAs(001). Due to their higher crystal symmetry, these cubic nitrides are expected to be intrinsically superior for (opto-)electronic applications than the widely employed wurtzite (α) counterparts. Confronted with the unavailability of a suitable substrate required for epitaxial stabilization, however, the debate is on whether these compounds can be prepared at all in sufficient quality such that the potential advantages of the zincblende lattice come into play. Due to the difficulties of obtaining single-phase crystals, many material constants of both fundamental interest and technological relevance are essentially unknown for the cubic nitrides.

The aim of this work was therefore twofold: First, to determine the basic optical and electronic properties of β -GaN and to shed some light on β -In_xGa_{1-x}N. Second, to push the technological limits of synthesizing device-relevant zincblende (In,Ga,Al)N heterostructures in a new, custom-designed MBE machine. One major achievement was the reproducible nucleation of smooth, monocrystalline β -GaN layers on GaAs using a high-nitrogen-flow RF plasma source. The optimization of a growth process for thick β -GaN layers with respect to phase purity and surface morphology has then opened the way for the synthesis of ternary β -(Ga,In,Al)N structures.

While the optical properties of wurtzite GaN are quite well established, a paucity of information prevails on the zincblende pendant. In order to fill this gap, temperature dependent reflectance and transmittance measurements were carried out on a monocrystalline β -GaN film grown with the RF plasma. On the basis of the theory for a stratified medium, a numerical method was developed which allows to extract from these data the complete set of optical constants for photon energies covering the transparent as well as the strongly absorbing spectral range (2.0 – 3.8 eV). Finite coherence effects due to interfacial roughness and inhomogeneities in the refractive index were elucidated and quantitatively analyzed by means of Monte Carlo simulations. The fundamental band gap $E_G(T)$ of β -GaN was determined for $5 \leq T \leq 300$ K and the room temperature density of states was investigated.

On the emission side, systematic studies of the band edge photoluminescence in terms of transition energies, lineshapes, linewidths, and intensities were carried out for both α - and β -GaN as a function of temperature. Average phonon energies and coupling constants, activation energies for thermal broadening and quenching were determined. In order to study the impact of nonradiative recombination processes, excitation density dependent PL measurements were carried out on cubic and hexagonal GaN microcrystals at 300 K. A recombination model was applied to estimate the internal quantum efficiency, the (non)radiative lifetimes, as

well as the ratio of the electron to hole capture coefficients for both polytypes. It is seen that the dominant nonradiative centers in the n-type material investigated act as hole traps which, however, can be saturated at already modest carrier injection rates.

It appears as if the abundant structural defects like stacking faults and dislocations are optically almost inert in both phases of GaN as opposed to other III-V compounds which are less ionic in bonding. An interesting finding is that the radiative centers, causing unwanted yellow luminescence, are less competitive to the band edge recombination in the case of zincblende GaN as compared to wurtzite at $T > 100$ K. In conclusion, despite large defect densities in β -GaN due to highly mismatched heteroepitaxy on GaAs, band edge luminescence was observed up to 500 K with intensities comparable to those of state-of-the-art α -GaN.

$\text{In}_x\text{Ga}_{1-x}\text{N}$ plays a key role in short wavelength light emitters. The growth of high-quality material with large x , however, is a challenging task due to the miscibility gap between GaN and InN in thermodynamic equilibrium and the weakness of the In-N bond as compared to the Ga-N bond. Currently, α - $\text{In}_x\text{Ga}_{1-x}\text{N}$ based blue-green light emitting diodes having In contents $0.3 \leq x \leq 0.5$ are commercially available while, in contrast, scarcely any data on β - $\text{In}_x\text{Ga}_{1-x}\text{N}$ are found in literature.

In order to investigate the optical as well as the structural properties of β - $\text{In}_x\text{Ga}_{1-x}\text{N}$, thick films with high In contents were grown on β -GaN templates. Blue and green photoluminescence were obtained at room temperature and above for In mole fractions of 0.17 and 0.4, respectively. Since this PL exhibits a large inhomogeneous broadening but a rather weak thermal dependence of peak energies, homogeneous linewidths, and intensities, it is assigned to transitions between localized states caused by compositional inhomogeneities. Transmittance and reflectance measurements reveal this luminescence to be band edge related. It is found that the apparent band edge of the cubic alloy is smaller by about 0.2 eV than that of the hexagonal polytype for the In contents $0 \leq x \leq 0.4$ considered. To the best of our knowledge, these optical data are the first published on β - $\text{In}_x\text{Ga}_{1-x}\text{N}$.

Apart from bulk-like β - $\text{In}_x\text{Ga}_{1-x}\text{N}$ films, the first coherently strained β - $\text{In}_x\text{Ga}_{1-x}\text{N}/\text{GaN}$ (multi) quantum wells with In contents as high as 50% and abrupt interfaces could be grown by RF plasma assisted MBE. This is an exciting result since it does not only show that by means of a nonequilibrium growth technique, a ternary alloy can be synthesized in a metastable crystal structure far beyond the miscibility limit of its binary constituents. In addition, $\text{In}_x\text{Ga}_{1-x}\text{N}/\text{GaN}$ interfaces with roughnesses of the order of 1 nm were achieved despite the handicap of highly lattice mismatched heteroepitaxy. Furthermore, the quantum wells are considerably strained. The well widths of these structures range between 4 and 7 nm and are thus beyond the theoretically expected critical thickness for the strain values observed. Since no indications of phase separation were found by HRTEM, it is to be expected that even higher In contents can be reached for film thicknesses below 5 nm. The potential application of such β - $\text{In}_x\text{Ga}_{1-x}\text{N}/\text{GaN}$ multi quantum wells with $x \geq 0.4$ would thus be diode lasers operating in the green-yellow range.

9.1 What we don't know about cubic nitrides

Despite their immaturity, promising results were achieved with zincblende group-III nitrides which make these compounds attractive for future (opto-)electronic device applications. Nevertheless, numerous issues are yet to be addressed before the first zincblende-based green laser is obtained that can compete with or even surpass the performance of devices based on alternative material systems (II-VI, wurtzite nitrides).

At first, the structural quality of cubic nitrides is to be further improved where special attention has to be paid to a reduction of defect densities right at the substrate interface. Systematic studies are necessary comparing the currently available cubic substrates under the aspects of heteroepitaxy as well as regarding device issues such as vertical transport, thermal mismatch, heat conductivity, and processing.

Not much is currently known about doping, impurity diffusion, and the (low-dimensional) transport properties of the zincblende (In,Ga,Al)N material system. Even such an important quantity as the hole mass of β -GaN is not yet established. Since so far, the intrinsic properties of the cubic nitrides are quite often masked by exceedingly large defect densities, it is not clear yet to which extent advantage can be taken of the higher crystal symmetry of these new materials as compared to their hexagonal counterparts.

A particular appealing topic for heterostructures is the quaternary β -In_xAl_yGa_{1-x-y}N system since it offers by the additional degree of freedom the prospect to tailor both the band gap and the lattice constant. The potential application of such an alloy would be as wide band gap barrier material for strained In_xGa_{1-x}N quantum wells being lattice-matched to GaN or Al_xGa_{1-x}N. To date, no reports exist on this promising quaternary compound.

The optical constants of β -In_xGa_{1-x}N presented herein are only the first few steps on a long walk towards a complete database of fundamental as well as device relevant material properties. Even if the structural quality of the constituent epilayers of a laser is in principle sufficient and the know-how and technology for tailoring the electronic and electrical properties is available, a smart device design is needed to reach the required carrier and photon confinement. Among the indispensable quantities for optimizing such a device structure are the refractive indices and the band gaps of the individual layers.

Bibliography

- [1] W. Seifert, A. Tempel, Kristall und Technik **9**(11), 1213-1221 (1974).
- [2] B. Baranov, L. Däweritz, V.B. Gutan, G. Junk, H. Neumann, H. Raidt, Phys. Stat. Sol. **A49**, 629 (1978).
- [3] M. Mizuta, S. Fujieda, Y. Matsumoto, T. Kawamura, Jpn. J. Appl. Phys. **25**, L945-L948 (1986).
- [4] M.J. Paisley, Z. Sitar, J.B. Posthill, R.F. Davis, J. Vac. Sci. Technol. A **7**, 701 (1989).
- [5] I. Petrov, E. Mojab, R.C. Powell, J.E. Greene, L. Hultman, J.-E. Sundgren, Appl. Phys. Lett. **60**, 2491 (1992).
- [6] S. Strite, D. Chandrasekhar, D.J. Smith, J. Sariel, H. Chen, H. Morkoç, J. Cryst. Growth **127**, 204 (1993).
- [7] C.R. Abernathy, J.D. MacKenzie, S.E. Bharatan, K.S. Jones, S.J. Pearton Appl. Phys. Lett. **66**, 1632 (1995).
- [8] W.-T. Lin, L.-C. Meng, G.-J. Chen, H.-S. Liu, Appl. Phys. Lett. **66**, 2066 (1995).
- [9] M. Suzuki, T. Uenoyama, J. Appl. Phys. **80**, 6868 (1996).
- [10] M. Nido, Jpn. J. Appl. Phys. **34**, L1513 (1995).
- [11] D. Ahn, S.-H. Park, Appl. Phys. Lett. **69**, 3303 (1996).
- [12] M. Fanciulli, T. Lei, T.D. Moustakas, Phys. Rev. B **48**, 15144 (1993).
- [13] T. Lei, T.D. Moustakas, R.J. Graham, Y. He, S.J. Berkowitz, J. Appl. Phys. **71**, 4933 (1992).
- [14] M.E. Lin, G. Xue, G.L. Zhou, J.E. Greene, H. Morkoç, Appl. Phys. Lett. **63**, 932 (1993).
- [15] P. Das and D.K. Ferry, Sol. State Electron. **19**, 851 (1976).
- [16] S. Strite, J. Ruan, Z. Li, A. Salvador, H. Chen, D.J. Smith W.J. Choyke, H. Morkoç, J. Vac. Sci. Technol. B **9**, 1924 (1991).
- [17] H. Okumura, S. Misawa, S. Yoshida, Appl. Phys. Lett. **59**, 1058 (1991).
- [18] R.C. Powell, N.-E. Lee, Y.-W. Kim, J.E. Greene, J. Appl. Phys. **73**, 189 (1993).
- [19] H. Okumura, S. Yoshida, T. Okahisa, Appl. Phys. Lett. **64**, 2997 (1994).

- [20] G. Ramírez-Flores, H. Navarro-Contreras, A. Lastras-Martínez, Phys. Rev. B **50**, 8433 (1994).
- [21] D.E. Lacklison, J.W. Orton, I. Harrison, T.S. Cheng, L.C. Jenkins, C.T. Foxon, S.E. Hooper, J. Appl. Phys. **78**, 1838 (1995).
- [22] S. Logothetidis, J. Petalas, M. Cardona, T.D. Moustakas, Mater. Sci. Eng. B **29**, 65 (1995).
- [23] C.G. Van de Walle, J. Neugebauer, Appl. Phys. Lett. **70**, 2577 (1997).
- [24] B. Gil, F. Hamdani, H. Morkoç, Phys. Rev. B **54**, 7678 (1996).
- [25] S. Chichibu, A. Shikanai, T. Azuhata, T. Sota, A. Kuramata, K. Horino, S. Nakamura, Appl. Phys. Lett. **68**, 3766 (1996).
- [26] I.A. Buyanova, J.P. Bergman, B. Monemar, H. Amano, I. Akasaki, Appl. Phys. Lett. **69**, 1255 (1996).
- [27] A. Shikanai, T. Azuhata, T. Sota, S. Chichibu, A. Kuramata, K. Horino, S. Nakamura, J. Appl. Phys. **81**, 417 (1997).
- [28] *Structural Data of the Elements and Intermetallic Phases* edited by K.H. Hellwege and A.H. Hellwege, Landolt-Börnstein, New Series, Vols. **6**, **17a**, **17b** (Springer Verlag, Berlin, 1971).
- [29] P. Lawaetz, Phys. Rev. B **5**, 4039 (1972).
- [30] J.A. Van Vechten, Phys. Rev. **182**, 891 (1969), *ibid.* **187**, 1007 (1969).
- [31] J.C. Phillips, Rev. Mod. Phys. **42**, 317 (1970).
- [32] F. Keffer, A.M. Portis, J. Chem. Phys. **27**, 675 (1957).
- [33] Y.M. Rumyantsev, F.A. Kuznetsov, S.A. Stroitelve, Kristallografiya **10**, 263 (1965).
- [34] V.A. Federov, V.A. Ganshin, Y.N. Korkishko, Phys. Status Solidi A **126**, K5 (1991).
- [35] R. Rapoport, C.W. Pistorius, Phys. Rev. **172**, 838 (1968).
- [36] J.A. Van Vechten, J.C. Phillips, Phys. Rev. B **2**, 2160 (1970).
- [37] K. Hübner, G. Kühn, Kristall und Technik **7**, 1185 (1972).
- [38] C.-Y. Yeh, Z.W. Lu, S. Froyen, A. Zunger, Phys. Rev. B **46**, 10086 (1992).
- [39] W.M. Kim, E.J. Stofko, J. Electrochem. Soc. Solid-State Science Technol. **119**, 381 (1972).
- [40] H. Luo, N. Samarth, F.C. Zhang, A. Pareek, M. Dobrowolska, J.K. Furdyna, K. Mahalingam, N. Otsuka, W.C. Chou, A. Petrou, S.B. Qadri, Appl. Phys. Lett. **54**, 1783 (1991).

- [41] N. Samarth, H. Luo, J.K. Furdyna, S.B. Qadri, Y.R. Lee, A.K. Ramadas, N. Otsuka Appl. Phys. Lett. **54**, 2680 (1991).
- [42] S. Froyen, S.-H. Wei, A. Zunger, Phys. Rev. B **38**, 10124 (1988).
- [43] T. Lei, M. Fanciulli, R.J. Molnar, T.D. Moustakas, R.J. Graham, J. Scanion, Appl. Phys. Lett. **59**, 944 (1991).
- [44] T.D. Moustakas, T. Lei, R.J. Molnar Physica B **185**, 36 (1993).
- [45] *Semiconductors: Intrinsic Properties of Group IV Elements and III-V, II-VI and I-VII Compounds*, edited by O. Madelung, W. van der Osten, U. Rössler, Landolt Börnstein, New Series III, **22a** (Springer, Berlin, 1987).
- [46] A. Trampert, O. Brandt, H. Yang, K.H. Ploog, Appl. Phys. Lett. **70**, 583 (1997).
- [47] J.W. Yang, J.N. Kuznia, Q.C. Chen, M.A. Khan, T. George, M. De Graef, S. Mahajan Appl. Phys. Lett. **67**, 3759 (1995).
- [48] X.W. Lin, M. Behar, R. Maltez, W. Swider, Z. Lilienthal-Weber, J. Washburn, Appl. Phys. Lett. **67**, 2699 (1995).
- [49] T. Makimoto, N. Kobayashi, Appl. Phys. Lett. **67**, 548 (1995).
- [50] M.E. Jones, J.R. Shealy, J.R. Engstrom, Appl. Phys. Lett. **67**, 542 (1995).
- [51] R.J. Hauenstein, D.A. Collins, X.P. Chai, M.L. O'Steen, T.C. McGill, Appl. Phys. Lett. **66**, 2861 (1995).
- [52] S. Gwo, H. Tokumoto, S. Miwa, Appl. Phys. Lett. **71**, 362 (1997).
- [53] A. Masuda, Y. Yonezawa, A. Morimoto, T. Shimizu, Jpn. J. Appl. Phys. **34**, 1075 (1995).
- [54] M. Sato, J. Appl. Phys. **78**, 2123 (1995).
- [55] H. Yang, O. Brandt, K. Ploog, Phys. Stat. Sol. (b) **194**, 109 (1996).
- [56] O. Brandt, H. Yang, A. Trampert, M. Wassermeier, K.H. Ploog, Appl. Phys. Lett. **71**, 473 (1997).
- [57] J. Menniger, U. Jahn, O. Brandt, H. Yang, K. Ploog, Phys. Rev. B **53**, 1881 (1996).
- [58] O. Brandt, H. Yang, J.R. Müllhäuser, A. Trampert, K.H. Ploog, Mat. Sci. Eng. B **43**, 215 (1997).
- [59] T.S. Cheng, L.C. Jenkins, S.E. Hooper, C.T. Foxon, J.W. Orton, D.E. Lacklison, Appl. Phys. Lett. **66**, 1509 (1995).
- [60] Y. Qiu, A. Nikishin, H. Temkin, V.A. Elyukhin, Y.A. Kudriavtsev, Appl. Phys. Lett. **70**, 2831 (1997).
- [61] H. Yang, O. Brandt, M. Wassermeier, J. Behrend, H.P. Schönherr, K.H. Ploog, Appl. Phys. Lett. **68**, 244 (1996).

- [62] O. Brandt, H. Yang, B. Jenichen, Y. Suzuki, L. Däweritz, K.H. Ploog, Phys. Rev. B **52**, R2253 (1995).
- [63] O. Brandt, H. Yang, K.H. Ploog, Phys. Rev. B **54**, 4432 (1996).
- [64] S. Logothetidis, J. Petalas, M. Cardona, T.D. Moustakas, Phys. Rev. B **50**, 18017 (1994).
- [65] T. Wethkamp, K. Wilmers, C. Cobet, N. Esser, W. Richter, O. Ambacher, O. Brandt, J.R. Müllhäuser, K.H. Ploog, M. Cardona To be published in Mat. Sci. Eng. B. (1998).
- [66] M.A. Vidal, G. Ramírez-Flores, H. Navarro-Contreras, P.C. Powell, J.E. Greene, Appl. Phys. Lett. **68**, 441 (1996).
- [67] A. Billeb, W. Grieshaber, D. Stocker, E.F. Schubert, R.F. Karlicek, Appl. Phys. Lett. **70**, 2790 (1997).
- [68] O.S. Heavens, *Optical Properties of Thin Solid Films*, Butterworths Scientific Publications (London, 1955).
- [69] R.M.A. Azzam, N.M. Bashra, *Ellipsometry and polarized light*, North-Holland Publishing Company (Amsterdam, 1976).
- [70] P.Y. Yu, M. Cardona, *Fundamentals of Semiconductors*, Springer-Verlag (Berlin, Heidelberg, New York 1996).
- [71] R. Schulze, Phys. Zeit. **34**, 24 (1933).
- [72] F. Goos, Z. Phys. **106**, 606 (1937).
- [73] D. Malé, C.R. Acad. Sci. Paris **230**, 286 (1950).
- [74] M. Garnett, J.C. Phil. Trans. **203**, 385 (1904); *ibid* **205**, 237 (1906).
- [75] H. Schopper, Z. Phys. **130**, 565 (1951).
- [76] E. David, Z. Phys. **114**, 389 (1939).
- [77] T.S. Moss, T.D.F. Hawkins, Infrared Phys. **1**, 111 (1961).
- [78] K.P. O'Donnell, X. Chen, Appl. Phys. Lett. **58**, 2924 (1991).
- [79] K.P. Korona, A. Wysmolek, K. Pakula, R. Stepniewski, J.M. Baranowski, I. Grzegory, B. Lucznik, M. Wroblewski, S. Porowski, Appl. Phys. Lett. **69**, 788 (1996).
- [80] A.J. Fischer, W. Shan, J.J. Song, Y.C. Chang, R. Horning, B. Goldenberg, Appl. Phys. Lett. **71**, 1981 (1997).
- [81] G. Ramírez-Flores, H. Navarro-Contreras, A. Lastras-Martínez, R.C. Powell, J.E. Greene, Phys. Rev. B **50**, 8433 (1994).
- [82] J. Petalas, S. Logothetidis, S. Bouladakis, M. Alouani, J.M. Wills, Phys. Rev. B **52**, 8082 (1995).

- [83] S. Nakamura, M. Senoh, S. Nagahama, N. Iwasa, T. Yamada, T. Matsushita, H. Kiyoku, Y. Sugimoto, T. Kozaki, U. Umemoto, M. Sano, K. Chocho, Jpn. J. Appl. Phys. **39**, L1568 (1997).
- [84] S. Chichibu, T. Azuhata, T. Sota, S. Nakamura, J. Appl. Phys. **79**, 2784 (1996).
- [85] M. Shinada, S. Sugano, J. Phys. Soc. Jpn. **21**, 1936 (1966).
- [86] D. Bimberg, M. Sondergeld, E. Grobe, Phys. Rev. B **4**, 3451 (1971).
- [87] H. Barry, E.W. Williams in *Semiconductors and Semimetals*, Vol. 8, pp. 227–241, edited by R.K. Willardson and A.C. Beer (Academic Press, New York, 1972).
- [88] M. Steube, K. Reimann, D. Fröhlich, S.J. Clarke, Appl. Phys. Lett. **71**, 948 (1997).
- [89] K. Reimann, private communication.
- [90] O. Brandt, K. Kanamoto, M. Gotoda, T. Isu, N. Tsukuda, Phys. Rev. B **51**, 7029 (1995).
- [91] W. Shockley, W.T. Read, Phys. Rev. **87**, 835 (1952).
- [92] R.N. Hall, Proc. Institut. Electric. Eng. **106B**, Suppl. No. 17, 923 (1959).
- [93] O. Brandt, H. Yang, K.H. Ploog, Phys. Rev. B **54**, R5215 (1996).
- [94] B. Monemar, Phys. Rev. B **10**, 676 (1974).
- [95] T.L. Tansley, C.P. Foley J. Appl. Phys. **59**, 3241 (1986).
- [96] S. Nakamura, M. Senoh, S. Nagahama, N. Iwasa, T. Yamada, T. Matsushita, Y. Sugimoto, H. Kiyoku, Appl. Phys. Lett. **69**, 3034 (1996).
- [97] S. Nakamura and T. Mukai, Jpn. J. Appl. Phys. **31**, L1457 (1992).
- [98] E.L. Piner, M.K. Behbehani, N.A. El-Masry, F.G. McIntosh, J.C. Roberts, K.S. Boutros, S.M. Bedair, Appl. Phys. Lett. **70**, 461 (1997).
- [99] I. Ho and G.B. Stringfellow, Appl. Phys. Lett. **69**, 2701 (1996).
- [100] K. Osamura, S. Naka, Y. Murakami, J. Appl. Phys. **46**, 3432 (1975).
- [101] A. Wakahara, T. Tokuda, X.-Z. Dang, S. Noda, A. Sasaki, Appl. Phys. Lett. **71**, 906 (1997).
- [102] R. Singh, D. Doppalapudi, T.D. Moustakas, Appl. Phys. Lett. **69**, 2388 (1996).
- [103] R. Singh, D. Doppalapudi, T.D. Moustakas, L.T. Romano, Appl. Phys. Lett. **70**, 1089 (1997).
- [104] T. Matsusoka, N. Yoshimoto, T. Sasaki, A. Katsui, J. Electron. Mater. **21**, 157 (1992).
- [105] M. Shimizu, K. Hiramatsu, N. Sawaki, J. Cryst. Growth **145**, 209 (1994).
- [106] K.S. Boutros, F.G. McIntosh, J.C. Roberts, S.M. Bedair, E.L. Piner, N.A. El-Masry, Appl. Phys. Lett. **67**, 1856 (1995).

- [107] B. Yang, O. Brandt, B. Jenichen, J.R. Müllhäuser, K.H. Ploog, J. Appl. Phys. **82**, 1918 (1997).
- [108] S. Nakamura and G. Fasol, *The blue laser diode*, (Springer, Berlin, 1997), pp. 200-215.
- [109] A.F. Wright, J.S. Nelson, Appl. Phys. Lett. **66**, 3051 (1995).
- [110] L.C. Jenkins, T.S. Cheng, C.T. Foxon, S.E. Hooper, J.W. Orton, S.V. Novikov, V.V. Tret'yakov, J. Vac. Sci. Technol. B **13**, 1585 (1995).
- [111] C.R. Abernathy, J.D. MacKenzie, S.E. Bharatan, K.S. Jones, S.J. Pearton, Appl. Phys. Lett. **66**, 1632 (1995).
- [112] C.R. Abernathy, J.D. MacKenzie, S.R. Bharatan, K.S. Jones, S.J. Pearton, J. Vac. Sci. Technol. A **13**, 716 (1995).
- [113] J.R. Müllhäuser, B. Jenichen, M. Wassermeier, O. Brandt, K.H. Ploog, Appl. Phys. Lett. **71**, 909 (1997).
- [114] J.R. Müllhäuser, O. Brandt, A. Trampert, B. Jenichen, K.H. Ploog, Appl. Phys. Lett. **73**, 1230 (1998).
- [115] J. Portmann, R. Brenn, University and Materials Research Center of Freiburg, private communication.
- [116] J. Menniger, U. Jahn, O. Brandt, Paul-Drude-Institute Berlin, private communication.
- [117] D. Chandrasekhar, D.J. Smith, S. Strite, M.E. Lin, H. Morkoç, J. Cryst. Growth **152**, 135 (1995).
- [118] J.C. Bean, L.C. Feldman, A.T. Fiory, S. Nakahara, I.K. Robinson, J. Vac. Sci. Technol. A **2**, 436 (1984).
- [119] J.Y. Tsao, B.W. Dodson, S.T. Picraux, D.M. Cornelison, Phys. Rev. Lett. **59**, 2455 (1987).
- [120] I.J. Fritz, S.T. Picraux, L.R. Dawson, T.J. Drummond, W.D. Laidig, N.G. Anderson, Appl. Phys. Lett. **46**, 967 (1985).
- [121] T.G. Andersson, Z.G. Chen, V.D. Kulakovskii, A. Uddin, J.T. Vallin, Appl. Phys. Lett. **51**, 752 (1987).
- [122] P.L. Gourley, I.J. Fritz, L.R. Dawson, Appl. Phys. Lett. **52**, 377 (1988).
- [123] Z. Sitar, M.J. Paisley, B. Yan, J. Ruan, W.J. Choyke, R.F. Davis, J. Vac. Sci. Technol. B **8**, 316 (1990).
- [124] A.S. Bykhovsky, B.L. Gelmont, M.S. Shur, Appl. Phys. Lett. **78**, 3691 (1995).
- [125] V.Y. Karasev, N.A. Kiselev, E.V. Orlova, M.A. Gribelyuk, A.K. Gutakovsky, Y.O. Kanter, S.M. Pintus, S.V. Rubanov, S.I. Stenin, A.A. Federov, Ultramicroscopy **35**, 11 (1991).
- [126] M.E. Sherwin, T.J. Drummond, J. Appl. Phys. **69**, 8423 (1991).

- [127] A.F. Wright, J.S. Nelson, Phys. Rev. B **51**, 7866 (1995).
- [128] A. Nakadaira, H. Tanaka, Appl. Phys. Lett. **70**, 2720 (1997).
- [129] K. Osamura, K. Nakajima, Y. Murakami, P.H. Shingu, A. Ohtsuki, Solid State Comm. **11**, 617 (1972).
- [130] C.I. Harris, B. Monemar, H. Amano, I. Akasaki, Appl. Phys. Lett. **67**, 840 (1995).
- [131] S. Chichibu, T. Azuhata, T. Sota, S. Nakamura, Appl. Phys. Lett. **70**, 2822 (1997).
- [132] K. Osamura, S. Naka, Y. Murakami, J. Appl. Phys. **46**, 3432 (1975).
- [133] O. Ambacher, M. Arzberger, D. Brunner, H. Angerer, F. Freudenberg, N. Esser, T. Wethkamp, K. Wilmers, W. Richter, M. Stutzmann, MRS Internet Journal of Nitride Semiconductor Research **2**, Article 22 (1997).
- [AT] TEM measurement by A. Trampert
- [MW] AFM measurement by M. Wassermeier
- [IP] SEM measurement by I. Poppe
- [UJ] SEM measurement by U. Jahn

List of Tables

1.1	History of zincblende group-III nitrides	2
1.2	Reported values for the direct band gap of β -GaN	3
2.1	Calculated structural energy differences per atom between wurtzite and zincblende phase and measured relaxation parameter of the wurtzite structure. [38]	6
2.2	Room temperature properties of prospective cubic (001) substrates for zincblende GaN [45]	8
4.1	Model parameters for $\bar{n}^2(E)$ of β -GaN at 300 K.	35
4.2	Model parameters for $n^2(E)$ of β -GaN at 10 K.	38
4.3	Model parameters for the temperature dependent band gap energy of β -GaN.	41
5.1	Model parameters for the temperature dependent band edge transition energies of α - and β -GaN.	52
5.2	Model parameters for the temperature dependent band edge transition widths of α - and β -GaN.	54
5.3	Activation energies for the thermal quenching of the band edge luminescence of β - and α -GaN as determined from (5.9) for the data shown in <i>Fig. 5.09</i>	56
6.1	Modell parameters for the excitation density dependent band edge transition intensity of α - and β -GaN.	68
6.2	Modelled radiative and nonradiative lifetimes for the band edge transition of α - and β -GaN assuming $n_o = 10^{17} \text{cm}^{-3}$	69
7.1	Lattice constants and group-III atom densities of zincblende nitrides [127] and GaAs.	74
8.1	Temperature dependent PL transition energies of the $\text{In}_{0.17}\text{Ga}_{0.83}\text{N}$ sample compared to the corresponding values of the β -GaN band edge transition X_C	91

Acknowledgements

I would like to thank everyone who made a positive contribution to this work and in particular

Prof. Dr. K.H. Ploog for having opened me the possibility to work at the Paul-Drude-Institute, for helping me to expand my knowledge about materials science, for his interest in this work, and his support;

Prof. Dr. I. Akasaki for having provided the α -GaN reference sample;

Prof. Dr. R. Brenn and *J. Portmann* for their cooperation regarding the structural and compositional analysis of my (In,Al,Ga)N samples by RBS;

Dr. O. Brandt for having supervised this work and for his skill to create a positive working atmosphere even under difficult circumstances;

Dr. L. Däweritz for having shared his experience in the fields of crystal growth and RHEED with me;

B. Drescher for having spent a lot of time and effort to prepare samples such that transmittance and reflectance measurements were possible;

Dr. G. Jungk for invaluable discussions about physics and his constructive criticism;

Dr. U. Jahn and *I. Poppe* for SEM and CL measurements;

Dr. B. Jenichen for having supported me in performing x-ray investigations;

Dr. M. Ramsteiner and *Dr. L. Schrottke* for assistance with optical setups;

I. Schuster for her never-ending motivation in doing (last-minute) photographic and repro jobs;

Dr. A. Trampert for analyzing many samples by means of (HR)TEM and SAD;

Dr. M. Wasserman for all the AFM and ellipsometry measurements he carried out and his encouragement;

G. Paris, *M. Reiche*, *H.-P. Schönherr*, *P. Schützendübe*, and *D. Spaniol* for technical assist;

and finally my parents and my friends for their moral aid and patience in times when my mind was filled but with MBE problems and my language was loaded with strange technical terms...

Curriculum Vitae of Jochen R. Müllhäuser

- 3/22/67 : Born in Freiburg, Germany
6/86 : *Abitur* at the *Kreisgymnasium Gundelfingen*
7/86–9/87 : Military service
10/87–10/93 : Studies of physics, mathematics and computer science
at the *Albert-Ludwigs-Universität zu Freiburg*
Physics Diploma (Prof. Dr. R. Brenn) :
High-resoluting XUV spectroscopy of fast ion-molecule collisions
Mathematics Diploma (Prof. Dr. G. Dziuck) :
Total-variation-diminishing schemes for hyperbolic equations
5–6/93 : Internship at Daresbury Laboratory, GB
Theory and Computational Science Division
Dr. P. Durham, Dr. D. Emerson
2/94–2/95 : Predoc at AT&T Bell Laboratories, Murray Hill, USA
Silicon Materials Research Department
Dr. L.C. Feldman
Since 2/95 : Doctoral student at the *Humboldt-Universität zu Berlin*
PhD thesis at the *Paul-Drude-Institut für Festkörperelektronik*, Berlin
Prof. Dr. K.H. Ploog, Dr. O. Brandt